# Mechanical Characterisation of Acetabular Soft Tissues: Experimental and Computational Study

Jiacheng Yao

Submitted in accordance with the requirements for the degree of
Doctor of Philosophy

The University of Leeds
School of Mechanical Engineering

December 2020

The candidate confirms that the work submitted is his/her own and that appropriate credit has been given where reference has been made to the work of others.

# Acknowledgements

I would like to thank everyone who have assisted with my work in this project. I would like to thank my primary supervisor, Dr. Alison Jones, in particular, for her helpful guidance and inspiring suggestions throughout the project. Special thanks to Dr. Marlène Mengoni and Professor Sophie Williams as well, for their great help and advice from their expertise in computational and experimental field. I also appreciate the bigger picture of this project provided by Professor Sophie Williams that links the two parts of my study together. This project cannot be done without the endless help from my supervision team.

I would like to thank every colleague in the institute of Medical and Biological Engineering (iMBE) who helped me to complete this project. Thanks to Dr. Qingen Meng, for his expertise in model solving; Dr. Aiqin Liu, for her experience in experiment set-up; Dr. Dawn Groves, for her expertise in experimental hip study; Dr. Anthony Herbert, for his experience in experimental loading; Dr. Nagitha Wijayathunga, for his absolute expertise in imaging techniques; and Phillip Wood, for his help and advice in experimental equipment and design. Special thanks to Dr. Fernando Zapata-Cornelio, although he has left iMBE by now, but the equipment (and experience) I borrowed from him played so important roles in my experimental study. Thanks to Professor Ruth Wilcox, Dr. Claire Brockett, and Dr. Louise Jennings, for their review and advice at the end each year during my study.

I am grateful for the love and support from my parents, my family and my fiancée. Their encouragement and trust are invaluable to me, and to my completion of this project. To my friends, either left Leeds or still in Leeds, I am grateful for your support and being very nice.

# Abstract

Abnormal hip contact mechanisms can be associated with acetabular soft tissue damage and the progression of osteoarthritis. One morphological cause of this abnormal mechanical environment is a cam-shaped femoral head that results in impingement with the acetabular rim and labrum during hip motions.

In this thesis, cam-type femoroacetabular impingement (FAI) related loading was mimicked on the acetabular cartilage-labral junction in vitro and in silico. During loading, computed tomography scans were obtained whereby radiopaque solution was used in order to separate acetabular soft tissues in the hip during contact. Measurements of overall cartilage strain were taken at the centre of the contact region and the labral apex displacement was established in three-dimensional space. The circumferential properties of the labrum were also assessed by re-loading the tissue sample following introducing a cut to the labrum.

Two-dimensional finite element models of the femoral head and acetabulum were developed based on an image slice through the centre of the contact region. Geometrical features of the acetabulum and femur at the contact site were captured in the models. Computational results were compared with experimental results. A parametric study was conducted on the models for verification and for investigation of hip parameters regarding the soft tissue behaviour under load.

Contact occurred at the anterior-superior region of the acetabulum in all samples, as would be expected if the conditions of cam-type FAI were replicated. The cartilage strain ranged from 20% to 60% and the labrum maximum displacement ranged from 1.5 to 5.0 mm, measured from CT scans in all samples. The circumferential effect in the labrum was demonstrated with an averaged factor of 1.4 of increase in the labrum apex displacement per applied force in labrum-cut cases. The cartilage strain and load distribution in soft tissues were found to be sensitive to the femoral head position in the computational models, with strain differences up to 41% and cartilage contact force differences up to 237%. The ratio between the cartilage and labrum Young's modulus affected the tensile strain at the cartilage-labral junction by up to 14%. The position of cartilage-labral junction affected the total contact force on the soft tissue by up to 49%.

This work measured the soft tissue behaviour under cam-type FAI loading via an experimental approach and characterised the soft tissue behaviour under various set-ups via computational approach. The importance of adapting reliable tissue alignment and three-dimensional modelling were highlighted. It can be concluded that, stiffer labrum compared to the cartilage, along with focused loading at the cartilage-labral junction, would cause high strain in the cartilage and concentrated tensile strain at the junction, suggesting the damage mechanism in hips with FAI.

# Table of Contents

## List of Figures

# List of Tables

# Abbreviations

| | |
|---|---|
| 2D | Two-dimension |
| 3D | Three-dimension |
| BW | Body weight |
| CAD | Computer-aided design |
| CCD | Centrum collum disphyseal |
| CE | Centre edge |
| CT | Computed tomography |
| DIC | Digital Image Correlation |
| DVC | Digital Volume Correlation |
| DVRTs | Differential variable reluctance transducers |
| ECM | Extracellular matrix |
| FAI | Femoroacetabular impingement |
| FE | Finite element |
| FEA | Finite element analysis |
| LCC | Labrum cut coefficient |
| MRI | Magnetic resonance imaging |
| NaI | Sodium Iodide |
| OA | Osteoarthritis |
| PBS | Phosphate-buffered saline |
| ROM | Range of motion |
| SD | Standard deviation |
| TAL | Transverse acetabular ligament |

# Chapter 1

# Introduction

## 1.1 Background

Musculoskeletal pain and degeneration are responsible for 30% of general practice consultations in England, with the resulting osteoarthritis (OA) conditions affecting more than 8.75 million people in the UK (NHS, 2019). OA is not only an issue of thinned cartilage (Versus Arthritis, 2018), but also associated with abnormalities in periarticular soft tissues such as ligaments, muscles, and nerves (Brandt et al., 2006). The factors which cause OA can be classified as genetic contributions, influence of aging and change in mechanical condition (Goldring and Goldring, 2007), all leading to alterations in the biomechanical environment of the joint. When an abnormal biomechanical environment is established, soft tissue damage is often involved, and the body responds to try to maintain the function of the joint. The articular cartilage thins and roughens under abnormal loading scenarios. Consequently, osteophytes grow at the bone edge and the synovium is thickened to provide more synovial fluid. Bony parts can rub against other tissues due to limited space in the joint during movement. Such soft tissue damage and alteration in joint structure cause further instability and pain in the joint, and ultimately progresses to OA.

Hip soft tissue damage in younger people can be caused by bony abnormalities and repetitive extreme loading conditions over time. Femoroacetabular impingement (FAI) is a hip mechanism associated with abnormal bony morphology, causing excessive contact and potential soft tissue damage (Leunig et al., 2009). FAI can be classified as follows: 1) cam-type, excessive bony part is found at the femoral head-neck junction; 2) pincer-type, over-coverage of acetabular rim is observed on the acetabulum; 3) mixed-type, both of cam-type and pincer-type are observed in the hip joint (Ganz et al., 2003). A previous study found that cam-, pincer-, and mixed-type FAI have accounted for 47.6%, 7.9%, and 44.5% of hips that underwent surgical intervention for symptomatic FAI

(Clohisy et al., 2013). The patient group had an average age of 28 (ranged from 11 to 68) and an average BMI of 25.1 (ranged from 15 to 53), with males predominantly diagnosed with cam-type FAI and females predominantly diagnosed with pincer-type FAI (Kuhns et al., 2015). FAI is often diagnosed clinically under magnetic resonance imaging (MRI) or computed tomography (CT) (Leunig et al., 2009). The abnormal contact caused by FAI leads to overloading of the soft tissues near the acetabular rim, primarily the labrum and the cartilage (Ganz et al., 2003). Frequently repeated activities with wide range of motion (ROM) can also lead to overloading, exacerbating the issue of bone abnormalities.

Chondral lesions are often observed, caused by either axial loading or rotation in hip movement, as a result of FAI (Ganz et al., 2003; Byrd 2013). In cam-type FAI, the non-spherical femoral head pushes the labrum away from the head centre through hip rotation and shears the edge of the articular cartilage. In pincer-type FAI, the anterior labrum is compressed from the apex by the femoral neck under hip flexion. Soft tissue defects at anterior-superior portion of the peripheral acetabulum are observed in approximately 70% of the symptomatic hips with FAI (Clohisy et al., 2013). Chondral lesions include cartilage delamination and labral tears (Tibor et al., 2012), causing hip pain and limited mobility in the patient.

Early-stage treatments for FAI aim to relieve pain and minimise damage, in order to delay the progression of OA and the need for a hip replacement. Femoral neck osteoplasty and periacetabular osteotomy are potential surgical interventions for cam- and pincer-type FAI respectively. The surgeries are designed to optimise the conformity of the hip joint and improve functionality. Chondroplasty, a surgical treatment for partial cartilage repair, is performed on damaged acetabular articular cartilage in 40% of the hips with FAI (Clohisy et al., 2013). Labral intervention is performed in two forms as refixation (48%) and as partial resection (28%) of the labrum. It has been suggested as advantageous to reattach the labrum when possible as the absence of labrum might lead to OA (Leunig et al., 2009).

However, soft tissue damage occurrence and progression are not yet well understood with respect to abnormal contact conditions. Therefore, there is a need to develop a method for characterising soft tissue behaviour before efficient treatment can be established. By understanding the *in situ* tissue properties, models can be developed to better predict the tissue behaviour under various pathologic loading conditions. The damage mechanism can be better understood regarding the type of damage seen clinically.

Finite element analysis (FEA) is a computational method which can aid the understanding of the mechanical environment and predict material behaviour under specific loading conditions. Chegini et al. (2009) developed parameterised hip models with cam- and pincer-type FAI for measuring contact pressure and stress under walking and stand-to-sit routines. Ng et al. (2012) and Jorge et al. (2014) investigated stress on cartilage using subject-specific hip joint models with cam-type FAI during standing, squatting, and joint compression with full rotation. Hellwig et al. (2015) investigated cartilage behaviour due to cam-type FAI using simplified hip joint geometry with and without cam feature.

The articular cartilage and the labrum were modelled as isotropic elastic materials by Chegini et al. (2009), Ng et al. (2012), and Jorge et al. (2014), and these material properties came from tests of the individual tissues measured in isolation from each other. The toe region of stress-strain curve in bovine labrum (Ferguson et al., 2000) was adapted by Chegini et al. (2009), Jorge et al. (2014) and Hellwig et al. (2014). Cartilage properties were adapted from knee models (Chegini et al., 2009 and Ng et al., 2012), or were measured from indentation tests in human cartilage osteochondral specimens (Jorge et al., 2014; Hellwig et al., 2014). The labrum was modelled as a triangular extrusion from the cartilage, hence an abrupt change of material properties was always formed at the acetabular rim.

Studies by Ferguson and Crawford have shown that the role of the labrum is more than simply an extension of cartilage. Ferguson et al. (2000) demonstrated the sealing effect of labrum, whereby the labrum circumferentially seals a layer of fluid inside the hip joint. Crawford et al. (2007) demonstrated improved joint stability with the aid of labrum, which further proved the circumferential stress it provides. From histologic perspective, Seldes et al. (2001) suggested a transition zone of 1 to 2 mm between the cartilage and the labrum tissue, demonstrating the importance of considering this in terms of how the tissue is modelled.

From an anatomical perspective, labral soft tissues are formed by collagen fibres connecting in a circumferential manner (Bsat et al., 2016). Excised tissue samples will therefore behave differently to tissues *in situ* since the internal tension is broken. Current experimental investigation of hip soft tissues have considered material properties in isolation but ignored the *in situ* effects. There is a research gap in experimentally quantifying acetabular soft tissue behaviour under FAI-related loading *in situ*. It is also important to perform verification and parametric studies that assess the experimental settings and model assumptions on follow-up finite element (FE) models.

## 1.2 Aims and objectives

The overall aim of this study was to characterise the behaviour of cartilage-labral junction tissues *in situ* under conditions which are relevant to cam-type FAI, in order to improve the representation of this critical area of the joint in current impingement modelling. The FE models can also be used to better understand the damage mechanism and predict tissue behaviour under cam-type FAI.

The aim of the experimental study was to measure the behaviour of the *in situ* tissues under the type of focused pressure on the cartilage-labral junction which is thought to generate damage in cam-type FAI. The aim of the computational study was to test the sensitivity of the tissue deformation to various experimental settings and typical modelling assumptions.

The objectives of this research were to:

1. Establish and test experimental methods to record cartilage-labral junction tissue behaviour *in vitro* under axial loading relevant to cam-type FAI. The contact was aimed at the anterior-superior region of the acetabular cartilage-labral junction through the femoral head, which matches the damaged contact region commonly observed in cam-type FAI in clinic.
2. Develop image processing and computational methods to quantify the cartilage-labral junction behaviour under loading relevant to cam-type FAI. The acetabular cartilage strain was measured, reflecting the mechanism for cartilage defibrillation. The labrum apex displacement was measured, reflecting the mechanism for labrum tear due to high deformation.
3. Investigate the effect of labrum circumferential tension by comparing the labrum apex behaviour with intact labrum and with labrum cut. In clinic, the labrum cut may occur in hips with torn labrum or after labrum resection.

4. Create parameterised FE models which capture the cartilage-labral junction with subject-specific features. The tensile strain at cartilage-labral junction was obtained, potentially reflecting the mechanism for cartilage delamination and labrum tear.
5. Conduct sensitivity analysis on the effect of: 1) femoral head position; 2) ratio of labrum to cartilage material properties; and 3) position of cartilage-labral junction; regarding the outputs of interest.

# Chapter 2

# Literature review

## 2.1 Introduction

The literature review includes the basic hip joint anatomy and previous studies of soft tissue damage assessment via experimental and computational approaches. Firstly, the hip joint morphology is introduced, including normal hip anatomy, hip mechanics and hip with FAI. Differences between hips with and without FAI are explained. The hip geometry can be quantified regarding the cam abnormality, which provides understanding and assessment criteria for FAI. Previous experimental quantification of soft tissue damage are included. The findings provide measurable parameters which have the potential to predict the tissue damage during impingement or hip motions. Finite element (FE) studies of hip with impingement condition are reviewed, offering effective model set up, computational methodology and damage investigation. The strengths and limitations of current methodologies are understood from previous studies on acetabular soft tissue.

## 2.2 Hip joint morphology

### 2.2.1 Normal hip anatomy

The hip joint is the articulation between femoral head and acetabular cavity (Palastanga et al., 2011). It is a major synovial joint that provides load support and facilitates locomotion. The hip joint is formed by the femur and acetabulum, and is surrounded by a ligamentous capsule. The subchondral bones are covered with articular cartilage, on both femoral and acetabular sides, to form the articulation. Femoral cartilage, acetabular cartilage and acetabular labrum are soft fibrous tissues that contribute to the functionality of hip (Figure 2.1 and Figure 2.3).

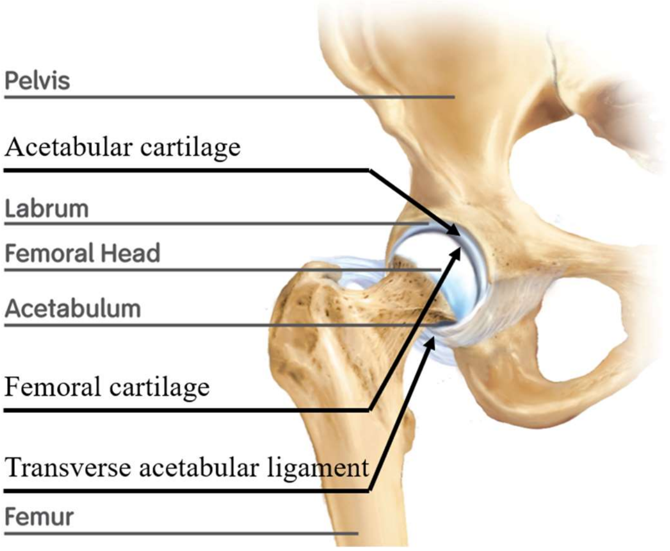

**Figure 2.1 Structure and components of human hip joint (figure source: Gileshugo 2011, under CC0 license).**

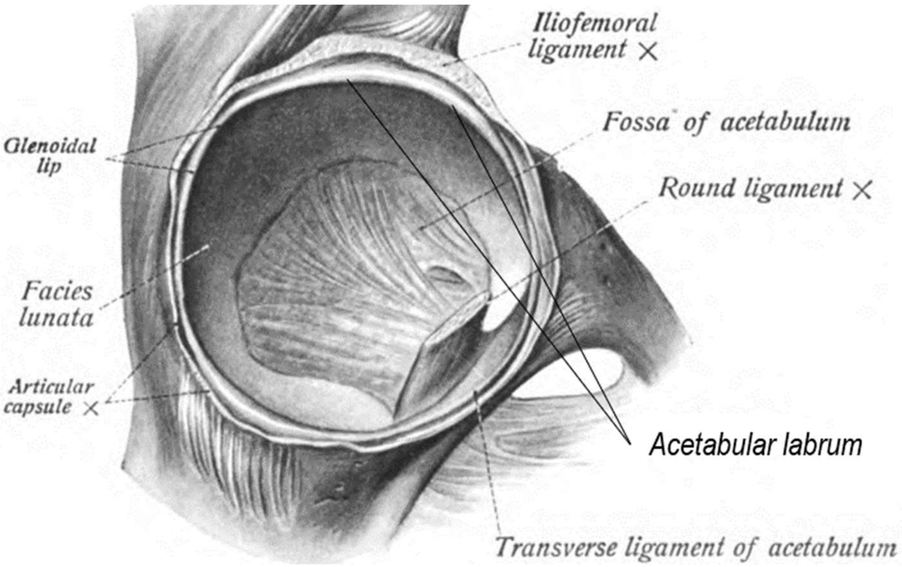

**Figure 2.2 Structure and components of human acetabulum socket (figure source: Sobotta 1909, under CC0 license).**

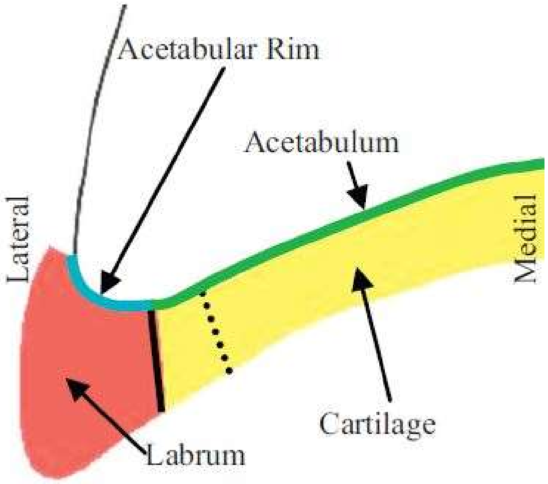

**Figure 2.3 Cross section view of acetabular rim. Solid line indicates the boundary between labrum and cartilage at the coincidence of concave acetabulum and convex rim. Dotted line suggests an alternative boundary at medial where the labrum is relatively longer. (figure source: Henak et al., 2011, under CC-BY license).**

The femur, also known as the thigh bone, is the longest bone in human body that connects the hip with the knee. The proximal end of the femur, or femoral head, is covered with articular cartilage and has contact with the acetabulum. The acetabulum forms at the union of ilium, ischium and pubis. The acetabular cavity is covered by articular cartilage and attached to the labrum at its rim (Figure 2.2). The transverse acetabular ligament (TAL) forms a closed soft tissue rim on the acetabulum by connecting the labrum at the gap of the acetabular edge. The joint is filled with synovial fluid that provides lubrication and prevents direct contact between the cartilage on the femoral head and acetabulum.

The acetabular capsule includes the iliofemoral, ischiofemoral and pubofemoral ligaments (Walters et al., 2014). The ligaments capsule surrounds the hip joint and prevents the hip from dislocation. The capsule originates at the bony rim of acetabulum and inserts into the femoral neck (Figure 2.2), creating small recess between the femoral cartilage and labrum. The capsule can therefore provide constraint to the joint when the hip achieves extreme motions.

Articular cartilage functions in terms of loading-bearing and as an articulating surface. Cartilage contains a fluid phase (water) and a solid phase which comprises collagen fibres and proteins. The fluid plays an essential role in instantaneous load support and lubrication. The collagen fibres contribute to the elastic behaviour of the cartilage.

The acetabular labrum is a cartilaginous soft tissue that is attached to the acetabular rim (Bsat et al., 2016). The location of labral attachment is illustrated in Figure 2.3. The labrum is triangular in cross-section, attaching to the bone and acetabular cartilage. The width of the labrum root measures up to 5.4 mm from the superior-anterior. The thickness of the labrum measures up to 5.5 mm from the superior-anterior (Seldes et al., 2001) The labrum joins the articular cartilage at an averaged thickness of 1.26 mm. It is worth noting that the transition zone of labrum and cartilage is of 1 to 2 mm wide instead of a distinct line (Seldes et al., 2001). The labrum plays a key role in sealing the joint fluid, as well as maintaining hip stability and increasing the contact area between femur and acetabulum.

Collagen fibres are oriented circumferentially in the labrum, which makes the labrum vulnerable to shear forces that act parallel to the articulating surface. One common labral pathology is labrum tearing, that often associated with hip abnormalities, which is discussed in section 2.2.3. Labral tears can be classified either by: 1) location, at tip or at cartilage junction; 2) aetiology, due to degeneration, idiopathic, trauma, and congenital; or 3) morphology, due to FAI or dysplasia. Labral tear regions often coincide with area with increased labrum strain, and found at the anterior-superior region specifically in FAI.

### 2.2.2 Hip movements and loads in anatomical planes

Locations in the body can be described with respect to three planes which are coronal, transverse and sagittal. Hence all the movements can be broken down into six directions based on anatomical planes (Figure 2.4). The orientation of the acetabulum cup is described by the inclination angle measured from the coronal plane, and the anteversion angle measured from the sagittal plane. It is also possible to describe morphological features by introducing parameters measured from coronal plane, which will be mentioned in section 2.2.3.

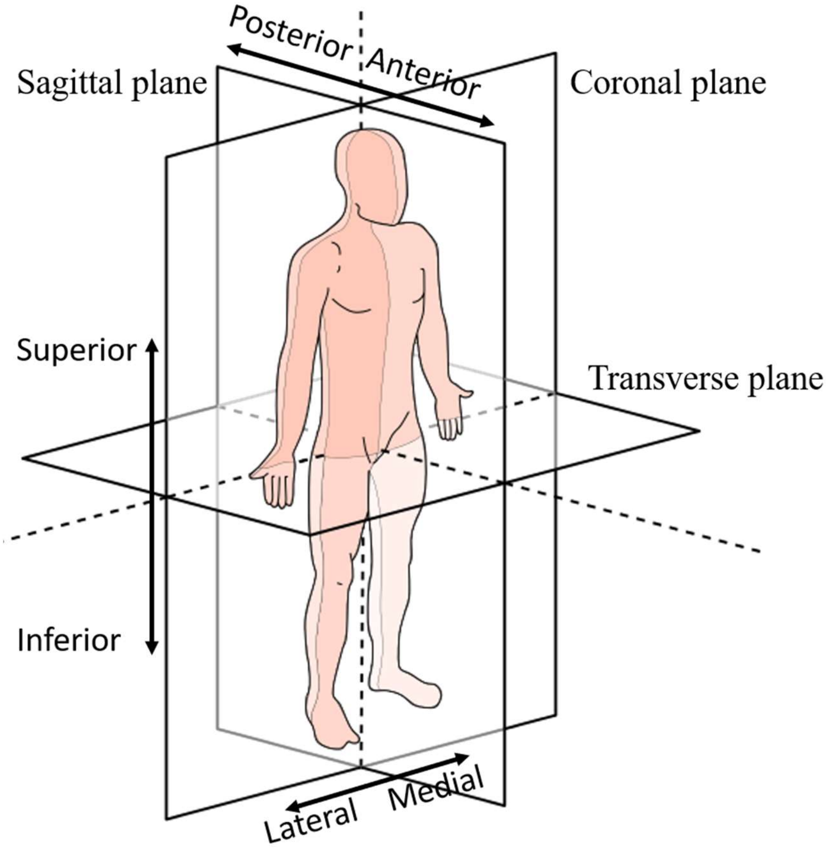

**Figure 2.4 Anatomical planes of human body and clinical directions (figure source: Carl Fredrik Sjöland 2014, under CC0 license).**

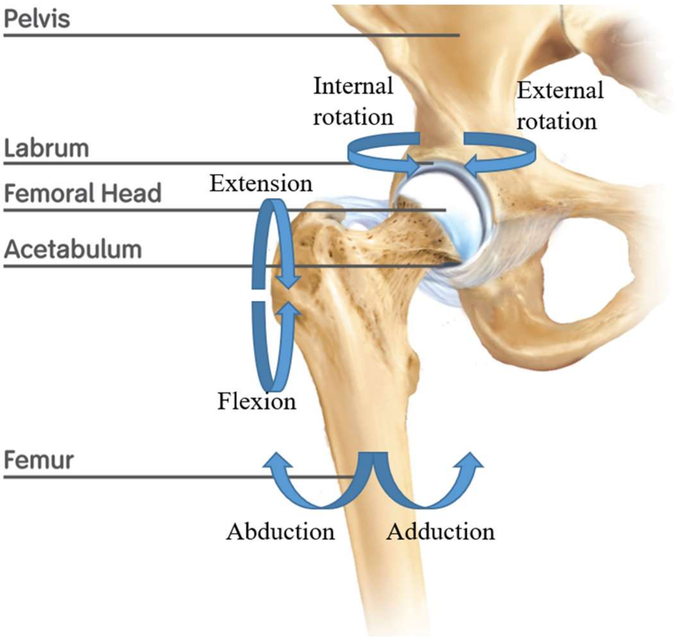

**Figure 2.5 Schematic of hip motions. (figure source: Gileshugo 2011, under CC0 license).**

The hip joint can be described as an enarthrodial (ball in socket) joint, which allows a wide range of motion (ROM) (Palastanga et al., 2011). All six basic motions including flexion and extension in sagittal plane, abduction and adduction in coronal plane and internal and external rotation in transverse plane are shown in Figure 2.5.

The ROM in activities is highly dependent on individuals. Hemmerich et al. (2006) recorded the ROM of 30 people, including 20 male and 10 female, whose mean age was 48.2 years with standard deviation (SD) of 7.6 years. The activities investigated were squatting, kneeling and sitting cross-legged. The mean values of the maximum angle of rotation in each direction during activities is shown in Figure 2.6. The SD were relatively high, compared to the data range. The variation could be caused by morphological features (Miki et al., 2007), gender differences (Czuppon et al., 2016), or muscle strength (Pua et al., 2007).

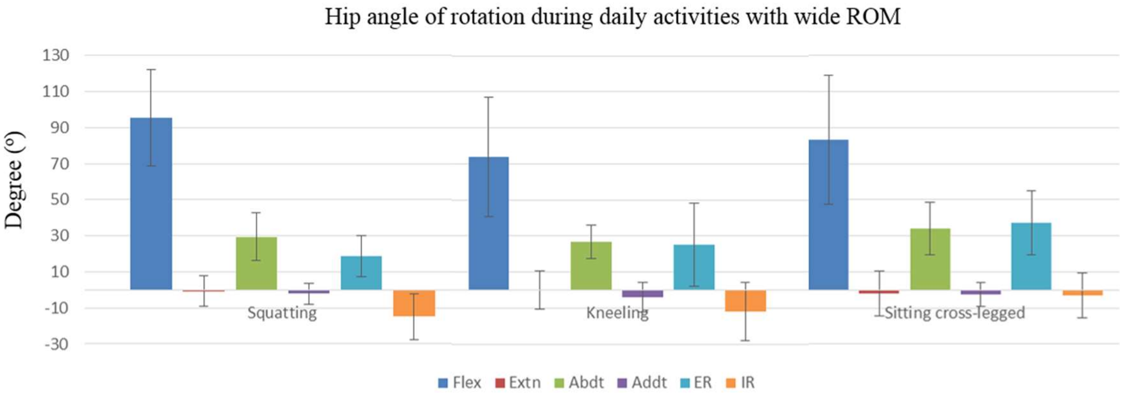

**Figure 2.6 Hip angle of rotation during daily activities with wide ROM. Flex, flexion; Extn, extension; Abdt, abduction; Addt, adduction; ER, external rotation; IR, internal rotation. (figure source: Hemmerich et al., 2006, under CC-BY license).**

An additional force vector is combined with the three rotation to fully describe the hip activities. Bergmann et al. (2001) calculated the hip contact force of total hip implants *in vivo*. Four patients were asked to perform nine activities including walking, standing up, sitting down, standing on one leg, knee bend, ascending and descending stairs. The mean peak loads for four patients ranged from 1.17 to 3.69 times of body weight (BW) during all daily activities investigated.

### 2.2.3 Morphology of hip joint with femoroacetabular impingement

Variation in shape and structure of tissues are observed in individuals for reasons that are not clear. These abnormalities can cause impingement between femur and acetabulum during hip movements. Zadpoor (2015) reviewed the prevalence of femoroacetabular impingement (FAI) in athletes. Evidence has shown that athletes experiencing repetitive impact-like activities, typically weight-bearing and high flexion angle together with rotation (Agricola and Weinans, 2016), undertake higher risk of development of FAI. Agricola et al. (2014) and Roel et al. (2014) reported increased chance of femoral deformity development in young athletes due to open growth plates. Roel et al. (2014) further reported higher risk of formation of the cam deformity during hip flexion and external rotation in young hip with open growth plate.

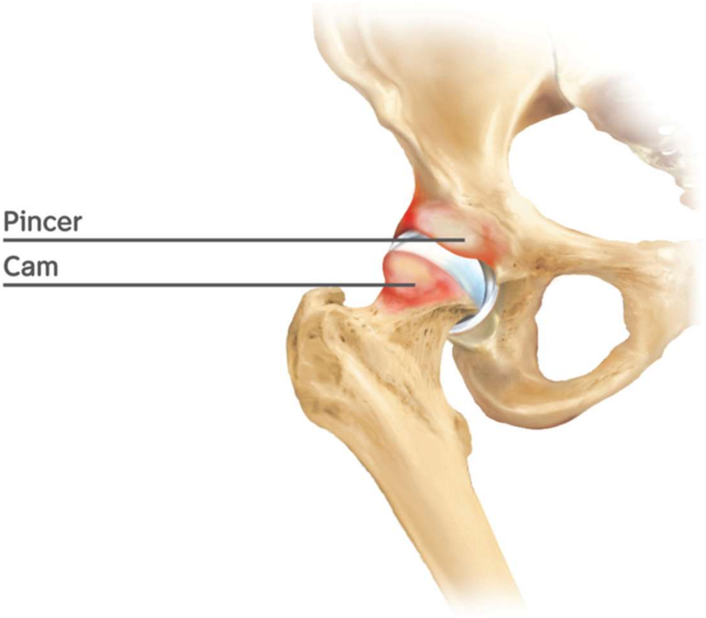

**Figure 2.7 Classification of femoroacetabular impingement (figure source: Smith & Nephew 2011, under CC0 license).**

FAI can be classified as pincer-type, cam-type and mixed-type (Figure 2.7) depending on the locations of the abnormalities. Pincer-type FAI is characterised by an extension of tissue at the acetabular rim which causes over coverage of femoral head. Cam-type FAI defines additional bony part at the anterior femoral head and neck junction which creates cam mechanism in hip movements, thus contacting the acetabular rim during rotation and flexion. Mixed-type FAI includes both type of abnormalities and counts for 44.5% of occurrence patients in a review among 1130 symptomatic hips (Clohisy et al., 2013), while 47.6% and 7.9% of hips had a diagnosis of cam and pincer respectively. All three FAI would lead to soft tissue damage, hip joint pain and reduced ROM. This project will be particularly focused on the cam-type FAI.

Assessment of cam deformity in 3D has been developed by Cooper et al. (2017) with the aid of CT images. Additionally, MRI is used for visualisation of soft tissue such as labral abnormalities (Leunig et al., 2009) in particular. However, clinical measurements are commonly taken from planar radiograph for diagnosing the severity of FAI (Streit et al., 2012). Measurements of three radiographic signs of hip abnormality in the coronal plane are shown in Figure 2.8.

The ROM of normal hip movement is listed in Table 2.1, summarised from Figure 2.6. Specific combination of hip rotations were established for clinical evaluation of impingement (Martin et al., 2010). The patterns include:

- Dynamic External Rotatory Impingement Test (DEXRIT)
- Dynamic Internal Rotatory Impingement Test (DIRIT)
- Posterior Rim Impingement (PRI)

**Table 2.1 Normal activities with high ROM and FAI testing patterns**

| | Flexion | Extension | Abduction | Adduction | Internal rotation | External rotation |
|---|---|---|---|---|---|---|
| High ROM activities | 95.4 | 1.9 | 34.1 | 4.0 | 37.1 | 14.9 |
| DEXRIT | 90 | 0 | Wide | 0 | 0 | Wide |
| DIRIT | 90 | 0 | 0 | Wide | Wide | 0 |
| PRI | 0 | Wide | Wide | 0 | 0 | Wide |

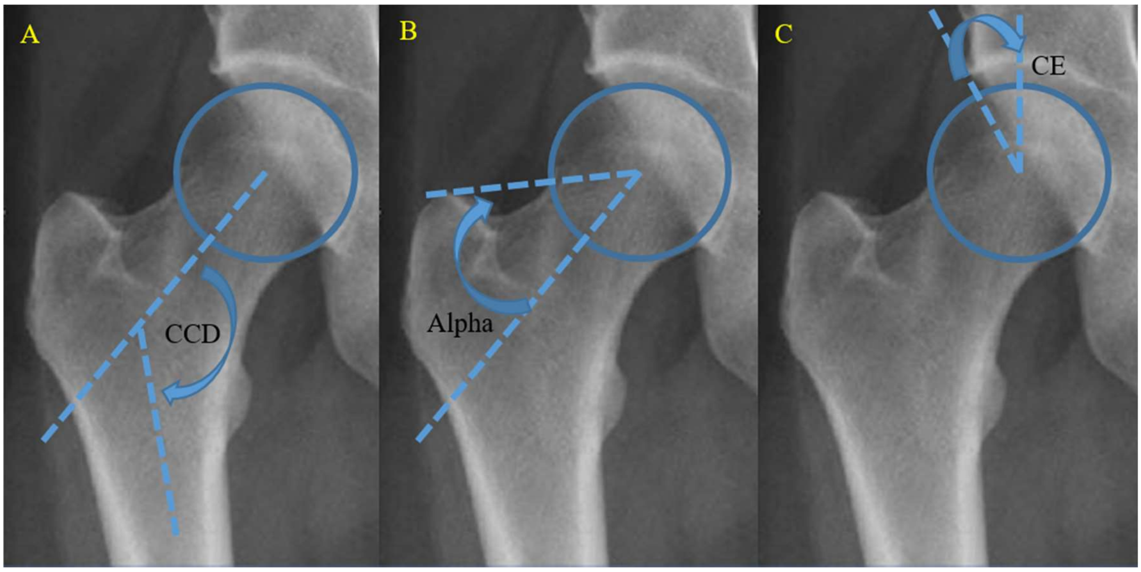

**Figure 2.8 Radiographic measurements for femoral head shape abnormality. A, measurement of centrum collum disphyseal; B, measurement of alpha angle; C, measurement of centre edge angle. (figure source: Röling et al., 2020, under CC-BY-SA license).**

The centrum collum disphyseal (CCD) angle (Figure 2.8-A), also known as the neck angle, is defined as the angle between the longitudinal axis of femoral neck and femoral stem (Tannast et al., 2007). The CCD angle indicates the extent to which the proximal end of the femur is straight. Normal CCD angle is greater than 125$^{o}$ while lower values can imply cam-type FAI.

The alpha angle (Figure 2.8-B) is used for assessing the sphericity of the femoral head. A line is drawn connecting the centre of femoral head and the point where the femoral head stop being spherical. The alpha angle is measured between the line and the neck axis. The alpha angle is commonly measured for the assessment of cam size. The alpha angle is usually less than 50$^{o}$ while higher values may indicate cam-type FAI (Tannast et al., 2007). Additionally, Harris et al. (2013) measured the alpha angle on the frog-leg lateral view. It is suggested that the alpha angle alone in the projection plane may not well-define the actual size of cam deformity.

The centre edge (CE) angle (Figure 2.8-C) is used for assessing the coverage of acetabular rim. A line is drawn connecting the centre of femoral head and the point where acetabular rim ends in the view. The CE angle is measured between the line and the superior-inferior axis. Normal CE angle is reported to range from

$25^o$ to $39^o$ (Tannast et al., 2007), whilst lower values can indicate dysplasia and higher values can indicate pincer-type FAI.

Traditional plain radiograph is often taken at the coronal plane of the body. However, the hip and its deformity are oriented in 3D. The cam may not be located purely coronally hence the plain radiograph may not be able to capture the full geometry of the hip abnormality. Therefore, 3D radiograph such as CT is required to better investigate the size and location of hip abnormality at various views. Masjedi et al. (2013) measured the cross-section area on the femoral head-neck junction in 3D along the neck axis for evaluation of the severity of the cam abnormality. The overall head-neck surface area ratio not only agreed that the cam hips (2.42±0.11) have “fatter” neck than the normal hips (2.67±0.09) do, but also showed that male have slightly “fatter” neck in normal hips and much severer deformity with cam-type FAI.

There is disagreement in the clinical literature about weather cam-type FAI subjects have particular acetabular features. Beck et al. (2004) diagnosed 149 hips into three categories: 1) cam-type, by the asphericity of the femoral head; 2) pincer-type, by the coxa profunda (deep socket); and 3) combination of the above two, which is believed to occur in most cases (123 out of 149) and the resulting damage to the cartilage often showed evidence of damage patterns of the two. However, Cobb et al. (2010) reported that there are differences in acetabulum geometry between hip impingement. The study showed that the cam hips were shallower than normal hips, and significantly shallower than pincer hips in subtended angles (84°±5°, 87°±4°, 96°±5° respectively). Therefore, the labrum rim could be in a smaller scale in cam hips and subject to different damage mechanism between cam and pincer FAI.

## 2.3 Tissue damage due to cam deformity

Cam deformity is responsible for the abnormal contact of the femoral head with the acetabular cartilage and labrum (Kuhns et al., 2015). The acetabular cartilage is subjected to compressive and shear forces when the cam lesion passes through the acetabulum during hip rotation. The labrum is translated away from the cavity and pushed outwards from the socket. Schematic drawings of cam-type FAI during hip movement are shown in Figure 2.9.

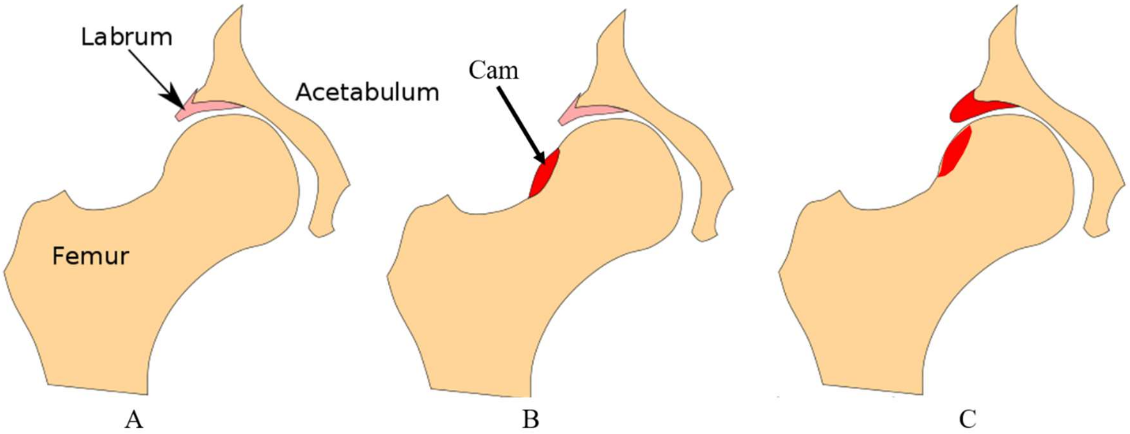

**Figure 2.9 A hip with cam-type FAI before and after rotation at the cross section view of the cam deformity. A, normal hip; B, hip with cam-type FAI; C, as the femoral head rotates, the cam was brought into contact with the rim, causing compressive and shear forces to the labrum. (figure source: Hellerhoff 2018, under CC0 license).**

Repetitive abnormal contact in the long term can ultimately cause soft tissue damage despite the viscoelastic property. The water content and collagen fibres in soft tissues play important roles in load bearing and recovery after load. The glycosaminoglycans (GAG) is trapped within the collagen fibres and are negatively charged to provide swelling pressure (Hingsammer et al., 2015). However, repetitive loading can cause fatigue in the tissue and lead to permanent damage. Loss of GAG content is one of the earliest signs of cartilage degeneration and is often associated with OA.

The abutment of the cam deformity is most evident during flexion with rotation, and results in labrum detachment and cartilage abrasion (Banerjee et al., 2011). Compressive and shear stresses at the superficial surface of cartilage can lead to delamination from the middle surface and labrum (Kuhns et al., 2015). The subchondral bone is reported to have increased thickness (Bieri et al., 2019) and increased modulus (Haider et al., 2016) in the patients with cam-type FAI. This abnormal hip contact would progressively load the cartilage and cause pain from the bone. Acetabular cartilage lesions are usually found at the superior and superior-anterior region with cam-type FAI (Beck et al., 2004). Strain and bending of labrum can cause labral tears around the transition zone, where the soft tissue properties gradually change from cartilage to labrum. Additionally, it has been observed practically that wide ROM such as the impingement test could also cause pain in hip joint tissue for most people even without radiographic evidence of FAI (Malviya, 2016). Furthermore, it has been suggested that FAI can be a precursor to OA. Ganz et al. (2003) highlighted the chondral injuries and labral detachment caused by cam impingement. The correlation of labral lesion with cartilage degeneration has also been noticed in the study of 400 hip arthroscopies. Agricola et al. (2013) conducted a follow-up study on 1002 early-stage OA patients. It is reported that severe (alpha angle > $83^o$) cam deformity has higher risk of progression to end-stage OA than moderate (alpha angle > $60^o$) cam deformity does.

Early-stage conservative treatment includes physiotherapy, use of anti-inflammatory drugs, or modification of activities, that aims to preserve the tissues and joint. Surgical treatment includes cam lesion resection, cartilage resurfacing, labrum resection, or labrum repair, that usually come with hip arthroscopy.

## 2.4 Experimental quantification of soft tissue behaviour

In order to gain better understanding of the level of soft tissue damage, research groups have attempted to quantify soft tissue behaviour during hip motions. This section will review the methodology and findings on experimental approach to measure labral strain during hip rotation.

Dy et al. (2008) investigated the labral strain on seven cadaveric acetabulums using strain markers and roentgen stereophotogrammetric analysis. Two rows of markers were implanted into the labrum, along with a third row on the free edge of the labrum and another row on the acetabulum. The area of investigation was focused to the anterosuperior location, which is prone to common labral injury. It was therefore important to prevent movement and slipping of the marker. Placing markers along the circumferential direction of the entire labrum could also help offer a general strain map of the labrum. The loading conditions were derived from the activities that would lead to labral injury, including axial loads, flexion-extension, external rotation, torque in abduction and torque in external rotation.

Mean radial strain was found to range from 2.1% to 6.9%, with the maximum value at 13.6%. Mean circumferential strain was found to range from -0.3% to 4.7%, with the maximum value at 8.4%. The results were not directly comparable with other studies due to different loading conditions applied, while the study provided a range of labral strain in axial and circumferential directions. Displacement of the femoral head was observed as a result of the applied moment, which may also be responsible for labral lesions. Among all the components of hip loading manoeuvres, external rotation and abduction were found to have a greater effect on labral strain than flexion and extension did. The donors had a mean age of 79±11 years, which is older than the population suffering hip joint damage. The influence of aging and degeneration of soft tissues should be taken into consideration.

Safran et al. (2011) investigated the labral circumferential strain on twelve cadaveric acetabulum. Differential variable reluctance transducers (DVRTs) were implanted into the midportion of the labrum by cutting windows of 10 *10 mm on the capsule. The procedure led to low reproducibility and provided labral strain at uncertain locations. The insertion primarily focused on the anterior, anterolateral, lateral and posterior portion of the labrum. The circumferential strain at midportion was determined under hip joint rotation, including flexion-extension, abduction-adduction, internal and external rotation. Mean changes in labral strain was found to range from -3.4% to 2.8%. The values were very low due to lack of loading and the location investigated. It is reasonable to expect higher deformation at the free edge of labrum than at the midportion. The labrum had limited width so that the strain was only measured in circumferential direction. The results could be improved if a more reliable apparatus was used. The same concern as mentioned before is that the average age of donors was greater than that of the population undergoing hip damage.

Dy et al. (2008) and Safaran et al. (2011) both investigated labral strain under hip motions. Results from both studies were not comparable due to the location of investigation and hip motions applied. Dy et al. (2008) considered rotational torque and measured at the superficial surface, while Safaran et al. (2011) only applied full degree of rotation and measured into the midportion of labrum. The strain marker could be placed in wider portion of labrum to obtain more general view of labral behaviour. It would also be possible to investigate the difference in deformation along the labral rim. Furthermore, hip loading is responsible for the progression of labral lesions which should be included in the hip motions. Force vector should be included and be derived on a subject-specific basis in order to replicate more realistic loading conditions. Additionally, variation in material properties due to donor age, morphological differences and diseases remains important in the prediction of quantification of hip tissue changes.

Ferguson et al. (2001) measured the compressive modulus and permeability of bovine labrum by taking 2 mm thick section at the labrum rim. Test specimens considered both circumferential and planar directions of the labrum, but in dissected labral sections. The circumferential tension was therefore not included in labrum deformation. Tensile strain was tested by taking rectangular specimens along the apex. The near-linear region of the stress-strain curve observed higher Young’s Modulus at the posterior (E=88.40±49.81 MPa) compared to that at the superior (E=60.90±55.53 MPa).

It can be learned that the labrum strain was measurable during hip movement, at 13.6% of local strain (Dy et al., 2008) or at ±3% *in situ* (Safran et al., 2011). The labrum Young’s Modulus vary along the rim and have an averaged value of 74.65±44.34 MPa in bovine labrum. However, there is a lack of study in measuring cartilage deformation with labrum displacement *in situ* during hip movement. There is a need for quantifying soft tissue behaviour *in situ.* The *in vitro* material properties can then be calibrated based on experiment observation, and hence improve the reliability of the FE prediction.

## 2.5 Finite element analysis of hip joint

### 2.5.1 Introduction

The finite element (FE) method is a numerical approximation technique used for approaching the solutions to complex models (Fagan 1992). FE method can be implemented into models with complex geometry and well-defined conditions. The complex geometry is divided into a series of small simple entities, also known as elements, that are linked by nodes. Nodes can be assigned to the structure at various density, depending on the area of interest. Elements can be created by connecting adjacent nodes on the model. A variety of element types are available for the structure analysis. Material properties are assigned to the model, defining how the elements behave under specified loading conditions. Interfaces and interaction can be defined to determine the bond or contact relationship between sets of elements. Loads and constraints are defined to replicate specific working condition of the model. FE analysis can then solve the model by solving the theoretical mechanics equations, while simplification and assumption were usually applied, and provides various outputs of interest such as stress and strain. Both commercial and open source software packages are available, for instance Abaqus (Dassault Systèmes Simulia Corp., Providence, RI, USA) and FEBio (Musculoskeletal Research Laboratories, University of Utah, Salt Lake City, UT, USA), which are designed for developing and processing FE models.

There is potential for FE models to help understand the mechanical environment and deforming mechanism in the hip joint. Once a model has been generated with adequate accuracy, it can be analysed to save experimental samples, or even in the way that is not doable in the experiment. Since each property and input are defined numerically, sensitivity tests can be performed easily that help identify the key factors governing the result. However, there are challenges remaining in the FEA of hip joint. The complexity of material properties needs to be established as an accurate representation of the real soft tissue. Loads and boundary conditions are required to replicate the hip movements as close as possible. Last but not least, verification and validation steps need to be conducted before results become reliable. This section includes the model set up from previous hip studies, followed by damage prediction measures using FEA.

### 2.5.2 Geometry representation

The geometry of an FE model describes the shape and structure of its parts, as well as the relative position of different components. Model geometry is either taken from images that are segmented and directly smoothed or is approximated by parameterisation of key features. Models built from segmented images allow clinical representation of a patient specific anatomy but often have the inconvenience that the geometry is not smooth enough to allow efficient FEA. The geometry and meshes often need resurfacing and smoothing (Ng et al., 2012). Advantages of parameterisation is that it allows geometrical sensitivity tests and variation of e.g. the CE angle and alpha angle (Chegini et al., 2008; Cooper et al., 2017) to study the effect of cam impingement and dysplasia. Parameterisation can be done with generic shapes forming the hip based on a spherical component (Chegini et al., 2008; Hua et al., 2015). Alternatively, the geometry can be generated by adapting subject-specific parameters from clinical images (Cooper et al., 2107). However the cartilage layer is usually built as an extension of the bone surface, either with constant thickness (Chegini et al., 2008), to fill the space between the femur and the acetabulum (Ng et al., 2012), or with some thinning towards the acetabular edge (Chegini et al., 2008).

The morphological features can be parameterised in the FE models. Mechanical characterisation can be done via parametric study by running the models under various conditions. Chegini et al. (2008) varied the CE angle from 0° to 40° and the alpha angle from 40° to 80°, in 10° increments. The femoral cartilage was created with 2 mm at the thickest point, and gradually reduced to zero toward the edge. The acetabular cartilage had a constant thickness of 2 mm. The articular cartilages were assumed to be spherical at the contacting surface. The anatomical horseshoe shape was also considered by altering the lateral acetabular coverage. The parametrised models were developed to study the effect of impingement and dysplasia during activities.

Beyond generalised mathematical shapes, the geometry of the femur may be captured from medical images. Cooper et al. (2017) obtained CT images and parameterised the femoral and acetabular components, including the cam deformity. Measurements including cam-radius, cam-angle and cam-width were taken, and clinically related angles such as CE angle were investigated at various planes in order to assess the overall severity of impingement in the hip joint.

Similarly, the acetabulum can be captured in CT scans and be represented via the parameterisation approach. Hua et al. (2015) generated segmentation-based models of the human hip from CT scans at voxel size of 73.6 μm and energy of 70kVp, 114μA. The articular surfaces were modified to be perfectly spherical on both the femoral head and acetabular cavity. Additionally, the parameterised model was developed by defining the cup angle, acetabulum radius, fossa radius and cavity position. Contact stress was investigated and found to have good agreement between segmented and parameterised models.

It is possible to generate FE models purely based on radiographs for accurate representation, but the computational cost may be high especially for contact problems. The contact surfaces may be smoothened via computer-aided design (CAD) software. Ng et al. (2012) constructed subject-specific hip models by segmenting CT radiographs. The CT slices were scanned with a thickness of 1.25 mm in the axial direction. The models were then resurfaced in Solidworks (Dassault Systèmes, Concord, MA, USA) to eliminate geometric artefacts and polygon surfaces. Cartilage layers were formed by extruding the acetabular surface onto the femoral head with offset. The thickness of the cartilage therefore varied across the cavity, and reduced marginally towards and ellipsoidal curvature to create joint space and prevent surface intersection.

Articular cartilage is a complex composition with collagen fibres in solid phase and water in fluid phase (Fermor et al., 2015). The mechanical property is governed by the extracellular matrix (ECM) and fluid content, and can provide low friction and load support (Taylor et al., 2015).

Animal tissues properties, for example porcine tissue, have also been investigated to support FE studies using such tissue (Ferguson et al., 2000; Fermor et al., 2015). Furthermore, Taylor et al. (2015) conducted comparison among human, ovine, bovine, and porcine femoral head which could help assess the similarity and reliability of studying animal hip joint. Porcine had thinner femoral cartilage (1.22 ± 0.05 mm) than human (1.82 ± 0.18 mm) and smaller head size (35.6 ± 0.7 mm compared to 46.8 ± 5.7 mm in diameter). Besides, calibration of human capsule properties was conducted by Elkins et al. (2011). A level of material complexity was firstly introduced and optimised such that the load-displacement data of the capsule model matched with that of a cadaveric capsule in the experimental test.

### 2.5.3 Material properties

Material properties define the mechanical behaviour of the material under specified conditions. Soft tissues usually have an inhomogeneous and multiphasic structure, and behave non-linearly with time-dependence (Freutel et al., 2014). Mechanical testing on human tissue samples have been performed to provide material properties data, including Young's Modulus (E) and Poisson's ratio (v), for FE models (Dalstra et al., 1995, Ishiko et al., 2004, Taylor et al., 2011).

Simplification can be made by treating the articular cartilage as isotropic linear elastic material. Chegini et al. (2008) and Ng et al. (2012) modelled the cartilage with E = 12 MPa and v = 0.45. The time-dependent behaviour was neglected due to the short time period for the load cycle, which was on the order of 1 Hz, during the activity analysed.

The time-dependent behaviour was considered during the investigation of labral sealing where a constant load was applied for over 200 seconds. Ferguson et al. (2000) modelled the cartilage as isotropic and poroelastic with E = 0.467 MPa, v = 0.167, permeability (k) = 7.358*$10^{-8}$ mm/s, specific weight of fluid= 9.81 kN/$m^3$ and solid fraction = 20%. Meng et al. (2013) also included the time-dependent behaviour of cartilage with E = 0.54 MPa, v = 0, void ratio = 4.0 and k = 0.004 $mm^4$/Ns. The biphasic cartilage models were used for comparison between two FE software, Abaqus and FEBio.

Multiple modulus in material directions and the poroelasticity may also be considered when applying load cycles of daily activities to the hip model. Hellwig et al. (2016) modelled the cartilage as orthotropic and poroelastic with compressive modulus ($E_1$) in radial = 1.18 MPa, tangential modulus in circumferential ($E_2$) and meridional ($E_3$) = 8.5 MPa, $v_{12}$ = 0.044, $v_{13}$ = 0.044, $v_{23}$ = 0.146, k = 8.98 *$10^{-4}$ $mm^4$/Ns and volumetric weight of water = 9.81*$10^{-6}$ $Nmm^{-3}$. The effect of cam impingement was studied under normal walking and sitting down maneuvres where both loadings were repeated by 60 cycles.

The acetabular labrum is an organised biphasic tissue with major collagen fibres orienting in the circumferential direction, parallel to the acetabular rim (Ferguson et al., 2000). However, Ng et al. (2012) neglected the existence of labrum in a CT image-based FE study due to lack of understanding in the labral properties. Kapron et al. (2014) constrained the deformation of labrum in order to investigate the femur-labrum contact region.

Similarly to the cartilage, simplification can be made by treating the labrum as isotropic linear elastic material. Chegini et al. (2008) modelled the labrum as isotropic and linear elastic with E = 20 MPa and v = 0.4 in the study of the effect of impingement and dysplasia conditions on hip. Ferguson et al. (2000) considered the collagen fibres that aligned in the circumferential direction, and modelled the labrum as transversely isotropic based on the properties of meniscus, while the circumferential stiffness varied between 50 MPa to 200 MPa. Sensitivity test were conducted on the labral properties and the resulting sealing ability was investigated.

The time-dependent behaviour of the labrum was considered when applying load cycles of daily activities to the model. Hellwig et al. (2016) modelled the labrum as orthotropic and poroelastic with $E_1$ = 0.157 MPa, $E_2$ = 26 MPa, $E_3$ = 3 MPa, $v_{12}$ = 0.04, $v_{13}$ = 0.04, $v_{23}$ = 0.1, shear modulus (G) = 1.5 and k = $4.89*10^{-09}$ mm/s, where the radial direction is denoted as “1”, the circumferential direction was denoted as “2”, and the meridional direction was denoted as “3”. . Contact pressure and pore pressure were both measured to investigate the effect of cam impingement.

Compared to cartilage and labrum, the bone has much higher elastic modulus in both of the trabecular bone and cortical bone shell (Dalstra et al. 1993). Three main methods of representing the bone have been established by researchers, considering it rigid, deformable and homogeneous material properties, and deformable and heteregeneous material properties (e.g. each element assigned a different material property).

Bone can be simplified as rigid body, since the modulus is much higher compared to that of soft tissue. Ferguson et al. (2000) and Hellwig et al. (2016) both considered the bone as rigid and impermeable in the study of hip joint under loading and rotation. Li et al. (2013) modelled the entire bone as impermeable and linearly elastic with E = 17 GPa and v = 0.3. The effect of having separate material properties for trabecular bone has been investigated and was found to have within 5% difference in terms of the peak contact stress and the peak fluid pressure.

Deformable bone may be considered when the bone is highly involved in the contact, such as edge loading or femoroacetabular impingement. Chegini et al. (2008) modelled the bone as isotropic and elastic with E = 20 GPa for cortical bone and E = 100 MPa for trabecular bone. However, no difference in cartilage stress was found in the pilot analyses that compared rigid and deformable bone structures. Therefore the bone structure was treated as rigid in the hip model for ease of computation. Ng et al. (2012) also considered the stiffness in three directions and modelled the entire bone as orthotropic and linear elastic with $E_1 = 11.6$ GPa, $E_2 = 12.2$ GPa, $E_3 = 19.9$ GPa, $G_{12} = 4.0$ GPa, $G_{13} = 5.0$ GPa, $G_{23} = 5.4$ GPa, $v_{12} = 0.42$, $v_{13} = v_{23} = 0.23$, where the medial-lateral direction was denoted as “1”, the anterior-posterior direction was denoted as “2”, and the superior-inferior direction was denoted as “3”.

### 2.5.4 Loads and boundary conditions

Loads and boundary conditions are created to replicate the hip movements in human body or hip simulator under specific constraints. Loads can be created by applying a force vector on a point or distributed force at the edge or surface. Examples of boundary conditions include partial fixation and constraint in any degree of motion during the loads. Work by Bergmann et al. (2001) has been widely used to replicate the daily activities, including walking, standing up, sitting down, ascending and descending stairs, in the FE hip models. Alternatively, FAI can be involved in the hip model. The following five studies analysed the hip contact with sensible load cycles.

Elkins et al. (2011) considered the sit to stand maneuver that applied high axial force combined with mainly flexion up to $105^{o}$. The rigid material property was assigned to the cup backing, distal femoral stem and the bony surfaces attached with capsule for the purpose of computational economy.

Anderson et al. (2008) (walking, ascending and descending stairs), Chegini et al. (2008) (normal walking and stand to sit) and Hellwig et al. (2016) (normal walking and sitting down) all applied load data extracted from Bergmann et al. (2001). Constraints were assigned to the iliac crest, the acetabulum and the bone-cartilage interface respectively.

Kapron et al. (2014) performed an impingement test on the pathological and asymptomatic hip joints which combined flexion up to 110°, adduction up to 10° and internal rotation up to 20°. The location of femur-labrum contact was determined under pure rotation of hip joints.

Ng et al. (2012) considered standing and maximum squatting in hip models which combined axial force and high flexion. Constraints were assigned to the proximal sectioned plane of the ilium and distal sectioned plane of the femur. The maximum shear stress was investigated for assessing the effect of cam FAI.

### 2.5.5 Damage prediction measures

In order to gain an insight into tissue behaviour during activities, research groups have developed FE models that replicate hip joints with FAI. This section will review the methodology, model set up and output measurement from previous work (Table 2.2). One exception is the study on cartilage contact pressure on healthy hip joint by Anderson et al. (2008). This is a good example in validation of FE models based on experimental results, although FAI was not considered.

**Table 2.2 Previous study on hip joints under loading using FE models**

| Authors | Aims | Methodology | Results |
|---|---|---|---|
| Anderson et al. (2008) | To develop and validate subject-specific hip FE model. Investigate cartilage contact pressure. | Subject-specific FEA, n=1. Pressure sensitive film for measuring contact pressure under walking, ascending and descending stairs. | Experimental peak pressure up to 10.0 MPa, and mean values ranged from 4.4 to 5.0 MPa. FE peak pressure up to 12.73 MPa, and mean values ranged from 5.1 to 6.2 MPa. |
| Chegini et al. (2008) | To investigate contact pressure during walking and stand to sit maneuvers, and the relationship between morphological changes. | Parameterised left hip joint models. CE angles ranged from $0^o$ to $40^o$ and alpha angles ranged from $40^o$ to $80^o$, both with $10^o$ increment. | Peak contact pressure of 3.69 MPa during stand to sit maneuver, 3.55 MPa during walking. Head centre translation between 0.2 – 0.3 mm. |

| | | | |
|---|---|---|---|
| Cooper et al. (2018) | To establish and assess the effect of geometric simplification and labrum parameterisation in FAI when assessing labrum displacement and cartilage-labral junction strain. | Four FE models were created with parameterised femur conditions, having two different cam radius (low and high) and two different cam position (anterior and superior). Flexion from 70º to 90º, followed by up to 35º of internal rotation.<br>Additional five FE models were created with five different labrum-bone conditions. | When cam parameters varied, the cartilage strain peaked at 0.38 with labral displacement of 2 mm when the cam had high radius and was located at anterior.<br>When labrum parameters varied, strain peaked at 0.40 when bone extent was decreased. Labral displacement peaked at 3.3 mm when labrum length was increased. |
| Hellwig et al. (2016) | To develop FE model of normal and FAI pathologic hips using biphasic material. Investigate cartilage stresses and fluid load support (FLS) under loading. | A normal hip and a cam-type hip, with alpha angle of 40$^{o}$ and 74$^{o}$. Normal walking (NW) and sitting down (SD) movements taken from Bergmann (2001). Initially applied 33.31% and 55.51% of the peak load respectively, and ramped over 1s and repeated for 60 cycles. | Cam hip compared to normal hip: Peak contact pressure (PCP) rose from 2.87 MPa to 3.66 MPa. Peak pore pressure (PPR) rose from 2.85 MPa to 3.76 MPa. Peak circumferential stress rose from 0.33 MPa to 2.26 MPa in the labral ring. |

| | | | |
|---|---|---|---|
| Kapron et al. (2014) | To identify femur-labrum contact region and the location of minimum bone-to-bone distance. Also compare femur-labrum contact region and the location of damage observed intraoperatively | One cam-type patient, one pincer-type patient, one mixed-type patient and six asymptomatic control subjects. CT arthrogram at 1 mm slice thickness. Dynamic hip articulation during impingement test was measured using dual-fluoroscopy and model-based tracking. | Femur-labrum contact occurred at the terminal position of the test except for one asymptomatic hip, however contact patterns varied among participants. Damage area observed intraoperatively qualitatively coincided with femur-labrum contact. |
| Ng et al. (2012) | To determine shear stress in two normal and two cam FAI hips during squatting. | Geometries were generated and reconstructed from CT images. The cartilage layer was extruded from the acetabulum surface. Two quasi-static loading scenarios of stance and max squatting were applied subject-specifically. | Peak maximum shear stress (MSS) on the cartilage layer were 4.1 MPa and 3.9 MPa in patients during standing and squatting. Peak MSS on the underlying bone were 3.6 MPa and 16.9 MPa respectively. |

Anderson et al. (2008) performed validation studies between experimental and computational approaches to the investigation of cartilage contact pressure. Pressure films for all three activities recorded contact pressures at the upper limit of the film which is 10 MPa. In comparison, FE predictions for peak pressure ranged from 10.78MPa to 12.73MPa. Computational predictions of average pressure were slightly higher than experimental values, 5.1- 6.2 MPa compared to 4.4 – 5.0 MPa. Experimental measures could be more valuable if pressure films with wider measurement limit were used. Additionally, the flexibility of pressure sensitive film and the consequential crinkle on the articulating surface may also cause error in experimental measurement. The bones were considered as rigid body in the models, which can save computational cost and also result in more concentrated pressure distribution in the cartilages. Pressure distributions were used to compare the contact patterns between experiment and computation. Good agreement was observed on the femoral component. It was also noted that the predicted peak pressures were sensitive to the cartilage material properties. Sensitivity test within ±10% of input could cause peak pressure changes up to 25%. Low sample number, large differences and modelling simplification made it incomparable to other studies, of which the peak pressures ranged from 4 – 9 MPa. The results from this study could be improved by investigating more samples and apply more accurate and realistic features to the FE models. Furthermore, accurate representation of *in vitro* material properties can also benefit future validation study.

Chegini et al. (2008) generated parameterised hip joint models that represent different levels of impingement and dysplasia pathology. Contact pressure and von Mises stresses were measured under walking and stand to sit manoeuvres. The effect of impingement and dysplasia were assessed according to the distribution of von Mises stresses. However, von Mises stress is an overall stress integrating three components of stresses together regardless of the direction. Compressive stress, tensile stress or strain in specific direction may be alternative output of interest that would help understand the mechanism during hip motions. The stress distribution in cartilage could be more reliable by including deformable bone structure which may also contribute to load bearing. The material properties could be improved by using human tissue properties and considering the fibre reinforcement. The effect of alpha angle and CE angle were investigated individually with respect to von Mises stress. Geometrical parameterisation turned to be a good application in model development that can be used for parametric sensitivity tests.

Cooper et al. (2018) established parameterised models for study of cam-type FAI. Two sets of parametric studies were performed in terms of the cartilage tensile strain and labral displacement measurement: 1) from femoral perspective, the cam size and cam position; and 2) from labral perspective, the bone extent and labrum extent. Two different cam radius (high and low) and two different cam positions (anterior and superior) were assigned to four models. The peak cartilage strain of 0.38 and the peak labral displacement of 2 mm were both observed in the same model with cam having the larger size and being located at the anterior. Large labral displacement was found in cam at the anterior meaning that the labral displacement is dependent on the cam location, under the same type of load cycle. Five different labrum conditions were further assigned to five models: 1) baseline model; 2) rim bone length increased by 10%; 3) rim bone length decreased by 10%; 4) labrum length increased by 10%; and 5) labrum length decreased by 10%. The minimum labral displacement was found in the case with shorter labrum as there was less tissue content covering the acetabular rim. Peak cartilage strain of 0.40 with decreased bone length. The cartilage tensile strain was dependent on the location of the labrum-bone junction. When the junction was further away from the centre of acetabulum, the cartilage was hence undertaking higher load due to the cam.

Hellwig et al. (2016) measured the contact pressure and pore pressure by assigning poroelastic material to cartilage and labrum. The load support by the ECM and the fluid contribution were determined under normal walking and sitting down. The effect of cam impingement was studied by including a normal hip and a cam hip, both generated based on parameterised models. However the variation in population was not considered. The results could be more valuable by segmenting multiple normal and cam hips from clinical images, from which more generalised understanding would be gained on the difference between normal and cam hips. Realistic material representation was developed by considering the contribution of highly organised collagen fibre and including the time-dependent behaviour.

Kapron et al. (2014) determined the location of femur-labrum contact and minimum bone distance by tracking the hip joint movements under impingement test. Hip models were developed based on CT images of six asymptomatic subjects and three pathological patients. The labrum was considered as rigid and moving with pelvis without deformation. The results shown the contact patterns on femur and acetabulum during impingement test that combined high degree of flexion, adduction and internal rotation. However, the highlighted location only indicated the initial contact since no deformation was considered. The impingement would progress after the first contact, causing pain for patients and deformation in the tissue. The results would be more valuable by including soft tissue deformation in the model and investigating the resulting contact area.

Ng et al. (2012) investigated the shear stress in the hip joint during maximum squatting. Hip FE models were generated based on CT scans of two normal subjects and two cam hip with alpha angle of $73^o$ and $83^o$. It is reasonable to expect shear stress in soft tissue during hip rotation, particularly for the soft tissue at the acetabular rim. The results could be improved by including the labrum attaching to the edge of cartilage. Standing and squatting combined axial force and high degree of flexion. The effect of cam impingement can be understood more widely by considering multiple activities such as kicking, climbing and running.

### 2.5.6 Summary

In summary, previous studies methodology have been reviewed including geometry generation, material presentation, loading environment and output measures, along with the purpose of the studies. A segmented and resurfaced geometry would be preferred in the experiment-based calibration study, since that parameterisation was used for studying the effect and morphology and had lack of accuracy in presentation of the original geometry. Time-dependent behaviour had the advantage of including the contribution of fluid content, however the feature could be ignored during instant loading scenario. Loads and boundary conditions varied between different researchers, and were usually a replication of the experiment loading environment. Contact pressure, shear stress and pore pressure were determined to assess the resulting tissue damage during impingement. However none of these parameters can be easily measured in the specimen.

## 2.6 Conclusions

In conclusion, the structure and components in hip joint were understood. The composition and functionality of soft tissue, cartilage and labrum in particular, were learned. Additionally, the morphology of hip anatomy, cam-type FAI in particular, were reviewed. Anatomical information may benefit in the development of loading scenario and the representation of those in FE models. Impingement-related loading conditions may therefore be designed and the more realistic representation of soft tissue may be generated.

Experimental approaches to quantify soft tissue changes have been reviewed. Possible methods for visualising and measuring soft tissue were learnt. It is possible to highlight the soft tissue portion and to capture the movement of highlighted soft tissue. Examples of experimental observation could be labral strain or labral deformation.

Theoretical mechanism of hip movements under cam impingement were described. Previous FE models have been reviewed regarding the model development and case analysed. It has been understood that the mechanical properties of soft tissue were dominated by the ECM. Time-dependent behaviour may also be considered when multiple cycles of loading condition are being replicated or the contribution of fluid phase are being investigated. Contact stress and shear stress can be examples of output parameters that assess the mechanical environment under cam FAI.

# Chapter 3

# General materials and methods for experimental study

## 3.1 Introduction

The aim of this chapter is to describe the preliminary development of the experimental methods, which includes: the consequences of the choice of animal tissue; the methods developed to enable separation of contacting soft tissues in a computed tomography image; the specification and design of a bespoke hip loading rig for applying stable load in the hip joint during imaging; and image processing and computational methods developed to quantify soft tissue movement in unloaded and loaded states. The acetabular cartilage strain and labrum apex displacement were measured in particular, through segmented CT slice and reconstructed labrum cloud point. High cartilage strain is often observed under impingement condition, reflecting the damage mechanism for cartilage lesion such as cartilage defibrillation. The labrum experience large deformation due to cam deformity which reflects the damage mechanism for labrum tear.

All natural hip studies in this thesis are performed using porcine tissue. The tissues are readily available from a local abattoir (John Penny and Sons, Rawdon, Leeds). The tissue can be requested flexibly, at a few days' notice throughout the year and is from a consistent age and weight of animal, due to being sourced from the food chain. The use of animal tissue for the development of a new methodology reduces the wastage of human samples. Section 3.2 describes in detail the differences between porcine and human hip tissue geometry and properties, as well as examples of other typical animals used in *in vitro* studies.

The broad aim of the experimental work is to take measurements from the whole natural hip joint under loading conditions which are relevant to bony impingement. Specifically, where the cartilage-labral junction is compressed.

The whole joint visualisation in this work is performed using micro computed tomography (CT) imaging. The XtremeCT scanner (Scanco Medical, Switzerland) is readily available from the Faculty of Engineering, and can be requested at a few days' notice. The magnetic resonance imaging (MRI) is available from a local hospital and is not easily accessible, which makes it difficult to keep tissue fresh. Unlike CT, MRI is capable of distinguishing labrum and cartilage without the aid of radiopaque solution. However, metal is restricted in the CT/MRI machine, which makes it difficult for the design of the loading rig. Therefore, all tissue samples in this work were scanned under CT machine, along with the radiopaque solution. The resolution allowed is from 41 to 246 μm nominal isotropic. The scan tube, for holding the sample, is open-ended with diameter of 176 mm. The maximum scan size is 126 mm in diameter and 150 mm in depth.

Since CT imaging assigns image values based on the density of the object, tissues with similar density appears similarly on the images as well. This work requires that measurements of tissue geometry are taken while the femoral head is in contact with the acetabular cartilage. The interface between the femoral and acetabular cartilage layers will not be visible in a CT image unless steps are taken to manipulate the contrast of one layer. Section 3.3 describes a series of small studies conducted to find the most effective way to use contrast agent in order to overcome this problem.

In order to measure tissue geometry under a compressive load, it is necessary to construct a device which could aid in constraining the porcine hip joint in the required orientation while it is inserted into the micro CT bore and for the duration of the imaging. In addition, there is a requirement for the displacement and load applied to the tissue to be recorded and controlled as much as possible. Section 3.4 describes the full specification and design of the device.

The targeted contact region is justified on the acetabulum side in Section 0. A set of dissection and alignment of the tissue samples are established, along with the assembly of the loading rig, so as to create loading scenario related to cam-type FAI in the porcine hip joint.

In order to establish the difference in tissue shape in unloaded and loaded states, image processing and data extraction methods are developed. These are aimed at measuring both cartilage strain and labral movement. Section 3.6 describes the rationale and procedure for measuring tissue movement.

Four porcine hip samples were used in this development work. These are listed in Table 3.1 along with the study they were used for.

**Table 3.1 Samples used in experiment development**

| No. | Sample code | Parts of tissue used | Purpose |
|---|---|---|---|
| 1 | PH01 | Acetabulum | Soft tissue separation |
| 2 | PH02 | Acetabulum | Soft tissue separation |
| 3 | PH03 | Acetabulum and femur | To apply load through cable-tie |
| 4 | PH04 | Acetabulum and femur | To apply load from hip loading rig |

## 3.2 Tissue acquisition

Animal hip tissues were used throughout this study instead of human hip tissues in order to save human tissues samples and the processing time of ethical issues, since that this was the first attempt of such methods development that investigates hip soft tissue behaviour *in situ*. This section explained the rationale for selection of animal tissues and the acquisition of hip tissue samples.

### 3.2.1 Animal tissue selection

A comparison of human and animal femoral head properties is presented in Table 3.2.

**Table 3.2 Femoral head geometry and mechanical properties of human and animal.** (Taylor et al., 2011)

| Species | Human | Bovine | Ovine | Porcine |
|---|---|---|---|---|
| Femoral head diameter (mm) | 46.8±5.7 | 64.4±4.0 | 23.2±1.4 | 35.6±0.7 |
| % difference to human | 0% | 38% | -50% | -24% |
| Femoral cartilage thickness (mm) | 1.82±0.18 | 1.32±0.13 | 0.52±0.10 | 1.22±0.05 |
| % difference to human | 0% | -28% | -71% | -33% |
| Cartilage permeability (E-17 m^4/(Ns)) | 19.6±2.05 | 27.0±1.08 | 2.63±1.07 | 63.3±9.04 |
| % difference to human | 0% | 38% | -87% | 223% |
| Articular cartilage modulus (MPa) | 4.89±0.76 | 1.86±044 | 3.94±2.52 | 1.18±0.17 |
| % difference to human | 0% | -62% | -19% | -76% |

Porcine femoral head had the closest diameter (35.6 mm) to human femoral head (46.8 mm), compared to bovine (64.4 mm) and ovine( 23.2 mm). Porcine acetabulum was believed to have similar size to the human acetabulum do since there was generally a good match between the femoral head and the acetabular socket in individual joints. However, due to the facts that the cam hips: 1) have larger overall size to normal hips (section 2.2.3); and 2) are more popular in young men, larger femoral head may be expected when studying the cam-type FAI. Regarding the femoral head-neck junction, coxa recta (cam deformity) was found in natural porcine femur, which is an advantage for replacing human cam hips. Porcine femoral cartilage thickness is approximately two-thirds of the thickness in human. The resolution of the CT images obtained in this thesis is limited to 82 μm in scanned images and 100 μm during image processing, which account for 6.7% and 8.2% of the cartilage thickness in porcine. Human cartilage had significantly high modulus and relatively low permeability, which made human cartilage stiffer and less sensitive to load time than articular cartilage in other species. However, the time-dependency in soft tissues is not considered in this study since the soft tissues behaviour was not recorded in real-time. Therefore porcine hip tissue was chosen within this study.

### 3.2.2 Dissection of porcine hind leg

Porcine hip tissue was supplied by a local abattoir (John Penny and Sons, Rawdon, Leeds). Pigs were slaughtered at between 6-12 months old, at a weight of 65-95 kg. Porcine hind legs were only available on the right side from the abattoir, which makes the development of alignment simpler.

The hip joint was roughly extracted from the leg (Figure 3.1) to save space in the freezer and the fridge. The capsule was kept intact and small portion of surrounding muscle was left on in order to keep the hip joint as fresh as possible. The whole joints were stored in the freezer instead of the fridge if the planned scan date was longer than two days away from the day of dissection.

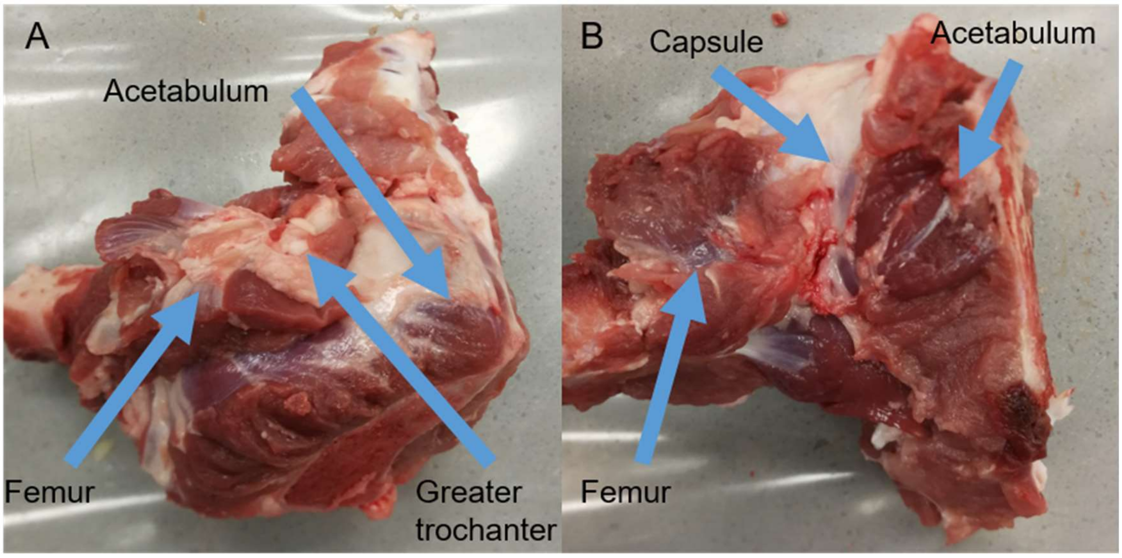

**Figure 3.1 Porcine hip joint dissected from right hind leg. A – porcine hip joint in sagittal view looking from lateral side, the greater trochanter was covered by ligament and highlighted in the figure. B – porcine hip joint in sagittal view looking from medial side, the capsule was kept intact and highlighted in the figure.**

### 3.2.3 Disarticulation of porcine hip joint

Frozen hip joints were moved to the fridge for defrosting (if needed) before disarticulation from one night to three days in advance of CT scanning. Tissues were taken out of the fridge directly for fine dissection. Surrounding muscles and ligaments were dissected while keeping the capsule intact (Figure 3.2). The outer surface of the acetabulum was protected from accidental cuts. The capsule was dissected along the femoral neck to open the hip joint. The acetabulum was disarticulated from the femur by cutting the ligament of the head of femur along the acetabular cartilage surface for the ease of removal of excess soft tissues in the socket. The ligament of the head of femur was then removed from the femoral cartilage surface. The hip joint was then disarticulated with no excess soft tissues around the labrum and cartilage surfaces. The acetabulum was ready for alignment and cementing while the femur was sprayed with Phosphate-buffered saline (PBS) and covered with tissues to keep femoral tissues hydrated.

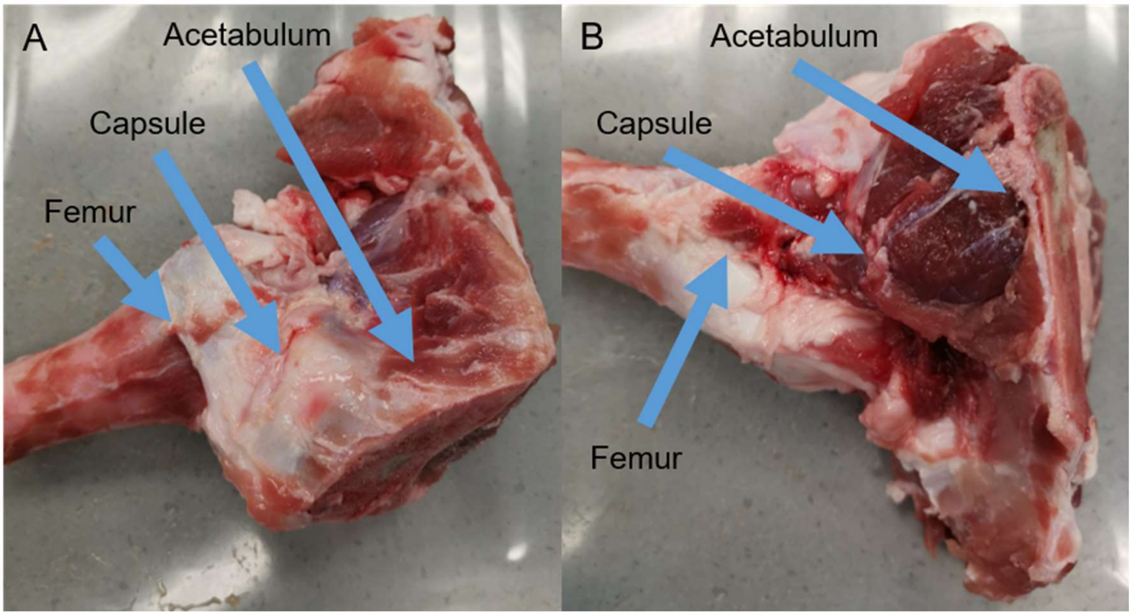

**Figure 3.2 Porcine hip joint with intact capsule. A – porcine hip joint in sagittal view looking from lateral, just before removal of the capsule. B – porcine hip joint in sagittal view looking form medial, just before removal of the capsule.**

## 3.3 Soft tissue separation in CT scans

The aim of this work was to separate the acetabular and femoral bone and cartilage within micro CT scans of the porcine hip joint. Firstly a general imaging processing method which was used to segment the bone, and to separate the bone from a bulk segmentation of all of the tissues, is described in Section 3.3.2. Radiopaque solution was introduced in order to separate the cartilage surfaces by highlighting one side of the articular cartilage. This method is tested for the acetabular and femoral sides and for a number of different exposure times, and is described in Section 3.3.3.

The CT images of porcine hips were obtained from XtremeCT scanner (Scanco Medical, Switzerland). The resolution allowed is from 41 to 246 µm nominal isotropic. The scan tube, for holding the sample, is open-ended with diameter of 176 mm. The maximum scan size is 126 mm in diameter and 150 mm in depth. The CT energy E was equal to 60kvp and the current I was equal to 900 µA.

### 3.3.1 Normal CT scans of porcine hip tissues

A normal CT scan of hip joint is shown in Figure 3.3. The acetabular bone and the femoral head bone turned bright in the image and were away from each other. However, the acetabular cartilage and labrum, together with the femoral cartilage, were next to each other and sharing the similar range of greyscale in the image.

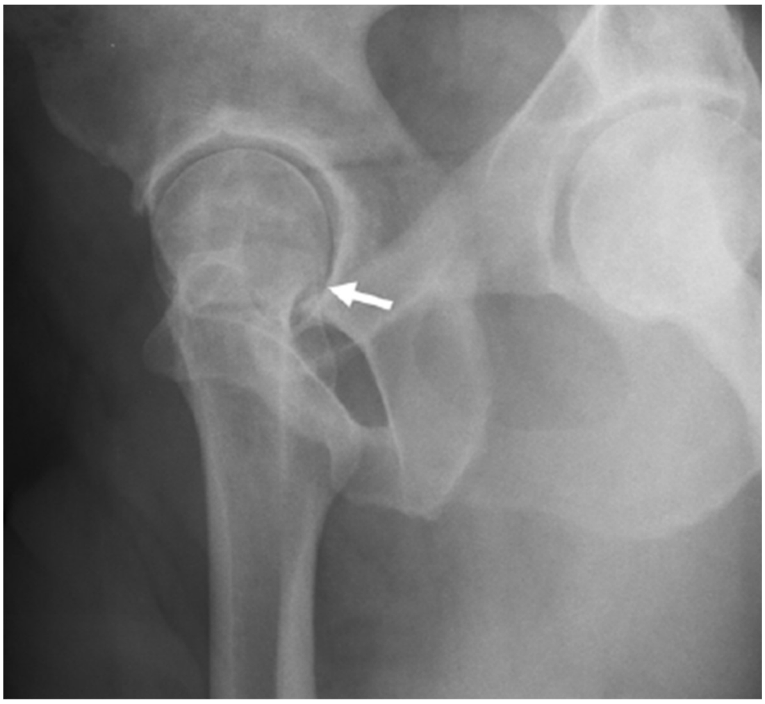

**Figure 3.3 CT scan of hip joint without the aid of radiopaque solution (Tannast et al., 2007). It was difficult to differentiate acetabular cartilage and femoral cartilage at the contact region (arrow).**

### 3.3.2 Image processing and bone segmentation

CT images were obtained from XtremeCT (Scanco Medical, Switzerland). The resolution was isotropic of 82 µm. Number of projection per 180 degrees was set to 750. The integration time was set to 300 ms. Image data were imported into ScanIP M-2017.06 (Synopsys, Mountain View, CA, United States) for post-processing (Figure 3.4). Cross-sectional view was allowed in three planes, associated with the local coordinate system. A 3D view was also generated to allow investigation of the scanned object in 3D space. The resolution was down-sampled to 0.1 x 0.1 x 0.1 mm to save computational cost while remaining the accuracy in measurement of soft tissues movement.

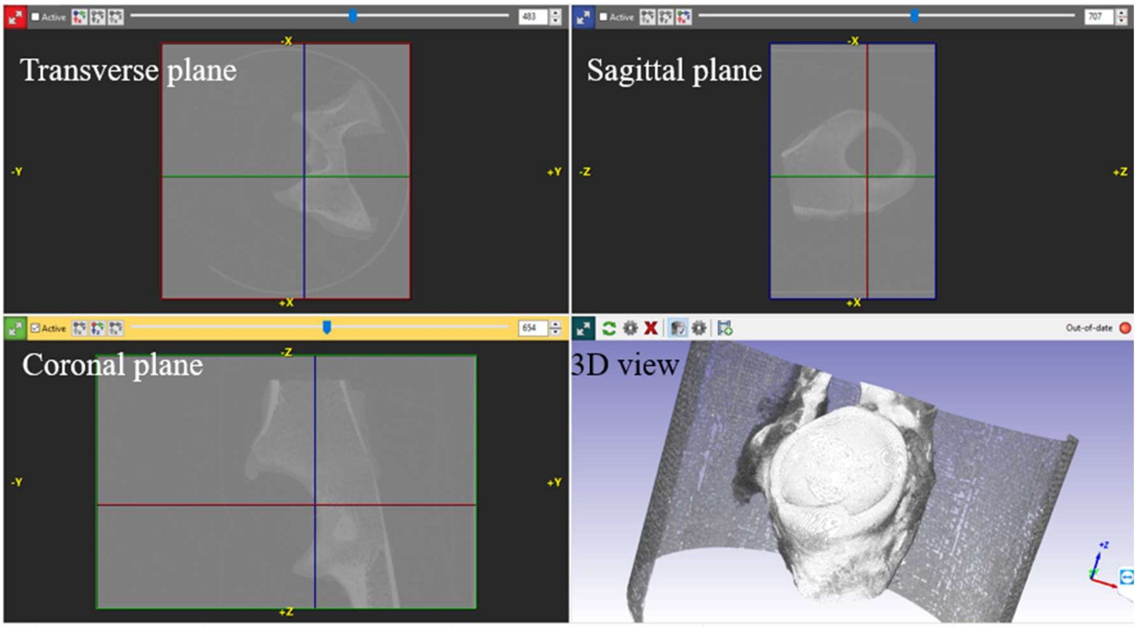

**Figure 3.4 Anatomical views and 3D preview of porcine acetabulum in ScanIP.**

The aim of the bone segmentation was to capture the subchondral bone surface. Capture of the trabecular structure and other bony structures away from that surface were not considered important. The basic steps for subchondral bone segmentation (Figure 3.5) are described below:

1) Threshold, to create a tissue mask by defining lower and upper greyscale value at 800 and 4000 respectively;
2) Morphological close, to dilate the tissue mask by 1 mm at all directions and to erode back by 1 mm, effectively merging any gap within in 1 mm in the tissue mask;
3) Recursive Gaussian, to smooth the tissue mask by 1 m; and
4) Flood fill, to eliminate unconnected surrounding tissues.

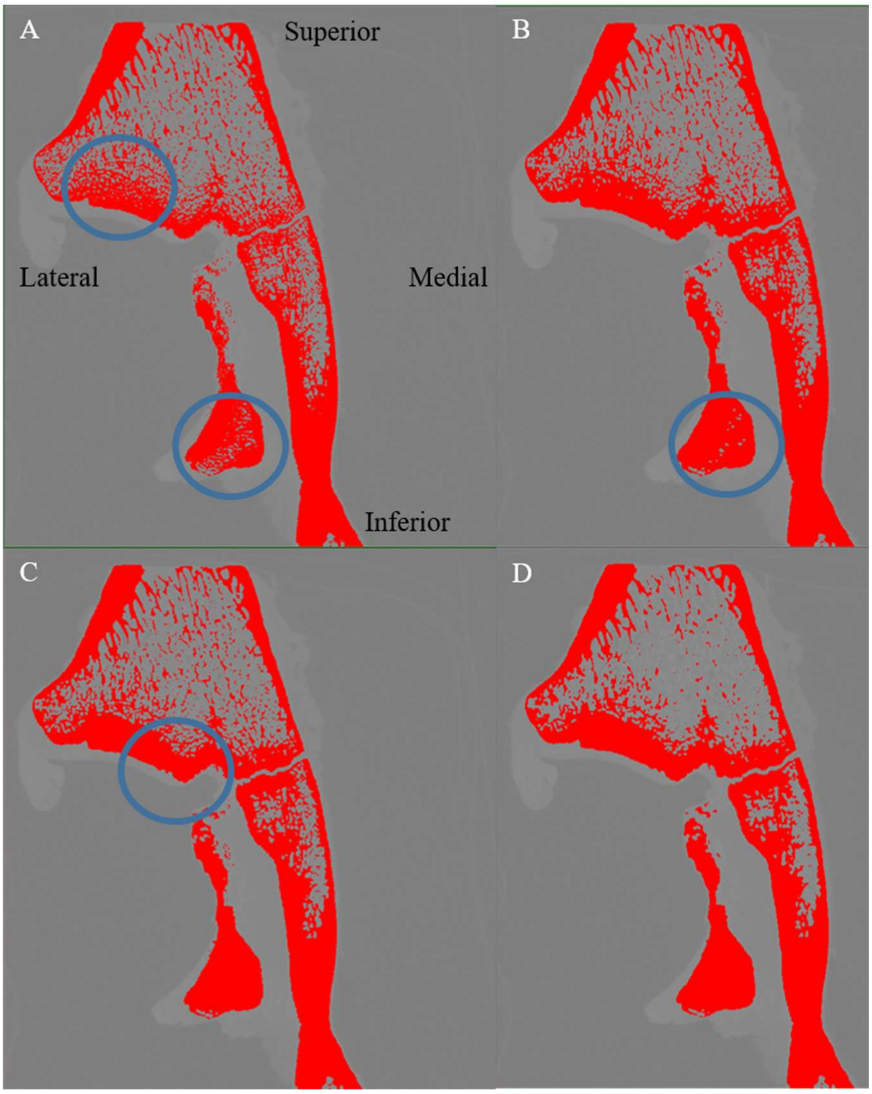

**Figure 3.5 One of the porcine acetabulum CT images in coronal view during image processing. A – bone mask after threshold. B – bone mask after morphological close by 1 pixel. C – bone mask after cavity fill. D – bone mask after recursive Gaussian by 1 pixel. Mask features, which had been modified due to post-processing, were highlighted in the previous step.**

### 3.3.3 Radiopaque solution

The acetabular cartilage and labrum, together with the femoral cartilage, shared the similar range of greyscale and were difficult to be separated in the images. Radiopaque solution was therefore introduced before the joint is again in contact and loaded, so as to help separate the cartilage surfaces in the images by highlighting one side of the joint.

Sodium Iodide (NaI) solution was used previously( Bint-E-Siddiq et al., 2019 and Gignac et al., 2018) in CT scan for soft tissue applications. The NaI solution was absorbed by the ligament and made the ligament distinguishable from surrounding tissues. Concentration of the NaI solution was 0.4 mol/L, leading to the resulting greyscale of the affected tissue half way between other soft tissues and the bone.

In order to investigate the differences in absorption time in cartilage and labrum, NaI solution was firstly applied on the acetabulum side. Various time period of: half minute, three minutes, five minutes and NaI being left on, were applied to the acetabular contacting surface. The effect of various application durations was investigated. NaI solution was then applied on the femur side, the less considered contacting surface in this work, so as to prevent the NaI solution from transferring in the acetabular surface and mixing up the cartilage with the bone in the image.

#### 3.3.3.1 Preparation of NaI solution

To obtain NaI solution with concentration of 0.4 mol/L, the following formula was used to find out the volumetric weight of NaI powder to be dissolved:

$$\text{Molecular weight of NaI} = 22.99\,\frac{\text{g}}{\text{mol}} + 126.90\,\frac{\text{g}}{\text{mol}} = 149.89\ \frac{\text{g}}{\text{mol}}$$

$$\text{Weight of NaI per litre solution} = 0.4\ \text{mol}\ * 150\,\frac{\text{g}}{\text{mol}} = 59.956\ \text{g}$$

Both NaI powder and NaI solution were stored in cabinet at room temperature.

#### 3.3.3.2 Effect of NaI solution with various application duration

The study of application duration was performed on two porcine acetabulum. Acetabular cartilage of each sample was divided into two portions, and each portion was applied with NaI solution under one of the application durations.

Sample PH01 was applied with NaI for 0.5 and 3 minutes. Sample PH02 was applied with NaI for 5 minutes, and another half was left with the solution. A sample cross-sectional view at coronal plane under each application duration were shown in Figure 3.6. Acetabular soft tissues with NaI solution applied for 0.5 minute (A) was not bright enough to be distinguishable from the untreated soft tissues. Tissues with NaI solution applied for 3 minutes (B) was distinguishable from raw tissues. However the NaI solution had not been absorbed by the entire cartilage layer. Tissues with NaI solution left on (D) were too bright to be distinguishable from the bone tissues. Therefore, 5-minute (C) was chosen as the appropriate time duration for application of NaI solution.

**Figure 3.6 Highlight of the effect of the NaI solution in acetabular cartilage CT images at the coronal plane. A – NaI applied for 0.5 minute before wiped off. B – NaI applied for 3 minutes before wiped off. C – NaI applied for 5 minutes before wiped off. D – NaI was left on the acetabular cartilage. The effect of NaI solution on the cartilage were highlighted in the images.**

#### 3.3.3.3 NaI solution assisted segmentation on the acetabular side

The aim of the soft tissue segmentation was to separate the acetabular soft tissue from the subchondral bone surface. The basic steps for soft tissue segmentation (Figure 3.7Figure 3.5) are described below:

1) Acetabular bone extraction, to perform bone segmentation as described in Section 3.3.2, and apply the “flood fill” on the acetabular subchondral bone;
2) Acetabular tissue segmentation, to perform similar segmentation as described in Section 3.3.2, except the greyscale value was defined from -200 to 4000 instead. The whole acetabulum was captured; and
3) Acetabular soft tissue segmentation, to subtract the acetabular bone and femur from the acetabular tissue mask.

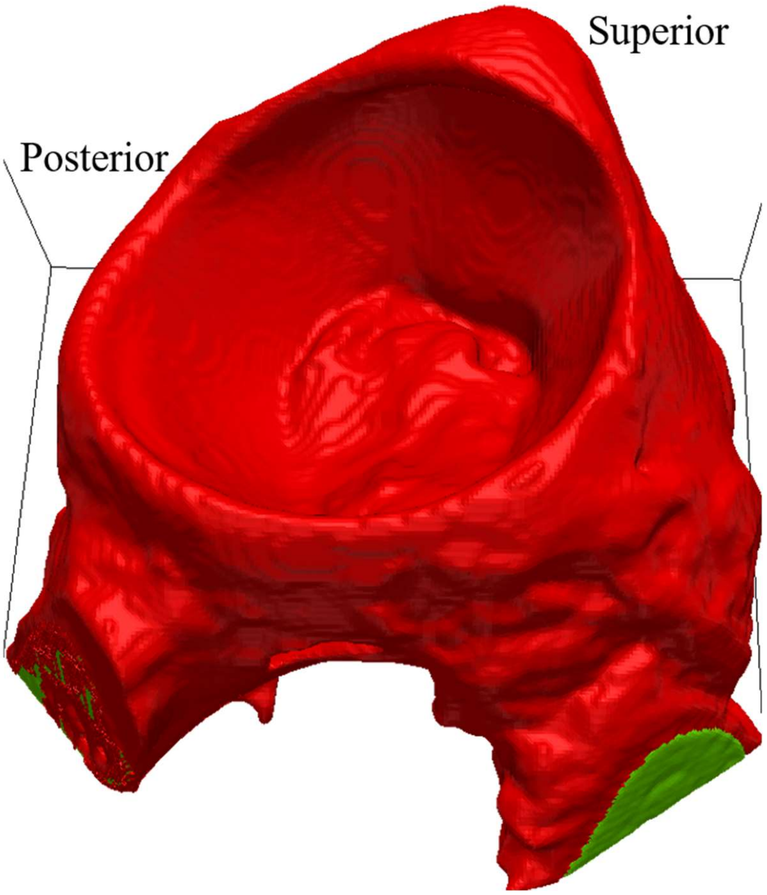

**Figure 3.7 Image processing that segment acetabular soft tissues from the acetabular bone. Red mask, acetabular soft tissue; Green mask, acetabular bone.**

In addition, the separation of acetabular soft tissues is shown in Figure 3.8 when NaI solution was left on the acetabulum. The bone tissue was obtained at grey value 1000 – 3000. A tissue mask with wider grey value range 600 – 3000 was segmented. The ring of acetabular rim was highlighted when subtracting the bone tissue from the second tissue mask. An apex ring was observed because there was more NaI content been absorbed by the tissue.

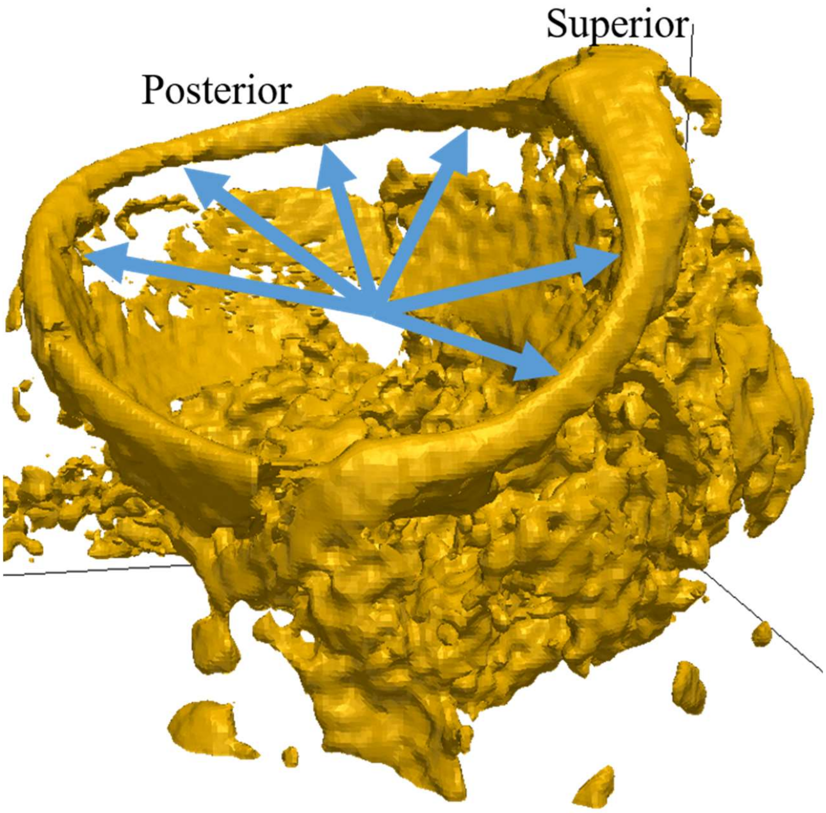

**Figure 3.8 An acetabular image thresholded from 600 to 1000 to demonstrate the bright ring coincidence with the labrum, which indicates preferential uptake of contrast solution in this area.**

This study demonstrated the capability of NaI solution in highlighting soft tissues in the CT image. Time period of 5-minute was decided for the NaI solution to leave on the surface, for separating the affected soft tissue from the bone and untreated soft tissue. Preferential uptake of the contrast agent was observed on the acetabular rim. A bright ring, which indicates a higher absorption rate, was segmented coincidence with the supposed location of the labrum. However, transferring of the contrast agent was noticed across the cartilage thickness that results in mixing up the affected soft tissue with the bone tissue in the CT image. Therefore, the NaI solution was decided to be applied on the femur side, with the femoral head being wrapped with cling film to prevent transferring of the contrast agent during contact.

#### 3.3.3.4 CT scan under preliminary loading using cable-tie

In preliminary loading study, cable tie was used to tighten the acetabulum and the femur up, after applying NaI solution on the femoral cartilage for five minutes, to create joint load in the porcine hip joint (Figure 3.9). The femoral head was then wrapped with cling film to prevent the contrast agent from transferring onto the acetabulum side. It was worth mentioning that the femoral head may slip out of the acetabular socket due to unstable load apply and absence of the ligament of the head of femur. Contact region of interest, such as rim loading, could not be achieved by using cable-tie.

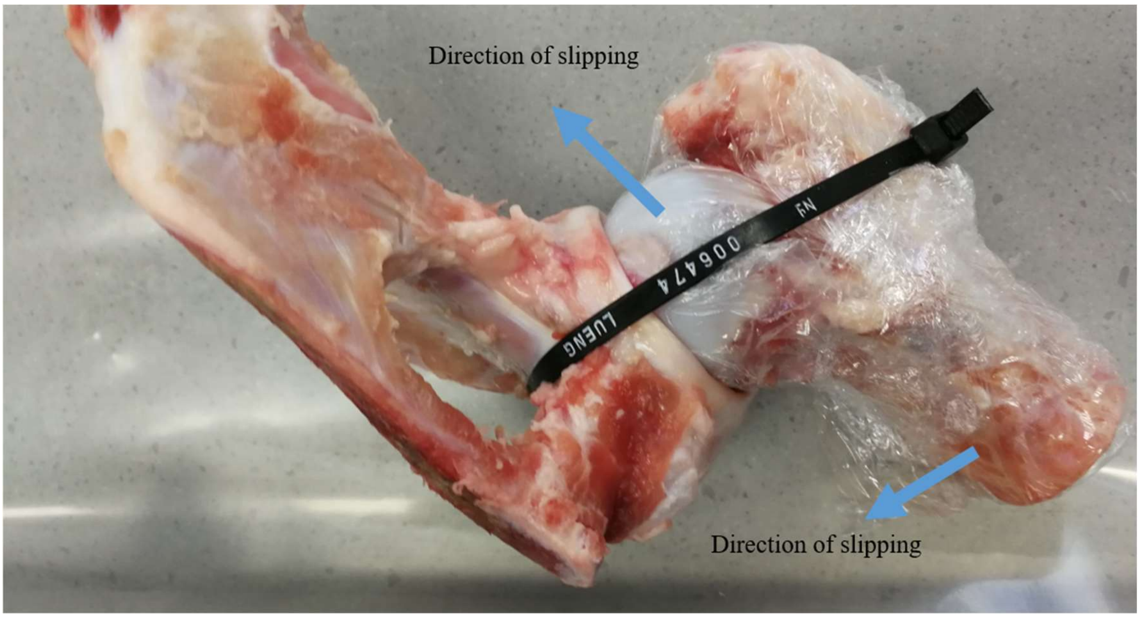

**Figure 3.9 Porcine hip joint loading by cable-tie. Directions of slipping of acetabulum were highlighted in arrows.**

Cross-sectional views at coronal plane of the acetabulum before and during load are shown in Figure 3.10. The change of acetabular cartilage thickness was visible and measurable on the CT images. However, cable tie loading was associated with instable hip joint assembly and uncertainty of direction of load.

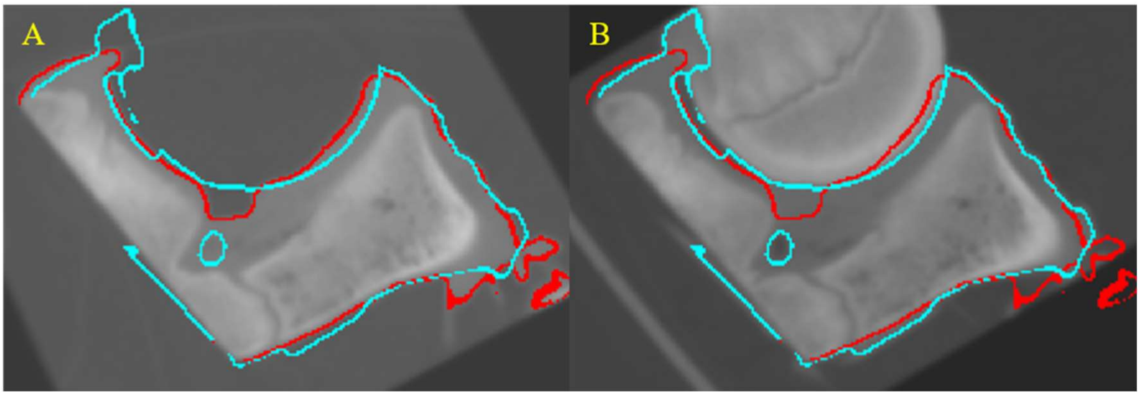

**Figure 3.10 Images of porcine hip joint from coronal view. A – acetabulum before loading. B – hip joint loaded with cable-tie. Red line, outline for unloaded soft tissues; cyan line, outline for loaded soft tissues.**

#### 3.3.3.5 NaI solution assisted segmentation on the femoral side

The aim of the acetabular soft tissue segmentation was to separate the acetabular soft tissue from the hip joint, so that the tissue behaviour can be measured by investigating the acetabular contacting surface. The basic steps for soft tissue segmentation (Figure 3.11Figure 3.5) are described below:

1) Acetabular bone extraction, to perform bone segmentation as described in Section 3.3.2, and apply the “flood fill” on the acetabular subchondral bone;
2) Femur extraction, to perform bone segmentation as described in Section 3.3.2, and apply the “flood fill” on the femoral side. Both femoral bone and femoral cartilage were captured;
3) Hip tissue segmentation, to perform similar segmentation as described in Section 3.3.2, except the greyscale value was defined from -200 to 4000 instead. The whole hip joint was captured; and
4) Acetabular soft tissue segmentation, to subtract the acetabular bone and femur from the hip tissue mask.

The segmented tissue mask of NaI aided femoral head is shown in Figure 3.11 in purple. Femoral cartilage was distinguishable from acetabular cartilage and femoral subchondral bone. Femoral bone and femoral cartilage were segmented and merged as the entire purple mask. However the femur interacted with labral apex at posterior region of the acetabulum. From the anatomy perspective, the highlighted purple mask belong to acetabular soft tissues.

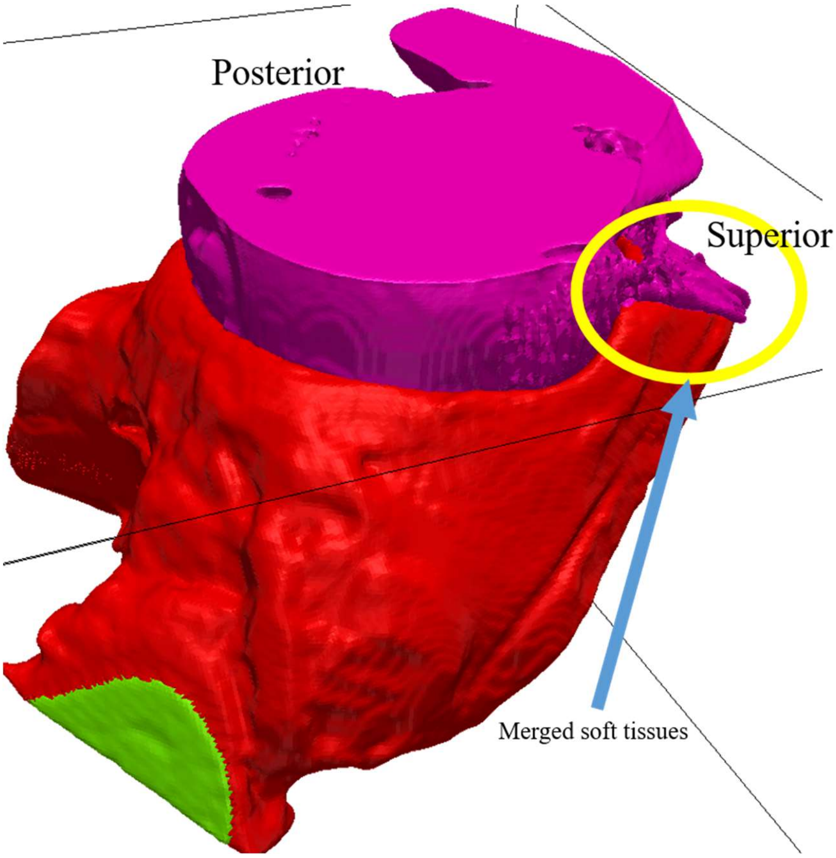

**Figure 3.11 Image processing that segment femoral head from the hip joint. Red mask, acetabular soft tissue; Green mask, acetabular bone; Purple mask, the femoral part.**

The acetabular soft tissue was separated from the hip in contact by applying NaI solution on the femoral head. The acetabular soft tissue was free of the contrast agent and was extracted completely across the thickness from the hip. The femoral neck was untreated and therefore merged with the acetabular rim at the posterior region.

## 3.4 Specification and design of the hip loading rig

The aim of this work was to create the loading condition relevant to cam-type femoroacetabular impingement (FAI) in the porcine hip joint. In Section 3.4.1, the design specification of a bespoke CT hip loading rig was established to meet the requirement of targeted loading conditions. The hip loading rig was re-designed based on an existing loading rig used for the vertebrae in the same institute. Two bespoke components are described in Section 3.4.3, for alignment of the femur and acetabulum. The rationale for choosing the targeted contact region was explained in Section 0, along with introduction to the alignment tools that help achieve the required contact in the porcine hip joint.

Design of experimental tools and geometry capture for computational models were performed in Solidworks 2018 (Dassault Systèmes, Vérlizy-Villacoublay, France). The bespoke tools, alignment connector base, acetabulum pot, and femur pot were all designed in Solidworks and manufactured in house.

### 3.4.1 Design specification of the hip loading rig

A hip loading rig was designed to provide stable and axial load between the acetabulum and the femur. A design specification is listed in

Table 3.3. The overall size of the loading rig should fit into the sample holder of 126 mm in diameter for the CT scanner. Transparent material was necessary for monitoring the loading conditions. Displacement-controlled load apply was preferred due to : 1) load drop in viscoelastic soft tissues with time-dependency; and 2) direct translation into finite element models. Delrin material was preferred for use with polymethyl methacrylate (PMMA) cement for tissue alignment.

**Table 3.3 Design specification of hip loading rig**

| Component | Requirement |
|---|---|
| Overall | Dimension 120 mm x 400 mm (øxL). Transparent material on the rig wall. |
| Load apply | Displacement controlled load apply up to 1 kN to the anterior-superior portion of the acetabulum |
| Femur pot | Suitable for PMMA cement, can hold femur in place |
| Acetabulum pot | Suitable for PMMA cement, can hold acetabulum in place |

The contact was aimed at the anterior-superior portion on the acetabulum through the femoral head. The contact region matched with the region of cartilage lesion in cam-type FAI. Axial load was applied from the femoral head, mimicking the increased and focused stress at the cartilage-labral junction due to the cam deformity. Due to limitation of the degree of freedom, femur rotation was not included in this cam-related loading. The acetabulum cup and femoral head were dissected to just fit into the limited space in the loading rig. Therefore, there is no reflection of inclination/anteversion angle related to clinical situation.

### 3.4.2 Available components from existing loading rig

A spine loading rig was previously used for providing axial load on vertebrae (Zapata-Cornelio et al., 2017). An exploded assembly view of the existing loading rig was shown in Figure 3.12. The load cell (between B and C) is made by RDP Group (Burgess Hill, UK), with maximum load of 4.4 kN and linearity error of ±0.2%. The load cell was calibrated in an Instron uniaxial testing machine (Instron Ltd, UK) up to 4.0 kN in compression.

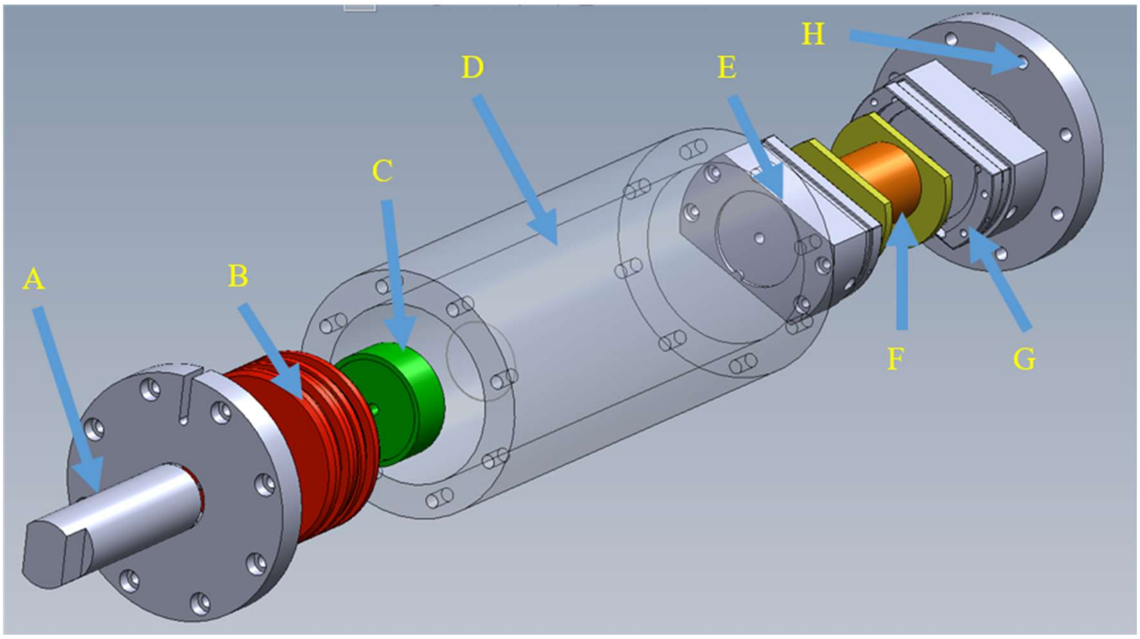

**Figure 3.12 Exploded assembly view of the spine loading rig. A – displacement-controlled load apply on a screw base; B – rotation eliminator that avoids any rotational force during the load apply; C – connector that connects the load cell with the sample pot; D, rig transparent tube; E, sample pot 1; F, sample under investigation; G, sample pot 2 that attaches to the rig base; H, rig base.**

### 3.4.3 Bespoke components for the hip loading rig

It was necessary to design an acetabulum pot and a femur pot so that the two tissue components can be constrained during load application and the contact region could remain consistent between specimens. The overall size of the tissue pots need to have sliding fit with the rig tube (Figure 3.12-D). The flat end of the tissue pots need to be attached to the connector (Figure 3.12-C) and the rig base (Figure 3.12-H) with tight fit. Screw holes are necessary to enable fixation of the tissue sample by inserting screws from the pot wall.

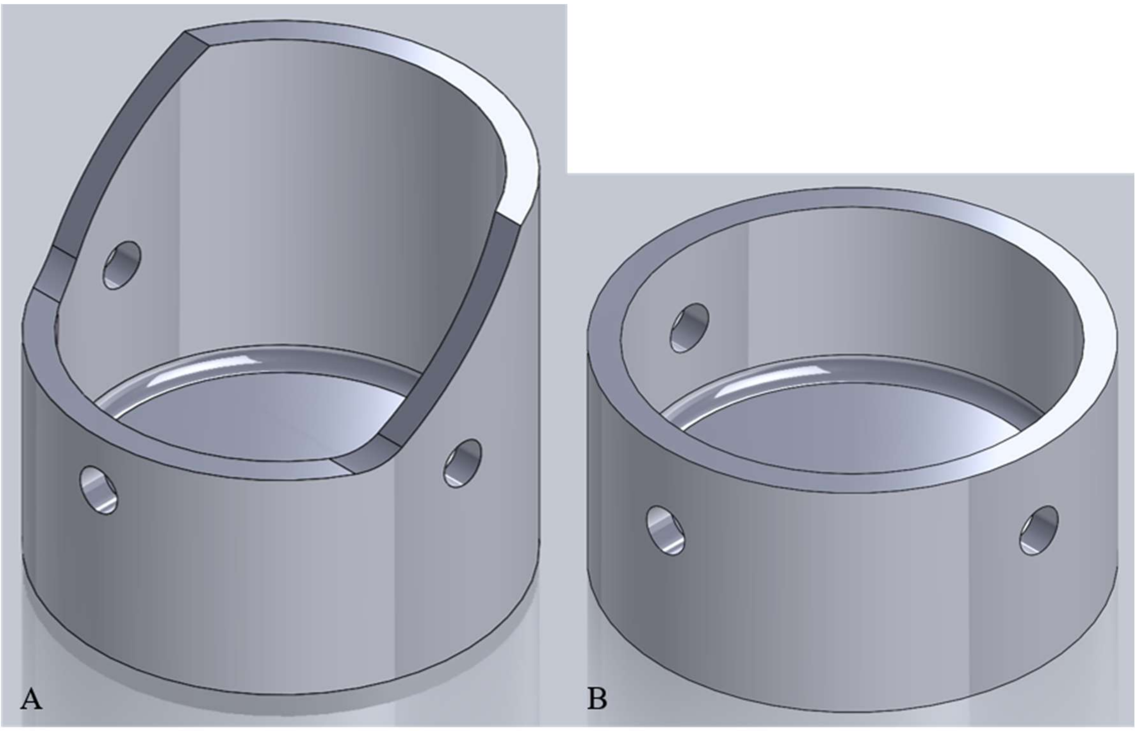

**Figure 3.13 3D CAD design for sample pots used in the hip loading rig. A, acetabulum pot; B, femur pot.**

The computer-aided design (CAD) model of the acetabulum pot is shown in Figure 3.13-A. The pot has a cylindrical shape with higher barrier at one side for supporting the acetabular bone at back of the socket. Screw holes were available from two directions for securing the acetabulum in position before the cement is cured. The bottom of the pot was designed to be attached to the connector. A detailed engineering drawing of the acetabulum pot can be found in Appendix A

The CAD model of the femur pot is shown in Figure 3.13-B. The femur pot has a cylindrical shape that holds the femur part. Screw holes were available from two directions for securing the femur in position before the cement is cured. The bottom of the pot was designed to be attached to the rig base. A detailed engineering drawing of the femur pot can be found in Appendix B.

Clearance is allowed between the inner wall of the tube and the outer wall of the tissue pots. The tissue pots can slide freely in the rig tube with the rig opened. However there could be two sources of friction: 1) air pressure when air is compressed with rig sealed; and 2) fluid tension when there are water drops between rig tube and tissue pots, which both prevent the load been applied.

## 3.5 Dissection and alignment of acetabulum socket and femoral head

The acetabulum and the femur were cemented in the bespoke pots throughout the load apply. The relative position of pots to the hip loading rig was also fixed due to the recess at the bottom of each pot. Hence the alignment of the acetabulum and the femur was conducted just before the cementing process.

### 3.5.1 Targeted contact region

The targeted contact region, shown in Figure 3.14, was chosen at the superior-anterior portion on the cartilage-labral boundary since acetabular cartilage lesions were often observed at 12 – 14 o'clock in clock face (Beck et al., 2004).

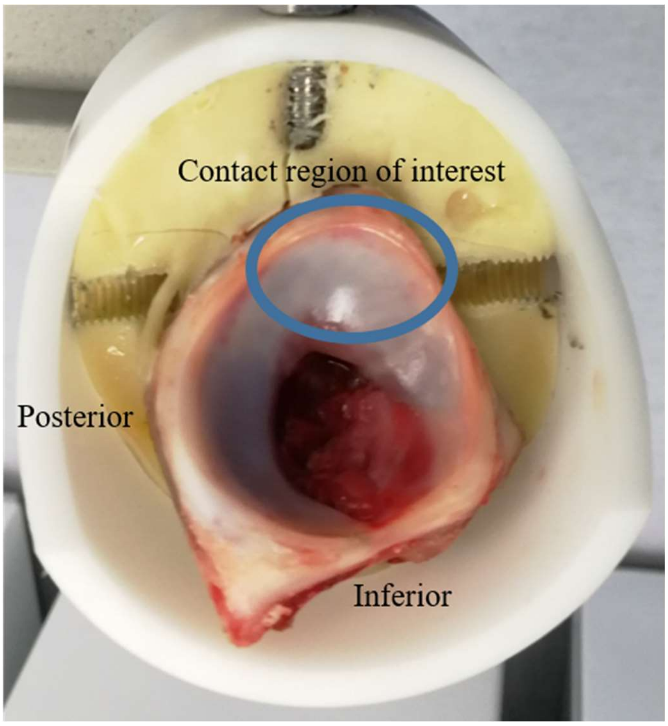

**Figure 3.14 Targeted contact region on the acetabulum socket.**

In addition, the superior portion of porcine acetabulum, from 11 – 1 o'clock, was soft and had sufficient content of labrum. However at the anterior or posterior region, beyond 1 o'clock or before 11 o'clock, felt hard and had much less content of labrum. Hence the study of porcine acetabular labrum was limited to the superior portion of the acetabulum.

### 3.5.2 Alignment apparatus

A concentric tool, shown in Figure 3.15, was previously used for alignment of acetabular socket with femoral head (Groves et al., 2017). An artificial femoral head was hung over the base. The femoral head is movable in vertical direction thus to allow alignment of the region of interest on the bottom sample to the centre of the base.

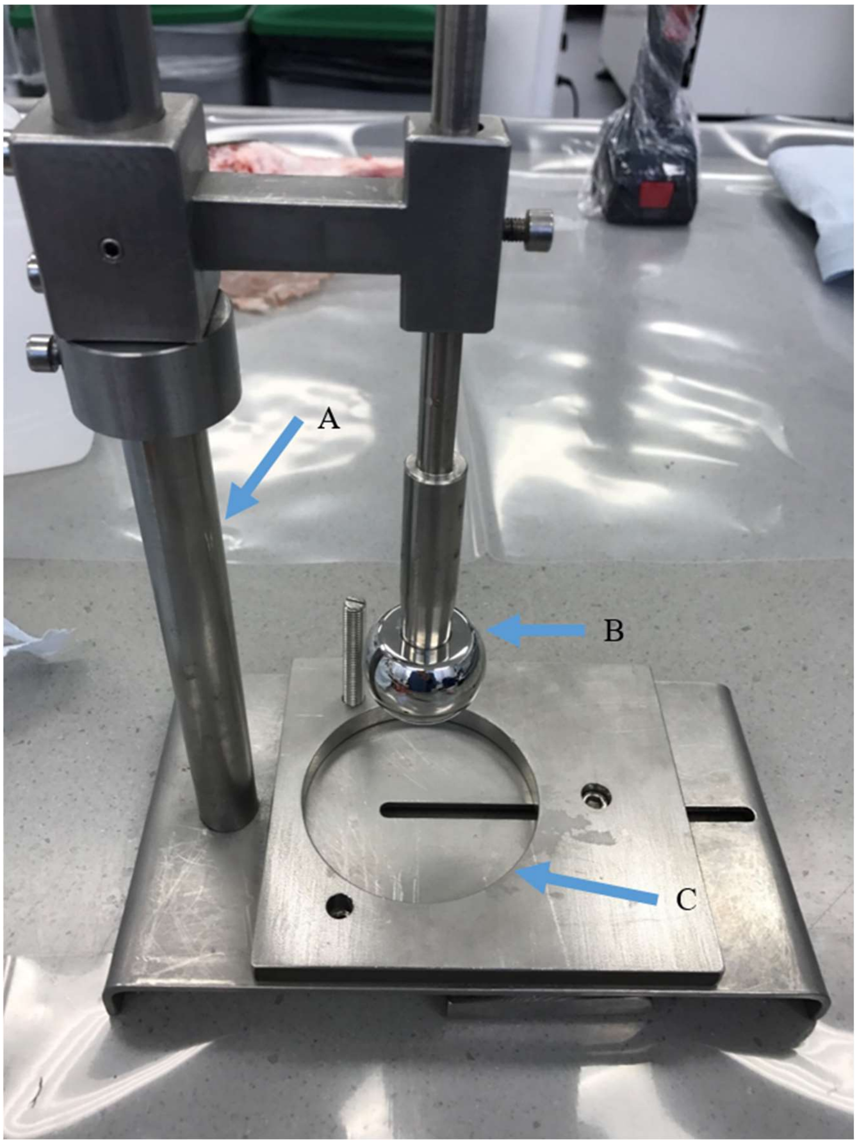

**Figure 3.15 Concentric tool used for alignment of acetabulum socket. A, concentric stand; B, artificial femoral head; C, connector base.**

A connector base was designed to connect the acetabulum pot with the concentric tool (Figure 3.15). The screw holes were coincident with the holes and groove on the concentric tool. The pot hole fits the acetabulum pot and is concentric with the artificial femoral head. Hence the acetabulum could be aligned so that the targeted contact region was at the centre of the pot.

### 3.5.3 Alignment and cementing of acetabulum

The bony structure of the acetabulum was shaped for fitting the acetabular component into the acetabulum pot (Figure 3.16). Excess bone on the posterior-inferior side of the acetabulum was dissected and removed. The bones at the back of superior region were kept as much as possible, which played an important role in supporting the superior acetabulum during load. The concentric tool (Figure 3.17) was used to align the centre of the acetabulum pot with the targeted contact region on the acetabulum. The targeted contact region was located in the superior-anterior portion at the labrum-cartilage junction due to the fact that the acetabular cartilage lesions were found to distribute at superior-anterior region (Beck et al., 2004). During alignment the acetabulum was held in place using three stainless steel screws to assure the artificial femoral head will come into contact with the acetabulum at the targeted contact region.

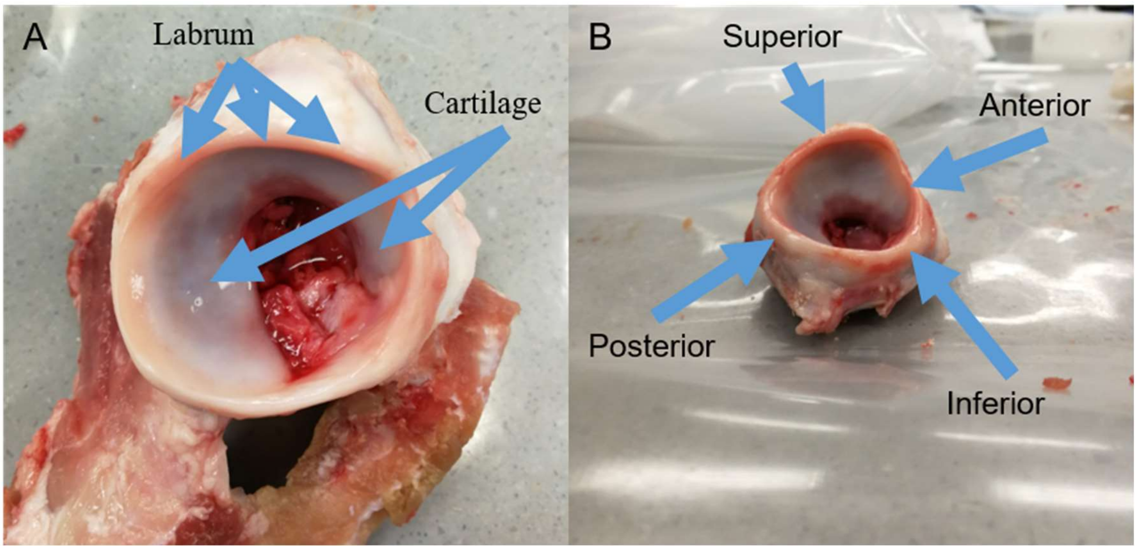

**Figure 3.16 Dissected acetabular socket for fitting into the acetabulum pot. A – acetabulum view with acetabular cup facing up. B – anatomical directions on the acetabular socket after dissection of excess bone.**

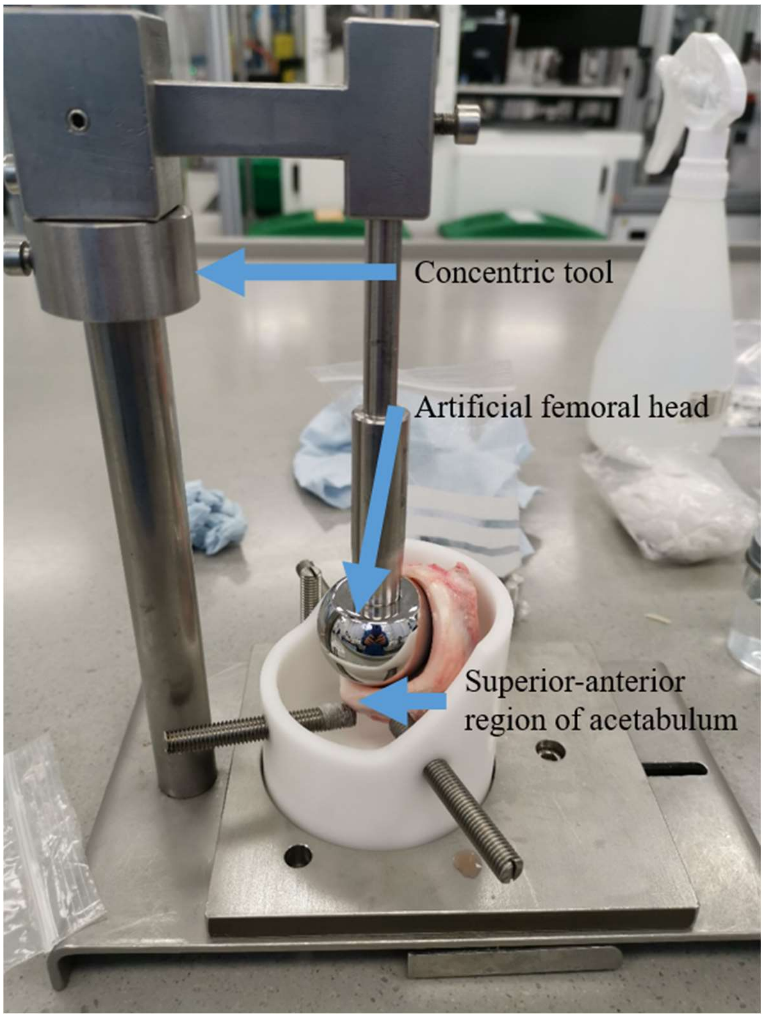

**Figure 3.17 Alignment of acetabulum using the concentric tool.**

Vaseline was applied onto the stainless steel screws before the pot was filled with liquid cement to avoid cementing of the supporting screws. The polymethyl methacrylate (PMMA) cement was prepared at weight ratio 2 rapid repair powder to 1 cold cure (PMMA Cement Handling, Leeds).

There was limited space in the pot and therefore the volume of bone support at the back of acetabulum was also limited. The cementing of acetabulum was expanded into two stages in order to assure the acetabulum was well supported by the cement. The acetabulum pot was inclined by approximately 40 degrees (Figure 3.29) during the first stage to provide cement support to the back of acetabulum socket. The femur was then ready for alignment and cementing while the acetabulum pot was being left for the cement to cure.

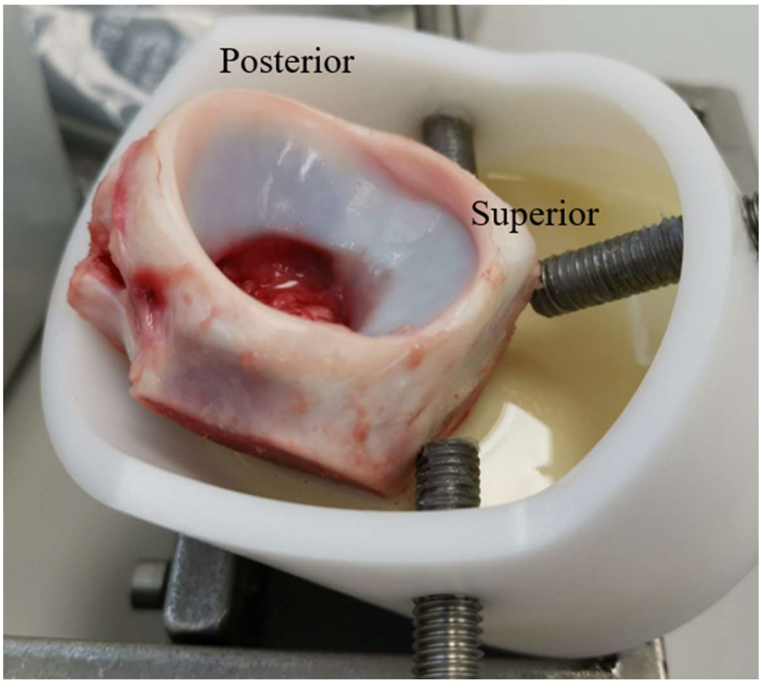

**Figure 3.18 Acetabulum pot inclined in order to cement the back of the acetabulum bone.**

### 3.5.4 Alignment and cementing of femur

The bony structure of the femur was further dissected in order to fit the femoral component into the femur pot (Figure 3.19). Three stainless steel screws were used to hold the femoral component in position. Alignment was performed manually by placing the femur pot above the acetabulum pot concentrically (Figure 3.20). The position of the femoral component was adjusted by the supporting screws until the femoral head came into contact with the acetabulum at the targeted contact region.

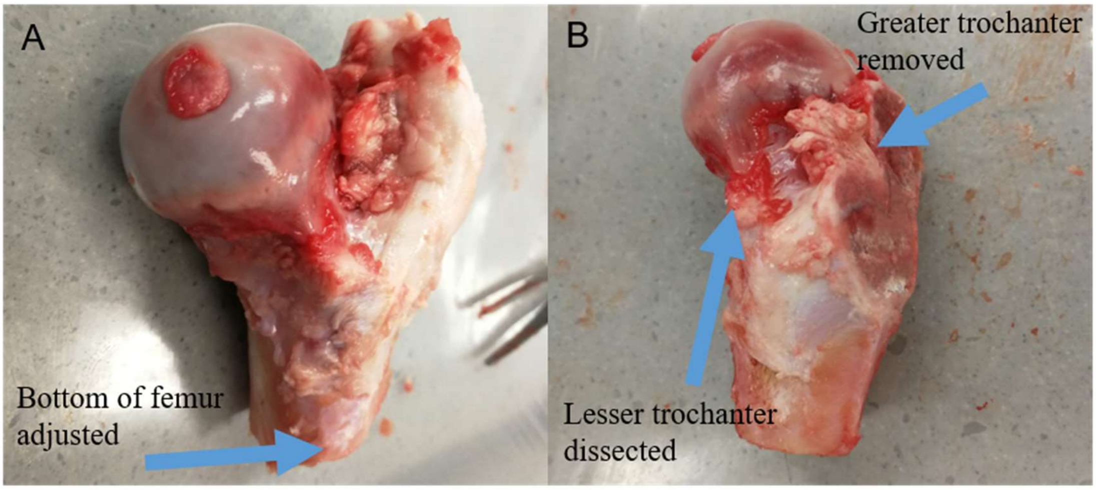

**Figure 3.19 Dissected femur component for fitting into the femur pot. A – femur after length adjustment. B – femur after adjustment of greater trochanter and lesser trochanter.**

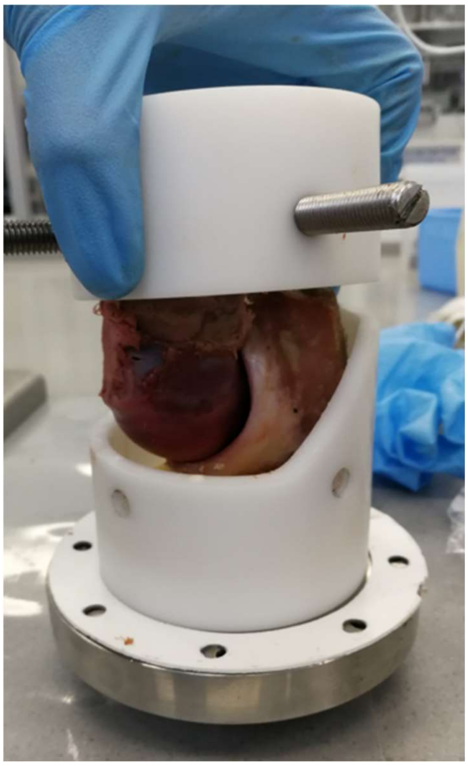

**Figure 3.20 Alignment of femur by pre-assembling the two pots.**

The femur pot was filled with the same cement, described in Section 3.5.3, while being placed horizontally. Meanwhile, after cooling of the acetabulum pot at the first stage, cement was filled vertically into the acetabulum pot for the second time for securing the lower bony support. (Figure 3.21).

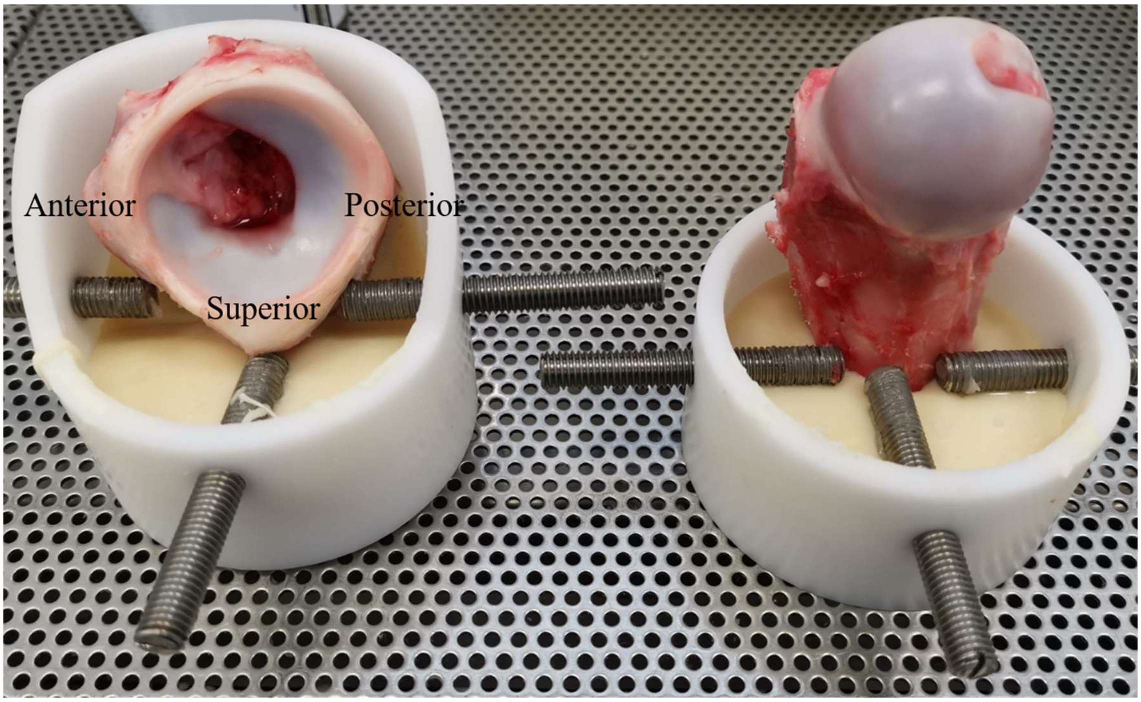

**Figure 3.21 Final cementing of acetabulum and femur pot.**

The cement provided physical fixation to the bony support on the tissues. The cement was poured into the pot as liquid, covering the complex bone structure, and cooled down to solidify. However, the cement shrinks during the curing process. Gap was therefore created between the Delrin wall and the cement (Figure 3.22). The gap could led to free rotation of the tissue and cause inconsistent contact region in the hip loading rig. A few cement drops were left intended on the junction, as shown in Figure 3.23, to fill the gap and prevent free rotation between cement and the pot.

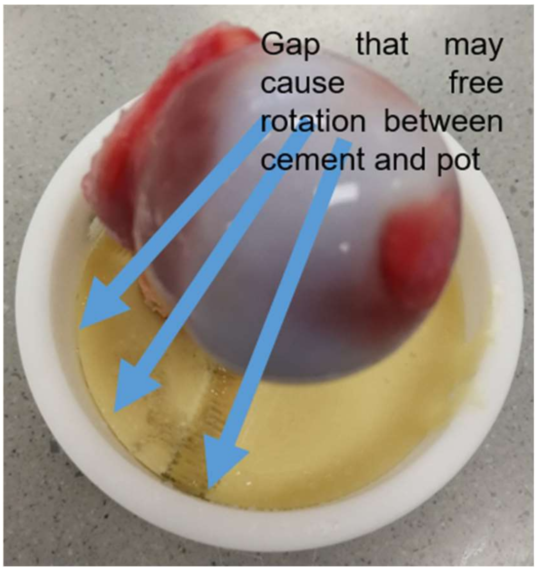

**Figure 3.22 Gap between cement and pot.**

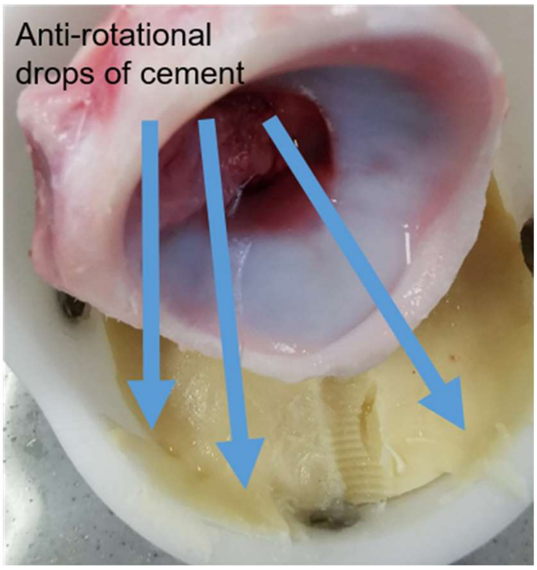

**Figure 3.23 Drops of cement on the Delrin wall to prevent gap.**

### 3.5.5 Application of NaI solution

Once the cement had fully cured, the screws were removed from the pots. The femoral head was soaked into NaI solution for five minutes (Figure 3.34). The femoral head was then covered with cling film to prevent absorption of the NaI solution from the acetabulum side.

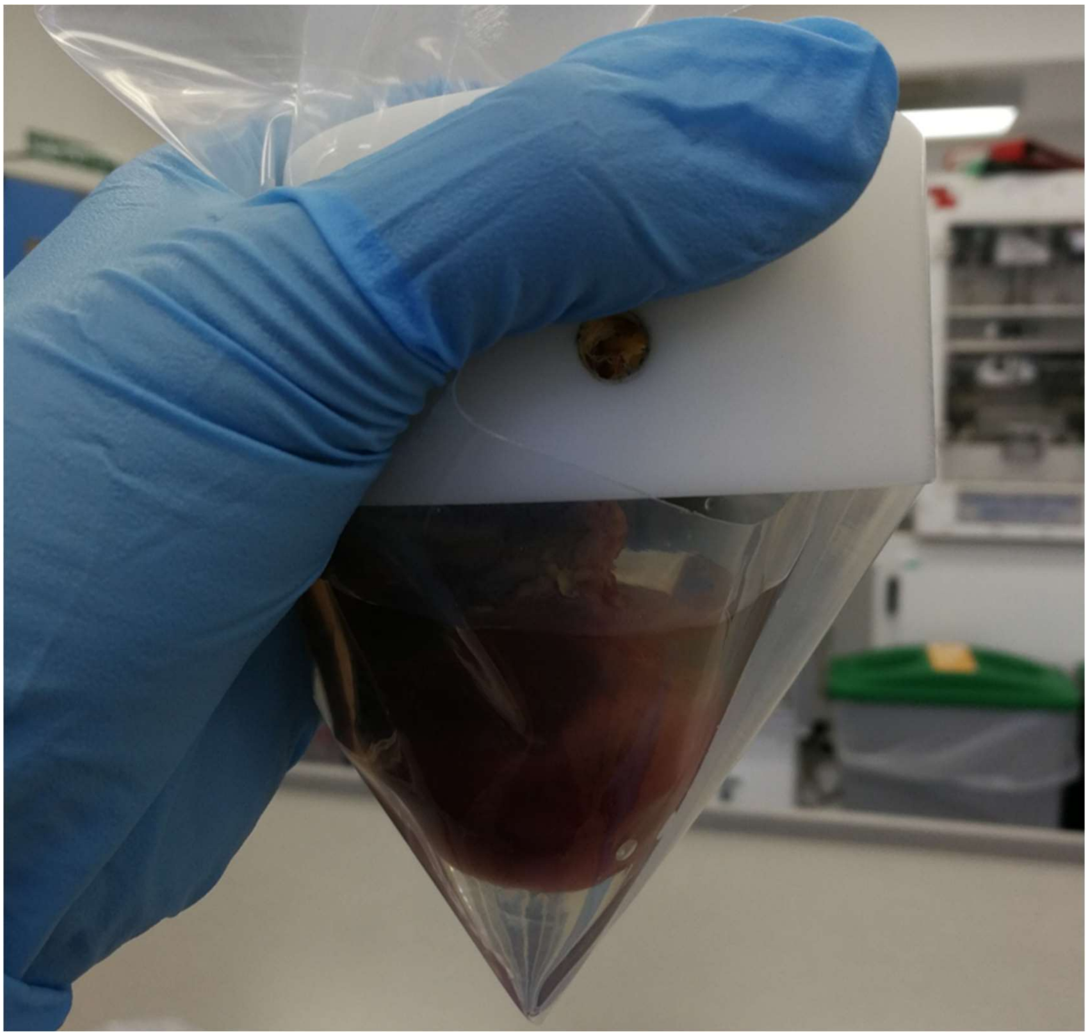

**Figure 3.24 Femoral head soaked into NaI solution**

### 3.5.6 Assembly of CT loading rig

Assembly of CT loading rig started with placing the acetabulum pot into the Perspex tube. The femur pot was then attached onto the connector and secured with the rig cap. The femoral head was aligned into the acetabulum socket before placing the femur pot into the Perspex tube (same as in Figure 3.20). The rig cap was secured onto the Perspex tube by placing screws between the two components. The displacement screw was turned clockwise to make sure the acetabulum pot came out of the Perspex tube. The rig base could then be attached to the acetabulum pot and secured onto the Perspex tube (Figure 3.25).

**Figure 3.25 Hip loading rig assembled and sealed.**

Displacement controlled load was applied onto the superior-anterior region at the acetabular cartilage-labral junction through the femur by turning the displacement screw on top of the hip loading rig. The acetabulum pot was fixed on the rig base, in such a way that the axial rotation and planar translation were constrained. The femur pot was attached onto the connector, while axial rotation was allowed but planar translation was constrained. Torsional force was eliminated in the rig, which means the femur had free rotation, in theory, relative to the acetabulum. The relative rotation between components is investigated in Chapter 4.

## 3.6 Measurement of soft tissue movement

This section describes the procedures and algorithms which were developed for the measurement of acetabular soft tissue position in unloaded and loaded states. Three areas of development are described. Firstly the registration of the images of the acetabular bones before and during load is described (Section 3.6.1). This step aligns the two images so that the soft tissues shapes before and during loading are aligned. Secondly the method for measuring cartilage strain within the area of the contact is described (Section 3.6.2). The strain values were taken in a two-dimensional plane and the method for selecting that plane also is detailed. Finally, the capture of the labrum shape in the unloaded and loaded states, and the extraction of quantitative labrum movement is described in Section 3.6.3. The labral movement is described in three-dimensional space.

Post-processing of the scanned images was performed in Simpleware ScanIP M-2017.06 (Synopsys, Mountain View, CA, United States). The post-processing included: image resolution adjustment; mask registration; measurement of soft tissue movement; capture of image slice; and export of meshed labral part.

MATLAB R2018a (MathWorks, Natick, Massachusetts, United States) was used as the numerical computing environment. The reference locations in mask registration process were calculated in MATLAB. The script for measurement of labrum apex displacement was also developed in MATLAB.

### 3.6.1 Registration of acetabulum before and during load

The aim of acetabular bone registration was to calibrate the position of the acetabulum before and during load. Since the bone was treated as rigid throughout the experiment, the soft tissues, before and during load, became comparable after the bony parts have been registered to the same location.

The acetabulum bone before load was separated from the CT images (Figure 3.26). The two highlighted gaps on the acetabulum were believed to be growth plates (Geiger et al., 2014) and may experience subtle deformation during load. Besides, the targeted contact region was mostly located at the superior portion of the acetabulum. Hence, the ilium was treated as the original reference. The local coordinate system was created by choosing three points (point A, B, and C) at the ilium corner and running a bespoke script (see Appendix C) in MATLAB R2018a (MathWorks, Natick, Massachusetts, United States). Coordinates of point P was calculated by the script to allow line PB being perpendicular to line PC. The acetabulum local coordinate system was then created based on line PB and PC.

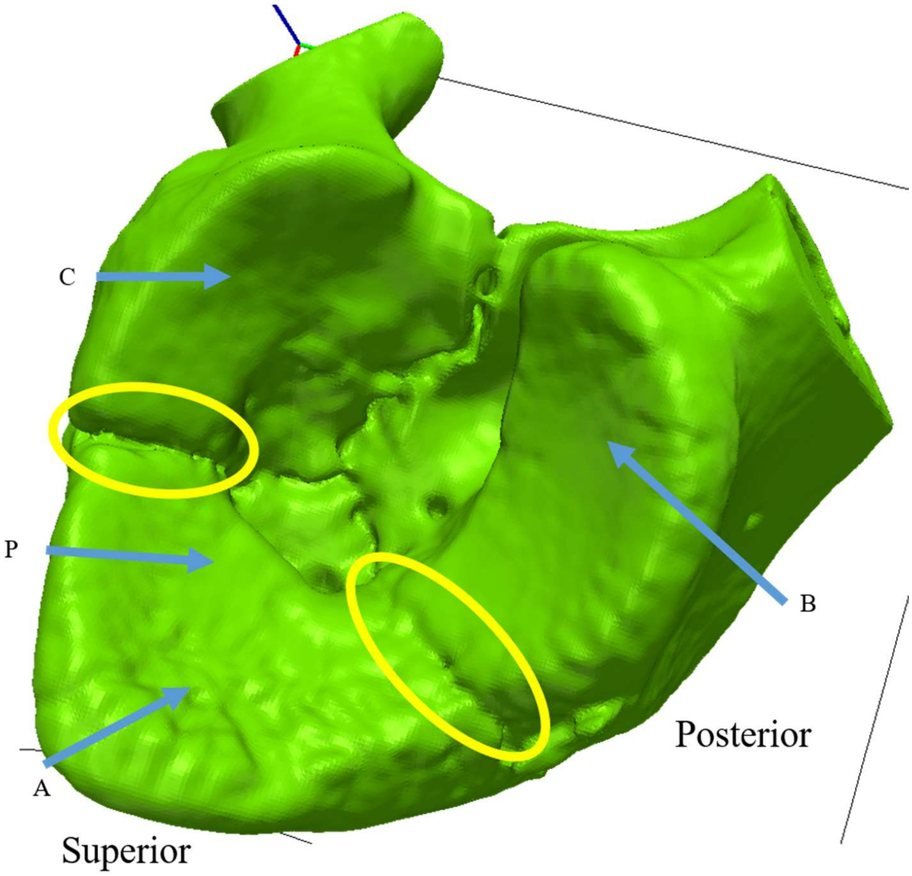

**Figure 3.26 Acetabular bone segmented for registration. Highlighted gaps demonstrate the existence of growth plates. Point A, B, and C are the approximate location for the reference points on the acetabular bone. P is the calculated origin of the local coordinate on this particular acetabulum.**

The same acetabulum bone, while during load, was also oriented based on the same three point chosen on the bone at rest (Figure 3.26). Once the two acetabular bones were aligned with the same coordinate system, the two sets of image data were brought together into the same space. The acetabular tissues during load was then offset by a vector, due to different local location of the two acetabulum, to complete the registration of acetabulum (Figure 3.27). The upper surface of the two acetabular bones showed a mix of two colours, which means the two bone surfaces have been close enough to each other.

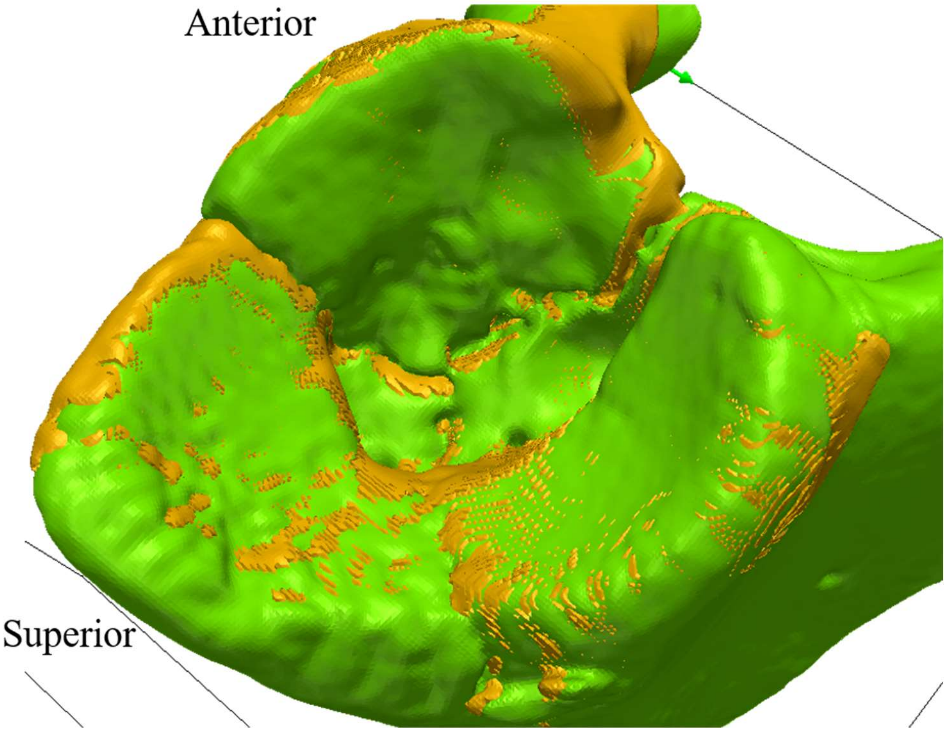

**Figure 3.27 Registration of the same acetabulum before and during load. Green mask, .acetabular bone before load; brown mask, acetabular bone under load.**

The soft tissues were segmented after registration (Figure 3.28). The soft tissues under load was deformed and illustrated below the unloaded soft tissues Therefore the actual contact region was implied by the unloaded (red) tissues that uncovered by the loaded (cyan) tissues.

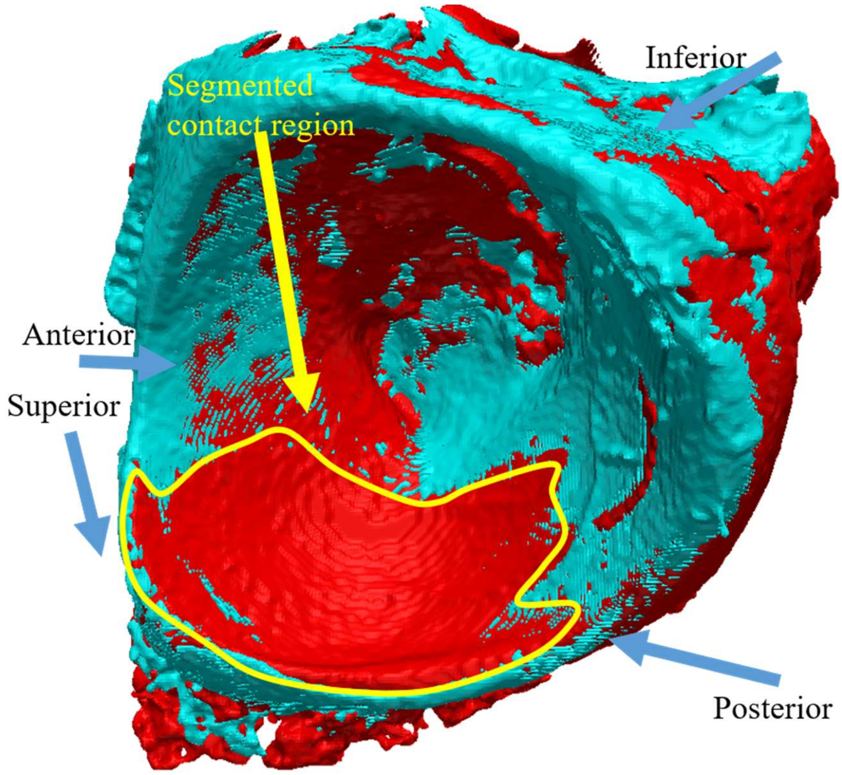

**Figure 3.28 Entire acetabulum, sample PH6, before and during load, segmented after registration. Red mask, tissues before load; cyan mask, tissues during load. The actual contact region was highlighted on the acetabulum.**

### 3.6.2 Measurement of acetabular cartilage strain

Acetabular cartilage strain was measured to investigate the cartilage deformation due to cam-type FAI related loading scenario. The strain was measured as the percentage change in cartilage thickness due to load. The actual contact area was narrowed down to a focused contact region. The acetabulum was then oriented according to the focused contact region so that the cartilage strain could be measured across the centre of the actual contact region.

The mask of acetabular soft tissues during load was gradually dilated so as to approach to the unloaded tissues. The contact area was thus narrowed down to a focused contact region where only large deformation occurred (Figure 3.29).

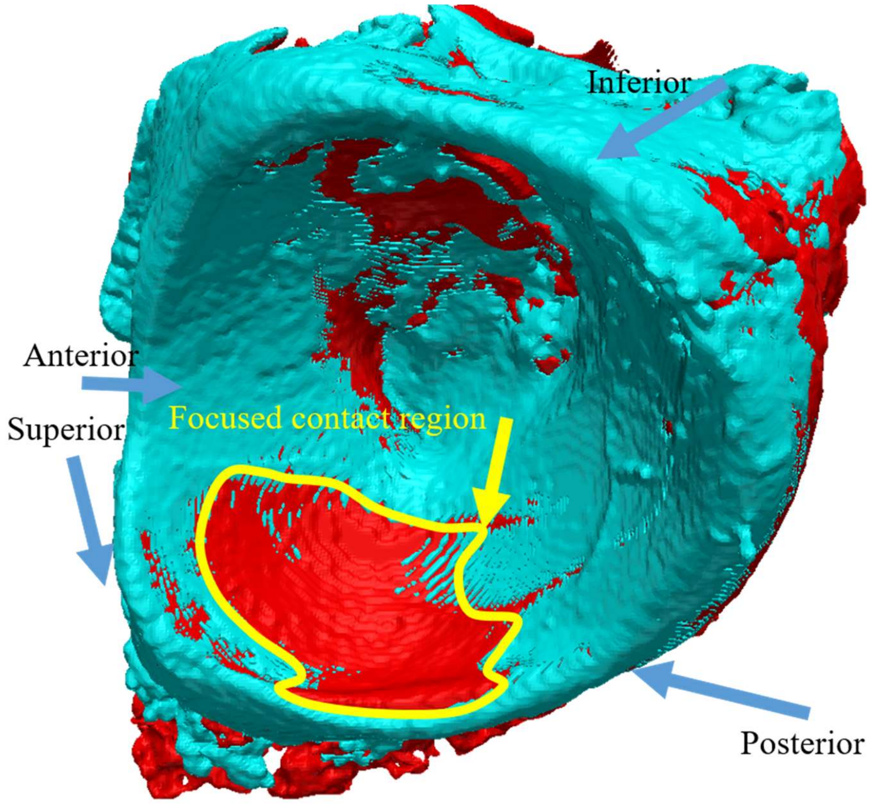

**Figure 3.29 Image processing that locate the focused contact region.**

In order to allow cross-sectional view across the centre of the focused contact region, the entire acetabulum was again oriented to have the focused contact region pointed at six o'clock (Figure 3.30 – B). As a result, the default cross-sectional view at y-z plane was able to pass through the centre of the focused contact region, allowing measurement of cartilage strain with respect to the distance to bony support.

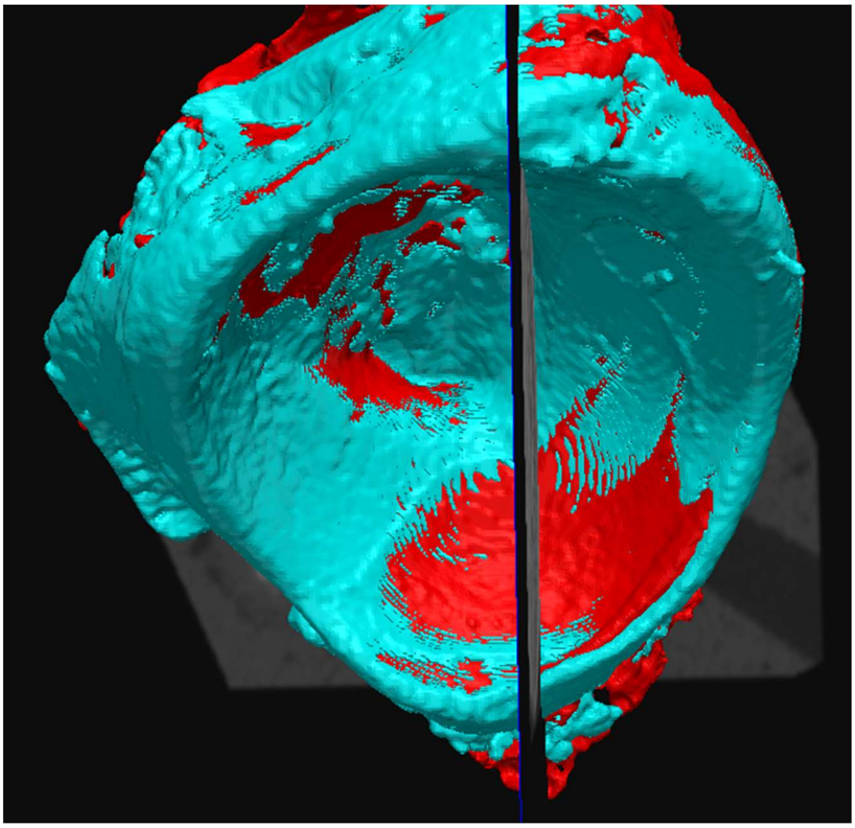

**Figure 3.30 Orientation of acetabulum to allow the centre of focused contact region parallel to six o'clock direction.**

The 2D image slice at the centre of the focused contact region, that bisects the acetabulum in Figure 3.30, was used for measurement of cartilage strain. A total number of eleven points were chosen on the subchondral bone surface, evenly distributed from bone support to the acetabular fossa.

Acetabular cartilage strain in the radial direction at each point was thus obtained using the following equation:

$$\text{Cartilage strain} = \frac{\text{Unloaded thickness} - \text{loaded thickness}}{\text{Unloaded thickness}} * 100\%$$

### 3.6.3 Measurement of acetabular labrum shape deformation

The labral displacement was measured to investigated the labrum behaviour due to cam-type FAI related loading scenario. The movement of acetabular labrum shape due to load was investigated by reconstructing the labral apex. Meshes of the acetabular labrum was generated where the element size was equal to the image resolution. The highest nodes, along the axial direction of the acetabulum, was recorded circumferentially and plotted together to produce a point cloud of the labral apex. The labral deformation was measured radially as the distance between apex points before and during load.

The acetabular labrum was considered as in a cylindrical coordinate system (Figure 3.31). The labrum was divided into a number of sectors by sweeping along the circumferential direction at a specified incremental angle. The figure only showed 10 sectors for simplification. In the actual labrum reconstruction, the cylindrical coordinate system was divided into 360 sectors. The highest node, along the longitudinal axis, at each slice was then recorded for reconstruction of labral apex

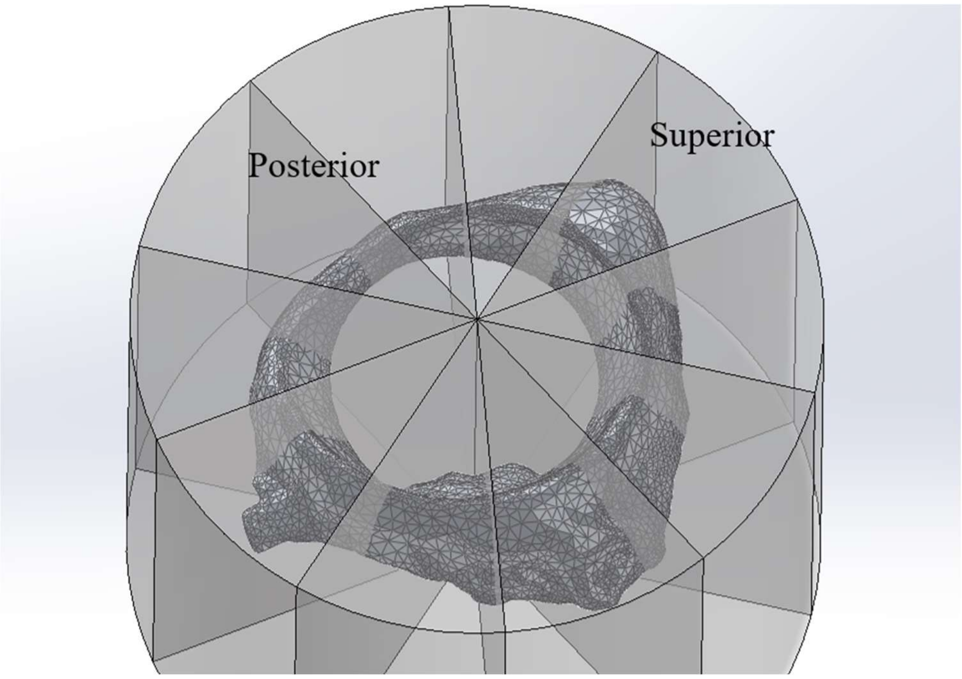

**Figure 3.31 Demonstration of local cylindrical coordinate system of the labrum for recording labral apex displacement.**

A bespoke script (see Appendix D) was written in MATLAB R2018a for automatic generation of labrum reconstruction, based on two input (.inp) files of the labrum model before and during load. Each input file contained the local coordinates of every node in the labrum FE models. A sample reconstruction of acetabular labrum is shown in Figure 3.32.Shape change of the labrum apex can be observed at the superior-anterior region as the blue dots (apex under load) displaced away from the red dots (apex before load).

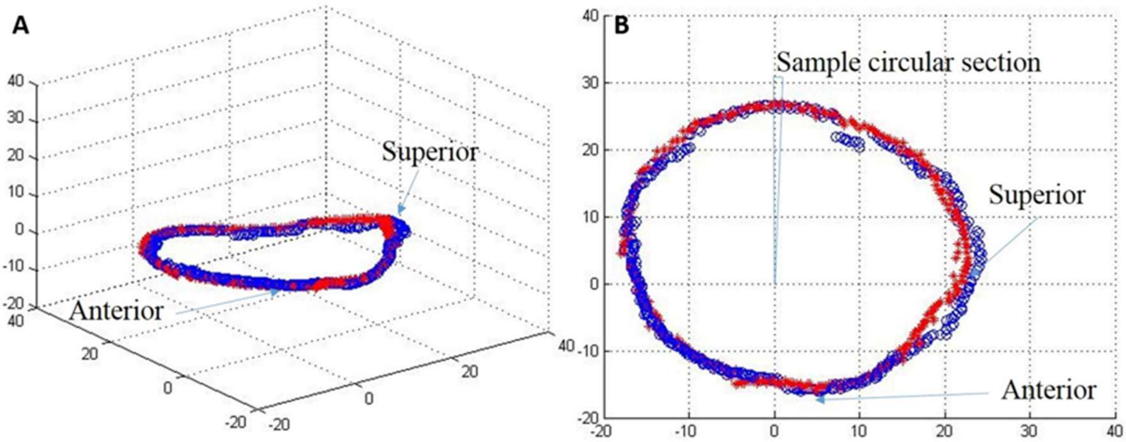

**Figure 3.32 Reconstruction of labral apex. Red dots, apex points before load; blue dots, apex points under load.**

## 3.7 Achievement and key findings

The preceding chapter described in detail the development of several experimental, imaging and algorithmic methods, which will be used in the subsequent studies. The achievements and findings were:

- A straight-forward methods for the separation of femoral and acetabular cartilage surfaces in a micro CT image of a compressed porcine hip joint.
- The design of a rig for the alignment and loading of porcine hip joint within the XtremeCT scanner.
- Image processing methods for the identification of a plane central to the joint contact area and measurement of cartilage strain within that plane.
- Image processing and algorithmic methods for reconstruction of the labral apex and measurement of labrum displacement within the apex point cloud.

Porcine tissues were used as preliminary material for human study. The hip joint in quadruped has naturally higher flexion angle (Hogervorst et al., 2009) and lower range of motion compared to biped. Since femoral rotation was not considered in this work, the differences between quadruped and biped have little effect on the axial loading. Hips from both species shared similar dimension in femoral head and acetabular socket. Therefore it was possible to create similar loading conditions in porcine hips to those observed in human hips. However, human acetabulum was surrounded with thicker and wider labrum (Seldes et al., 2001) while porcine labrum existed at part of the acetabular edge (section 3.4.5.1). Consequently, porcine labrum may play a less important role in hip loading as human labrum does. In addition, porcine cartilage was thinner and more water-permeable than human cartilage. As a result, porcine hip may be found less stiff and react quicker to load.

Acetabular cartilage surface was separated by applying NaI solution on the femoral head and have the femoral head covered with cling film. Bone registration successfully calibrated the two acetabular bones, before and during load, to the same location. Hence, the two segmented acetabulum were comparable regarding investigation of soft tissue movement. It is suggested that the NaI solution could have covered the femoral neck and the lesser trochanter, in order to separate femur from acetabulum at posterior region.

The soft tissue movement due to load was captured by comparing the segmented CT images before and during load via image registration. Ridzwan et al. (2018) investigated bone fracture by applying digital volume correlation (DVC) that determines the displacement of voxel patterns in the CT images. However, the cartilage and labrum were continuous in the CT images without clear reference point for DVC. Gustafson et al. (2016) measured vertebral body strain by applying digital image correlation (DIC) that determines the tissue strain from applied strain rosette. However, it was difficult to apply strain markers on the labrum due to slippery surface, limited width, and inadequate speckle for DIC.

Two growth plates were observed in porcine acetabulum images (Figure 3.33). Hence the acetabular bone sample was formed by three bony parts connected by two cartilages, suggesting that the entire acetabulum bone structure would not always be rigid under load. Since the targeted contact region was located on the superior-anterior portion of acetabulum, the acetabulum local coordinate system was therefore developed based on reference points all located at the superior acetabular bone section.

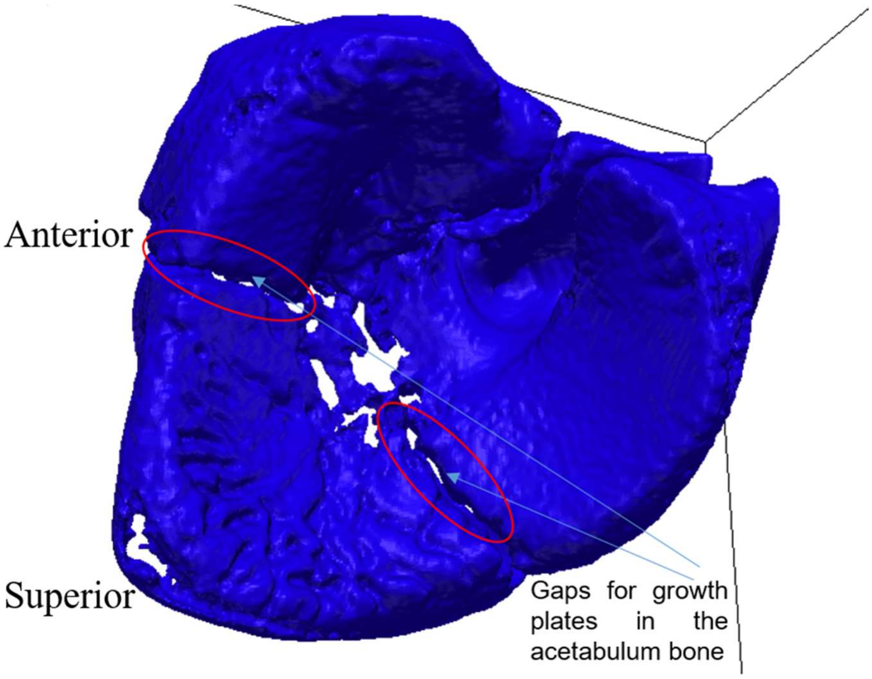

**Figure 3.33 Evidence of growth plates in acetabular bone.**

An apex ring was observed on the acetabulum when NaI was first applied on the acetabular soft tissue surface. This was due to more NaI been absorbed by the tissue at the rim. The different ability in NaI absorption may reflect the differences in tissue structure and properties. However, the cartilage-labral junction is still not clear and there is no evidence that the highlighted apex rim is effectively the labrum tissue.

A focused contact region was defined at the location where large deformation occurred. Cartilage strain was measured at the centre slice of the focused contact region. However, the focused contact region was mostly observed on the labrum because the labrum was more flexible than articular cartilage. Due to the oval shape of femoral head, the focused contact region on the labrum did not necessarily point towards the focused contact region on the cartilage.

A schematic drawing of possible labrum apex movement is shown in Figure 3.34. By dividing the labrum into cylindrical sectors, radial movement A and D can be captured correctly. However, movement B and C results in inconsistent reference points in the labrum apex measurement. In axial loading, the acetabular rim is more likely to experience movement A, C and D. The labrum will have more degrees of freedom if hip rotation is also considered.

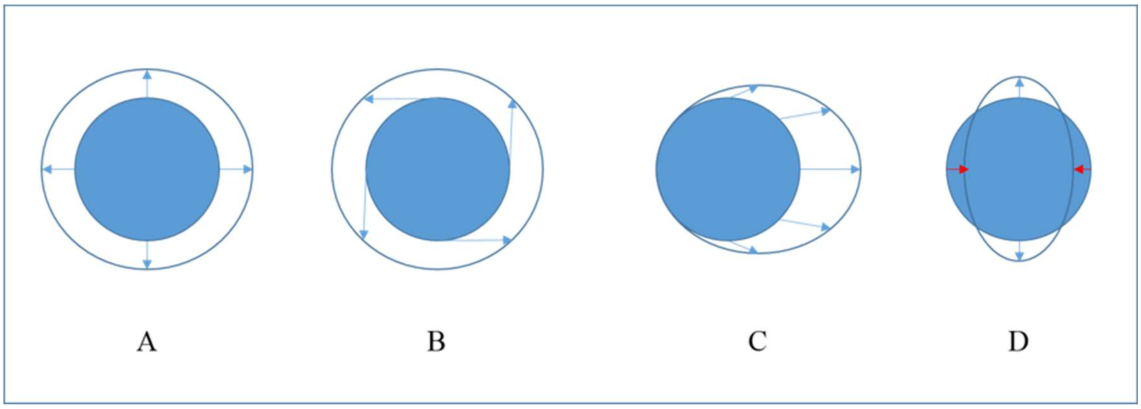

**Figure 3.34 Schematic diagrams of possible labrum apex movement. A, radial expansion; B, rotational displacement; C, offset expansion; D, elongation and compression.**

# Chapter 4

# Experimental study on acetabular soft tissues behaviour under load

## 4.1 Introduction

The aim of this chapter is to quantify acetabular soft tissue displacement under FAI related loading scenario, based on the methods developed in Chapter 3. Acetabular tissue damage is a factor implicated in osteoarthritis (OA) (Brandt et al., 2006 and Makela et al., 2012) and a cause of hip pain and limited hip mobility. However, the damage mechanism on soft tissues is poorly investigated. In addition, the connection between soft tissue and bone, as well as the initial constraint within soft tissue in the joint, are neglected when performing loading tests on tissue samples. The investigation of acetabular soft tissues behaviour *in vitro* could lead to improvement in the understanding of the biomechanical environment during hip motions. In this study, six porcine right hip joints were used for measuring the cartilage strain and labral displacement under load conditions relevant to cam-type FAI. Besides the measurement described in Chapter 3, this chapter investigated the effect of labrum circumferential tension by comparing the labrum behaviour with intact labrum and with labrum cut. The loss of labrum can be associated with labrum tear or labrum resection. The hypothesis is that the labrum will deform more easily under labrum cut.

The tissue preparation followed the procedures developed in Chapter 3 and is briefly described in Section 4.3.1. The porcine hip joints were dissected with intact labrum and disarticulated for alignment. The femoral head was applied with NaI solution and wrapped with cling film for separation of the acetabular soft tissue in the CT image. Cam-type FAI-related load was created in the hip loading rig by loading the acetabulum at the superior-anterior region.

Three sets of CT scans were performed on each sample in this study, which is described in detail in Section 4.3.2. Firstly, the tissue sample was scanned in the rig before load when the femur and the acetabulum were just in contact. Secondly, the tissue sample was scanned under a displacement-controlled load.

In addition to the methods developed in Chapter 3, labrum cut was created after the second load for each sample. The labrum cut was at the site close to the contact region since labral tears were found to occur at the superior region clinically due to anterior impingement (Grant et al., 2012). Similar load conditions were applied to the tissue sample where the third scan was performed.

The image processing and measurement of soft tissue behaviour were developed in Chapter 3 and briefly described in Section 4.3.3. Acetabular bone registration was performed on each tissue sample, followed by the segmentation of the acetabulum tissue. Acetabular cartilage strain was measured at the centre of the focused contact region, on a selected 2D plane. Acetabular labral displacement was measured from the acetabular rim by reconstructing the labrum apex in a cylindrical coordinate system in 3D space.

This study investigated the soft tissue behaviour under loading scenario relevant to cam-type FAI, which improved the understanding of the acetabular mechanism in such load conditions *in situ*. Quantification of the tissue behaviour enhanced the understanding of the extent of tissue displacement and also allowed comparison of the experimental results with further FE studies on hip joint.

## 4.2 Aims and objectives

The aim of this study was to apply the porcine hip alignment and loading protocol (Chapter 3) to the six specimens and assess the effectiveness. The soft tissue displacement was quantified in CT images. Acetabular cartilage strain measurement in 2D, described in Chapter 3, was applied to assess inter-subject variation and measurement uncertainty. Acetabular labrum displacement measurement in 3D, described in Chapter 3, was applied to asses inter-subject variation and measurement uncertainty. The objectives of this study were as follows:

1. To apply appropriate loading scenario in porcine hip joint that replicates the abnormal contact at cartilage-labral junction.
2. To create labrum cut and to re-load the tissue sample.

3. To obtain CT images of the porcine tissues: 1) unloaded and with intact labrum; 2) loaded and with intact labrum; and 3) loaded with labrum cut.
4. To measure the cartilage strain and labrum deformation through image processing.

## 4.3 Methods

The aim of this section is to describe the experimental protocol, partly based on the methods developed in Chapter 3, and explain the rationale of extracting the acetabular soft tissue displacement from CT images. The porcine hip samples used were coded from PH10 to PH15 in this study. The experimental study consisted of three parts (Figure 4.1): 1) porcine hip tissue dissection; 2) CT scan of porcine hip before and during load; and 3) Measurement of soft tissues movement due to load. A full laboratory protocol of the experimental study is given in the Experiment Procedure (see Appendix E) and was applied to all six samples in this study.

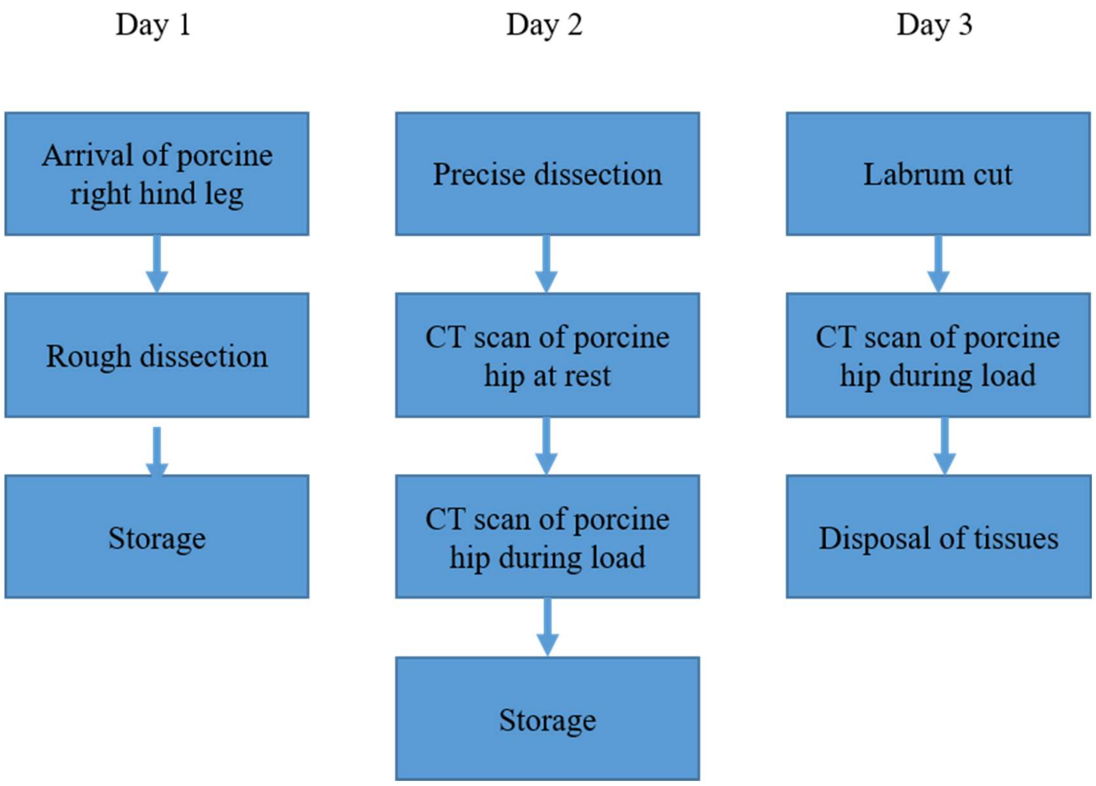

**Figure 4.1 Flow chart of the experimental methods for each sample.**

### 4.3.1 Tissue preparation

Six porcine right hind legs were used in this study. Porcine hip tissue was supplied by a local abattoir (John Penny and Sons, Rawdon, Leeds). Pigs were slaughtered at between 11-12 months old, at a weight of 92-108 kg. Porcine hind legs were only available on the right side from the abattoir, which makes the development of alignment simpler.

Tissue samples were prepared in three separate laboratory sessions: 1) dissection of porcine right hind leg on the day of tissue arrival, 2) disarticulation (to dissect the capsule and the ligament of the head of femur that connect the acetabulum with the femur), alignment and cementing of the hip joint after being stored in the fridge; 3) to create labrum cut at the site close to the contact region and re-load the tissue sample. One freeze-thaw cycle was applied to the sample where there were more than two days between the day of dissection and disarticulation. Tissue samples were stored at 4°C when in the fridge and at -20°C when in the freezer.

The porcine hip joint was dissected from the leg as shown in Figure 4.2. Acetabular cartilage and labrum were exposed, with surrounding soft tissues and capsule removed. The ligament of the head of femur was dissected to leave the articular cartilage surface clear. Details of the dissection and storage procedure were explained in Chapter 3 as part of the experiment protocol.

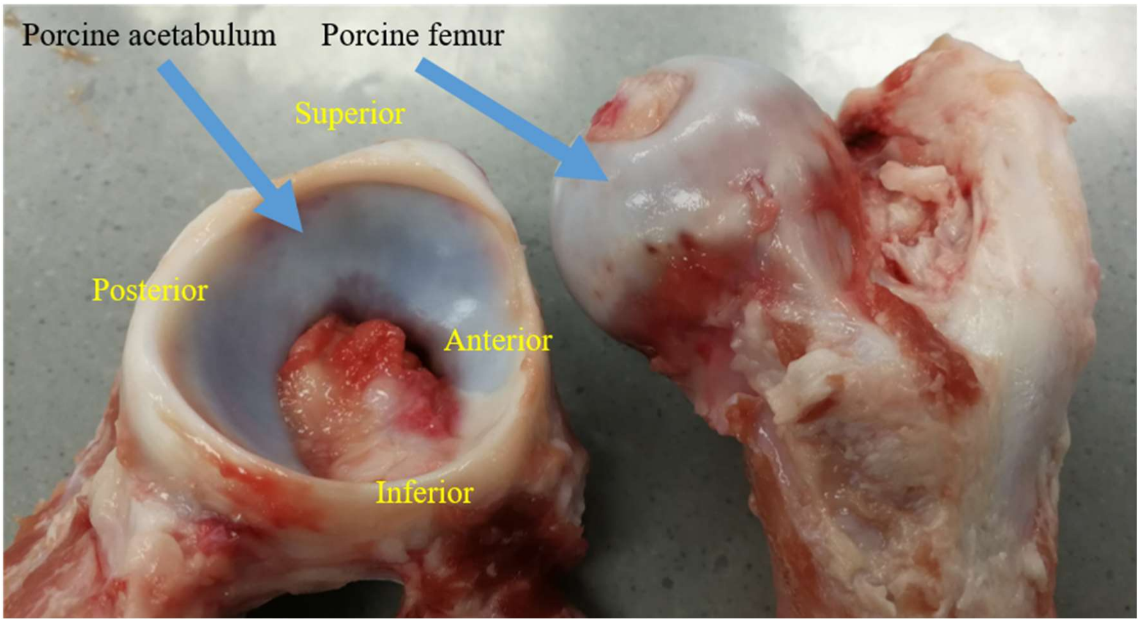

**Figure 4.2 Porcine acetabulum and femur. Surrounding soft tissues were removed, and the components shown were used directly in the study.**

The tissues samples were then cemented, treated with contrast agent, aligned, and loaded in the hip loading rig as described in Chapter 3.

### 4.3.2 CT scan of porcine acetabulum and femur

CT images of samples were obtained at three stages: 1) at rest, the hip joint was at rest where the acetabulum and the femur just came into contact; 2) during load, the acetabulum was being loaded by applying constant displacement through the femoral head; and 3) with labrum cut, after creating a labrum defect close to the contact region, the acetabulum was again being loaded by applying constant displacement through the femoral head.

#### 4.3.2.1 Initial position and the first CT scan

A load indicator was connected to the load cell allowing real-time reading of the load value (Figure 4.3).

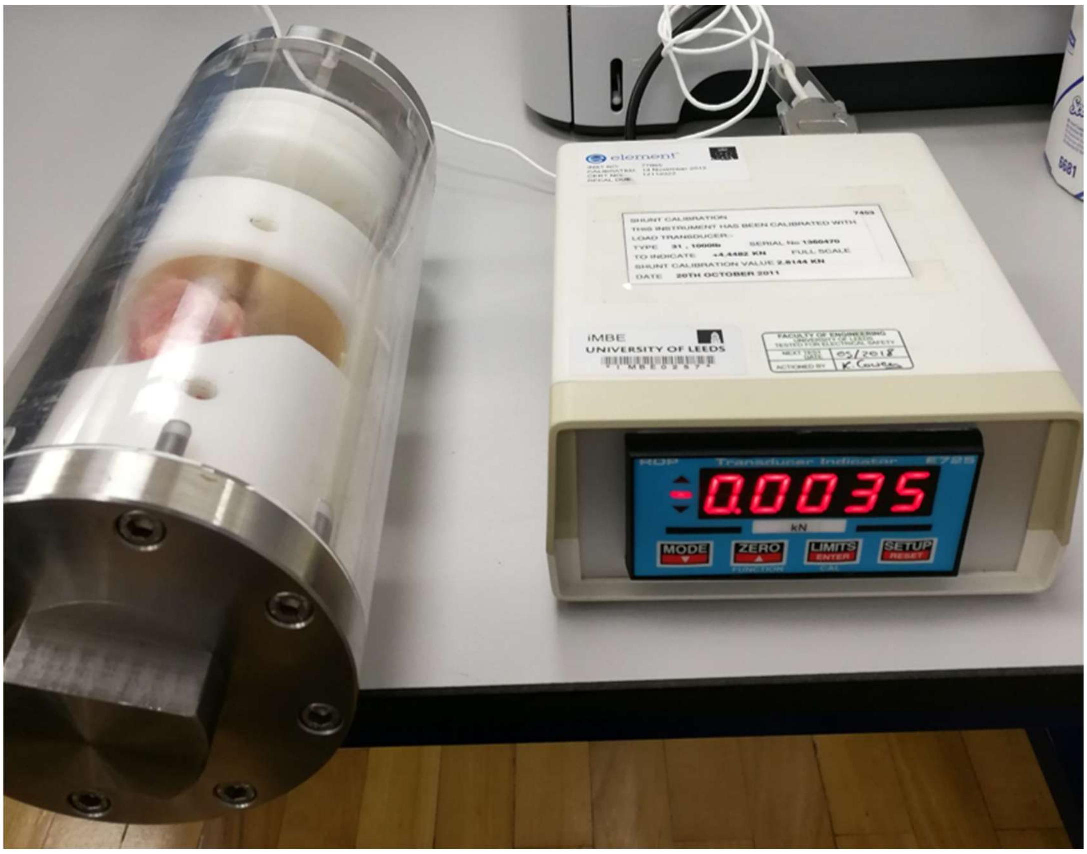

**Figure 4.3 Indicator providing real-time load reading of the load cell.**

With the aid of the transparent Perspex tube, soft tissue displacement due to contact could be observed from outside of the loading rig. The displacement screw was turned clockwise to close the gap between the acetabulum and the femur. The manual displacement was stopped just after the acetabular labrum started to move, with the load indicator starting to report a positive load value at the same time. The displacement was then reversed until the acetabular labrum recovered to the original position (Figure 4.4), with the load reading returning to zero. The initial position was therefore achieved, and the hip loading rig was ready for CT scanning.

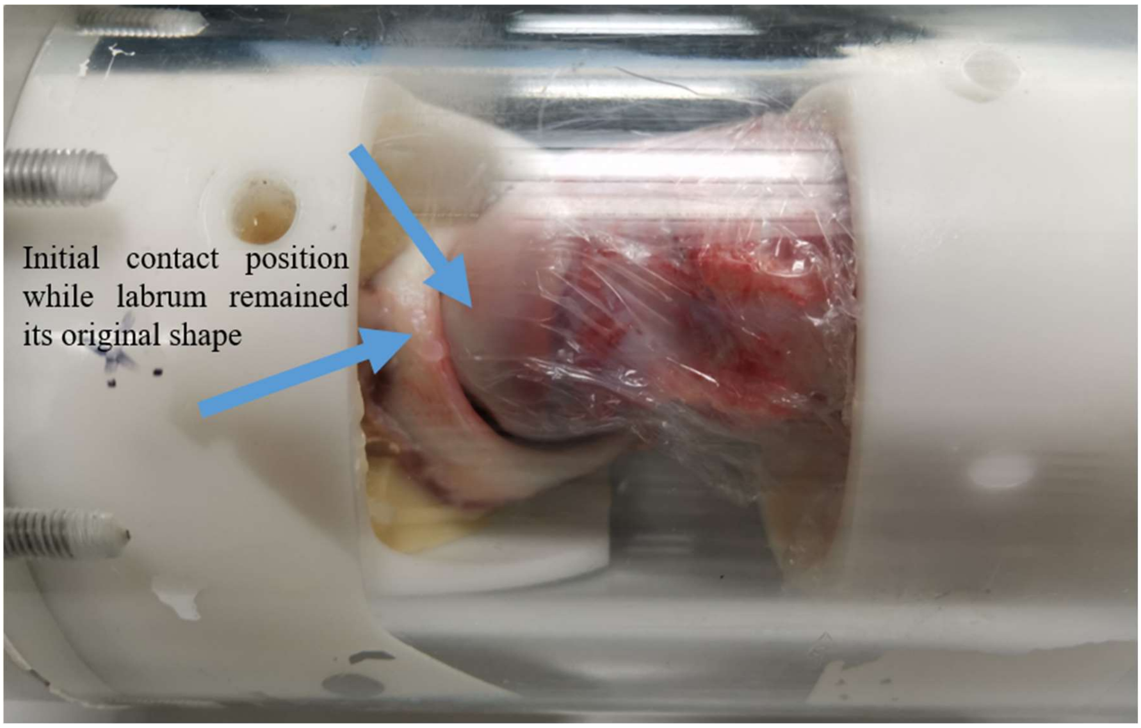

**Figure 4.4 Initial position of acetabulum and femur before the first scan**

The scanning configuration was pre-set in the control file for porcine tissues. The resolution was isotropic of 82 μm. Number of projection per 180 degrees was set to 750. The integration time was 300 ms. The scan lasted between 40 and 60 minutes each time. The volume of interest was set from the bottom of the acetabulum for capturing sufficient tissue in the hip joint to just beyond the femur pot, which enabled measurement of the distance change between the two pots (Figure 4.5).

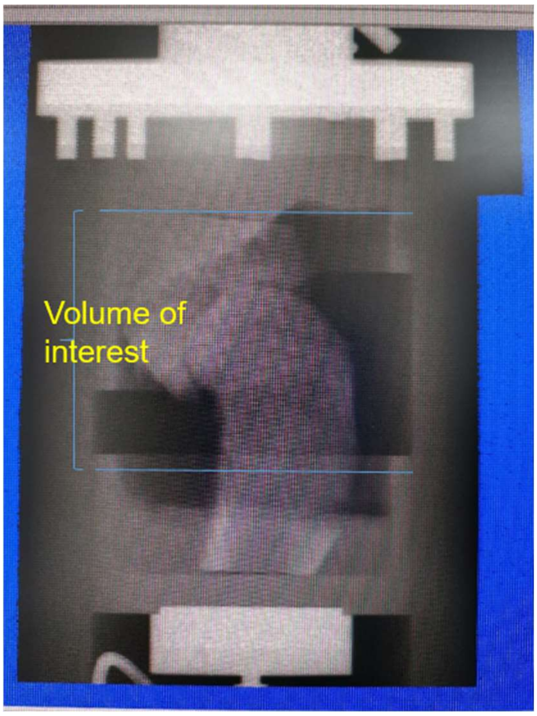

**Figure 4.5 Range of scout view and volume of interest for tissue scanning**

#### 4.3.2.2 Load apply and the second CT scan

A displacement-was then applied and the load was monitored through the femoral head by turning the displacement screw clockwise by four to six full turns, depending on the sample behaviour (discussed in Section 4.5). The aim was to cause certain amount of soft tissue deformation that is measurable in CT images.

The load response was time-dependent under constant displacement since acetabular soft tissues are viscoelastic materials (see section 2.5.2). As shown in Figure 4.6a displacement of 4.5 mm settled after eight minutes while a peak reaction force of 1042 N was observed. The load dropped to 266 N after one hour of relaxation and kept dropping at a rate of slower than 1.5 N/minute. The load reading was recorded manually using video shooting, due to failure of connecting the load indicator to a computer. The camera stopped video shooting automatically after 1800 seconds, and a gap was left (Figure 4.6) before the second manual operation of the camera. However the load reading followed a smooth curve against the relaxation time, the gap between 1800s and 2700s was therefore not very important regarding the decision of soft tissue relaxation time.

All six samples were placed for sixty minutes before the second CT scan in order to reduce the effect of relaxation when scan was in operation.

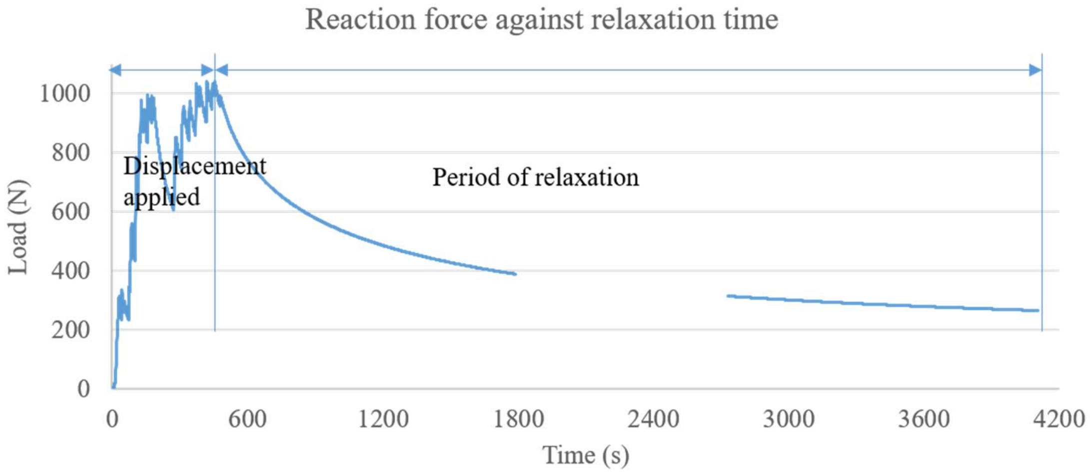

**Figure 4.6 Load variation against relaxation time of one sample tissue. The soft tissue started to settle down after one hour.**

The scanning configuration remained the same as mentioned in previous section for the second CT scan. A picture of the acetabulum and the femur was taken after the second scan. This allowed the comparison between unloaded sample and the sample after recovery ready for reloading. In addition, the actual contact region was indicated from the colour change on the cartilage surfaces. An example of record of tissue condition can be found in Figure 4.7.

**Figure 4.7 Actual contact region on the tissue samples**

#### 4.3.2.3 Load with labrum cut

Tissues remained in pots to achieve a consistent contact position during the experimental process. Exposed tissues were covered with PBS and stored in fridge over night for recovery. A labrum cut was created close to the actual contact region at the superior-posterior portion of the acetabulum (Figure 4.8). NaI solution and cling film were once again applied to the femur before the third CT scan.

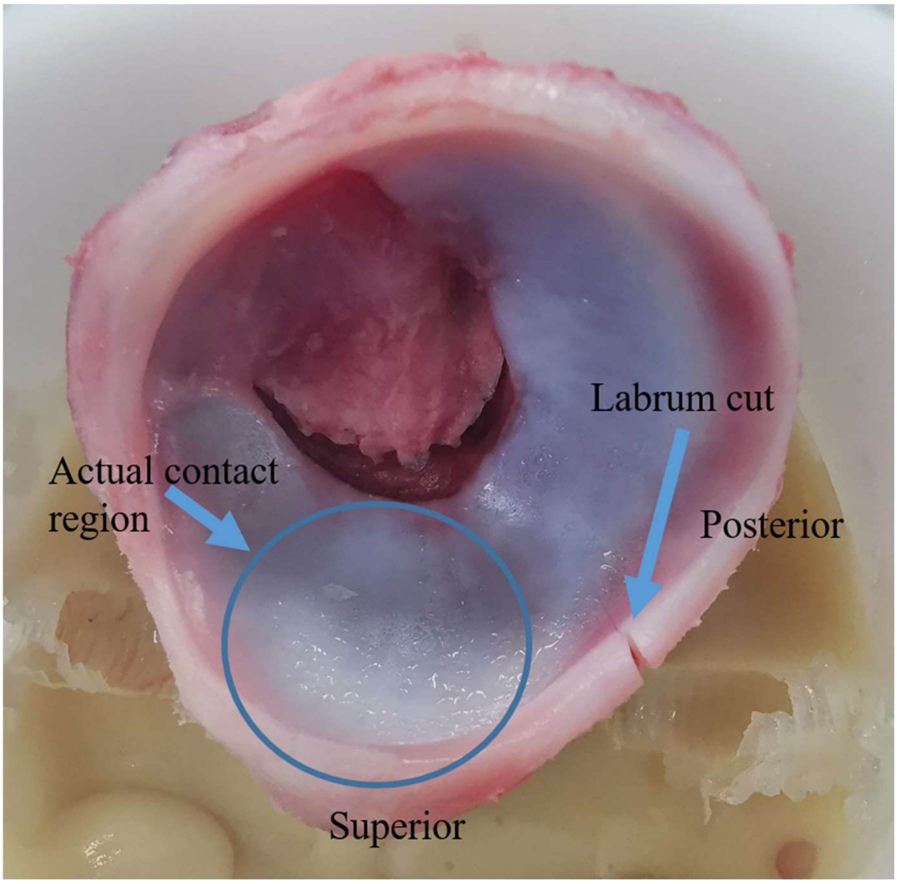

**Figure 4.8 Labrum cut at the superior-posterior portion**

### 4.3.3 Measurement of acetabular soft tissue displacement

Acetabular soft tissues were displaced due to load applied through the femoral head. The displacement was captured by performing image processing and thus measuring the differences before and during load. Three sets of CT images were obtained for each sample as described in the previous section. The first and the second scan were compared to investigate the acetabular soft tissue behaviour under load with intact labrum. The first scan was re-used for comparison with the third for investigation of the acetabular soft tissue behaviour under load with labrum cut.

The acetabulum bone was treated as a rigid component throughout the loading process as discussed in Section 3.6. The segmentation of surrounding soft tissues then allowed the comparison of tissue position before and after load. The actual contact region was indicated by the position difference in acetabular soft tissues surfaces. The cartilage thickness was measured in a 2D CT slice, selected near the centre of the focused contact region, at various points across the acetabulum radius. The labrum movement was measure in 3D point cloud as the change in overall shape.

#### 4.3.3.1 Image processing and acetabulum registration

The process of acetabulum bone registration remained the same as mentioned in Section 3.6, and as shown in Figure 4.9. Both bone masks were visible on the top surface, alternately providing the evidence that the two acetabulum were almost coincident. The superior region is the ilium part which is coincident with the contact region.

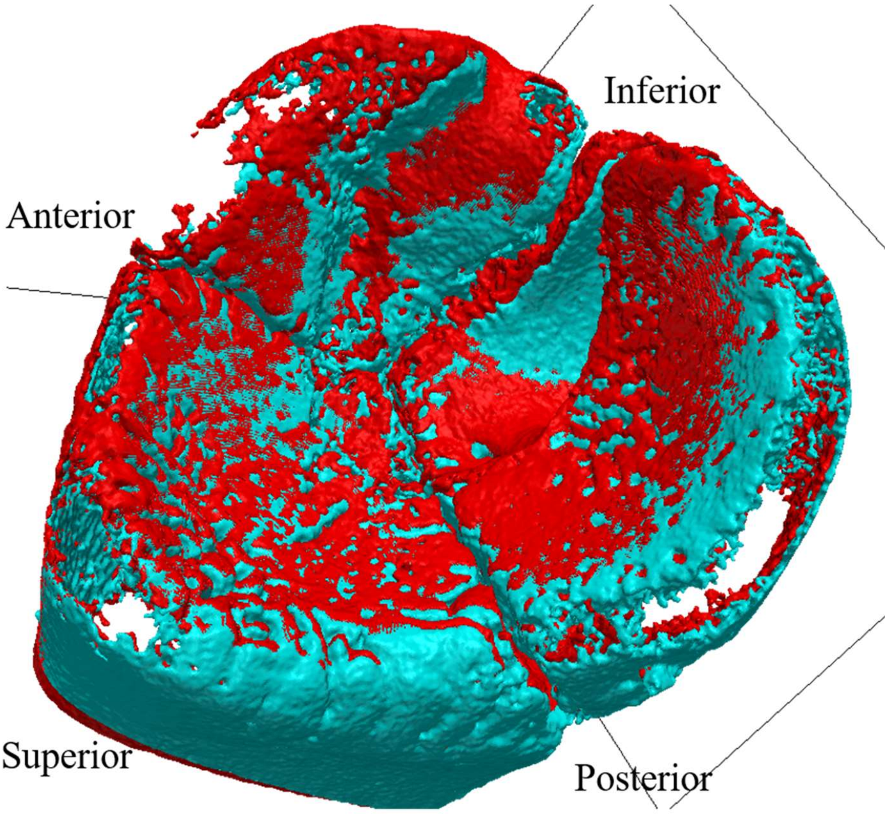

**Figure 4.9 Registered acetabular bone for PH15. Red, bone before load; cyan, bone during load.**

Colour difference was observed on the acetabular top surfaces after segmenting the whole acetabulum before and during load (Figure 4.10). Acetabulum surface region that filled with unloaded tissues were assumed to be the actual contact region since the loaded tissues were invisible and were believed to deform beneath the unloaded tissues due to the applied force through the femoral head.

The reliability of the bone registration was assessed by calculating the rough offset thickness between bone masks before and during load. The error in thickness was calculated from the offset volume and the offset surface area:

$$Ebr = \frac{V(br\ subtract\ bl)}{2 * A(br\ subtract\ bl)}\ (mm)$$

where Ebr is the thickness error in the unloaded bone mask, br subtract bl is to subtract the loaded bone (bl) mask from the unloaded bone mask (br), V stands for volume, A stands for surface area. The mask of br subtract bl was nearly film-shaped. Therefore the thickness was considered as half of the volume divided by the surface area. The Ebl, error on the loaded bone mask, was also calculated.

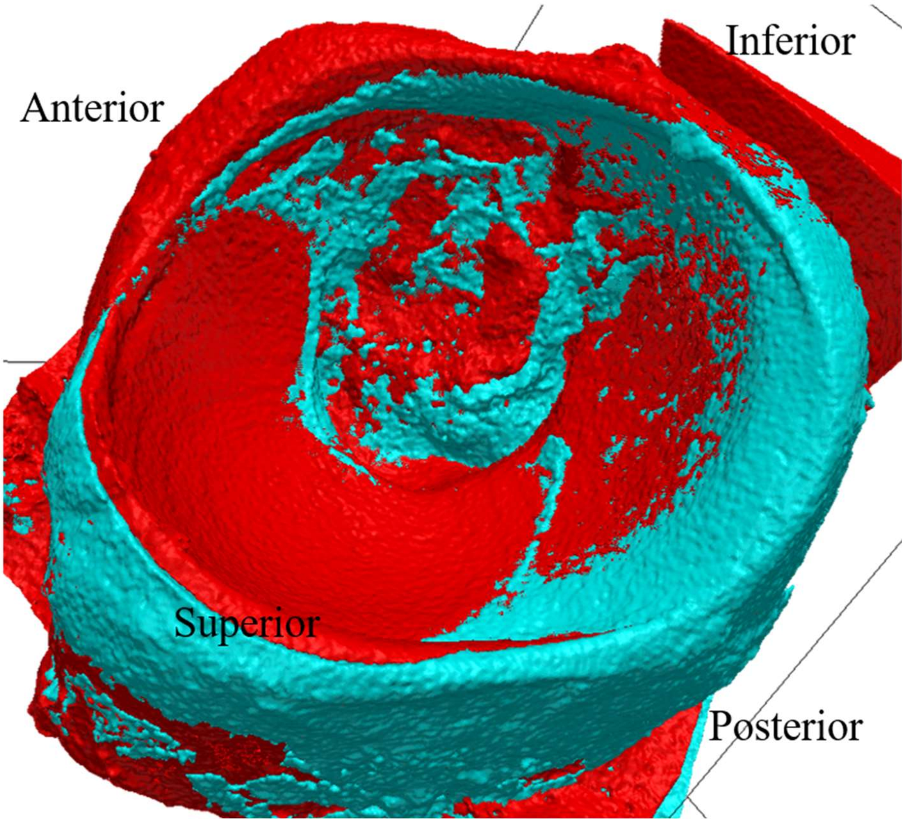

**Figure 4.10 Registered acetabulum bone with soft tissues for PH15. Red, soft tissues before load; cyan, soft tissues during load.**

#### 4.3.3.2 Measurement of cartilage deformation in 2D

The focused contact region was achieved by dilating the mask of tissue during load. A 2D image slice was selected near the centre of the focused contact region. Distribution of acetabular cartilage strain was measured across the acetabulum radius as the change in cartilage thickness before and during load. An example of cartilage strain measurement was shown Figure 4.11.

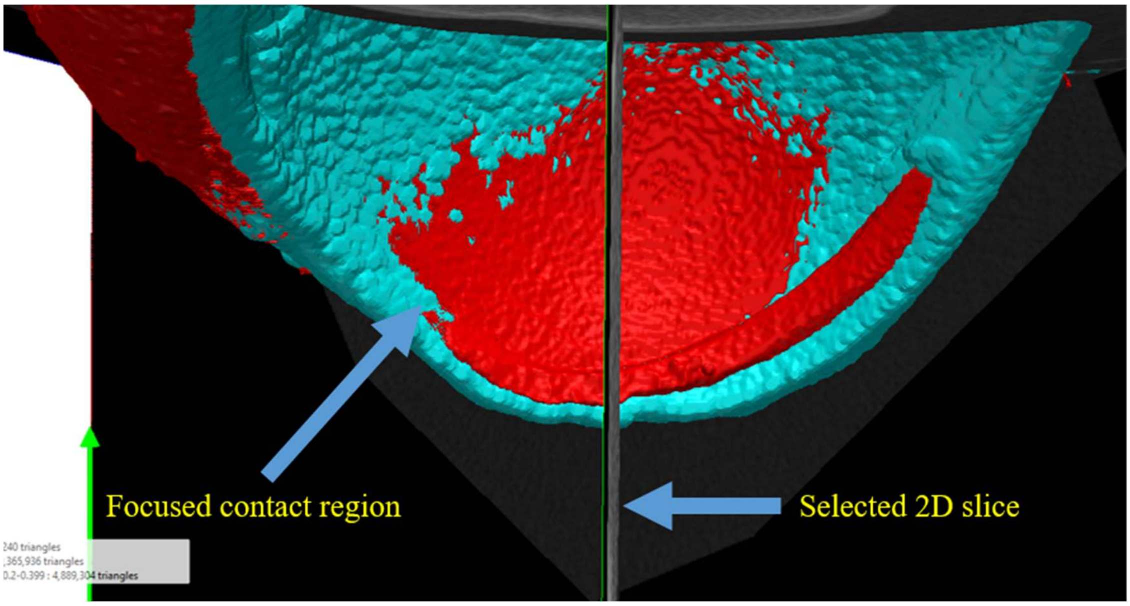

Figure 4.11 Selection of 2D slice for cartilage measurement for PH15.

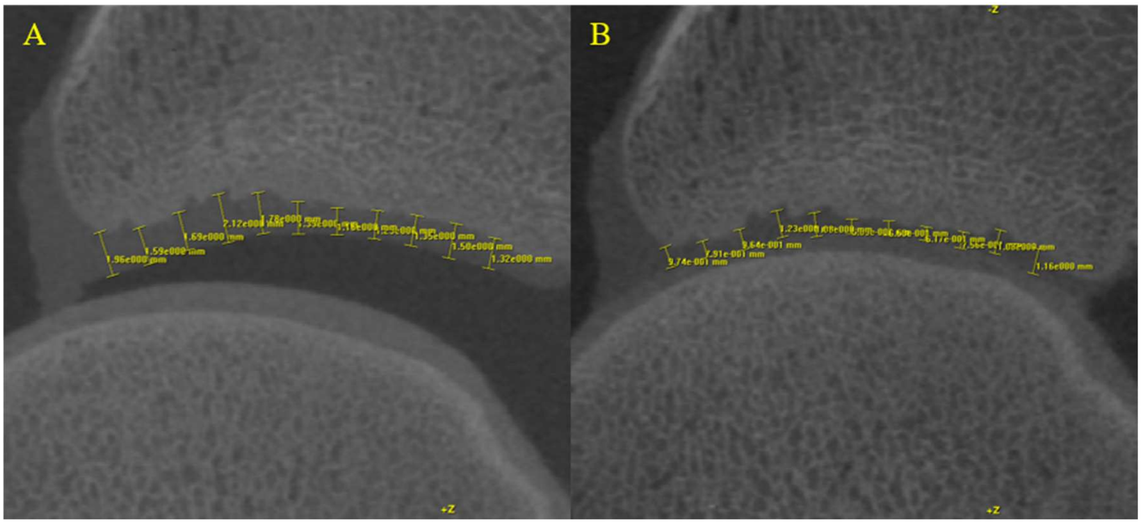

Figure 4.12 Measurement of acetabular cartilage strain for PH15. A – Cartilage before load. B – Cartilage during load.

Cartilage thickness was measured from the same baseline point set on the acetabular subchondral bone. The other point was selected along the direction perpendicular to the tangential line (Figure 4.12), as described in Section 3.6.2. Acetabular cartilage strain was obtained using the same equation.

#### 4.3.3.3 Measurement of labrum shape change in 3D

The process of reconstructing labrum apex remained the same as mentioned in Section 3.6.3. An example of labrum apex reconstruction before and during load was illustrated in Figure 4.13. The two shapes were coincident on approximately three-quarters of the edges, which provided evidence of good registration. Labrum shape change was observed at around one-quarter of the edge where large displacement suggested a concentrated force. Displacement of labrum apex could only be measured in radial direction (as discussed in Section 3.7) as a measurement of the labrum shape change in 3D.

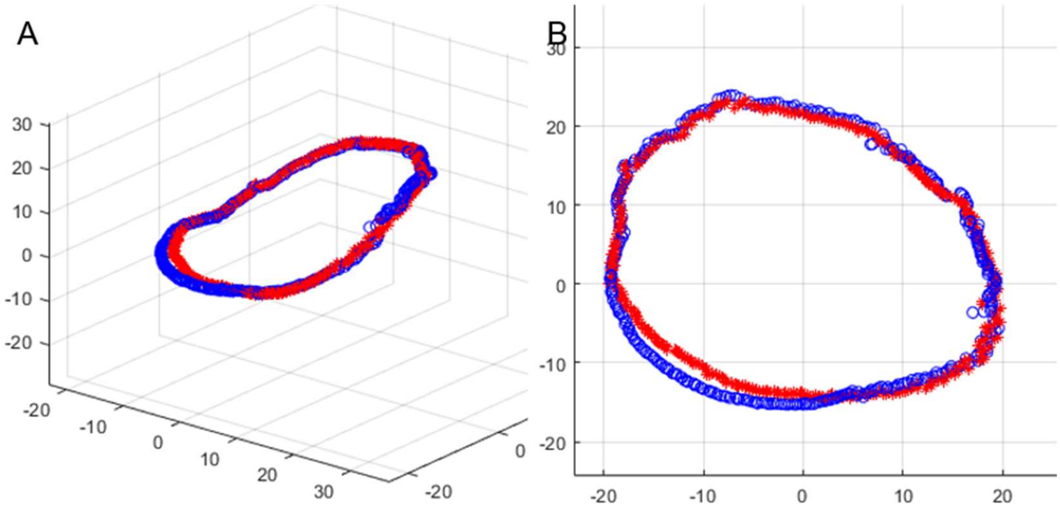

**Figure 4.13 Reconstructed labral apex in 3D space for PH15. A - labrum apex point cloud from isotropic view. B – Labrum apex point cloud from top view, normal to the rim plane. Red, tissue before load; blue, tissue during load.**

## 4.4 Results

This section presents and discusses the experimental results of porcine hip samples (n=6) that underwent the experiment protocol described in Section 4.3. Loading scenario of each sample was recorded for inter-subject comparison. The quality of image registration was assessed, hence the selection of contact region can be further justified. Measurement on cartilage and labrum deformation was presented, and then discussed along with the corresponding loading scenario of each sample.

### 4.4.1 Verification of loading scenario related to cam-type FAI

The loading scenario of each sample is divided into two parts, one from the mechanical perspective on the CT loading rig and the other one from the structural perspective on the tissues. The displacement was measured and the force was monitored, where both play important roles in the magnitude of the subsequent tissue movement. The actual contact region on both acetabular and femoral cartilage surfaces was recorded, which acted as a result of the sample alignment and as a factor of selection of the labrum cut site. The location of the labrum cut was also recorded to be discussed along with the subsequent change in labral movement during load.

#### 4.4.1.1 Displacement and reaction force

The loading scenario in the CT loading rig was recorded for each sample and can be found in Table 4.1.

**Table 4.1 Loading scenario in the CT loading rig**

| Sample code | Case | Relaxation time (minute) | Screw turns | Displacement of pot (mm) | Reaction force* (N) | End force (N) |
|---|---|---|---|---|---|---|
| PH10 | Loaded† | 60 | 4 | 3.8 | 224 | 183 |
| | Cut‡ | 60 | 4 | 4.2 | 340 | 281 |
| PH11 | Loaded | 60 | 4.5 | 4.5 | 265 | 213 |
| | Cut | 61 | 3.5 | 4.6 | 284 | 228 |
| PH12 | Loaded | 63 | 4.5 | 4.3 | 299 | 230 |
| | Cut | 60 | 4.5 | 4.5 | 257 | 201 |
| PH13 | Loaded | 61 | 4.5 | 4.3 | 186 | 152 |
| | Cut | 60 | 5.5 | 4.5 | 193 | 154 |
| PH14 | Loaded | 60 | 6 | 6.2 | 100 | 81 |
| | Cut | 60 | 6 | 6.5 | 58 | 41 |
| PH15 | Loaded | 60 | 4.5 | 4.3 | 209 | 178 |
| | Cut | 61 | 5 | 4.1 | 133 | 104 |

Reaction force*, two readings were recorded, before and after CT scan respectively. Loaded†, porcine hip samples during load. Cut‡, porcine hip samples during load with labrum cut.

The relaxation time was 60.5±0.9 minutes, which allowed a consistent period of time for the soft tissues to relax and keep stable during the CT scan. Load drop of 20.3±3.6% of the original load, before the CT scan, was observed in the loading rig after the CT scan. The tissues were therefore not completely stable during the CT scan and could have had small movement during the scanning process.

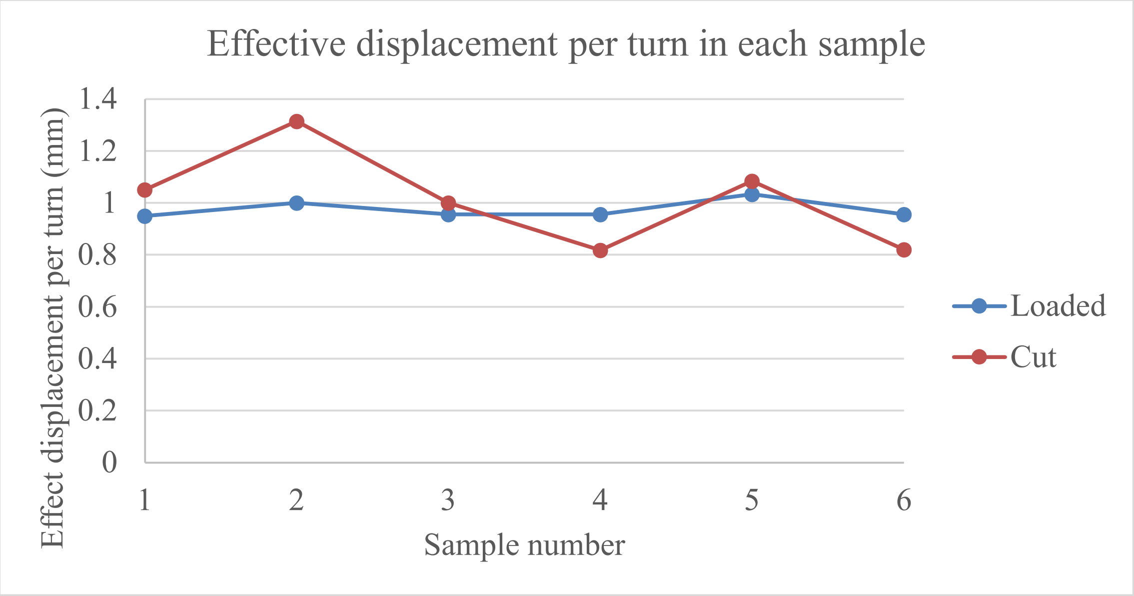

**Figure 4.14 Effective displacement per turn in each sample.**

The effective displacement of the pot per screw turn was calculated by dividing the pot displacement by the number of screw turns. The effective displacement per turn in the loaded case was 0.98±0.03 mm. The displacement of the femoral pot was well controlled by the screw on the CT loading rig. The effective displacement per turn in the cut case was 1.01±0.19 mm. For a displacement of five screw turns, the error of the pot displacement could be as high as ±0.96 mm. The transfer of displacement from screw onto tissues was more reliable in the loaded case than in the cut case where the whole system was reloaded after the loaded case.

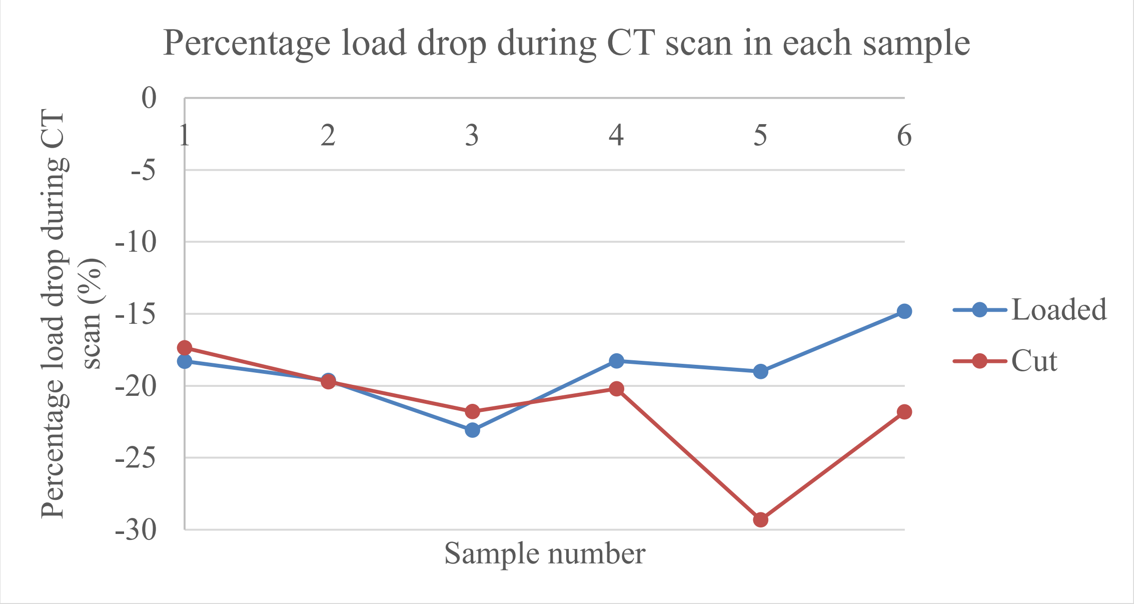

**Figure 4.15 Percentage load drop during CT scan in each sample.**

The load drop during CT scan was measured as a percentage of the original load before the CT scan. The percentage load drop in the loaded and the cut case was -18.9±2.7% and -21.7±4.1% respectively. The load drop was slightly higher in the cut case, which would result in even more noise in the image data when measuring the scanned tissues. The magnitude of percentage load drop in sample 5 under the cut case was significantly higher than that in other samples. The substantial load drop could be caused by the contact properties in sample 5 and is explained in detail in section 4.4.2.3.

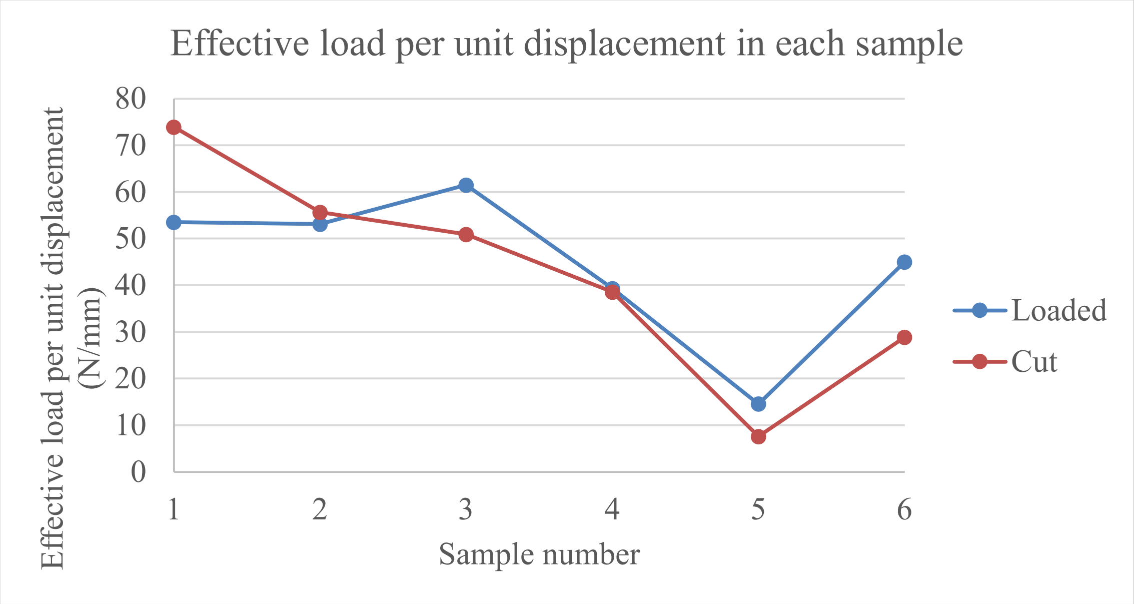

**Figure 4.16 Effective load per unit displacement in each sample.**

The effective load per unit displacement was a measurement of the reaction force due to every 1 mm of pot displacement. The effective load per unit displacement in the loaded and the cut case was 44.5±16.5 N/mm and 42.6±23.0 N/mm respectively. The higher the effective load rate was measured, the more sensitive and responsive the tissues were to the displacement. Relatively low effective load rate was found in sample under both loaded and cut cases. The contact properties in sample 5 could be responsible for this soft tissue behaviour and is explained in detail in section 4.2.3.

#### 4.4.1.2 Actual contact region and labrum cut site

The loading scenario from the structural perspective of each sample consists of three figures (Figure 4.17 - Figure 4.20): 1) the actual contact region on the acetabulum after the first load; 2) the location of the labrum cut at the acetabular edge; and 3) the actual contact region on the acetabulum with labrum cut. The actual contact region on the acetabular cartilage and labrum was indicated by the faded or flattened area on the acetabulum after loading. The contact region experienced an averaged load of 191.4 ± 76.3 N for approximately two hours, and was believed to coincident with the faded or flattened area on the acetabular top surface.

The actual contact region from tissue perspective was not only an assessment of the accuracy and consistency of tissue alignment, but also a validation for the contact region from segmented image data. The labrum cut site was recorded for comparison between samples and may be responsible for the labrum movement under the cut case.

As a result, the highlighted contact patches on the acetabulum were all located at the superior-anterior region on the cartilage-labral junction in both loaded and cut cases. The contact region was observed at generally the same location for each sample between loaded and cut cases. The actual contact regions seem consistent and therefore the labrum cut site was just next to the contact region, as planned in the experiment methodology.

The highlighted contact patches on the femur were basically located at the superior region next the ligament of the head of femur. However, for sample PH11, PH12, and PH14 (Figure 4.18-BCE and Figure 4.20-BCE), the root of the ligament was also involved in the contact surface. The cartilage has much higher compressive modulus to the ligament. Therefore the so called “femoral cartilage strain” would be very high if the ligament was compressed and defined as part of the “femoral cartilage thickness”.

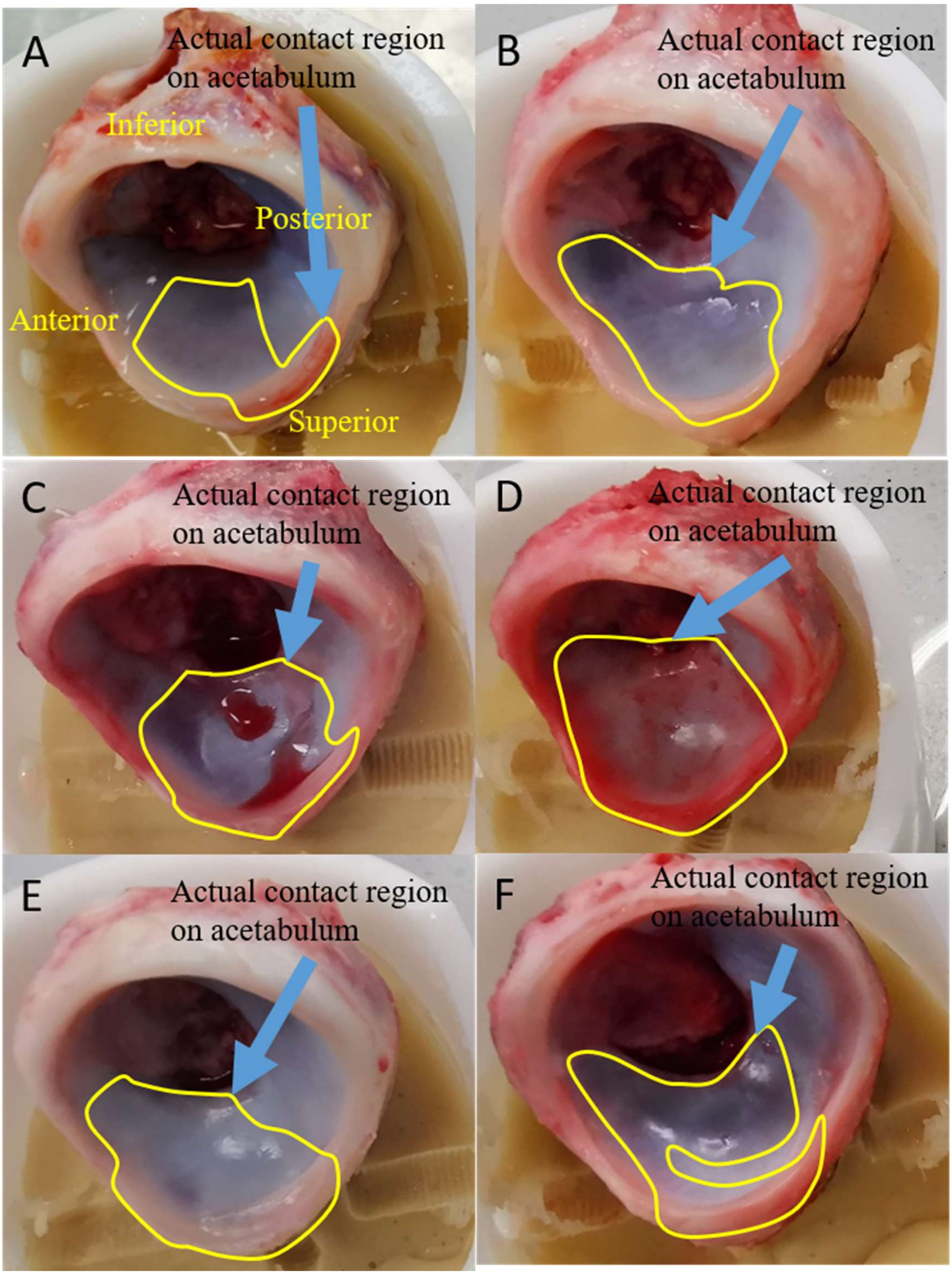

**Figure 4.17 Actual contact region on the acetabulum under loaded cases. A, PH10; B, PH11; C, PH12; D, PH13; E, PH14; F, PH15.**

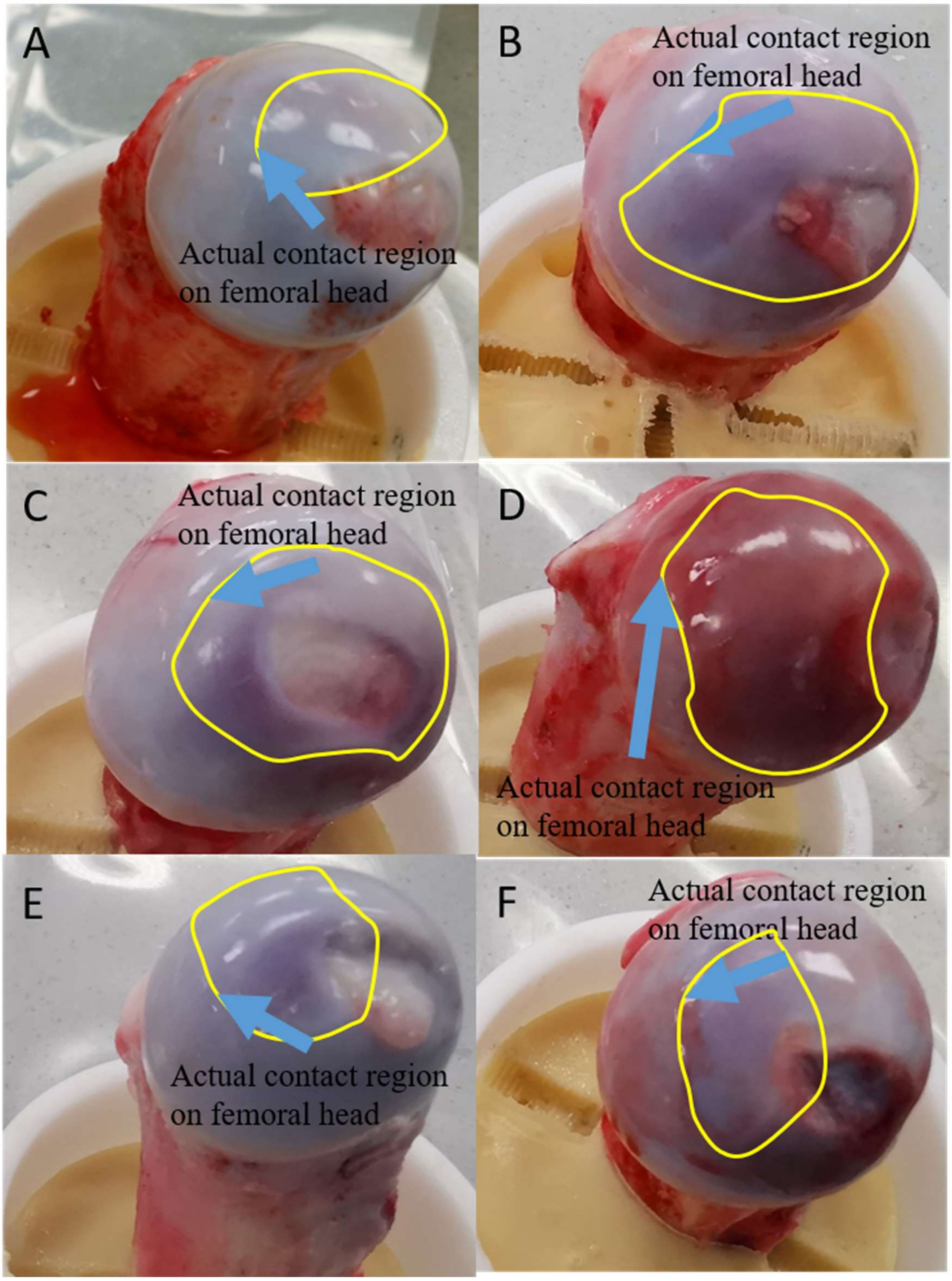

**Figure 4.18 Actual contact region on the femoral head under loaded cases. A, PH10; B, PH11; C, PH12; D, PH13; E, PH14; F, PH15.**

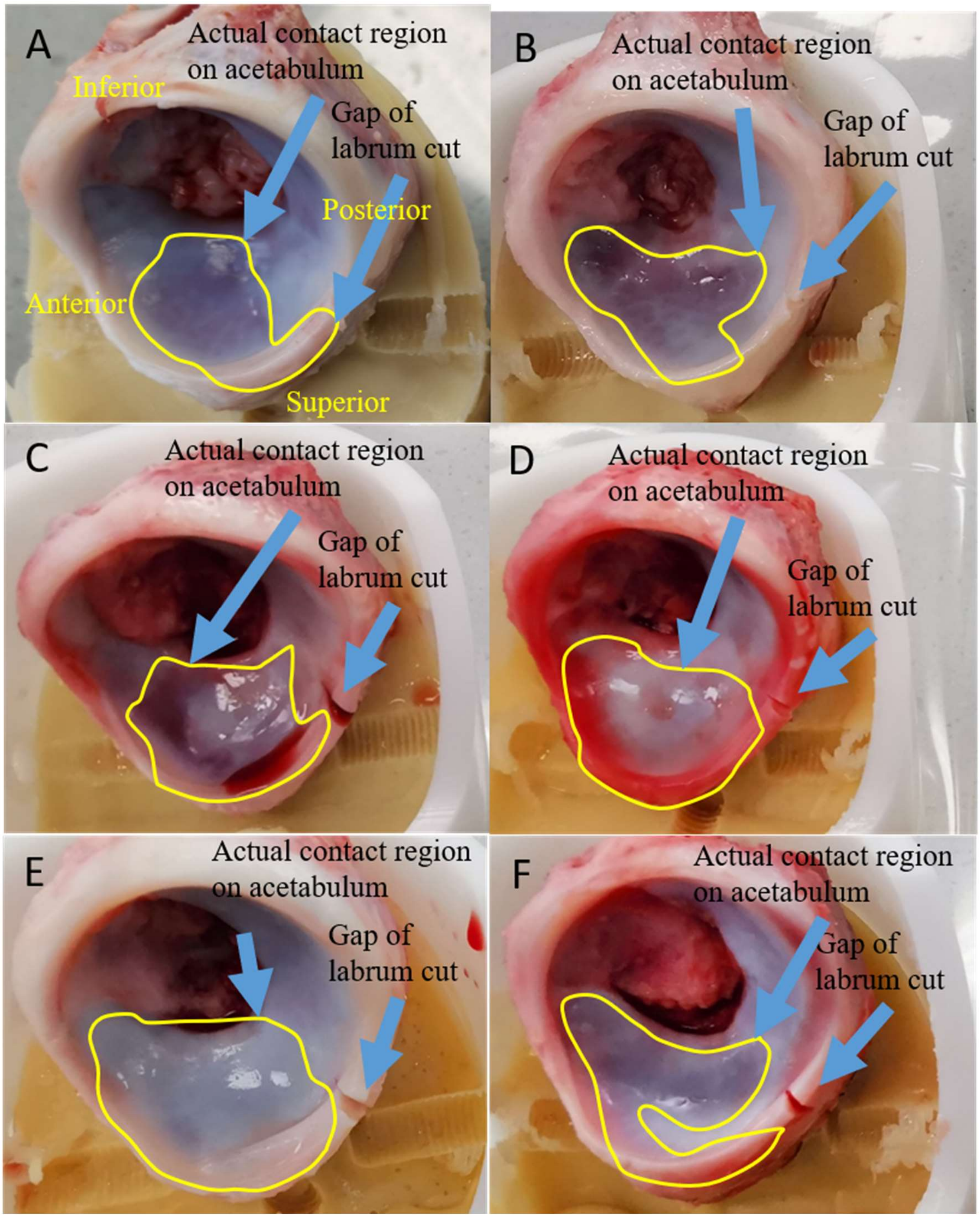

**Figure 4.19 Actual contact region on the acetabulum under cut cases. A, PH10; B, PH11; C, PH12; D, PH13; E, PH14; F, PH15.**

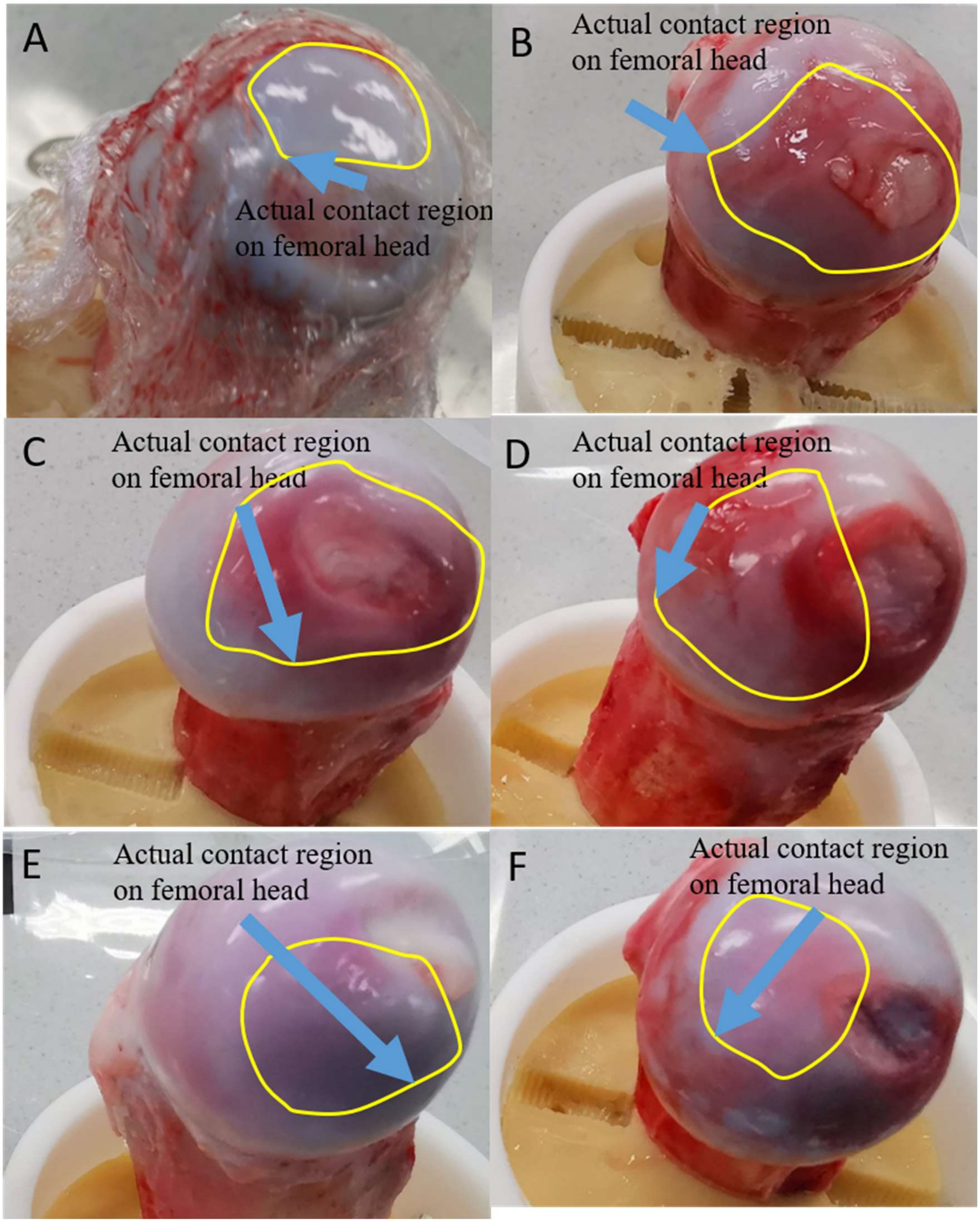

**Figure 4.20 Actual contact region on the femoral head under cut cases. A, PH10; B, PH11; C, PH12; D, PH13; E, PH14; F, PH15.**

### 4.4.2 Image processing

The results of image processing of each sample consist of two parts, the quality of acetabulum registration and the selection of focused contact region. The extent of coincidence of acetabulum was assessed to ensure that the segmented soft tissues, before and during load, were compared based on subchondral surfaces at the same location. The indicated contact region could be referred back to the actual contact region presented in section 4.4.2.2, and be used to locate the centre of contact region for measurement of acetabular cartilage strain. As introduced in section 4.3, for any figures regarding segmented tissues, the red mask represented unloaded tissue, the cyan mask represented deformed tissue under the loaded case, and the green mask represented deformed tissue under the cut case.

#### 4.4.2.1 Acetabular bone registration

A robust quantitative assessment of bone registration was presented in

Table 4.2. The error was measured in percentage of un-registered tissue volume in the total tissue volume, with respect to the tissue sample before and under load. The percentage errors were between 13.5% and 30.4%, with two exceptions PH12 and PH14. In addition, the total volume of tissue before and during load had a big difference relative to the other samples. The source of error and the different volume of the same tissue sample are discussed further in Section 4.5.

**Table 4.2 Quality of bone registration assessed by thickness of difference in bone masks before and during load.**

| Sample | Case | vr ($mm^3$) | vl ($mm^3$) | Ebr (mm) | Ebl (mm) |
|---|---|---|---|---|---|
| PH10 | Loaded | 14591 | 14634 | 0.050 | 0.052 |
| | Cut | 14575 | 14567 | 0.044 | 0.045 |
| PH11 | Loaded | 12027 | 11477 | 0.102 | 0.084 |
| | Cut | 12027 | 11691 | 0.063 | 0.059 |
| PH12 | Loaded | 2308 | 1963 | 0.086 | 0.065 |
| | Cut | 2307 | 1789 | 0.103 | 0.075 |
| PH13 | Loaded | 3268 | 3264 | 0.056 | 0.057 |
| | Cut | 3269 | 3307 | 0.046 | 0.052 |
| PH14 | Loaded | 8785 | 8534 | 0.044 | 0.034 |
| | Cut | 8780 | 8228 | 0.094 | 0.081 |
| PH15 | Loaded | 8432 | 8377 | 0.066 | 0.065 |
| | Cut | 8432 | 8401 | 0.045 | 0.043 |

vr, volume of the mask of unloaded bone; vl, volume of the mask of loaded bone; Ebr, thickness error in unloaded bone mask; Ebl, thickness error in loaded bone mask.

Registered acetabulum tissues for each sample under both loaded and cut case were presented in Figure 4.21 – Figure 4.26. Due to the flood fill operation (see section 3.3.2) that eliminates unconnected tissues, the acetabular bone in PH12 and PH13 were only left with the superior (ilium) region. The is because the anterior (pubis) and posterior (ischium) part of the acetabulum were completely isolated from the superior region due to the existence of growth plate.

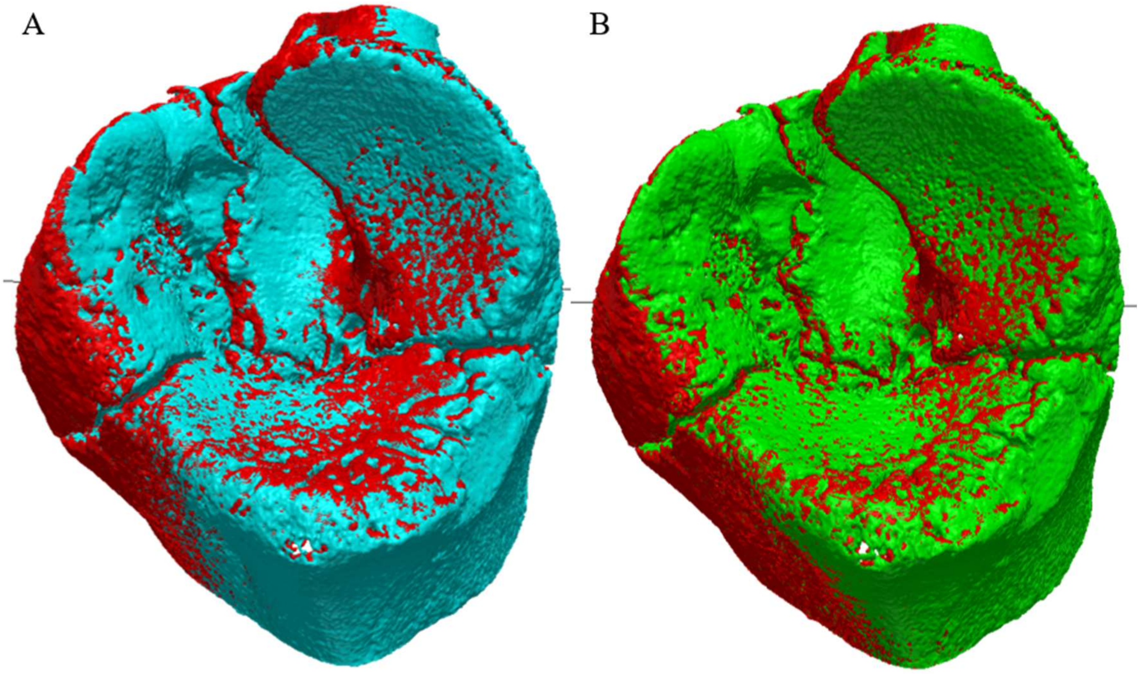

**Figure 4.21 Acetabulum registration for PH10. A – Segmented acetabular bone under the loaded case. B – Segmented acetabular bone under the cut case.**

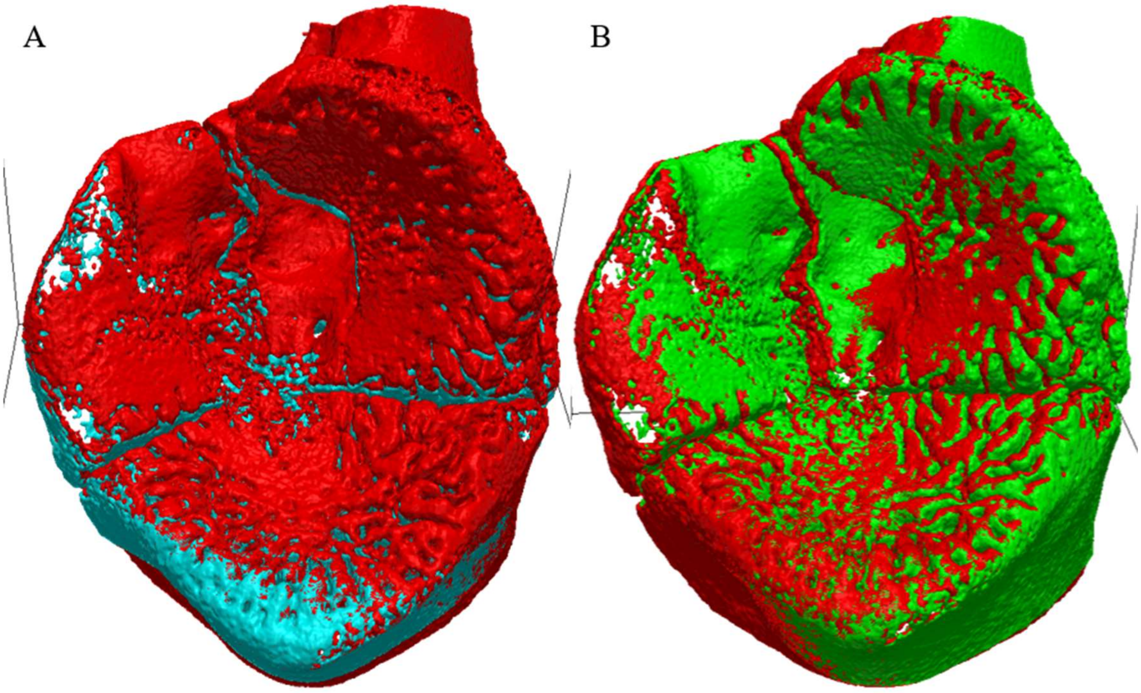

**Figure 4.22 Acetabulum registration for PH11.A – Segmented acetabular bone under the loaded case. B – Segmented acetabular bone under the cut case.**

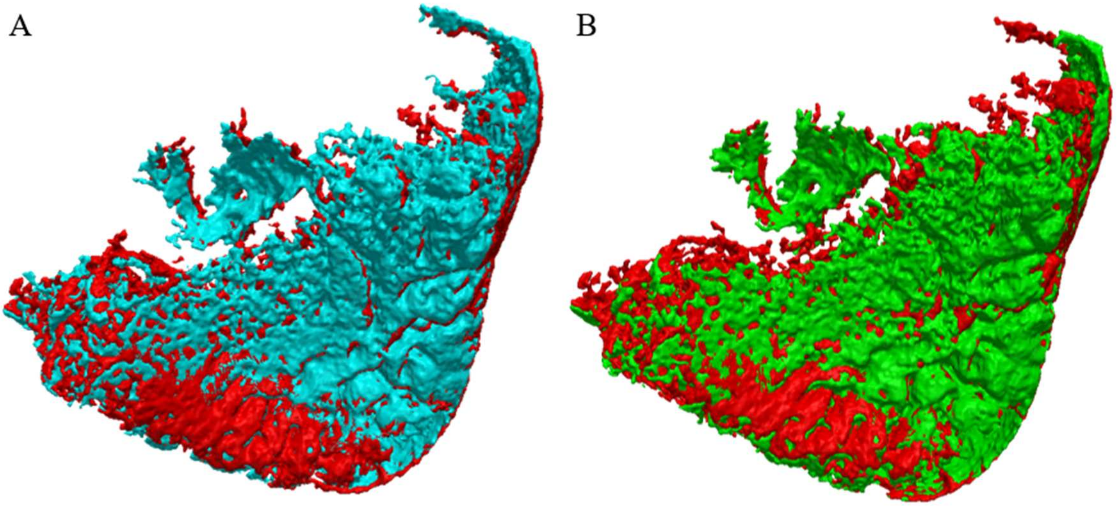

**Figure 4.23 Acetabulum registration for PH12. A - Segmented acetabular bone under the loaded case. B – Segmented acetabular bone under the cut case.**

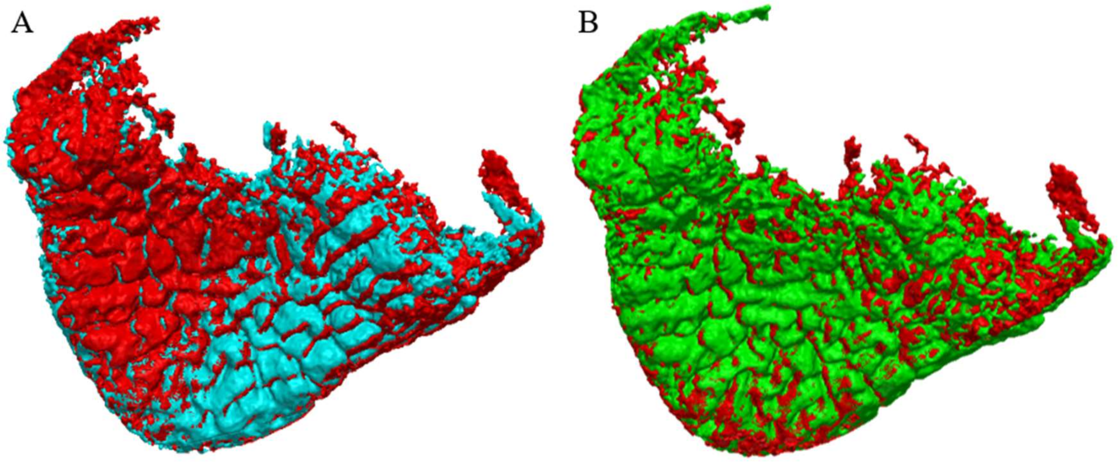

**Figure 4.24 Acetabulum registration for PH13. A – Segmented acetabular bone under the loaded case. B – Segmented acetabular bone under the cut case.**

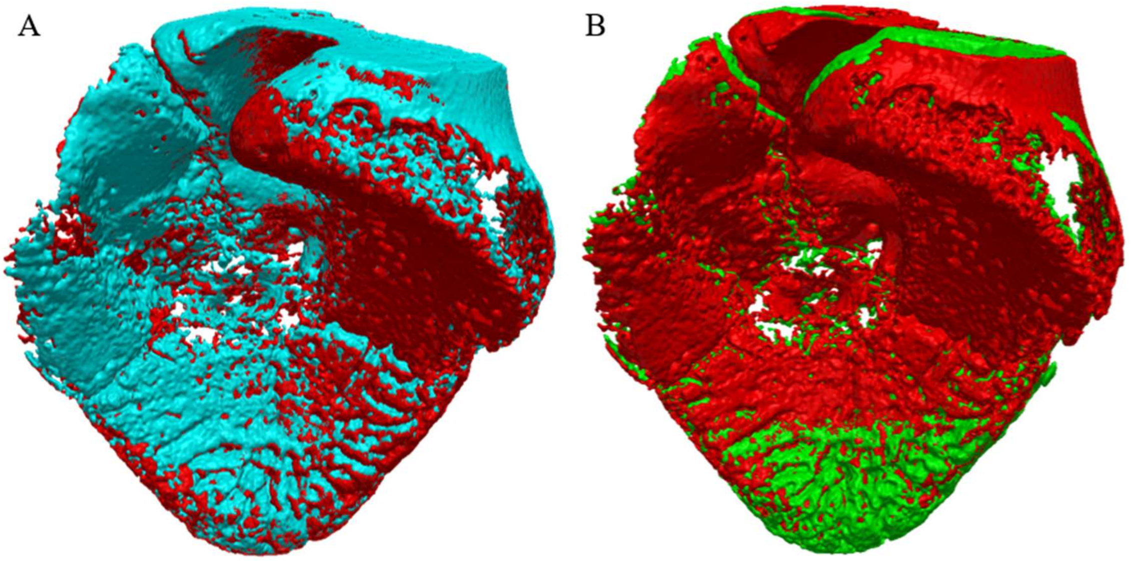

**Figure 4.25 Acetabulum registration for PH14. A – Segmented acetabular bone under the loaded case. B – Segmented acetabular bone under the cut case.**

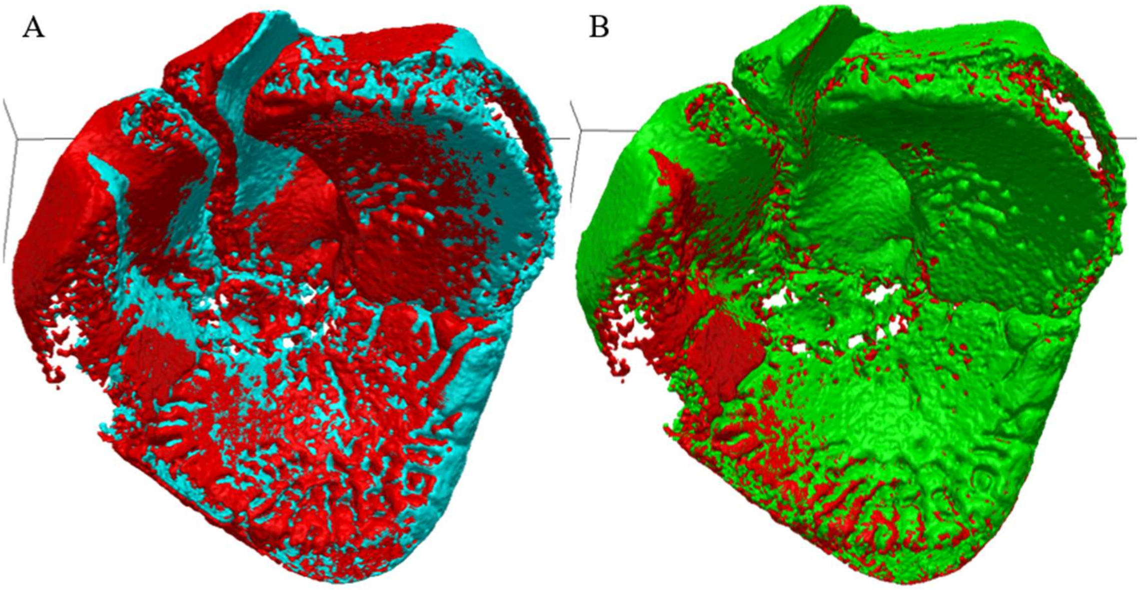

**Figure 4.26 Acetabulum registration for PH15. A – Segmented acetabular bone under the loaded case. B – Segmented acetabular bone under the cut case.**

#### 4.4.2.2 Focused contact region

Soft tissues were segmented after acetabular bones were registered. The actual contact region was implied by the red mask on the acetabulum that being surrounded by mask of deformed tissues. The mask of deformed tissue was then dilated by 5 to 15 pixels to locate the focused contact region on the acetabulum during load (Figure 4.27 - Figure 4.32). One slice of image was chosen at the centre of focused contact region for each case for modelling purpose (introduced in Chapter 5).

The actual contact region from segmented CT image can be verified from the experimental contact region observed on the tissue samples (Figure 4.27 - Figure 4.32, -C and -F) referring to Section 4.4.1.2. The focused contact region can be compared within each sample between loaded and cut case, in order to assess the consistency of the contact region in two loading processes. In addition, the focused contact region was reported to justify the selection of 2D plane for cartilage strain measurement.

For all cases, the experimental contact region was located within the segmented contact region. The segmented focused contact regions were all located at the cartilage-labral junction. For each sample, good consistency was shown at the segmented contact region between loaded and cut cases.

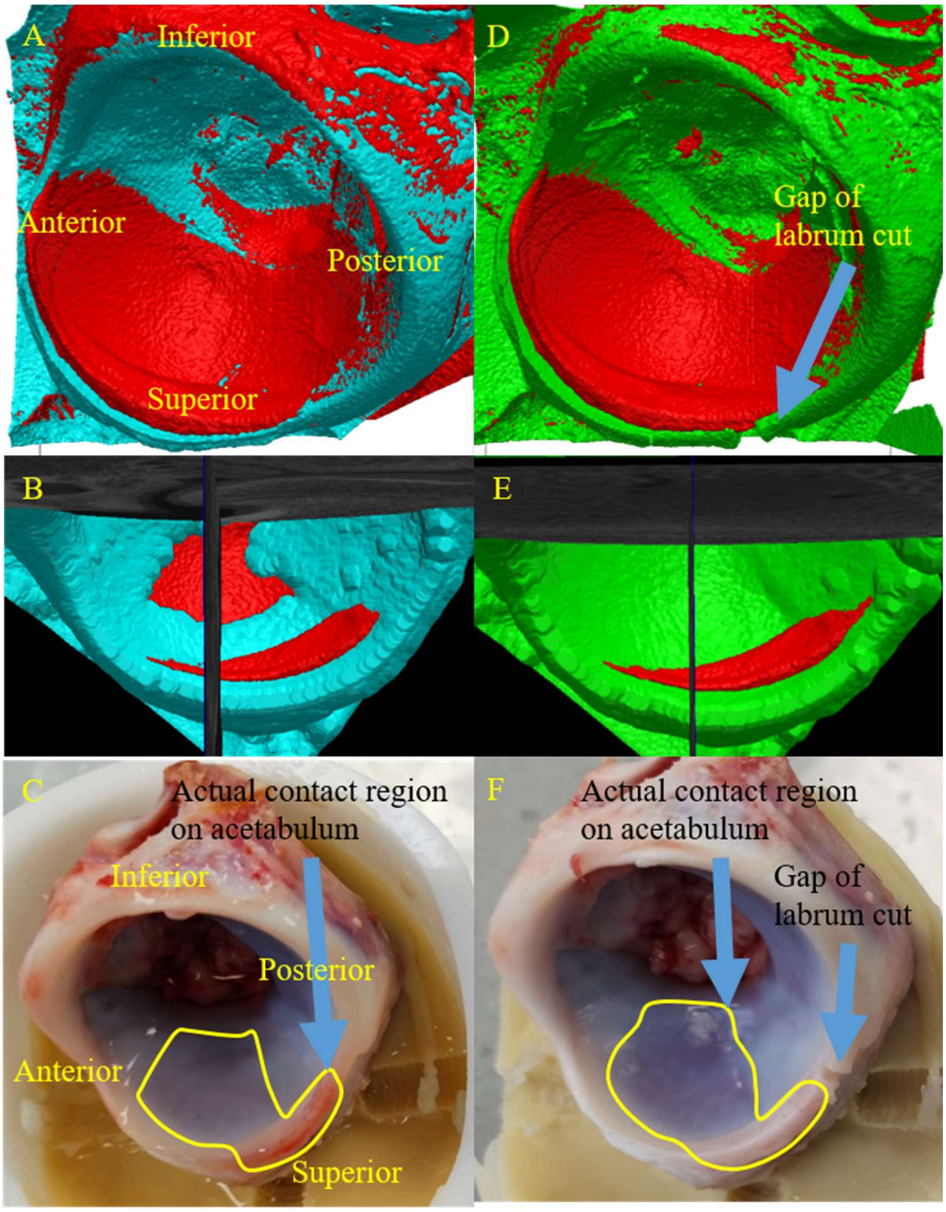

**Figure 4.27 Segmented contact region compared with experiment results for PH10. Left column for loaded case, right column for cut case. AD, segmented actual contact region; BE segmented focused contact region; CF experimental contact region.**

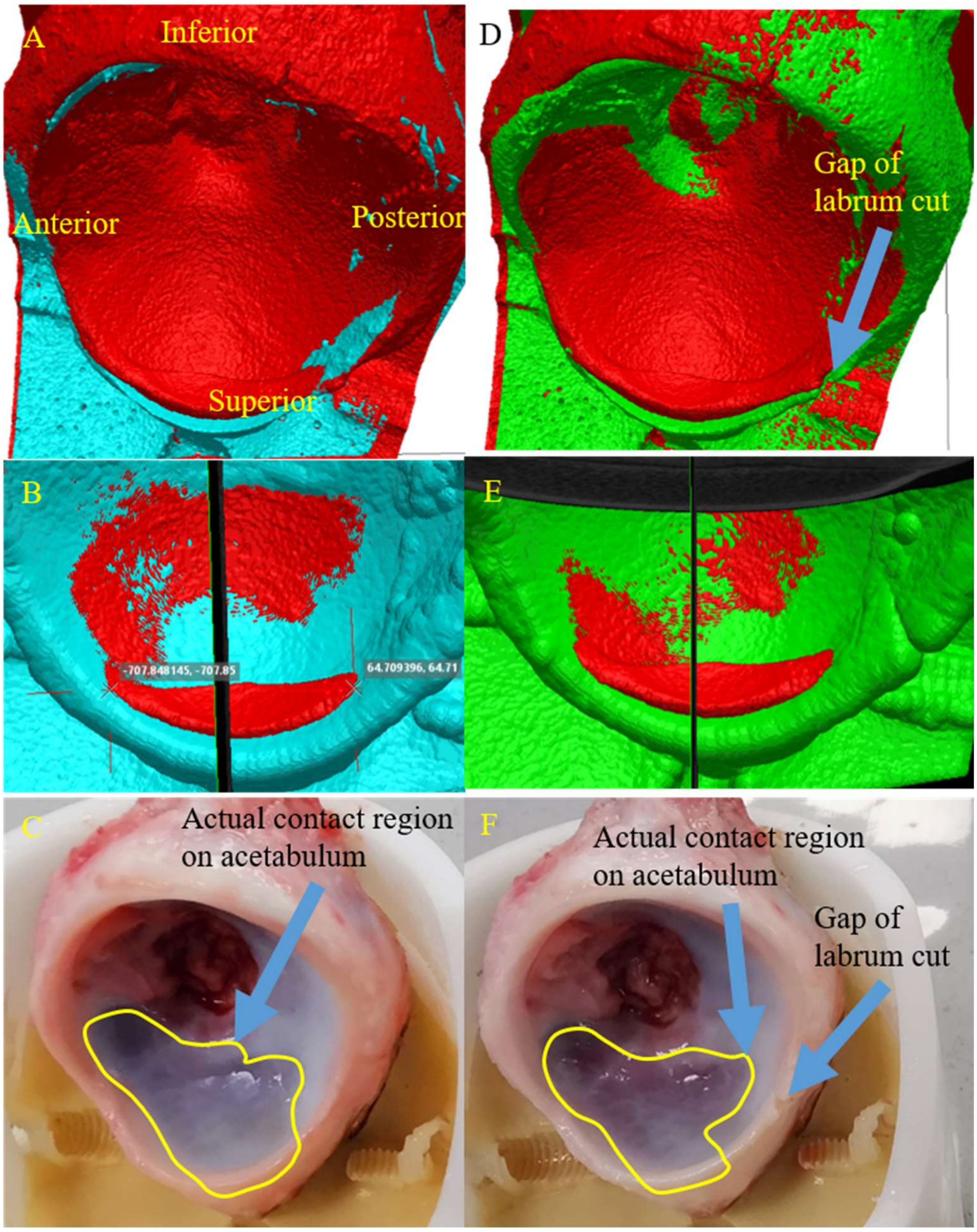

**Figure 4.28 Segmented contact region compared with experiment results for PH11. Left column for loaded case, right column for cut case. AD, segmented actual contact region; BE segmented focused contact region; CF experimental contact region.**

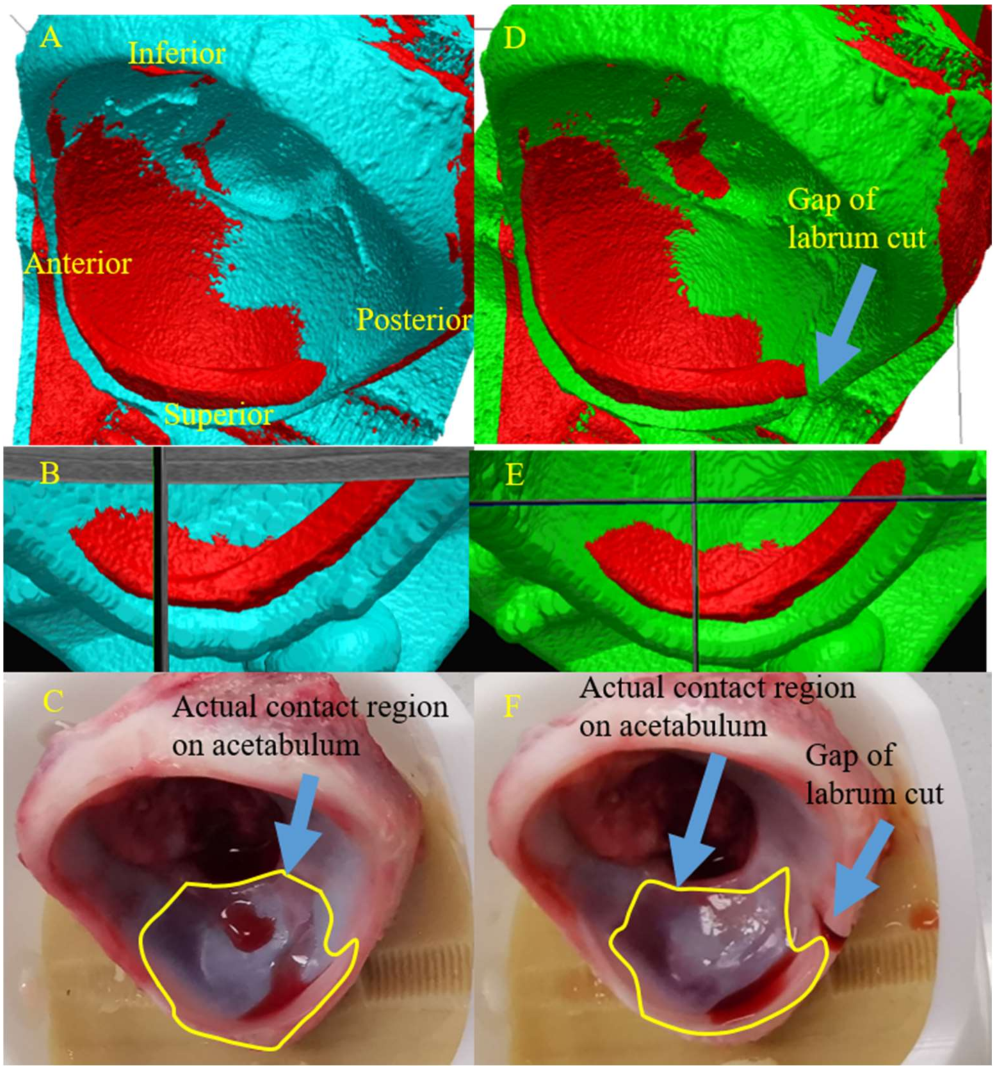

**Figure 4.29 Segmented contact region compared with experiment results for PH12. Left column for loaded case, right column for cut case. AD, segmented actual contact region; BE segmented focused contact region; CF experimental contact region.**

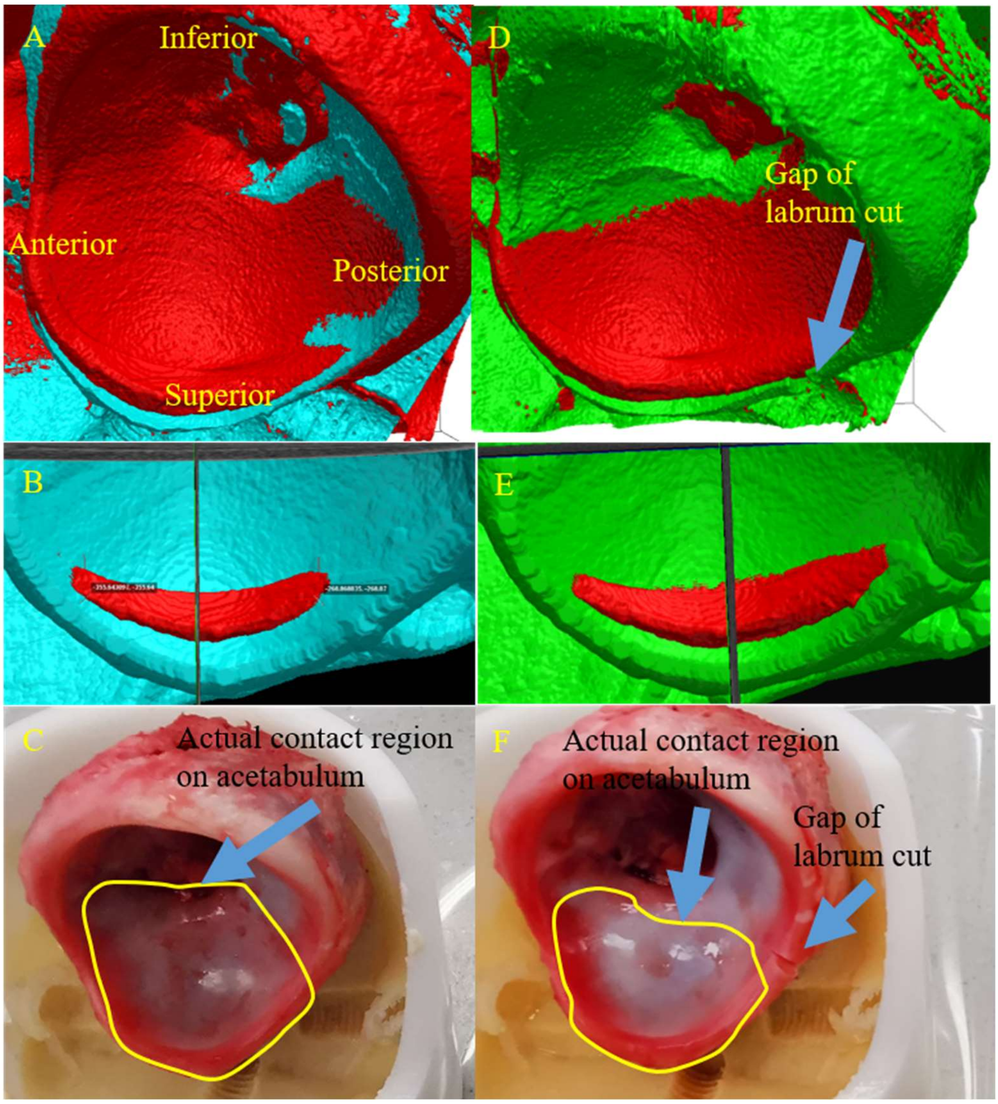

**Figure 4.30 Segmented contact region compared with experiment results for PH13. Left column for loaded case, right column for cut case. AD, segmented actual contact region; BE segmented focused contact region; CF experimental contact region.**

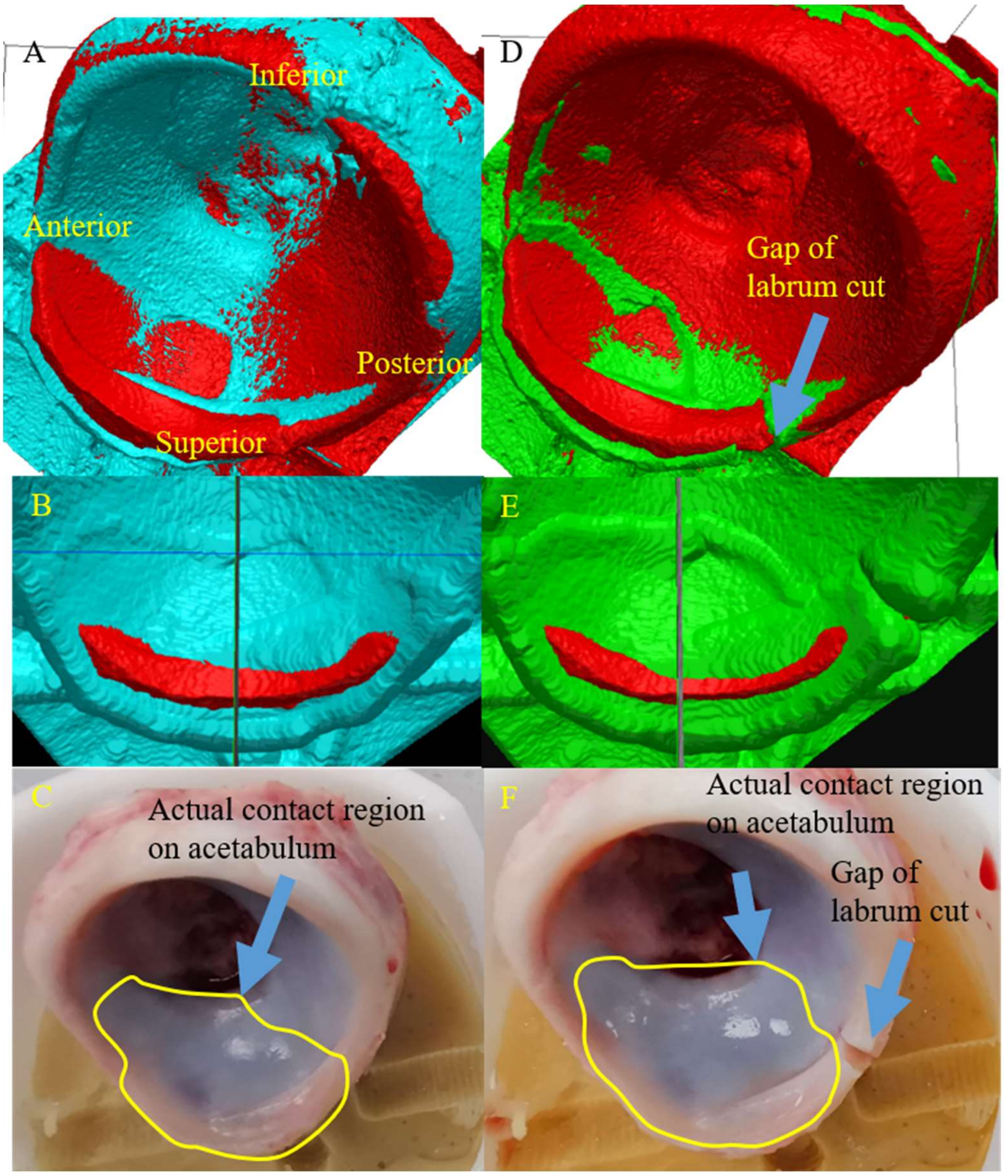

**Figure 4.31 Segmented contact region compared with experiment results for PH14. Left column for loaded case, right column for cut case. AD, segmented actual contact region; BE segmented focused contact region; CF experimental contact region.**

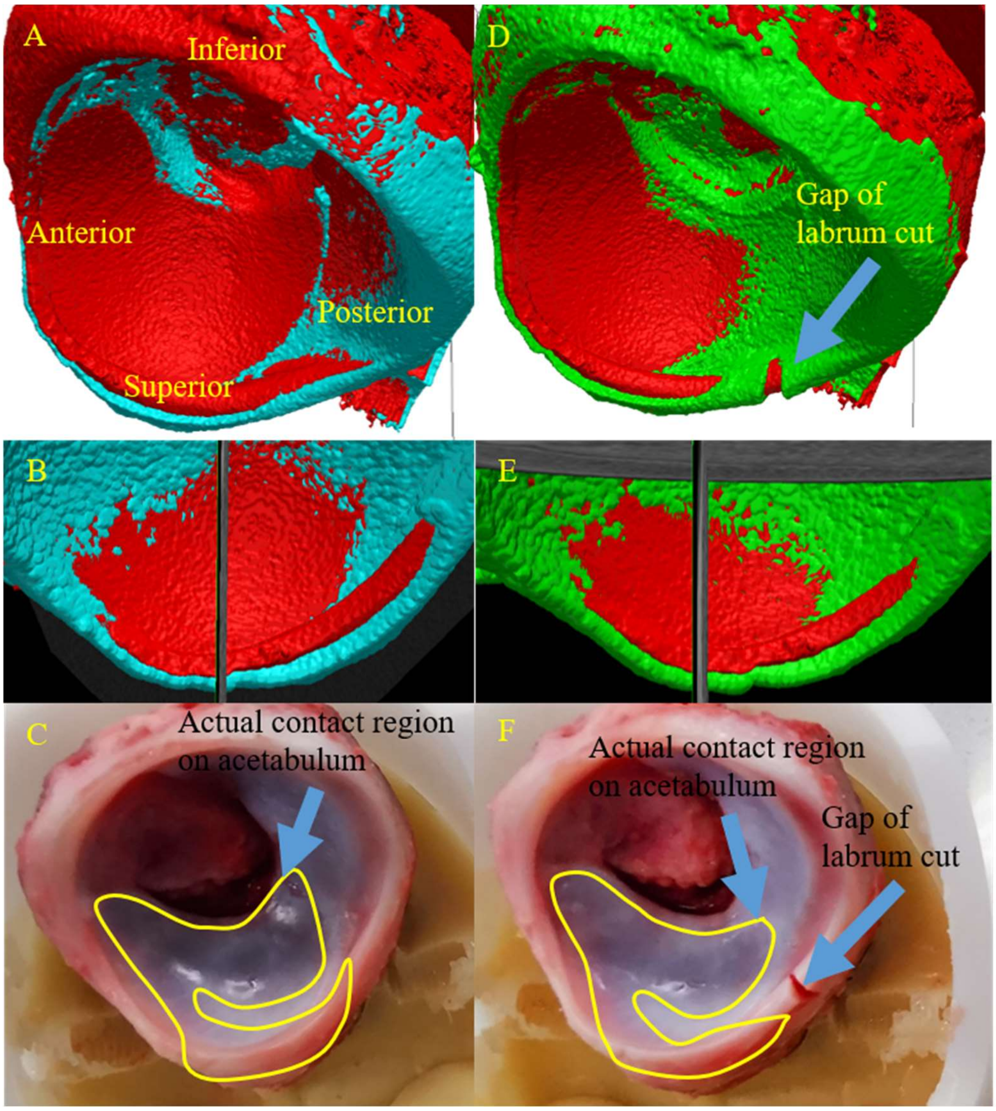

**Figure 4.32 Segmented contact region compared with experiment results for PH15. Left column for loaded case, right column for cut case. AD, segmented actual contact region; BE segmented focused contact region; CF experimental contact region.**

### 4.4.3 Measurement of soft tissues deformation

Soft tissues deformation was quantified in two ways: 1) the acetabular cartilage strain at the centre of the focused contact region; and 2) the acetabular labrum movement at the labrum apex in radial direction. The cartilage strain across the acetabulum socket is a measurement of pressure distribution on the cartilage surface during load and is comparable to other studies from literature. The labrum movement is a measurement of the labrum being compressed by the femoral head and may also be associated with the location of labrum cut.

#### 4.4.3.1 Measurement on acetabular cartilage strain

The measurement of acetabular cartilage thickness was recorded for both unloaded and loaded 2D slice. The variation of calculated cartilage strain across the acetabulum radius was illustrated and compared between the loaded and the cut case. The error bar implied the potential error in strain calculation due to error in thickness measurement caused by image resolution.

The acetabular cartilage strain values and trends vary between cases. In sample PH10, PH12, and PH15, the cartilage strain decreased from the cartilage-labral junction towards inside the socket. The sample PH11 had the strain increased from the rim towards inside the socket. The ligament of the head of femur was just next to the contact region on the femur in sample PH11. Sample PH13 and PH14 had relatively small strain across the acetabulum socket. It is also noticed in the segmented 2D slice (Figure 4.37 and Figure 4.41) that, the femoral head was almost displacing towards the cartilage-labral junction through the ligament of the head of femur. The ligament was subject to high deformation due to low compressive strength.

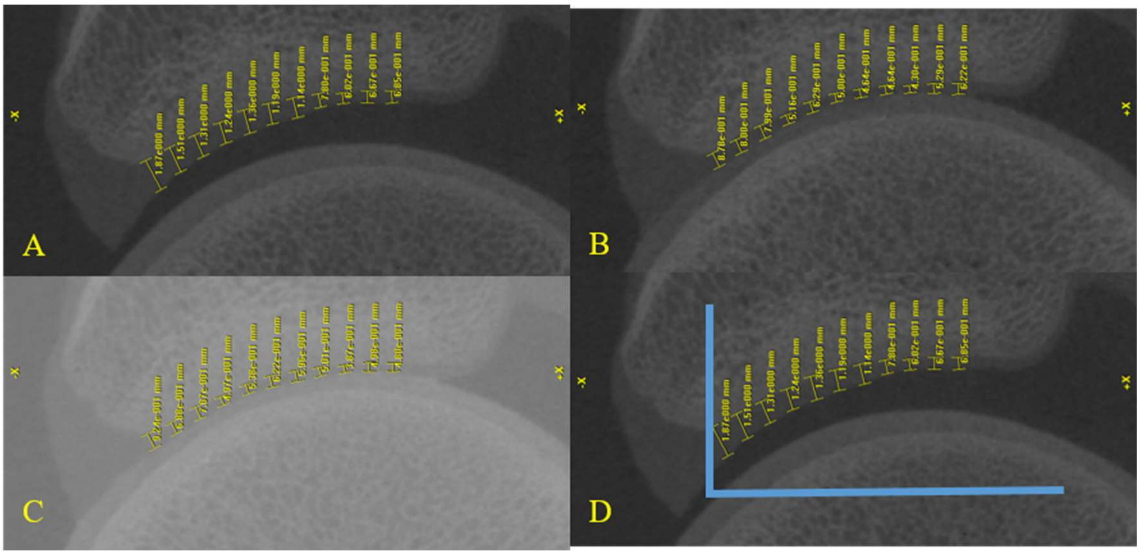

**Figure 4.33 Measurement of cartilage thickness for PH10. A, unloaded cartilage thickness; B, cartilage thickness under load with intact labrum; C, cartilage thickness under load with labrum cut; D, schematic coordinate system regarding the bone support.**

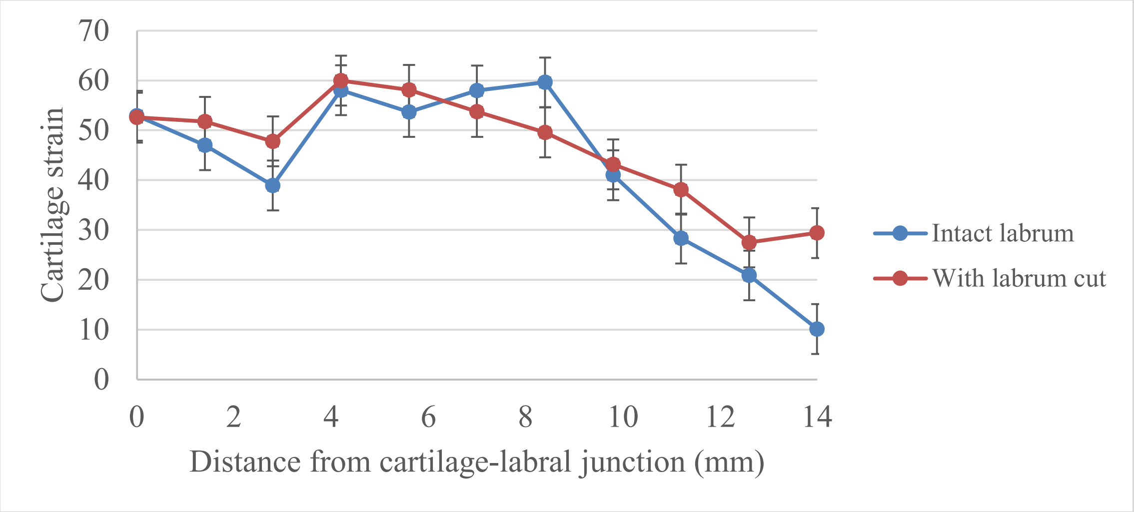

**Figure 4.34 Cartilage strain across acetabulum radius for PH10.**

The cartilage strain varied between 40 – 60% at 0 - 8 mm to the bone support. The strain decreased along the subchondral bone. The variation in cut case was within 10%.

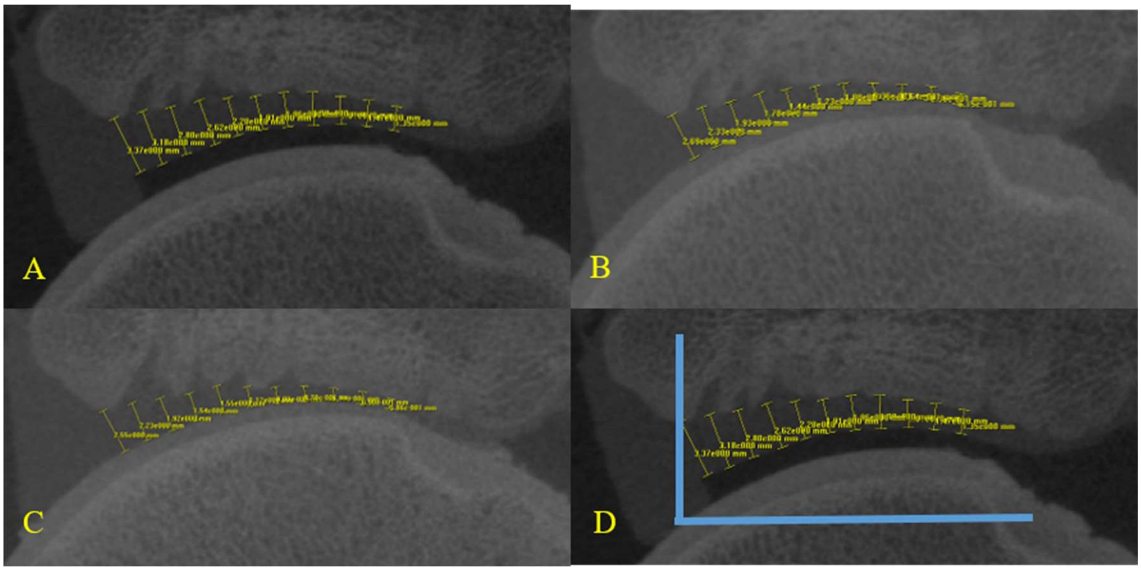

**Figure 4.35 Measurement of cartilage thickness for PH11. A, unloaded cartilage thickness; B, cartilage thickness under load with intact labrum; C, cartilage thickness under load with labrum cut; D, schematic coordinate system regarding the bone support.**

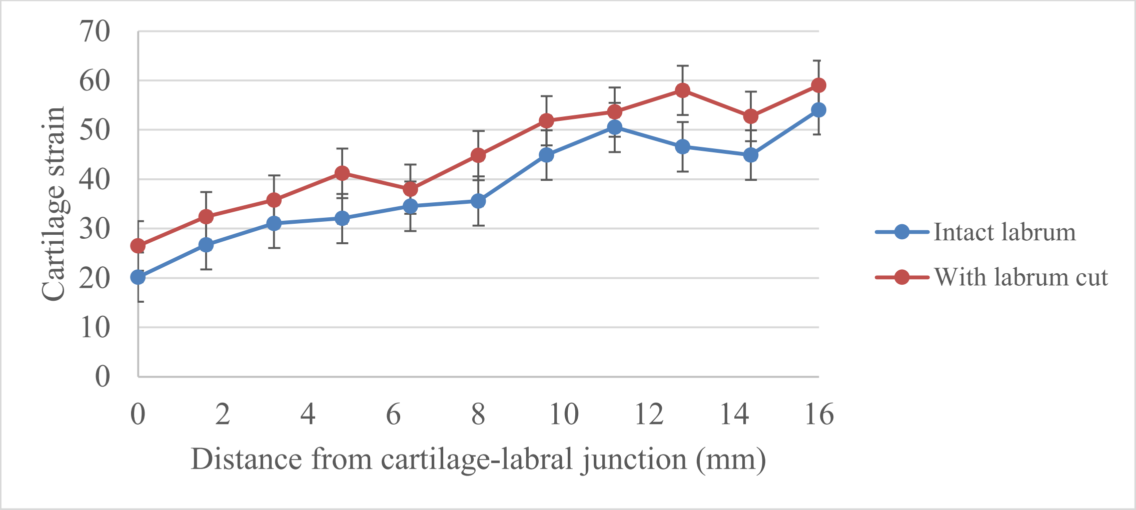

**Figure 4.36 Cartilage strain across acetabulum radius for PH11.**

The cartilage strain varied between 20 – 40% at 0 – 8 mm to the bone support. The strain increased along the subchondral bone. The cut case had an increase in strain within 10%.

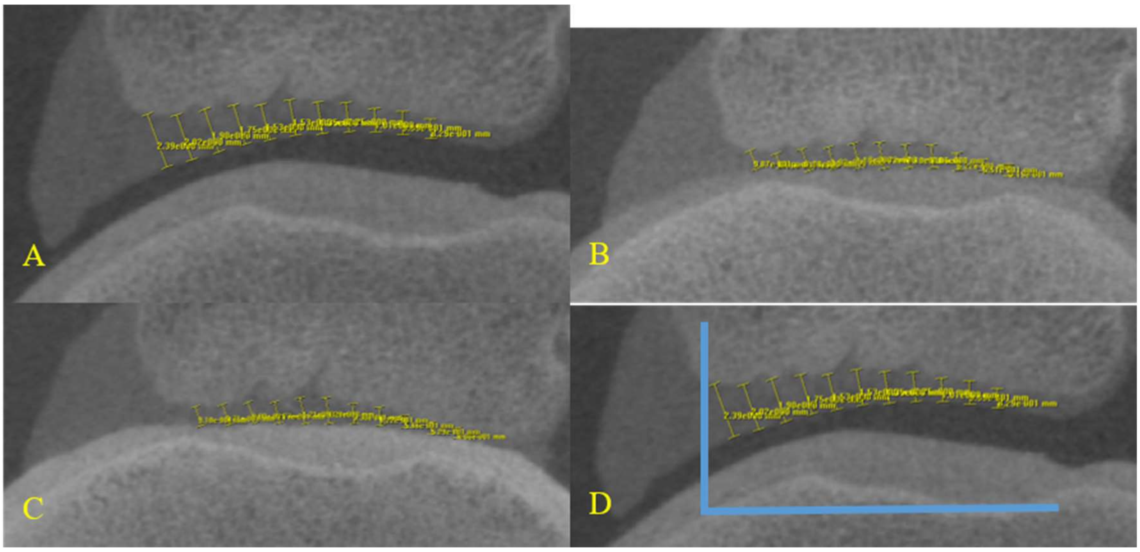

**Figure 4.37 Measurement of cartilage thickness for PH12. A, unloaded cartilage thickness; B, cartilage thickness under load with intact labrum; C, cartilage thickness under load with labrum cut; D, schematic coordinate system regarding the bone support.**

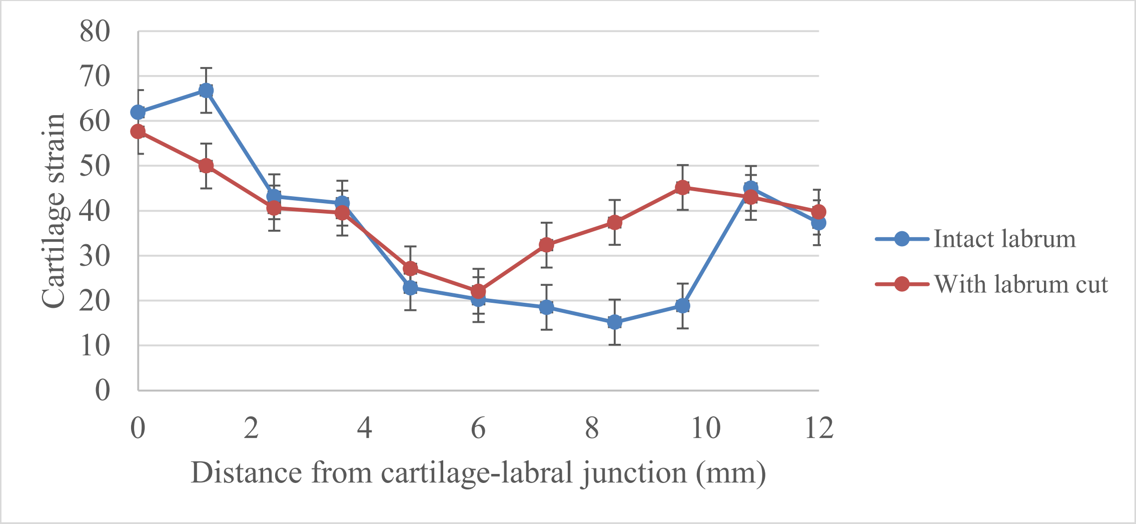

**Figure 4.38 Cartilage strain across acetabulum radius for PH12.**

The cartilage strain varied between 20 – 67% at 0 – 8 mm to the bone support. The strain decreased along the subchondral bone. The variation of cartilage strain in cut case was within 17%.

The root of the ligament of the head of femur was in contact with the acetabular cartilage starting at 4 mm from bone support. The ligament has a lower modulus than cartilage, therefore the acetabular cartilage was experiencing lower reaction force than expected and was undergoing lower strain.

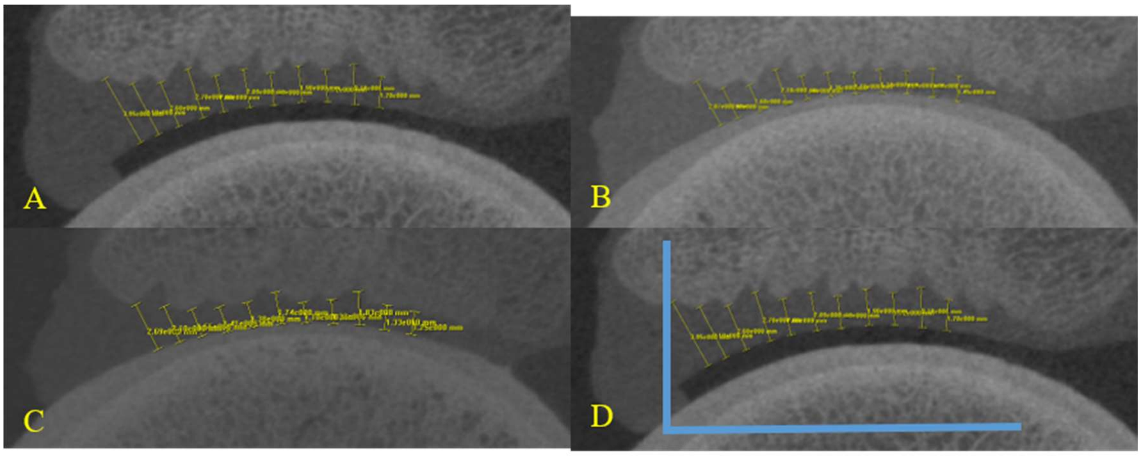

**Figure 4.39 Measurement of cartilage thickness for PH13. A, unloaded cartilage thickness; B, cartilage thickness under load with intact labrum; C, cartilage thickness under load with labrum cut; D, schematic coordinate system regarding the bone support.**

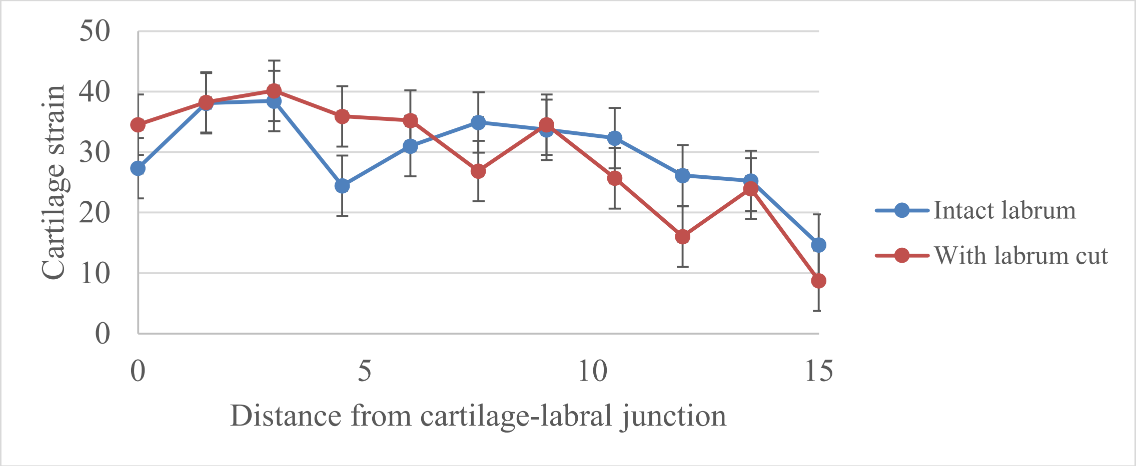

**Figure 4.40 Cartilage strain across acetabulum radius for PH13.**

The cartilage strain varied between 20 – 40% at 0 – 8 mm to the bone support. The measured strain was unstable but remained in the same range along the subchondral bone. The variation of cartilage strain in cut case was within 12%.

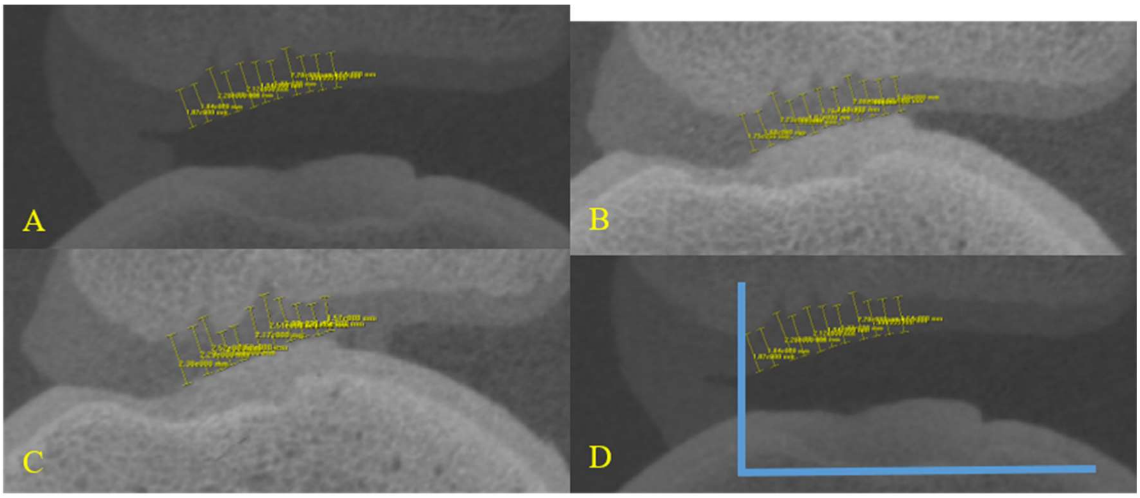

**Figure 4.41 Measurement of cartilage thickness for PH14. A, unloaded cartilage thickness; B, cartilage thickness under load with intact labrum; C, cartilage thickness under load with labrum cut; D, schematic coordinate system regarding the bone support.**

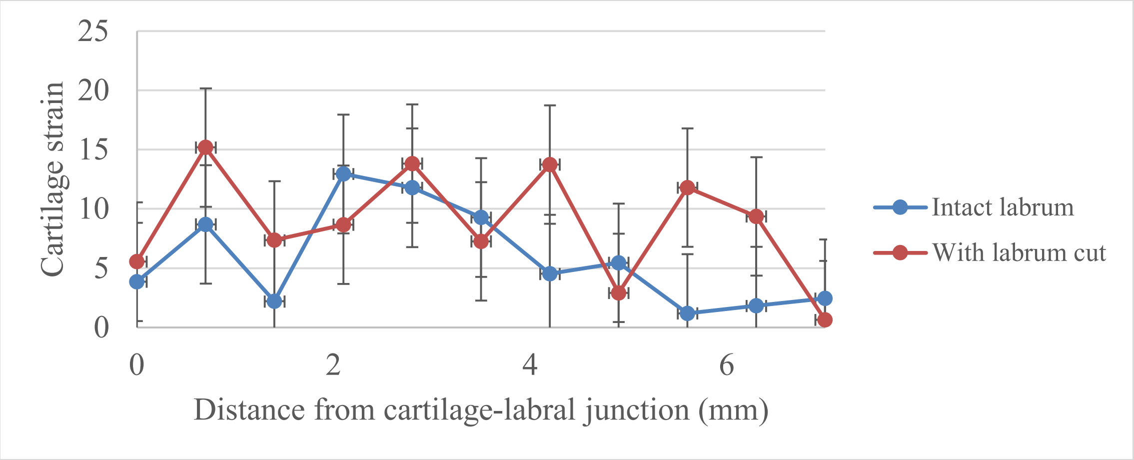

**Figure 4.42 Cartilage strain across acetabulum radius for PH14.**

The cartilage strain varied between 2.2 – 13% at 0 – 8 mm to the bone support. The measured strain was unstable but remained in the same range along the subchondral bone. The variation of cartilage strain in the cut case was within 8%.

The femoral head was almost displacing towards the labral rim in the top left direction in the figure. The acetabular cartilage was experiencing lower normal force than expected, and against the ligament of the head of femur similar to PH12. Therefore, the cartilage strain was particularly small in this sample.

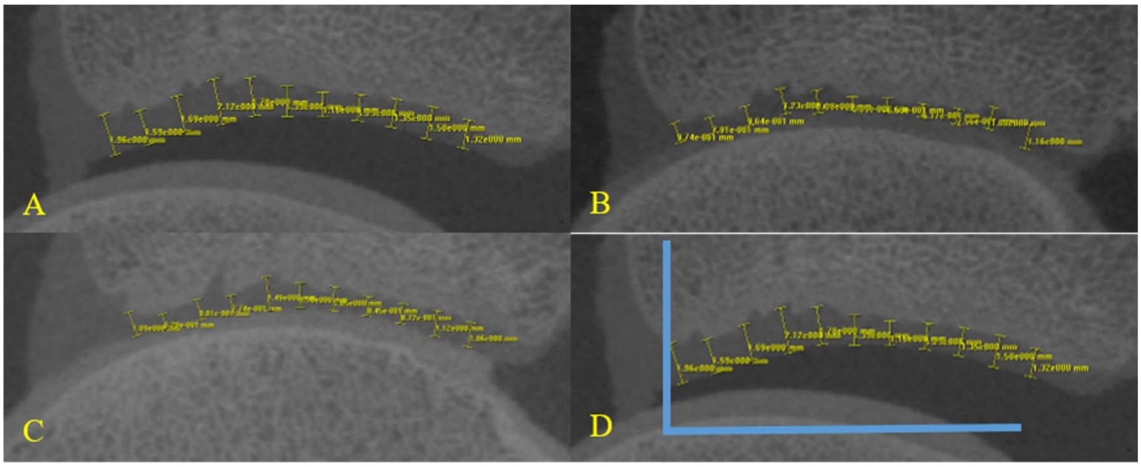

**Figure 4.43 Measurement of cartilage thickness for PH15. A, unloaded cartilage thickness; B, cartilage thickness under load with intact labrum; C, cartilage thickness under load with labrum cut; D, schematic coordinate system regarding the bone support.**

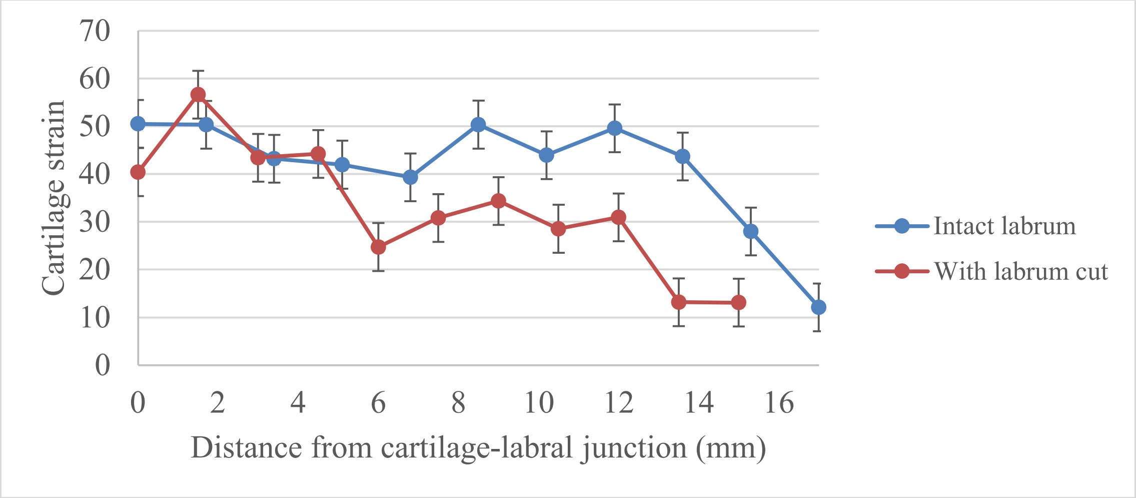

**Figure 4.44 Cartilage strain across acetabulum radius for PH15.**

The cartilage strain varied between 40 – 50% at 0 – 8 mm to the bone support. The strain remained in the same range along the subchondral bone. The cut case had a decrease in strain at 5 – 8 mm to the bone support of about 15%.

#### 4.4.3.2 Measurement on acetabular labrum movement

The acetabular labrum movement was quantified by measuring the labrum shape shift, before and during load, in radial direction at the reconstructed labrum apex (Figure 4.45 – Figure 4.56). Red and blue nodes represented the labrum apex tissue before and during load respectively. Magnitude of ten largest radial distances, and the corresponding apex location from the horizon (in degrees), were recorded (Table 4.3 –

Table 4.8) and compared between the loaded and the cut case for each sample.

The reconstructed labrum apex deformed further away at the superior-anterior portion with the labrum cut, except for sample PH14 and PH15. For clarification of the effect of labrum cut on all samples, a more generic assessment of labrum movement is introduced in section 4.4.3.3. However, the sample PH14 had the labrum rim separated during load. The superior-anterior region, where the pressure was focused, seemed to be pushed towards the socket. The both sides were seemed to expand outwards from the socket. The load condition for sample PH14 is discussed in particular in section 4.5.2.

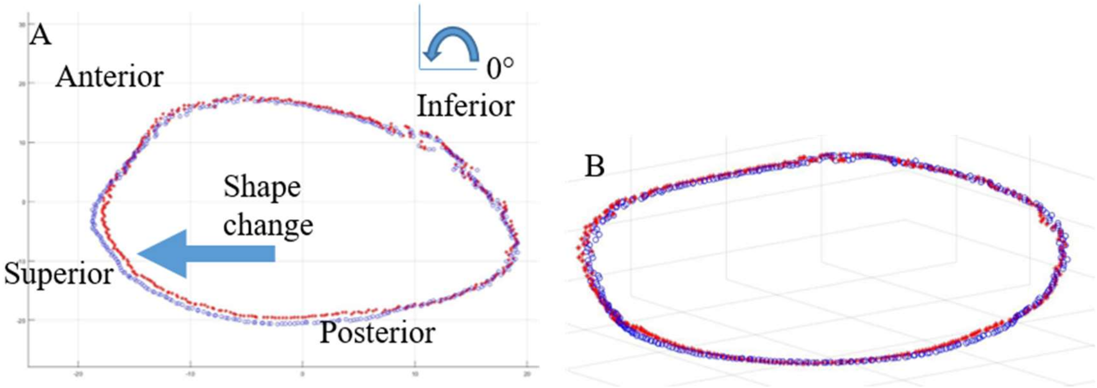

**Figure 4.45 Reconstructed labrum apex for PH10 under loaded case. A – Socket normal view. B – Isotropic view.**

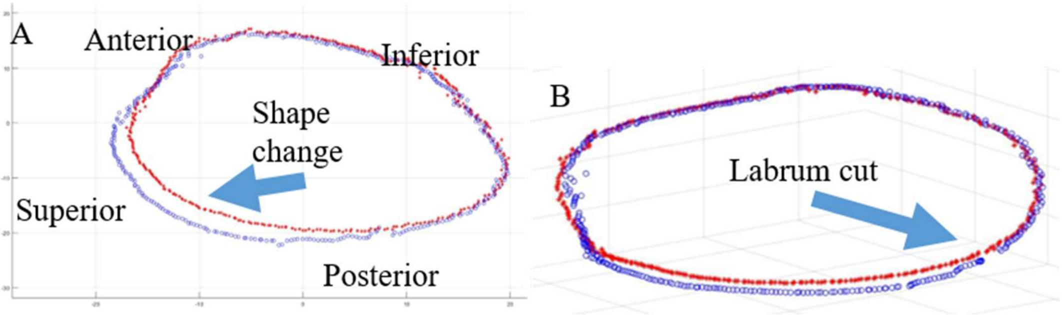

**Figure 4.46 Reconstructed labrum apex for PH10 under cut case. A – Socket normal view. B – Isotropic view.**

**Table 4.3 Labrum shape shift in PH10 under loaded and cut case.**

| Loaded case | | Cut case | |
|---|---|---|---|
| At angle (°) | Displacement (mm) | At angle (°) | Displacement (mm) |
| 282 | 1.5 | 246 | 3.4 |
| 277 | 1.3 | 264 | 3.3 |
| 284 | 1.2 | 265 | 3.2 |
| 285 | 1.2 | 250 | 3.0 |
| 288 | 1.2 | 254 | 2.9 |
| 280 | 1.1 | 261 | 2.9 |
| 278 | 1.1 | 257 | 2.9 |
| 290 | 1.1 | 258 | 2.9 |
| 257 | 1.1 | 262 | 2.8 |
| 283 | 1.0 | 260 | 2.8 |

The maximum labrum apex displacement in loaded case was about 1.0 – 1.5 mm at posterior region between 277 and 290 degrees. The maximum labrum apex displacement in cut case was about 2.8 – 3.4 mm at superior-posterior region between 246 and 265 degrees. The maximum displacement increased from 1.5 mm to 3.4 mm. The location where maximum displacement occurred shifted superiorly.

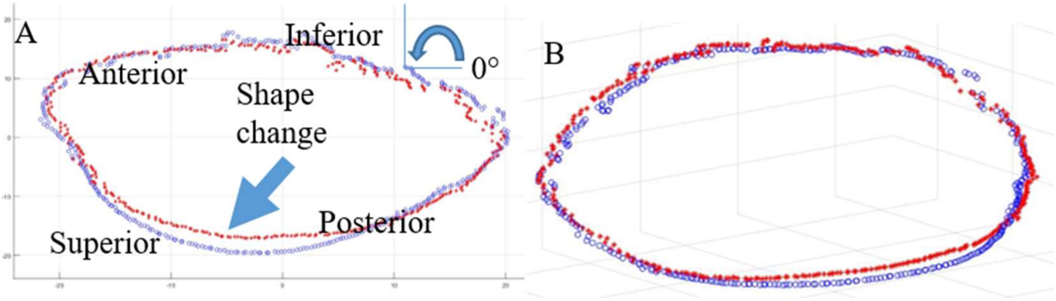

**Figure 4.47 Reconstructed labrum apex for PH11 under loaded case. A – Socket normal view. B – Isotropic view.**

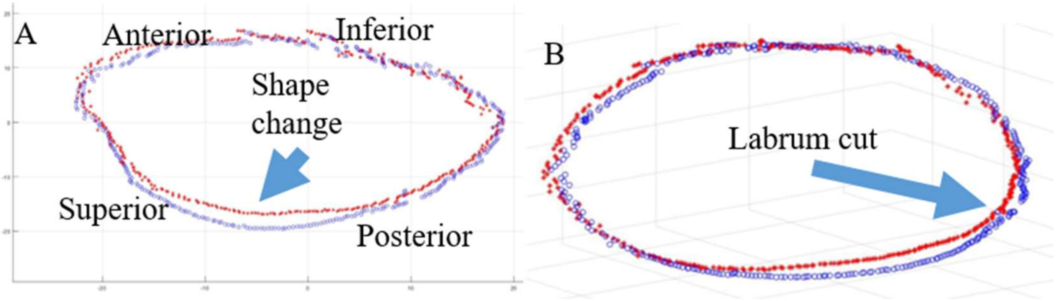

**Figure 4.48 Reconstructed labrum apex for PH11 under cut case. A – Socket normal view. B – Isotropic view.**

**Table 4.4 Labrum shape shift in PH11 under loaded and cut case.**

| Loaded case | | Cut case | |
|---|---|---|---|
| At angle (°) | Displacement (mm) | At angle (°) | Displacement (mm) |
| 271 | 2.8 | 264 | 3.1 |
| 269 | 2.7 | 253 | 3.0 |
| 268 | 2.7 | 254 | 3.0 |
| 270 | 2.7 | 258 | 2.9 |
| 272 | 2.6 | 262 | 2.9 |
| 273 | 2.6 | 263 | 2.9 |
| 264 | 2.5 | 265 | 2.9 |
| 254 | 2.4 | 266 | 2.9 |
| 275 | 2.4 | 267 | 2.8 |
| 277 | 2.3 | 269 | 2.7 |

The maximum labrum apex displacement in loaded case was about 2.3 – 2.8 mm at superior-posterior region between 264 and 277 degrees. The maximum labrum apex displacement in cut case was about 2.7 – 3.1 mm at superior-posterior region between 253 and 269 degrees. The maximum displacement increased from 2.8 mm to 3.1 mm. The location where maximum displacement occurred shifted slightly to the superior region.

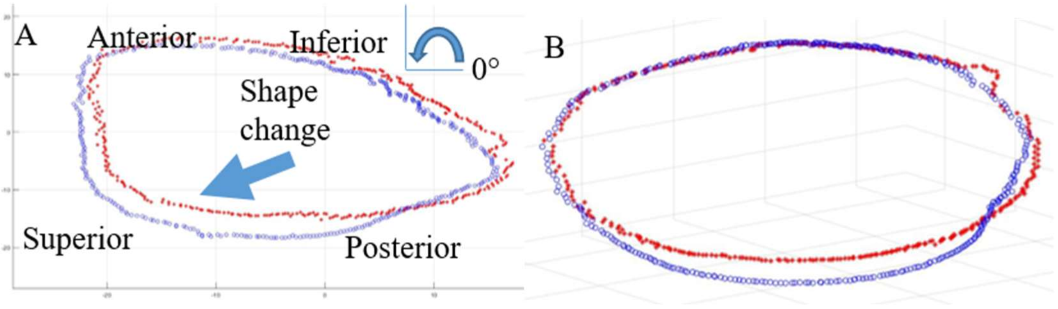

**Figure 4.49 Reconstructed labrum apex for PH12 under loaded case. A – Socket normal view. B – Isotropic view.**

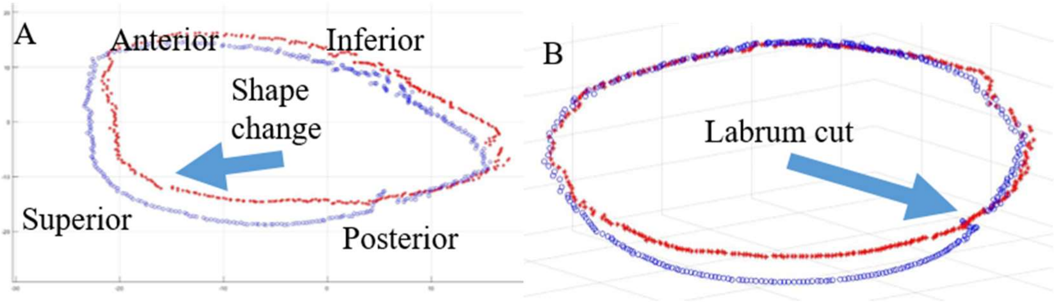

**Figure 4.50 Reconstructed labrum apex for PH12 under cut case. A – Socket normal view. B – Isotropic view.**

**Table 4.5 Labrum shape shift in PH12 under loaded and cut case.**

| Loaded case | | Cut case | |
|---|---|---|---|
| At angle (°) | Displacement (mm) | At angle (°) | Displacement (mm) |
| 239 | 5.0 | 224 | 5.3 |
| 241 | 5.0 | 226 | 5.3 |
| 243 | 4.8 | 233 | 5.2 |
| 244 | 4.6 | 237 | 5.2 |
| 257 | 4.6 | 234 | 5.1 |
| 256 | 4.5 | 240 | 5.1 |
| 233 | 4.5 | 243 | 5.0 |
| 249 | 4.5 | 244 | 5.0 |
| 254 | 4.4 | 253 | 5.0 |
| 250 | 4.4 | 248 | 4.9 |

The maximum labrum apex displacement in loaded case was about 4.4 – 5.0 mm at superior-posterior region between 239 and 257 degrees. The maximum labrum apex displacement in cut case was about 4.9 – 5.3 mm at superior region between 224 to 253 degrees. The maximum displacement increased from 5.0 to 5.3 mm. The location where maximum displacement occurred shifted superiorly.

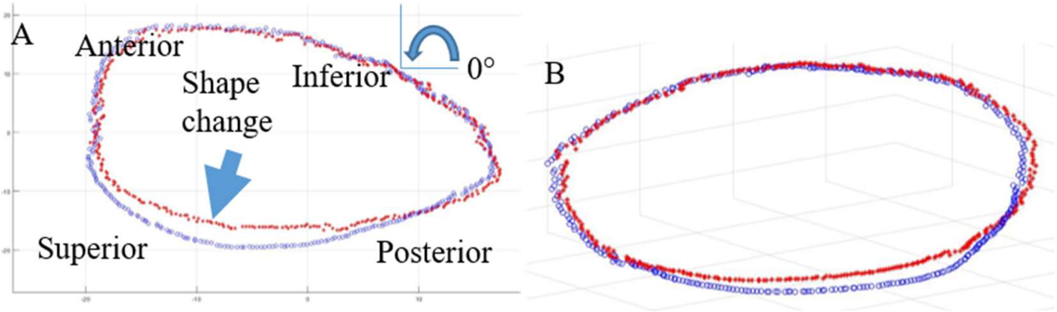

**Figure 4.51 Reconstructed labrum apex for PH13 under loaded case. A – Socket normal view. B – Isotropic view.**

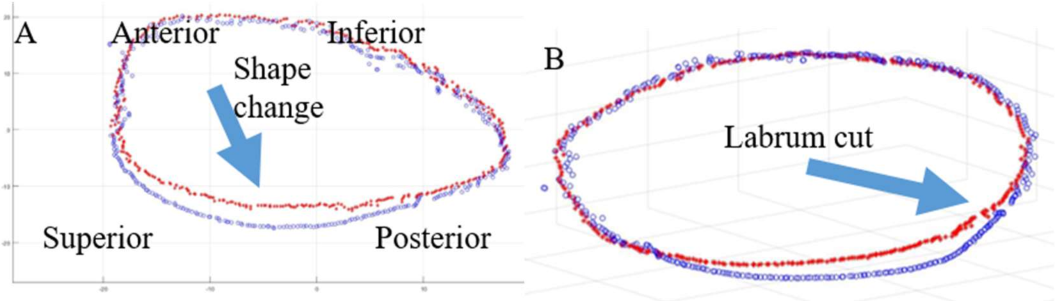

**Figure 4.52 Reconstructed labrum apex for PH13 under cut case. A – Socket normal view. B – Isotropic view.**

**Table 4.6 Labrum shape shift in PH13 under loaded and cut case.**

| Loaded case | | Cut case | |
|---|---|---|---|
| At angle (°) | Displacement (mm) | At angle (°) | Displacement (mm) |
| 251 | 3.8 | 258 | 4.5 |
| 252 | 3.7 | 259 | 4.3 |
| 253 | 3.7 | 264 | 4.1 |
| 259 | 3.6 | 266 | 4.1 |
| 257 | 3.6 | 271 | 4.1 |
| 258 | 3.6 | 272 | 4.1 |
| 270 | 3.5 | 273 | 4.0 |
| 268 | 3.4 | 274 | 3.8 |
| 267 | 3.3 | 276 | 3.6 |
| 269 | 3.3 | 279 | 3.5 |

The maximum labrum apex displacement in loaded case was about 3.3 – 3.8 mm at superior-posterior region between 251 and 270 degrees. The maximum labrum apex displacement in cut case was about 3.5 – 4.5 mm at posterior-superior region between 258 and 279 degrees. The maximum displacement increased from 3.8 mm to 4.5 mm. The location where maximum displacement occurred shifted slightly to the posterior region.

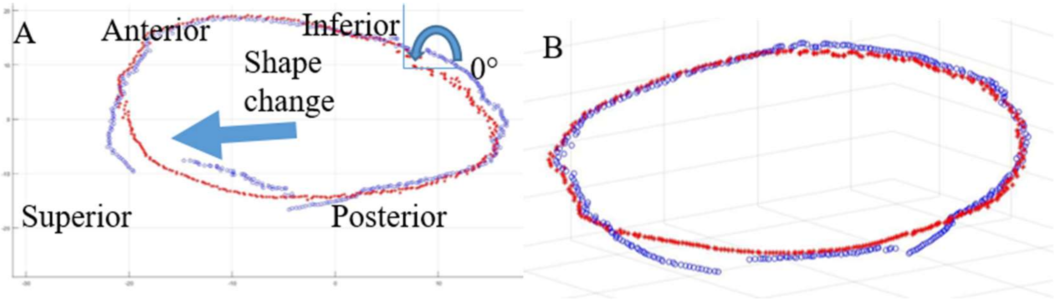

**Figure 4.53 Reconstructed labrum apex for PH14 under loaded case. A – Socket normal view. B – Isotropic view.**

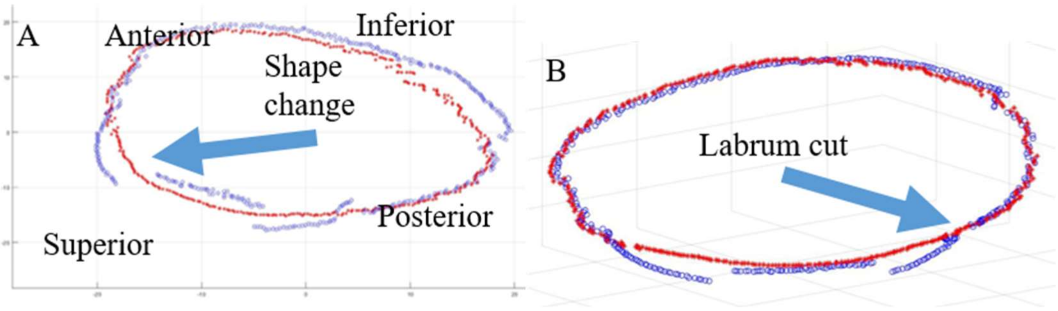

**Figure 4.54 Reconstructed labrum apex for PH14 under cut case.A – Socket normal view. B – Isotropic view.**

**Table 4.7 Labrum shape shift in PH14 under loaded and cut case.**

| Loaded case | | Cut case | |
|---|---|---|---|
| At angle (°) | Displacement (mm) | At angle (°) | Displacement (mm) |
| 229 | 4.4 | 208 | 3.8 |
| 220 | 4.4 | 235 | 3.8 |
| 223 | 4.2 | 290 | 3.6 |
| 230 | 4.2 | 239 | 3.4 |
| 228 | 4.2 | 241 | 3.3 |
| 231 | 4.1 | 238 | 3.3 |
| 233 | 3.9 | 258 | 3.2 |
| 227 | 3.8 | 259 | 3.2 |
| 235 | 3.8 | 254 | 3.1 |
| 237 | 3.5 | 261 | 3.1 |

The maximum labrum apex displacement in loaded case was about 3.5 – 4.4 mm at superior region between 220 and 237 degrees. The maximum labrum apex displacement in cut case was about 3.1 – 3.8 mm at superior region between 235 and 261 degrees. The maximum displacement reduced from 4.4 mm to 3.8 mm. the location where maximum displacement occurred shifted posteriorly. However, as mentioned in the previous section, the femoral head displaced towards the labral rim in this sample. The labrum was normally compressed from the centre instead of being loaded from inside the acetabulum. The script struggled to find the “highest” apex point along the circumferential direction. Figure 4.54 and Figure 4.55 illustrated that the outer side of the labrum at superior was compressed downwards by the femoral head, and the inner side of the labrum has been pushed up consequently.

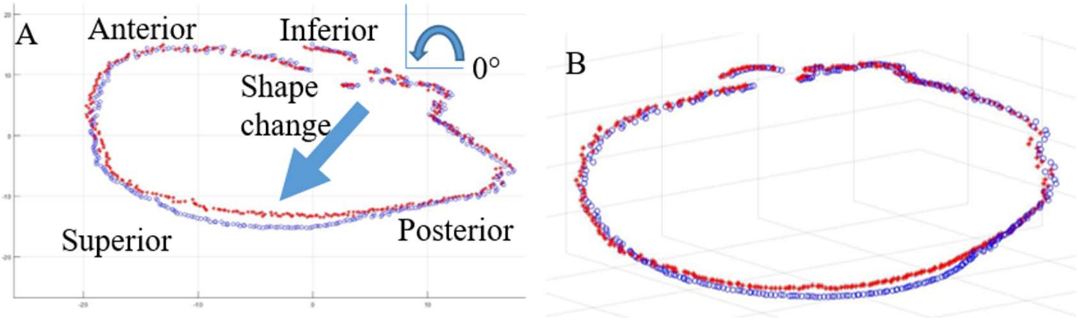

**Figure 4.55 Reconstructed labrum apex for PH15 under loaded case. A – Socket normal view. B – Isotropic view.**

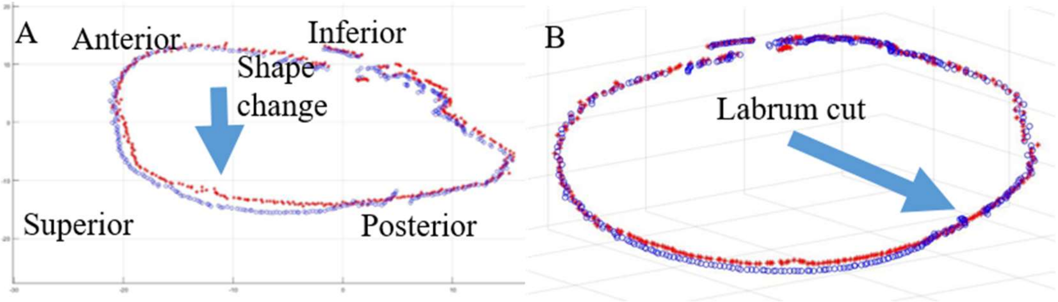

**Figure 4.56 Reconstructed labrum apex for PH15 under cut case. A – Socket normal view. B – Isotropic view.**

**Table 4.8 Labrum shape shift in PH15 under loaded and cut case.**

| Loaded case | | Cut case | |
|---|---|---|---|
| At angle (°) | Displacement (mm) | At angle (°) | Displacement (mm) |
| 254 | 2.6 | 225 | 2.6 |
| 247 | 2.6 | 221 | 2.5 |
| 251 | 2.5 | 226 | 2.2 |
| 264 | 2.4 | 227 | 2.2 |
| 341 | 2.3 | 228 | 2.2 |
| 261 | 2.3 | 243 | 2.1 |
| 253 | 2.2 | 245 | 2.1 |
| 259 | 2.2 | 248 | 2.1 |
| 266 | 2.2 | 341 | 2.0 |
| 267 | 2.1 | 345 | 2.0 |

The maximum labrum apex displacement in loaded case was about 2.1 – 2.6 mm at superior-posterior region between 247 and 267 degrees. The maximum labrum apex displacement in cut case was about 2.0 – 2.6 mm at superior region between 221 and 248 degrees. The maximum displacement remained the same at 2.6 mm. The location where maximum displacement occurred shifted superiorly. The gap at the posterior demonstrated poor segmentation of soft tissue where inferior acetabular labrum merged with the femoral neck. The separation was done by manual hand-drawing of the separation line. Artefacts were left at the posterior however the gaps were far away from the region of interest in this study.

#### 4.4.3.3 Labrum cut coefficient

Due to the inconsistency of load applied to each sample, a generalised labrum cut coefficient (lcc) was calculated to investigate the labrum circumferential effect:

$$\text{Labrum compliance} = \frac{\text{Labrum maximum displacement}}{\text{End reaction force}} * 1000\ (\frac{\text{mm}}{\text{kN}})$$

$$\text{Labrum cut coefficient} = \frac{\text{Labrum compliance under cut case}}{\text{Labrum compliance under load case}}$$

**Table 4.9 Labrum cut coefficient for porcine hip samples**

| Sample | Case | Labrum maximum displacement (mm) | End reaction force (N) | Labrum compliance (mm/kN) | Labrum cut coefficient |
|---|---|---|---|---|---|
| PH10 | Load | 1.5 | 183 | 8.20 | 1.48 |
| | Cut | 3.4 | 281 | 12.10 | |
| PH11 | Load | 2.8 | 213 | 13.15 | 1.03 |
| | Cut | 3.1 | 228 | 13.60 | |
| PH12 | Load | 5.0 | 230 | 21.74 | 1.21 |
| | Cut | 5.3 | 201 | 26.37 | |
| PH13 | Load | 3.8 | 152 | 25.00 | 1.17 |
| | Cut | 4.5 | 154 | 29.22 | |
| PH14 | Load | 4.4 | 81 | 54.32 | 1.71 |
| | Cut | 3.8 | 41 | 92.68 | |
| PH15 | Load | 2.6 | 178 | 14.61 | 1.71 |
| | Cut | 2.6 | 104 | 25.00 | |

The labrum cut coefficient is worked out as the ratio of the labrum compliance ($p<0.1$ across all samples, $p<0.05$ if PH14 is excluded) regarding the labrum cut. The larger the value of lcc is (if greater than 1), the larger impact the cut has on the labrum, which made the apex easier to deform. The averaged lcc was 1.4±0.3

for all samples. The labrum maximum displacement was not much affected by the labrum in PH11. However, in PH14 and PH15, the labrum cut contributed an increase factor of 1.71 to the labrum maximum displacement.

## 4.5 Discussion

The preceding chapter reported the study of six porcine hip joint, following the methodology developed in Chapter 3, that quantified acetabular soft tissue behaviour under FAI-related load. The achievements and findings were:

- Loaded the acetabulum at the targeted contact region, superior-anterior portion of the socket, in all six samples.
- Created labrum cut close to the actual contact region, and applied similar load conditions in all six sample.
- Obtained three sets of CT image: 1) unloaded tissue; 2) load case, tissue loaded with intact labrum; and 3) cut case, tissue loaded with labrum cut, for all six sample.
- Effective displacement per screw turn was 1 mm for tissue at the first load. The effective displacement varied from 0.8 mm to 1.2 mm in the second load.
- The percentage volumetric error of bone registration was mainly between 13.5% and 30.4%, with exception up to 49.5%. The actual contact region agreed well with the contact patch observed on the tissue sample after CT scan.
- The acetabular cartilage experienced strain mainly between 20% and 60% with exceptions at 5% - 15%, depending on the contact conditions.
- The labrum apex experienced displacement between 1.5 mm and 5.0 mm in loaded case, and between 2.6 mm and 5.3 mm in cut case. The labrum cut coefficient was found to be 1.4, which means the labrum cut contributed a ratio of 1.4 to the labrum maximum displacement in labrum cut cases. The location of maximum displacement shifted superiorly, towards to the contact region, in 4 out of 6 samples.

### 4.5.1 Experiment protocol

The porcine hip used has a small femoral head, potentially narrow but thick labrum, compared to the human hip. The femoral head diameter was found to be 37.9 ± 2.0 mm across all samples, which is smaller than the human hip with 46.8 ± 5.7 mm (Taylor et al., 2011). The labrum width by thickness was measured at 5.5 ± 1.2 mm by 6.4 ± 0.89 mm, compared to human labrum with 5.4 ± 2.3 mm by 5.5 ± 1.5 mm (Seldes et al., 2001). The porcine labrum used was about the same width but thicker than human labrum. However, the labrum width may be overestimated due to the overhang tissue at superior (discussed in Section 5.2.1).

One freeze-thaw cycle was applied to the samples when the storage time was longer than two days between dissection and CT scanning. The aim of freezer was to keep tissue sample fresh during storage. Defrosting the tissue was necessary before the scan for ease of dissection. Storage should also try to maintain the material properties of soft tissue for consistent tissue response between samples. Solid porcine muscle (Figure 4.57) and frozen synovial fluid (Figure 4.58) were observed in tissues where the defrost time was less than 24 hours. Frozen porcine soft tissues brought difficulties to the precise dissection where differentiation of various tissue types could not be made from one piece of consolidated tissue.

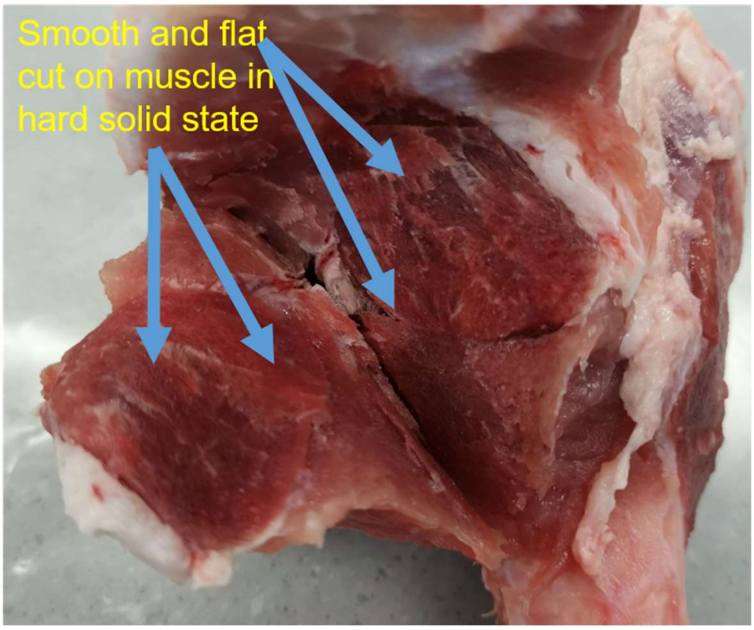

**Figure 4.57 Frozen muscle slice around the hip joint**

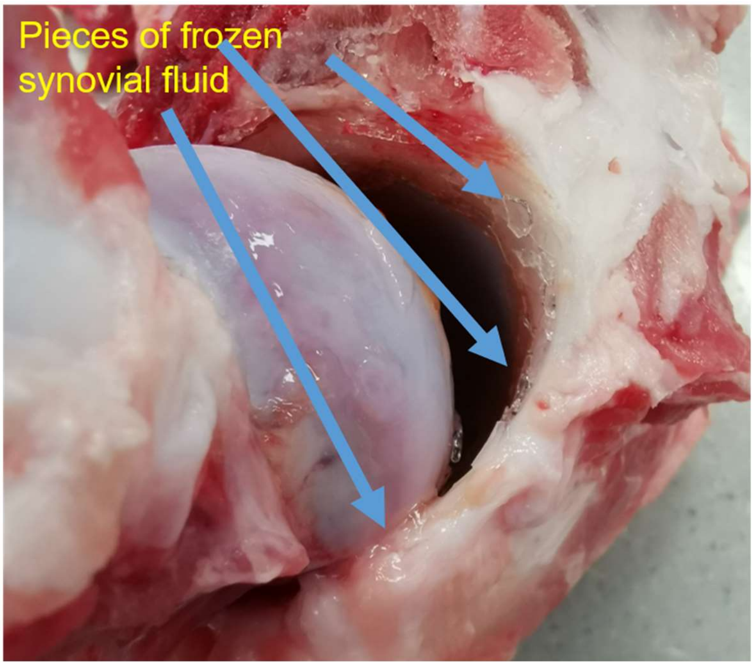

**Figure 4.58 Frozen synovial fluid pieces on the acetabular cartilage**

The experimental contact regions shown good consistency and were located at the superior-anterior portion of the acetabulum at the cartilage-labral junction. The segmented focused contact region all matched with the experimental observation and were located at the cartilage-labral junction. However, the contact patch on the femoral head varied. In 3 out of 6 samples, the root of the ligament of the head of femur was involved in the contact. The ligament is soft and subject to high deformation in this type of focused axial loading. The so called “femoral cartilage strain” would be misleading since the ligament was defined as part of the “femoral cartilage thickness”. It is still worth mentioning that the role of load share of the labrum may be better understood by comparing the femoral cartilage strain across the labral and the junction regions.

The acetabulum socket was aligned with aid of the concentric tool. The aim was only to align the centre of the pot coincident with the targeted contact region, around superior-anterior portion at the acetabulum. The femur was then aligned manually to make sure that the femoral head would come into contact with the acetabulum at the targeted contact region. However, due to limited space in the pot and random error during manual operation, the acetabular rim always kept a sharp angle with the femoral neck (Figure 4.59). In Figure 4.59-A, the posterior of the acetabulum, transverse acetabular ligament, came into contact with the femur when assembled into the hip loading rig. The contact led to a source of load error that increased the load reading when applying femoral head displacement.

In addition, multiple soft tissues were difficult to be separated by automatic image processing technique without support of radiopaque solution. Applying NaI solution on the femoral neck was suggested for future work to highlight the soft tissue on the femur component that close to the acetabulum. Alternatively, more soft tissues could be removed, such as lesser trochanter, during the dissection of femur.

In Figure 4.59-B, the posterior acetabulum socket covered part of the femoral head. Therefore the hip joint had to be reassembled before placing the pots into the Perspex tube, rather than as illustrated in Figure 4.60. Hence the hip joint already experienced small force and rotation before the first scan in this study. Advanced alignment tools and larger space in the rig could be developed to allow more consistent and flexible relative positions between the acetabulum and the femur.

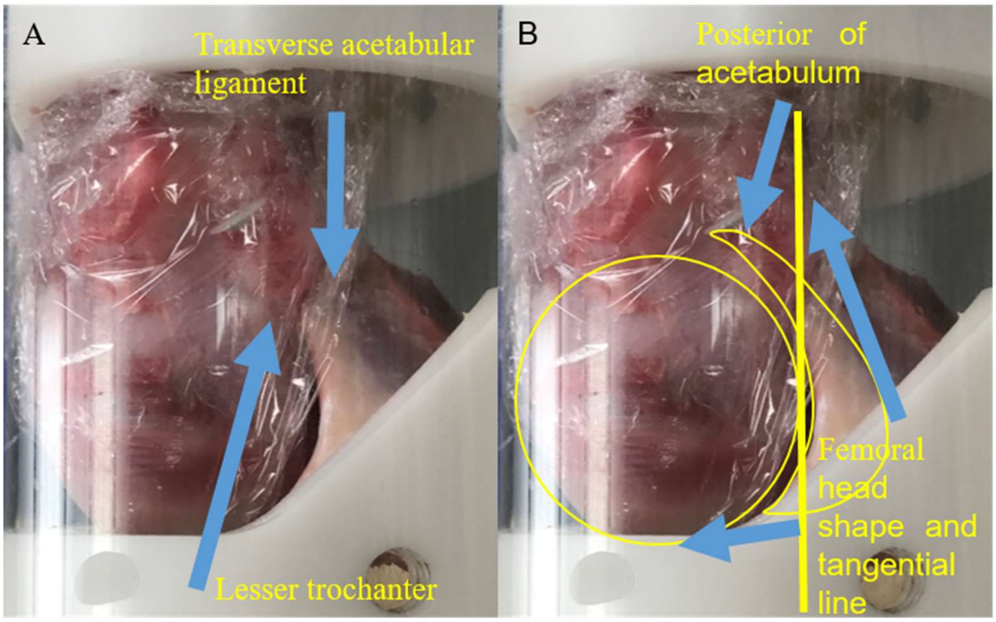

**Figure 4.59 Relative position of acetabulum and femur. A - Unnecessary contact between lesser trochanter and TAL. B - Femoral head being blocked by acetabular socket vertically.**

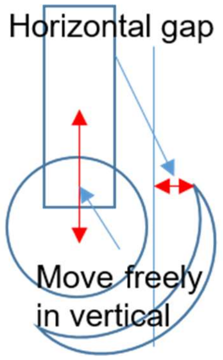

**Figure 4.60 Ideal position of femur and acetabulum that allows free movement in vertical.**

Load relaxation was observed when applying constant displacement through the femur. The load reading was at 212N on average before CT scan and dropped to 171 N after CT scan. Hence there were small movement in the tissues during the scanning process. This could lead to error in analysing soft tissue behaviour based on image data. The effect of load relaxation could be improved by either reducing scan time or applying constant force to the acetabulum.

The third scan was taken after the sample had been loaded once and aimed to investigate the circumferential effect of the labrum. However, the differences between soft tissues been loaded and reloaded were unclear. The tissues were stored in the fridge, sprayed with PBS solution, overnight after the second scan. The labrum may be compressed down (Figure 4.61) and stayed below the original position (Figure 4.62). The tissue behaviour between loading and reloading is worth investigating in order to have better understanding on the tissue recovery.

The labrum cut was created close to the contact region which is at the superior-anterior of the acetabulum due to clinical observation of labrum damage. The other anatomical reason was that, the porcine acetabular rim felt hard on the anterior portion and felt soft on the posterior portion, which indicated that there was sufficient labrum content on the posterior portion compared to the anterior portion.

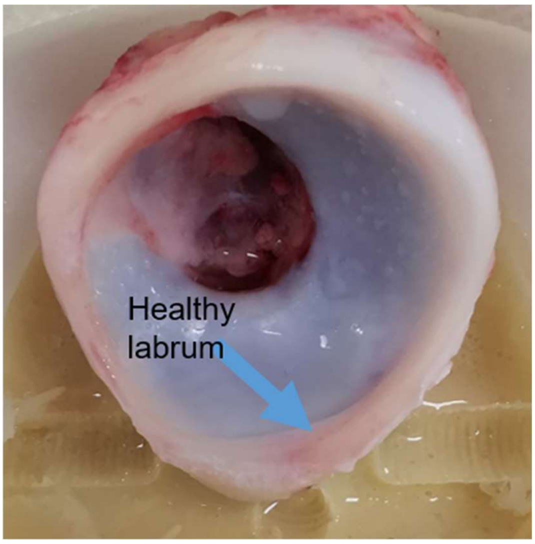

Figure 4.61 Healthy acetabular labrum before loading.

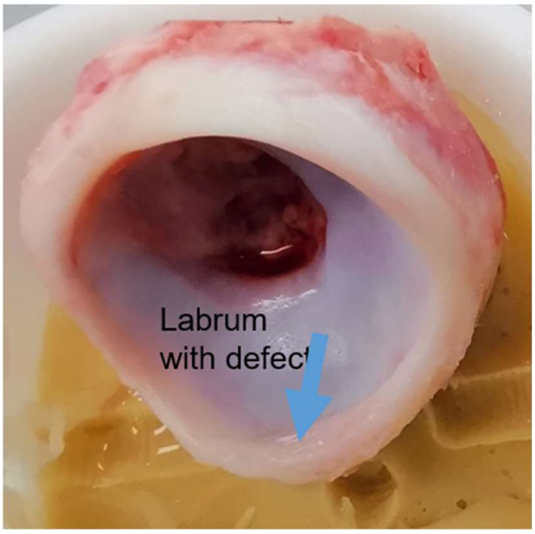

Figure 4.62 Labrum with defect after loading and recovering overnight. The highlighted region was flattened due to previous load. The labral rim cross-section was at a triangular shape before load. The rim cross-section then became trapezoidal and was hard to recover to the original shape after load.

The image resolution was down-sampled from 82 μm to 100 μm, balancing the computational cost of the image processing with the measurement accuracy. Any measurement based on CT images would then have an error of ± 0.1 mm. The subtraction of acetabulum bone before and during load can be found in Figure 4.63. Masks visible after subtraction on the screen indicated the volume of bone that were not perfectly registered. Although acetabulum bone was treated as a rigid component, the bone was still a piece of elastic tissue.

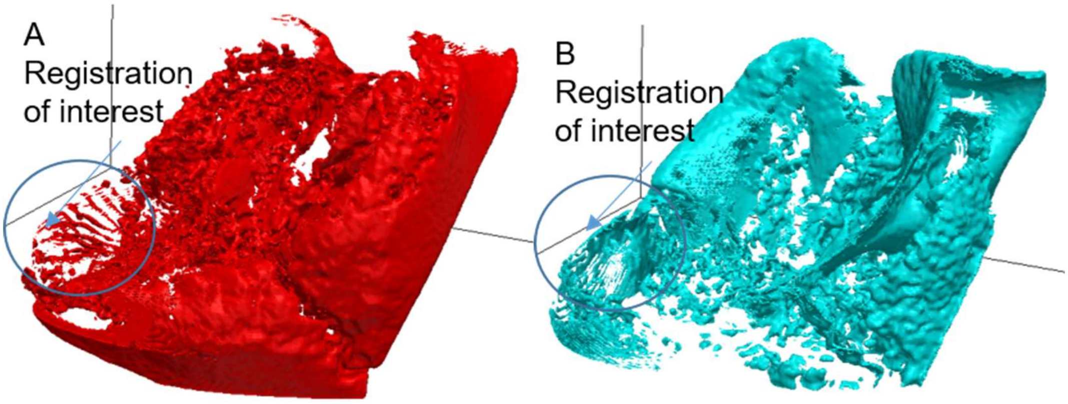

**Figure 4.63 Residual bone tissues during registration. A – Residual bone tissue before load; B – Residual bone tissues under load.**

The established experimental methodology is capable of targeting the focused compressive load at the superior-anterior portion of the acetabulum. The concentrated load aimed to replicate the loading conditions relating to cam-type FAI. However, the load was in axial direction and femoral rotation was not included. The existing methods can be used for investigation of tissue behaviour at specific portion on the acetabulum during axial loading. The combined CT-scan and image processing provided quantification of soft tissue movement, which are cartilage strain and labrum apex displacement in particular. The quantification methods can be used for further investigation of *in situ* tissue behaviour under static load. However, dynamic loading monitoring is not applicable under this protocol due to the time required by the CT scan session. The methods can be used to better understand the short term *in situ* tissue behaviour under specific pathologic loading, rather than investigating the long term effect under such load.

### 4.5.2 Experiment results

Overall cartilage strain was measured as the percentage change in cartilage thickness in the 2D image slice that bisects the acetabulum at the focused contact region. Cartilage thickness was measured from the same set of point on the subchondral bone surface, to the outer cartilage surface in the two cases for each sample. The superior portion (ilium) of the acetabulum had a rough surface which is observed in both 3D view and 2D slice. The set of starting point was difficult to be located, which resulted in unstable thickness/strain measured in the image slice. Considering the error in acetabular bone registration, the set of starting point may be shifted out-of-plane between unloaded and loaded acetabulum. Variation in cartilage thickness was noticed as the cartilage became thinner towards the fossa. The error from image resolution and inconsistent starting point was taking more account of the cartilage thickness close to the fossa. Therefore only the cartilage thickness at 0 – 8 mm from the cartilage-labral junction were considered as a reliable length of measurement.

The labrum apex displacement was measured by reconstructing the apex cloud point before and during load. The effect of labrum cut was also investigated. The change in labrum apex shape during load has shown the role of load support of the labrum (Henak et al., 2011) in this particular loading condition. The extent of labrum apex displacement was assessed and has increased by a factor of 1.4 ± 0.3 due to labrum cut. The increased labrum deformation demonstrated the *in situ* circumferential tension of the acetabular labrum.

A robust quantitative methods was established to assess the reliability of the acetabular bone registration. The thickness error in the bone masks difference ranged from 0.04 mm to 0.1 mm, which is just below the image resolution. The bone registration was generally successful under the limitation of image resolution. The differences in bone masks before and during load was considered in the film shape. Therefore the surface area of one side was calculated as half of the total surface area. The thickness error was then calculated by dividing the mask volume by the surface area on one side. The estimation would underestimate the thickness error if the thickness within the bone mask was actually high. In addition, the bone registration did not seem perfect in visualised 3D view. The main sources of error are illustrated in Figure 4.64. Firstly, as in

PH12 and PH14, there were percentage differences of tissue volume before and during load between 6% and 22%. In order to reduce computational cost, the tissue sample before and during load were segmented separately, and brought together after appropriate cropping process. The tissue may lose some of the volume during the cropping and result in an underestimated un-registered volume of the tissue sample. Consequently, the tissue sample in one particular case (Figure 4.64-A) may have extra volume and result in higher percentage volumetric error. Secondly, the error in tissue volume could come from inconsistent use of reference points and poor registration at the upper surface of the contact region (Figure 4.64-B). Finally, the error could be caused by misalignment of ischium and pubis ((Figure 4.64-C). This may due to:1) rotational mis-registration of the ilium; or 2) deformation of the growth plates.

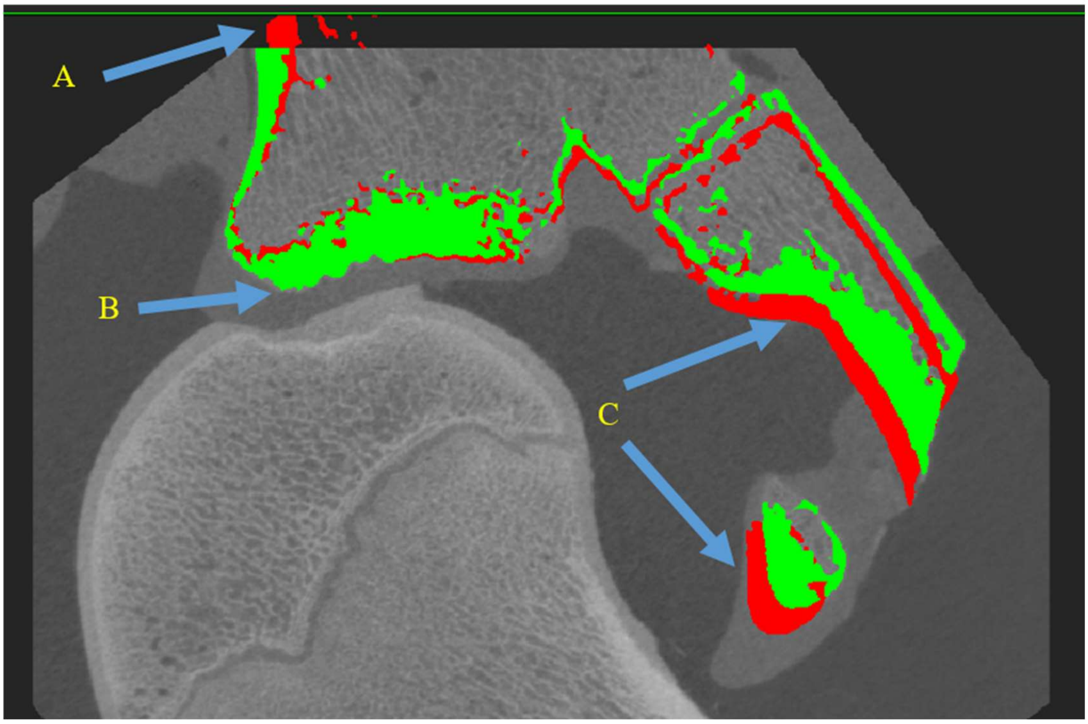

**Figure 4.64 Selected 2D plane at the centre of contact region for PH14 in cut case. Red mask, tissue before load; green mask, tissue under load. A, extra volume on the unloaded tissue; B, region of interest in the registration process; C, misalignment of acetabular bony parts far from contact region.**

Large labrum apex displacement occurred at the superior region, which coincided with the targeted contact region. From the anatomy perspective, more soft tissues content were observed at the superior-posterior region than at the superior-anterior region. This may result in the fact that the labrum apex was more likely to deform at the superior-posterior region than in the superior-anterior region, throughout the six samples. In addition, the femur has an ellipsoid-shaped head instead of a perfect sphere. This may cause the offset between focused contact region and the location of peak labrum displacement.

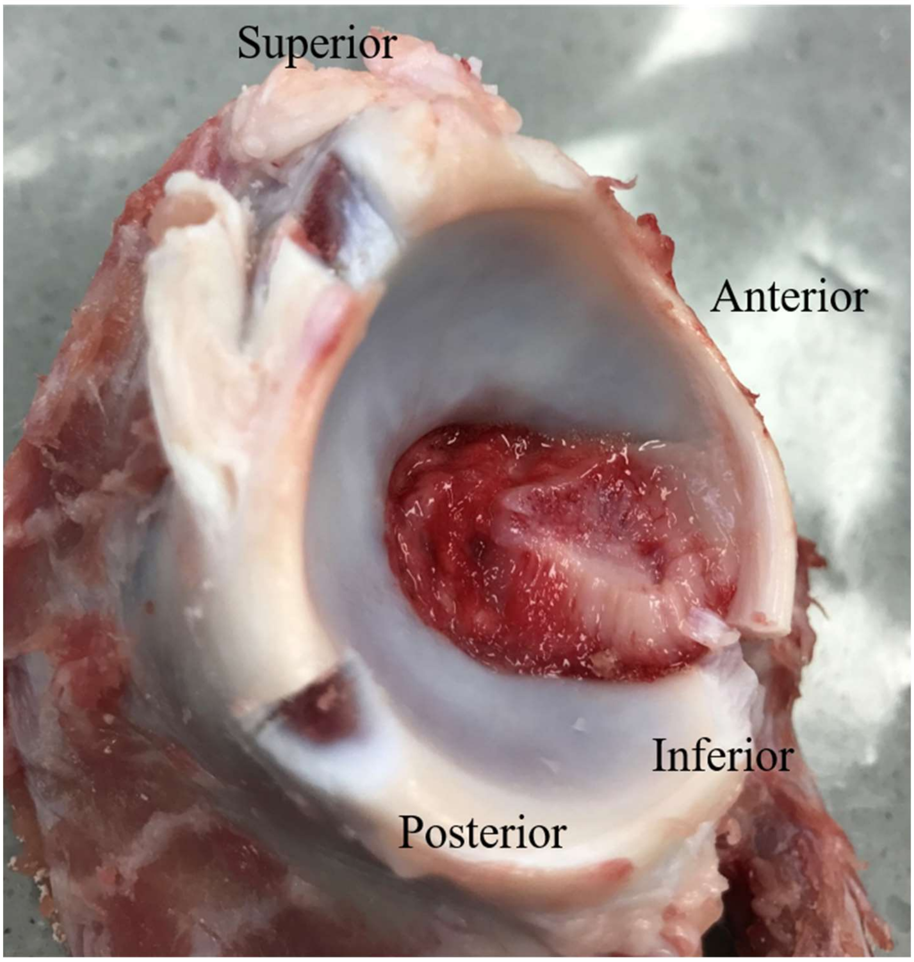

**Figure 4.65 Cross-section of the acetabular rim, demonstrating the content of soft tissues (white) around the rim.**

PH14 was a special case throughout the study where the femoral head displaced into the acetabular rim. The overall displacement was high while the reaction force remained low. The focused contact region was at the bone support on the acetabulum. Therefore the acetabular cartilage did not deform as much as in other samples. The labrum apex was compressed rather than been pushed away from the socket.

The displacement of the acetabulum pot was applied through the rig screw at a steady rate of 0.98±0.03 mm per full turn under the loaded case. However, the rate of displacement transfer was 1.01±0.19 mm per full turn under the cut case, which implied the potential assembly error within the CT loading rig.

The peak load reached as high as 1000 N when displacement was being applied. After relaxation and scanning, the tissue started to wobble in the cement, and the fixation of cement was therefore not as rigid as before the load was created. More displacement may be applied due to cover the gap between tissue and cement surfaces before the contact was established. Alternatively, less displacement may be applied due to unexpected hard contact because of the tissue falling out from the cement.

There was no big difference in percentage load drop and effective load per unit displacement between loaded and cut case for each individual sample, except PH14 which is discussed along with the actual contact region later in this section.

There was a load drop of 20.3±3.6% during scanning which may cause small tissue movement in the rig during CT scan. The level of tissue movement is hard to be detected and therefore hard to eliminate. The measurement error caused by load drop during scan can be improved by either allowing longer period of relaxation time or shortening the scan time. Dynamic bony motion can be produced under 4D CT with resolution at 0.234 mm in plane and 0.4 mm in thickness, although the resolution is still low for investigation of soft tissue behaviour (Kakar et al., 2016). The tissues were allowed enough recovery time of approximately 16 hours (1700 to next day 0900) so that the level of load drop and effect load per unit displacement had no big difference when tissues were being loaded for the second time. The bond between cement and tissues started to break after the first load due to high magnitude and long period of load experienced on the acetabulum. The fixation of cement can be strengthened by either allowing more bone support to be involved or using advanced dissection to create physical block in the direction of tissue potential movement.

The actual contact region on the acetabular cartilage surface was found at the superior-anterior portion of the acetabulum socket in all six samples. The contact patches on the articular cartilage showed the consistency in the alignment methods regarding the acetabulum socket. The actual contact region on the acetabular labrum was found at the superior-anterior region in three out of six samples, while the rest showed the actual contact region at the superior-posterior region. The actual contact regions on the femoral cartilage was found at similar region, and close to the ligament of the head of femur. The overall actual contact region was therefore influenced by the orientation of the femoral head due to the oval shape.

The labrum cut site was chosen at the posterior region of the acetabulum, close to the actual contact patch. No visual difference was observed in the actual contact region before and after cuts. However there was an increase in the labrum apex displacement in the cut case. The labrum cut coefficient defined the ratio between labrum maximum displacement before and after labrum cut. The lcc was found to be 1.4±0.3 for all porcine hip samples. The reaction force of the whole system was involved in the calculation. Hence the consistency of the loading scenario, direction of the femoral head movement and targeted contact region, were important for the two cases for each sample. The location where peak labrum displacement occurred shifted towards the centre of contact region in 5 out of 6 samples. This change in the labrum apex deformation demonstrated the circumferential stress in the porcine labrum. The effect is expected to be more influential in human body since the human labrum has a wider coverage on the acetabulum than the porcine labrum does.

The acetabulum registration calibrated the two acetabular bones, before and under load, together for investigation of the soft tissue behaviour under load. Both acetabulum mask appeared on the top surface after registration, which indicated a close match between the two subchondral bone surfaces. The image resolution and manual operation were still two sources of error. The tissue started wobble in the cement, as mentioned earlier, may also cause rotational error in the bone registration. The evidence of growth plate has been illustrated in chapter 3 and implied in section 4.4.3.1. The deformation of growth plate under high load may cause change in the relative position among ischium, ilium and pubis, which made it difficult to establish good match between the acetabular bone in the registration process.

Focused contact region was achieved by dilating the loaded tissue by 15, 12, 15, 15, 15, and 5 pixels for sample PH10 to PH15 respectively. The value of dilation gave an idea of the depth the soft tissue surface being compressed. The centre of focused contact region was defined at the midpoint of the cartilage labrum junction in contact. However when the focused contact region on labrum had an offset to that on cartilage, in PH10, PH12 and PH15, the centre of focused contact region was defined in the middle of the cartilage in contact. The selection of the centred slice tended to be at the same location for each sample. The location of centred slice was however not consistent on individual sample since the acetabulum was registered and segmented independently for the loaded and the cut case. A final crop of acetabulum under both cases can be performed to ensure the acetabulum was oriented and placed in identical position for each sample under both cases.

# Chapter 5

# Computational study of acetabular soft tissue behaviour under various cartilage-labral junction conditions

## 5.1 Introduction

This chapter reports the development of finite element (FE) models based on the porcine tissue samples used in Chapter 4. Specimen-specific FE models can be constructed from scanned images (Pawaskar et al., 2011; Hua et al., 2015) for modelling purposes, keeping most of the subject-specific features in the individual sample. However, simplifications may be applied to help the models proceed while losing some of the subject-specific features. Ferguson et al. (2000) developed axisymmetric human hip model via 2D sketch, with uniform cartilage layers and symmetric labrum sealing the joint. In this chapter, the porcine hip models were developed through a semi-subject-specific approach.

In this work the focus was on the soft tissues involved in cam impingement, which were represented explicitly, while the bone tissue was eliminated from the main model and represented as rigid boundary conditions. A parameterised approach was taken to geometry capture, meaning that the subject-specific geometric features could be generated in a semi-automated manner, but some precision of feature capture was lost. An additional advantage of a parameterised model is the ability to quickly run sensitivity tests on specific geometric features. The FE models are simplified to two-dimension (2D), which improved the model stability when solving complex contact problems with components experiencing large strains and rapid changes in geometrical features. The 2D model also balanced the ability to finely describe the tissues at junction, with model computational cost.

In this part of the work, the number of samples was reduced from six porcine hips, for the experimental study, to two porcine hips, for the computational study. The other four porcine hips were not applicable for this finite element analysis due to inappropriate contact region (see Section 5.2.1). The models outputs of the two remaining samples were compared to the respective tissue samples in terms of the subject-specific geometry and the two measurable outputs from the experiment, overall acetabular cartilage strain and labrum apex displacement. The tensile strain on the cartilage surface and the contact force on the soft tissue surface were also investigated, as a way to assess the acetabular soft tissue behaviour (see rationale in Section 5.2.4).

Considering the manual aspect of the sample alignment and the practical variation in loading the hip in the CT, the femoral head position was investigated regarding its effects on the outputs of interest. To verify the simplification made to the bone tissues, alternative model settings were applied to acetabular subchondral bone surface. Labrum material properties and cartilage-labral junction location were also investigated due to the nature of the hip anatomy (see justification in section 5.2.4).

The aims of this chapter were to:

1. Develop and verify the FE models of sample PH10 and PH12, acetabulum geometry generated based on CT images (Figure 5.1).
2. Validate the acetabulum geometry by comparing the unloaded acetabular cartilage thickness from FE models and from the experiment
3. Compare the resulting cartilage strain and labrum displacement from both experiment samples and computational models.
4. Investigate the subchondral surface boundary conditions, understand the modelling techniques in representing the subchondral bone surface
5. Investigate the effect of femoral head position to the acetabulum, understanding the error from experiment setup as well as the importance of femoroacetabular conformity in clinic
6. Investigate the effect of ratio of labrum and cartilage Young’s modulus, understanding the sensitivity of labrum material properties as well as the impact of tissue degenerated in clinic
7. Investigate the effect of cartilage-labral junction location in the acetabulum, understanding the sensitivity of the junction representation in the FE model.

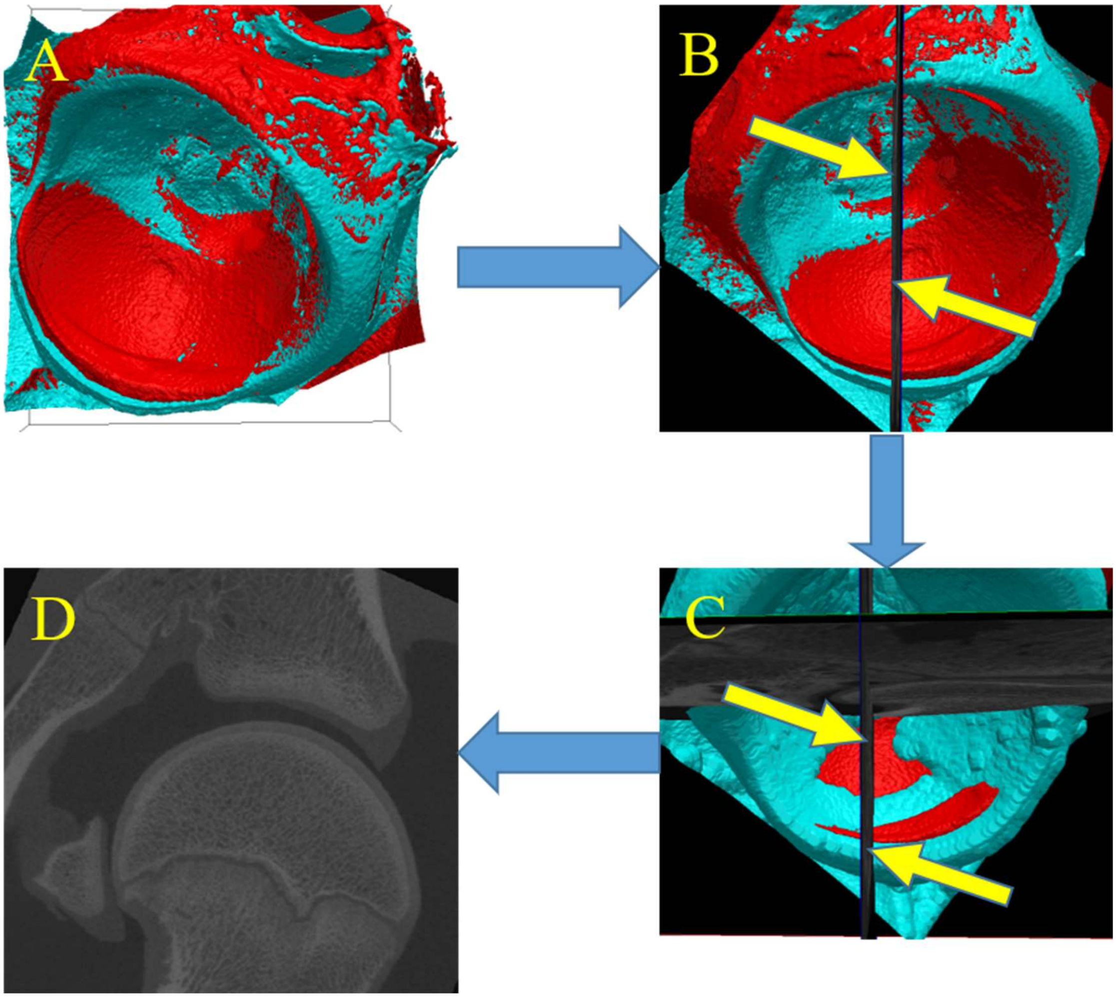

**Figure 5.1 Flow chart of image processing from ScanIP masks to Abaqus geometry. A, Segmented and registered acetabulum before and during load under experimental orientation, the femur was hidden for better visualisation of contact region; B, Acetabulum orientated to align the “centre of acetabulum to centre of contact patch” along with one of the main axis; C, Loaded tissue, in blue, dilated to narrow down the concentrated contact patch; D, The segmented 2D slice taken from ScanIP highlighted in yellow arrows for Abaqus geometry development.**

The computer used throughout this work packed an Intel 2.6GHz Xeon 4112 CPU and 32GB of RAM. All of the FE models in this research were developed, meshed and analysed in ABAQUS 2017 (Dassault Systèmes Simulia Corp., Johnston, RI, USA). The geometry sketches of acetabulum and femur were obtained in Solidworks 2018 (Dassault Systèmes, Vérlizy-Villacoublay, France).

## 5.2 Methods

### 5.2.1 Introduction

The aim of the work in this section was to develop the methodology for the computational study. The methods covered the following aspects:

1. FE models development: semi-subject-specific geometry; material properties; interactions; constraints; and justification of outputs of interest.
2. Model verification and validation: meshing strategy; selection of element type and justification of element size; effect of boundary condition simplification on the acetabular subchondral surface; quantification of measurement errors in the model, and comparison with experimental results.
3. Sensitivity studies of the model to investigate the effect of selected parameters: femoral head position; labrum Young's modulus; and cartilage-labral junction location in the model.

The number of porcine samples studied was reduced to two, PH10 and PH12, in the finite element analysis (FEA). The criteria for sample selection referred to the focused contact region and the labrum overhang (Figure 5.2). The 2D image slice in Figure 5.2-B was taken from the focused contact region in Figure 5.2-A. The labrum overhang formed a thick portion of soft tissue with sharp angle up to 90° as part of the acetabular contacting surface. In addition, Figure 5.2-B demonstrates the cross-sectional structure of the labrum overhang which showed a folded-up shape. The overhang tissue covers the acetabular edge while the gap was exaggerated for demonstration. The characteristic structure of the labrum overhang made the FE models difficult to complete (see Appendix F) and was out of scope for this study. The smoothness of the contact surfaces play a role in this type of surface-to-surface contact problem, particularly when isotropic elastic materials are assigned. The sharp angle on one of the contact surfaces, due to the tissue overhang, will lead to concentrated local contact pressure and cause the model to fail. Therefore, only PH10 and PH12 were chosen in the FEA since the labrum overhang were small on the CT images (Figure 5.3) for the two samples.

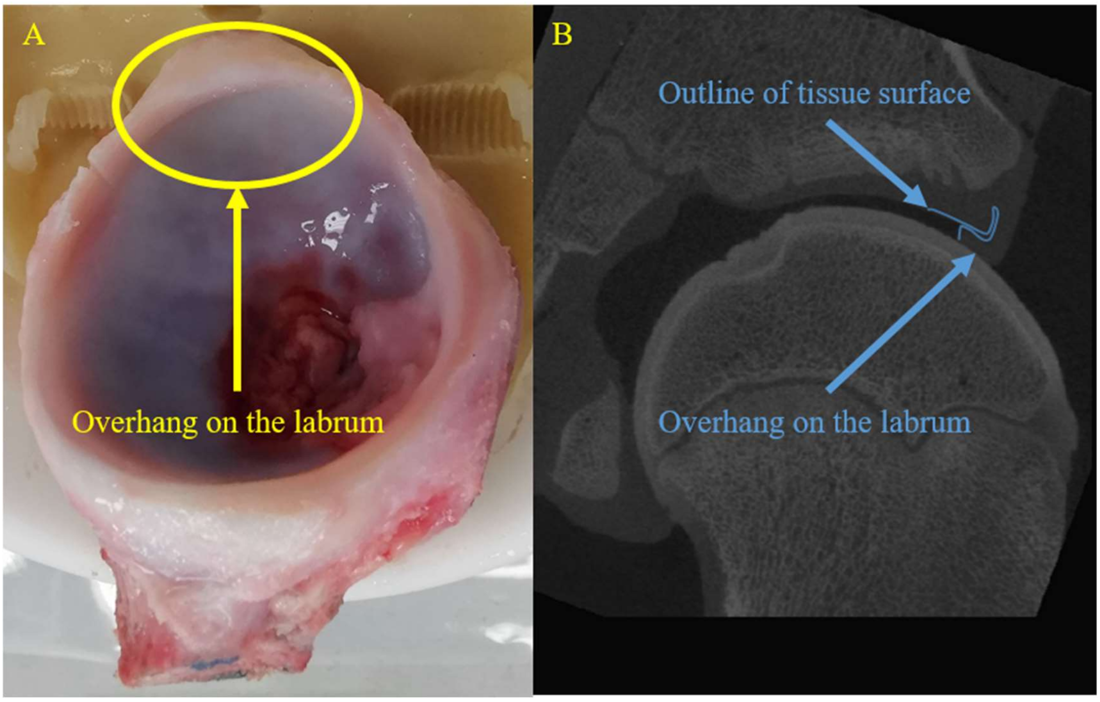

**Figure 5.2 Overhang tissue folded on the acetabular edge for sample PH11.**

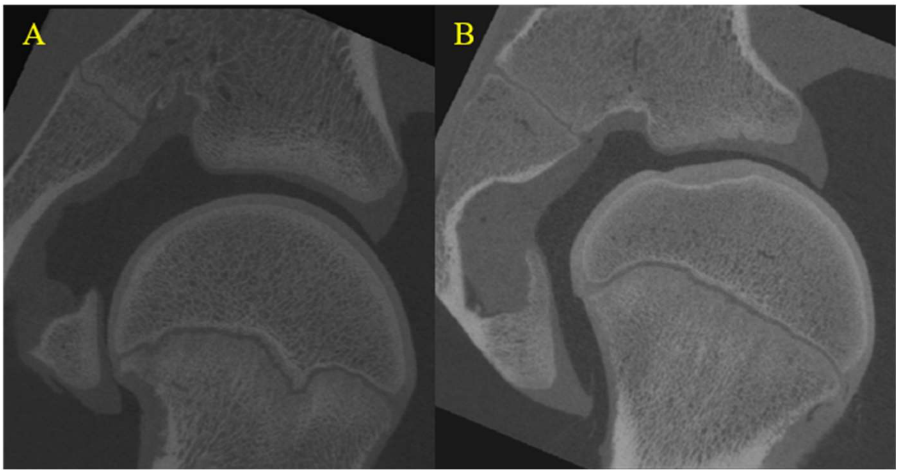

**Figure 5.3 Selected cross-sectional image slice for sample PH10 (A) and PH12 (B).**

### 5.2.2 Model geometry

The cross-sectional image slice was obtained at the centre of the focused contact region (see rationale in section 4.3.3.2) for PH10 and PH12 (Figure 5.4-Figure 5.5). Geometry of the porcine hip joint model was generated in 2D. The geometry was reconstructed from the CT image slice via a semi-subject-specific approach. Reference points (Figure 5.6) were manually selected at the characteristic geometrical features on each sample so as to form the shape of the FE models. The coordinates of the reference points have an error of ±0.1 mm since the image resolution in ScanIP was set to be 0.1 mm.

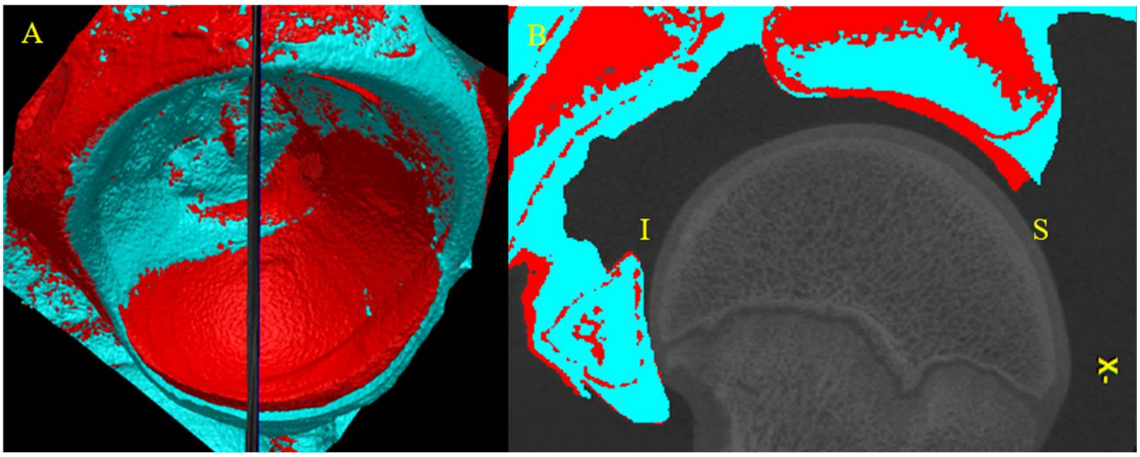

**Figure 5.4 Image slice selection for sample PH10; 3D view (A) and 2D slice (B). Blue mask, loaded tissue; red mask, unloaded tissue, also indicate the contact region.**

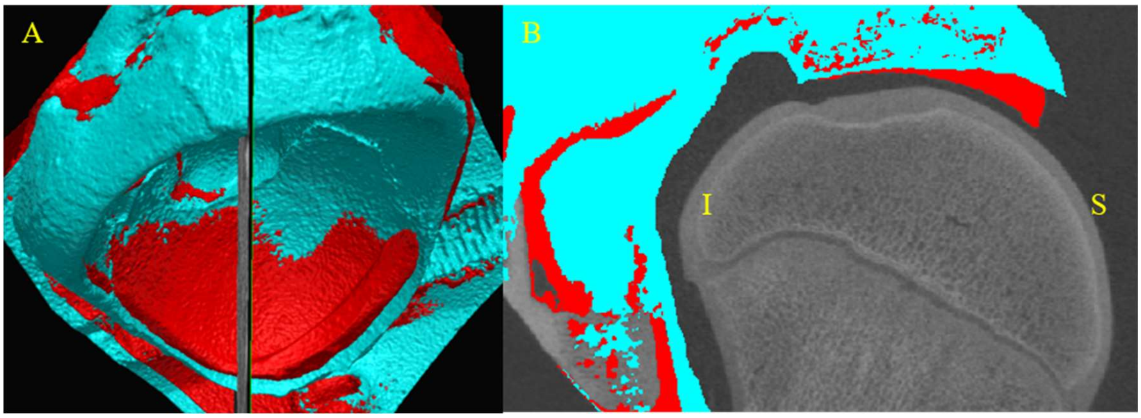

**Figure 5.5 image slice selection for sample PH12; 3D view (A) and 2D slice (B). Blue mask, loaded tissue; red mask, unloaded tissue, also indicate the contact region.**

The acetabular bone was considered as a rigid part. Therefore the acetabulum model consisted of the labrum, the cartilage, and the subchondral bone surface. The femoral bone was considered rigid as well. The femoral neck was not included since the contact only happened between cartilages and labrum according to the experimental loading scenario. The femoral part was therefore treated as portion of a ring, of which the width represents the femoral cartilage thickness. The geometry capture was done in SolidWorks 2018 (Dassault Systèmes, USA) and was illustrated in Figure 5.6 and Figure 5.7, followed by a list of porcine hip joint reference points presented in Table 5.1.

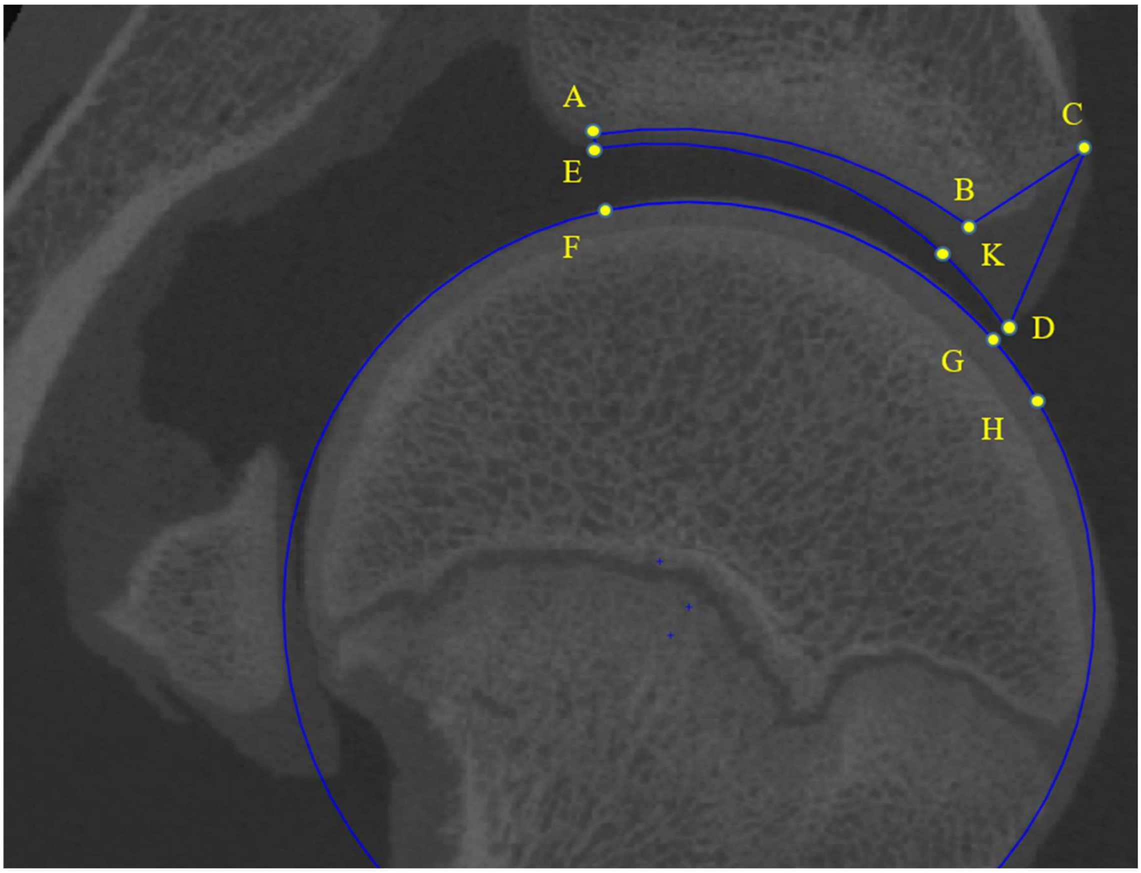

**Figure 5.6 Illustration of the nine structure points (A-H and K) which are manually identified for each sample in order to generate the semi-subject-specific model. Curves showed the surfaces generated for the model of sample PH10. Details listed in Table 5.1.**

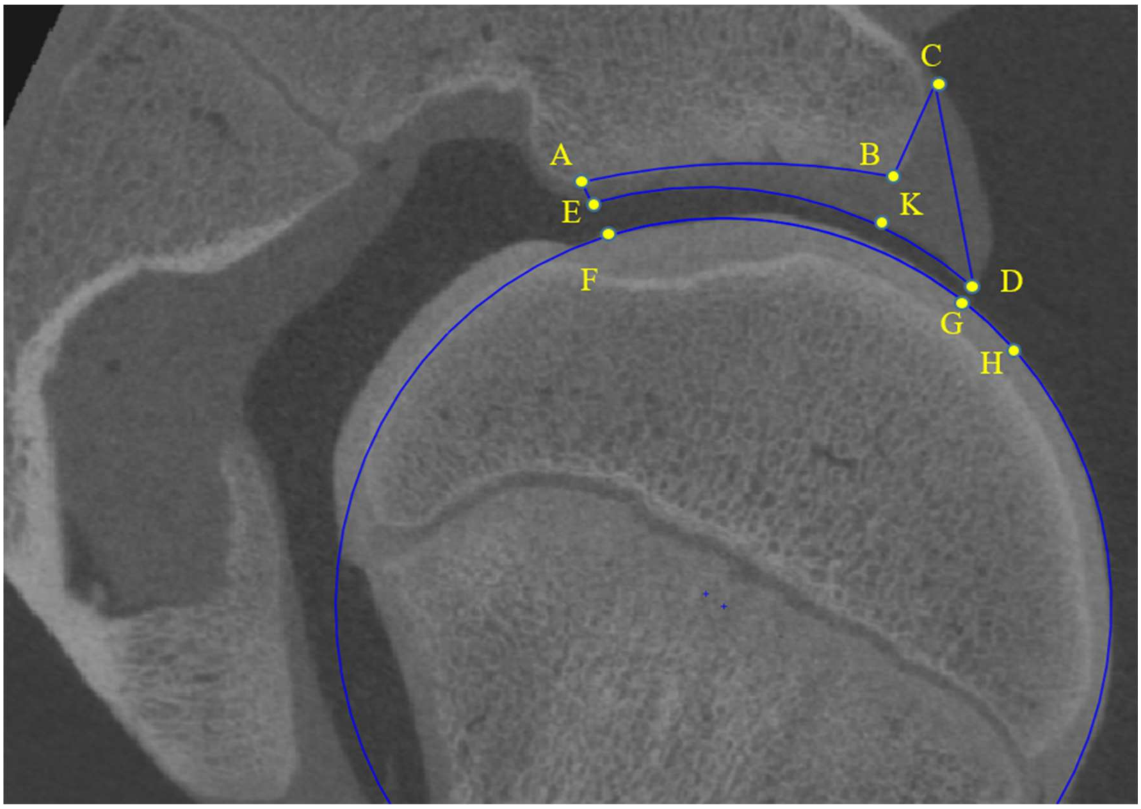

**Figure 5.7 PH12 Geometry development for sample PH12.**

**Table 5.1 List of geometrical reference points**

| Model part | Point | Description |
|---|---|---|
| Acetabulum | A | Internal subchondral bone end |
| | B | End of bony support |
| | C | End of labral integration into the bone |
| | D | External soft tissue end (Labrum apex) |
| | E | Internal soft tissue end |
| | K | Cartilage-labrum reference point (see section 5.2.3) |
| Femur | F | Internal femoral cartilage end |
| | G | Femoral cartilage contact site |
| | H | External femoral cartilage end |

The acetabular subchondral bone surface was formed by a best-fit-arc and a straight line: starting from the point at the fossa edge where acetabular cartilage stops following the curvature of the acetabular cup (A), to form a best-fit-arc at the cup upper edge (B), and connected to the point at the cup lower edge where acetabular labrum starts to grow (C). The soft tissue surface was formed by another best-fit-arc and two straight lines: starting from the point at the cup lower edge (C), connecting to the point at the apex defining the width and depth of the labrum (D), and to form a best-fit-arc at the fossa edge defining the curvature of the soft tissue upper layer (E). Once the two end points were defined on the cartilage surfaces, a third point was allocated near the centre of the cartilage in order to fit an arc onto the cartilage surface, so-called the best-fit-arc. Variation in acetabular cartilage thickness was captured by visually fitting two arcs to the subchondral and superficial surfaces individually. Post-processing of the geometry (Figure 5.8) was done in Abaqus 2017 (Dassault Systèmes, USA) by adding fillet of 0.2 mm at each corner on the soft tissue surfaces. A fillet of 3 mm was also added to the subchondral bone in order to smoothen the surface. Deviation between the cartilage thickness in the model and in the images was investigated and is presented in the results.

The femoral cartilage surface was formed by one point opposite to the edge of the acetabular fossa (F), one point at the contact site closest to the apex (G), and another point slightly beyond the contact site (H). Geometry of the femur was dominated by the shape around the femoral contact region in order to replicate the experimental contact conditions. The femoral head was treated as a perfect sphere with uniform cartilage thickness of 1.3 mm according to the measurement from the 2D image slice. The femoral subchondral bone was hence formed by the second arc on the head. Post-processing of the geometry (Figure 5.8) was again done in Abaqus 2017 by adding fillet of 0.2 mm at each corner on the cartilage surface.

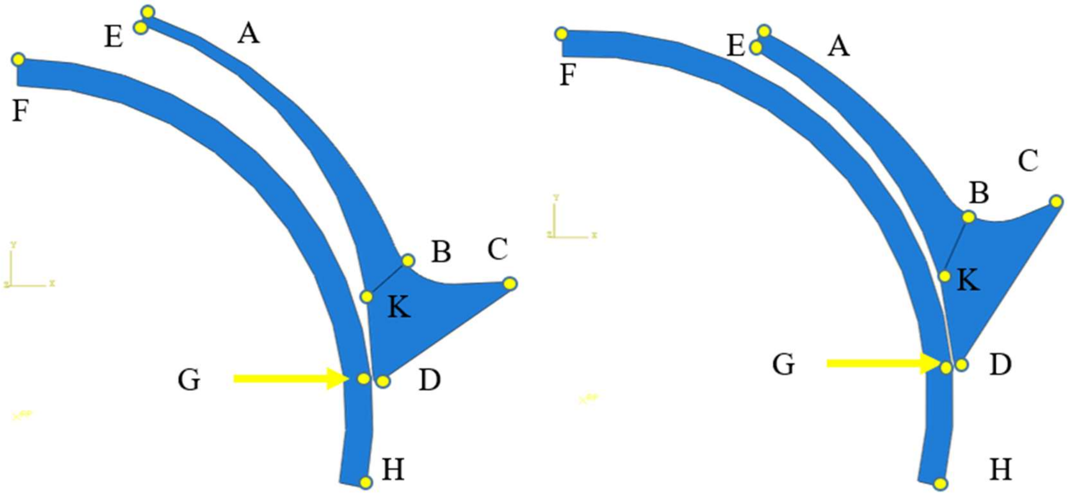

**Figure 5.8 FE models assembly of model PH10 (left) and PH12 (right).**

### 5.2.3 Model settings

The two models used identical settings, interactions, and boundary conditions. Therefore only data and figures from model PH10 is presented in the following methodology for demonstration.

The soft tissues were treated as isotropic elastic materials. The values assigned to the Young's modulus and Poisson's ratio of cartilage and labrum were adopted from a previous study (Jorge et al., 2014, see

Table 5.2). The acetabular soft tissue was separated into two material sections, for cartilage and labrum respectively, by creating partition from a straight-line. The partitioning line was drawn from the bone support edge (B) across the acetabular cartilage, and ended at the cartilage-labrum reference point (K, see Figure 5.8). Such angle of the line BK was selected in order to avoid sharp angle at the junction between cartilage, labrum, and bone for both cartilage and labrum model sections.

**Table 5.2 Material properties for cartilage and labrum (Jorge et al., 2014).**

| Tissue type | Young’s Modulus (MPa) | Poisson’s Ratio |
|---|---|---|
| Cartilage | 12 | 0.4 |
| Labrum | 20 | 0.4 |

Surface-to-surface contact was defined (Figure 5.9) between femoral cartilage outer surface and acetabular outer surface including both cartilage and labrum. Frictionless contact was assumed in the tangential direction. Hard contact was defined in the normal direction. Finite sliding was hence used in this contact to allow sliding between contacting surfaces.

The femoral subchondral bone surface movement was controlled by the femoral head centre at all planar degrees of freedom using a kinematic coupling. Consequently, the femoral bone was modelled as a rigid part.

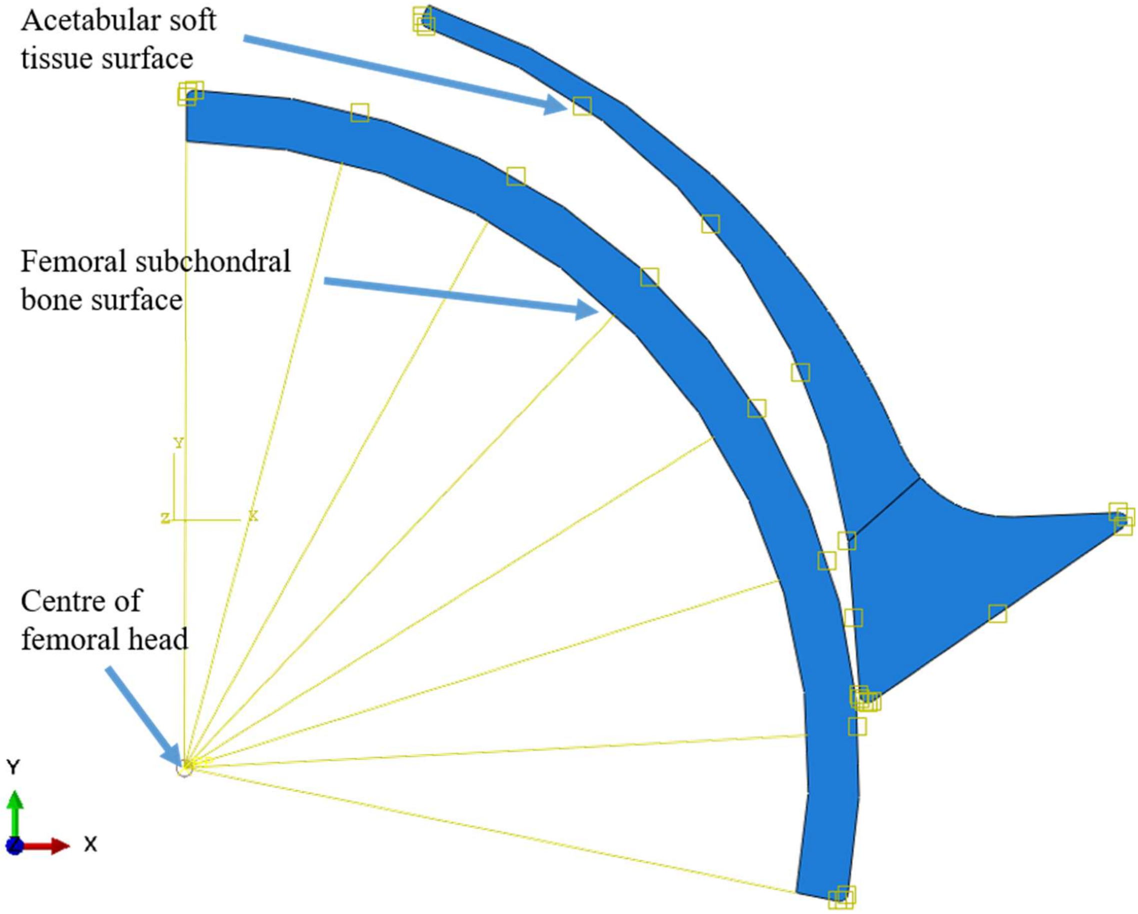

**Figure 5.9 Coupling constraint and contact interaction of model PH10. Yellow squared boxed defined surface-to-surface contact between the acetabular soft tissue and the femoral cartilage. Yellow straight lines defined the coupling constraint of the femoral subchondral bone with the femoral head centre.**

The acetabular subchondral bone surface was constrained at all degrees of freedom to remain fixed during the displacement steps. A small displacement of 0.1 mm was applied from the femoral head centre, in the same direction as measured in the CT scan, towards the acetabulum to initiate the surface contact. The second displacement step was a replication of the axial displacement in the experimental study where the previous small displacement was deactivated. Total displacement of 1.8 mm (1.5 mm in x and 1.0 mm in y) and 2.1 mm (1.7 mm in x and 1.1 mm in y) was applied to PH10 and PH12 respectively, replicating the femoral head movement measured in the scan.

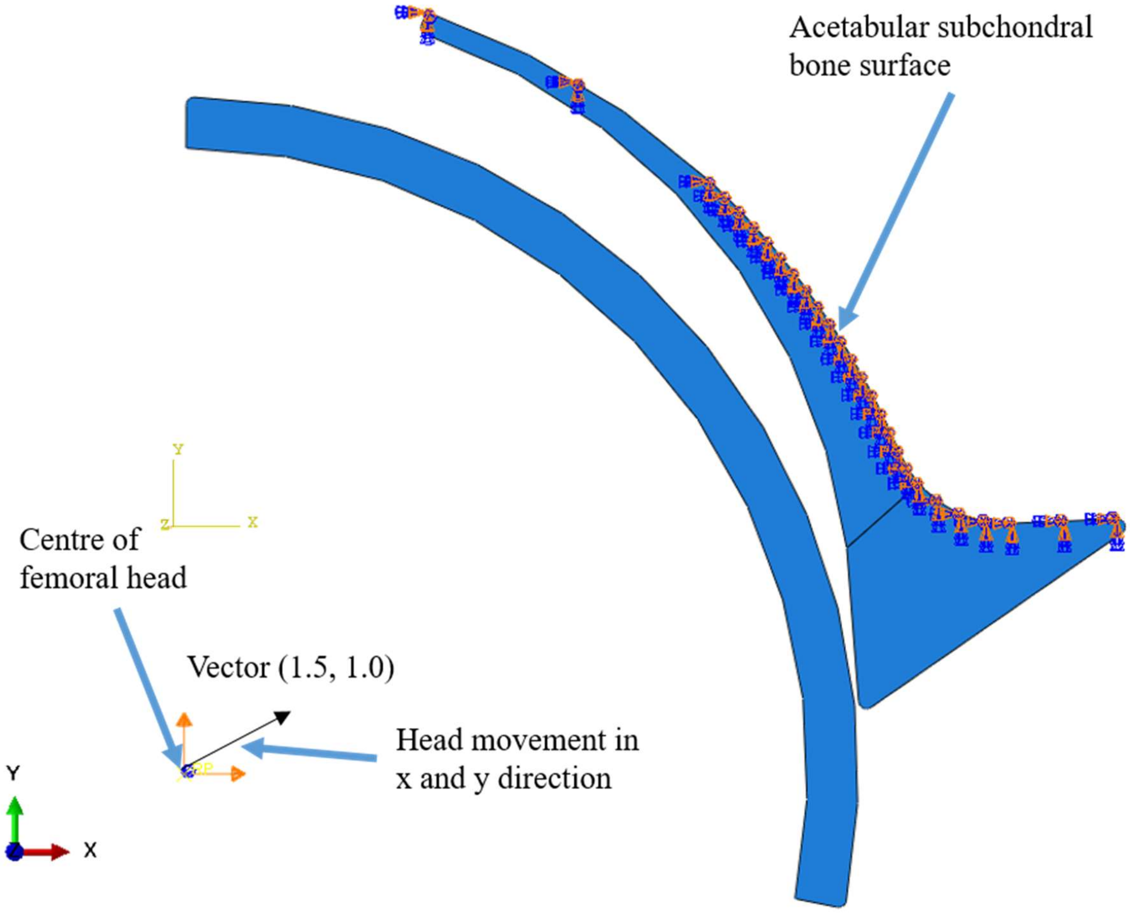

**Figure 5.10 Boundary conditions and displacement step of model PH10. Blue symbols with orange arrows defined the constraint on the acetabular subchondral bone surface. The yellow coordinate symbol with orange arrows indicated that displacement in x and y direction was assigned to the femoral head centre.**

### 5.2.4 Outputs of interest

To allow comparison with the experimental study, the overall acetabular cartilage strain and the labrum apex displacement were measured for each model. A set of points was selected on the acetabular subchondral surface (Figure 5.11). The points were treated as cartilage baseline points and used for cartilage thickness measurement. Hence the overall cartilage strain was always measured from a consistent location despite how much the cartilage superficial surface deforms. Points were selected on the other side of the cartilage along the line perpendicular to the tangential line at the baseline point (section 3.5.2.3). The location of each baseline points is again noted as “distance from cartilage-labral junction" as described in section 4.3.3.2. Larger the distance is recorded, closer the point is to the fossa. Overall cartilage strain was obtained as the percentage change in the thickness.

The apex point was highlighted (Figure 5.11) in the model geometry and used to extract the magnitude of apex displacement at the end of loading.

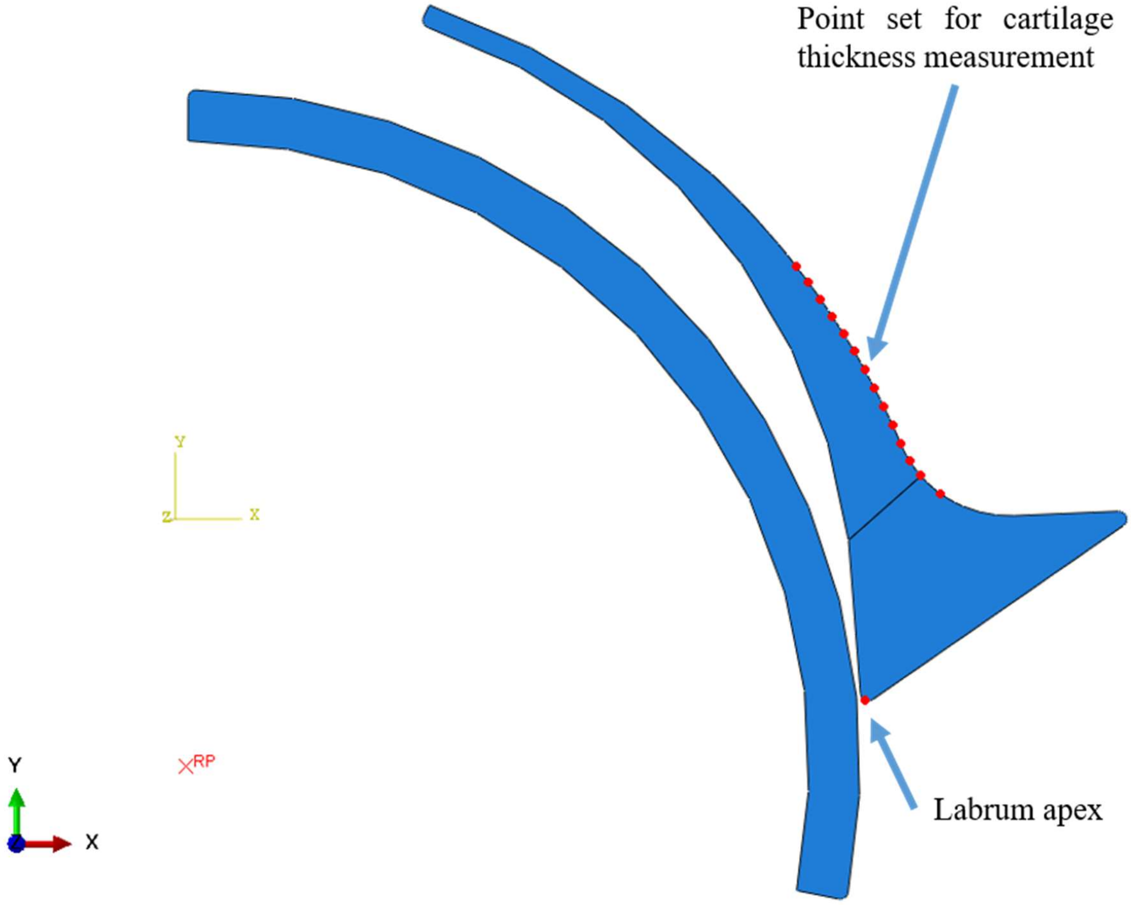

**Figure 5.11 Point set of model PH10 for cartilage thickness measurement and apex displacement monitoring.**

The total contact force was investigated on the acetabular cartilage surface and acetabular labrum surface individually. Comparison was made between the contact force and the experimental load reading, as part of the validation .The contact force was also used for assessing the load distribution in the acetabular soft tissues. The load undertaken by the acetabulum was measured as the total contact forces due to frictional stress and contact pressure in Abaqus. The load distribution between each tissue type can be also measured by the contact force on each material section separately.

Tensile strain was investigated in previous studies (Greaves et al., 2010) for assessing labrum damage in the hip. The tensile strain was recorded on the acetabular cartilage outer surface, and at the first five surface nodes next to the cartilage-labral junction. The junction was represented by a straight-line and thus provided an abrupt material property change at the partitioned region. The sudden change could lead to spurious strain concentration at the transition line. Averaged value was taken from the five data collected in order to obtain a general strain value near the junction.

### 5.2.5 Model verification and validation

#### 5.2.5.1 Meshing strategy

The FE models of the porcine hip joint was meshed in Abaqus 2017. Plane strain elements were assigned since the dimension of the cross-sectional view being modelled was smaller than the axis normal to the plane. The models were meshed with quadrilateral-dominated, standard linear elements, allowing unstructured grids at filleted corners.

The element size adopted was determined from the mesh sensitivity test on model PH10. The seed size varied from 0.14 mm to 0.035 mm (Figure 5.12). Plotted data points were highlighted at element size of 0.14 mm, 0.07 mm and 0.035 mm where the seed edges were halved. For each model with different element sizes, three outputs were investigated: 1) labrum apex displacement; 2) tensile strain on the cartilage superficial surface; and 3) total contact force on the acetabular side. The accuracy needed for labrum apex displacement would be no smaller than 0.01 mm, since the image resolution was 0.1 mm. The accuracy needed for cartilage strain would be no smaller than 0.4%, giving that the cartilage was 2.5 mm thick at the thickest portion.

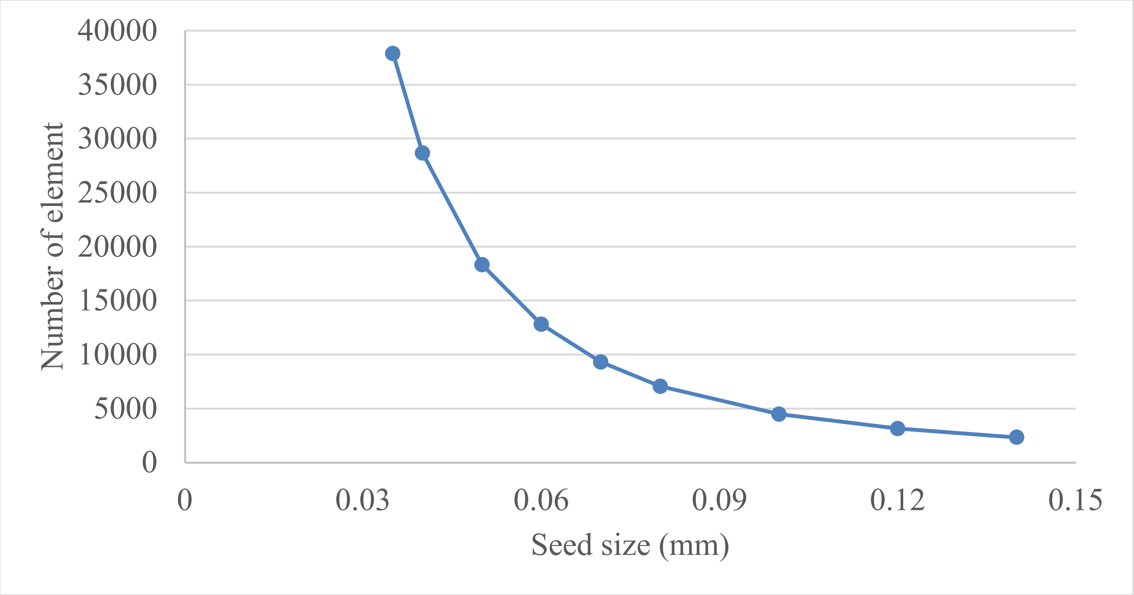

**Figure 5.12 Number of element under various seed sizes in model PH10.**

#### 5.2.5.2 Effect of subchondral bone constraint

The model only included a portion of the acetabular bone which is in the focused contact region for simplification. The subchondral bone surface was constrained in all degrees of freedom so that the bone remained rigid. However, due to the incomplete modelling of bone edge, the soft tissues were able to deform around the corner and wrap the bone edge, effectively penetrating through the bone surface, which is impossible in reality. An extended rigid plate was tied to the acetabular subchondral bone surface in order to correct the soft tissue behaviour around bone edges (Figure 5.13). Surface contact was defined between rigid bone plate and soft tissue edges. All degrees of freedom were constrained at the reference point on the bone plate instead of the subchondral bone surface. The edges of subchondral bone were relatively far from the region of interest, comparing to femoral cartilage or cartilage-labral junction. However, the shorter the bone is, the larger effect it would have on the results. The modification of subchondral bone was only performed and compared in PH12.

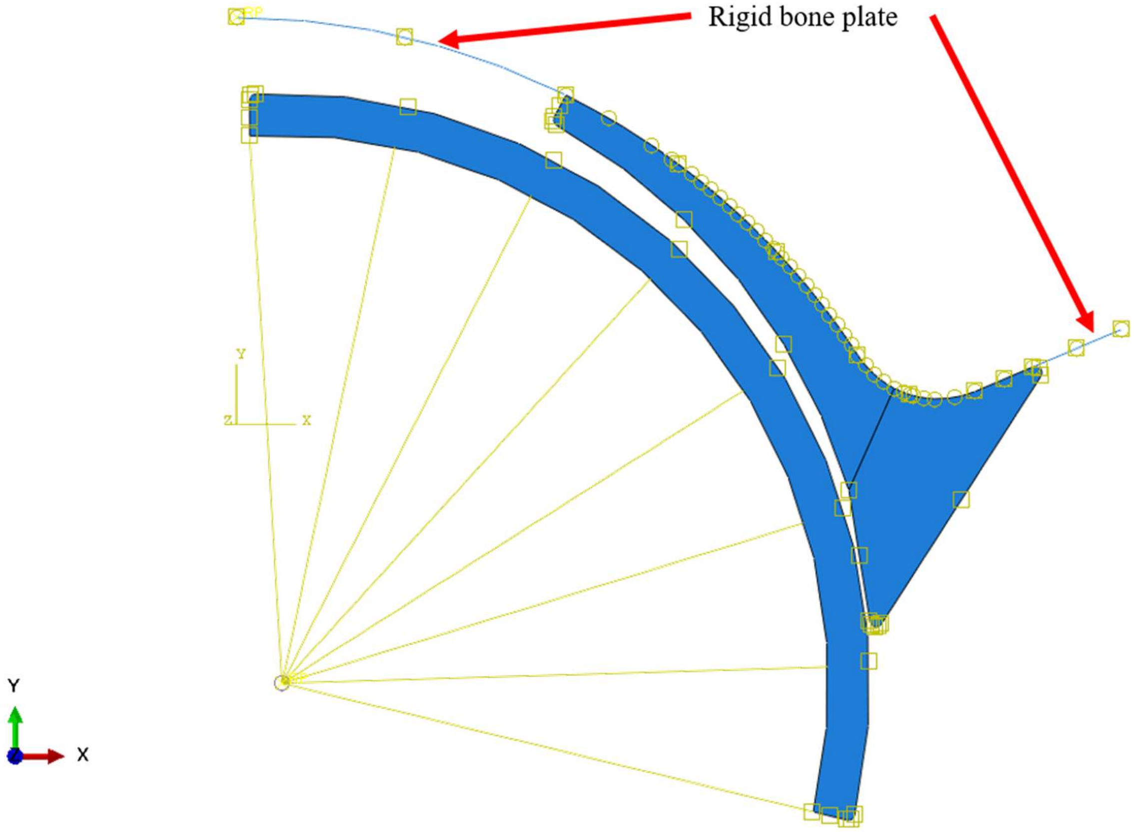

**Figure 5.13 Rigid subchondral bone plate in model PH12.**

### 5.2.5.3 Repeatability of cartilage thickness measurement

The acetabular cartilage thickness was measured for calculation of overall cartilage strain. The cartilage was composed of two arcs with different centre location and radius value, as mentioned in Section 5.2.2. The thickness measurement started from consistent point set (Section 5.2.4), and the end point was selected on the other side of the cartilage along the line perpendicular to the tangential line at the baseline point. The unloaded acetabular cartilage thickness were measured three times across the socket on PH10, in order to assess the accuracy in taking measurement from model assembly. The modelled cartilage thickness was then compared with the tissue cartilage thickness measured in CT images, for verification of the geometry capture in the FE models.

#### 5.2.5.4 Comparison with experimental results

Comparison was made on the overall cartilage strain achieved in the experiment and in the models, as part of the validation. Although the load progress was under displacement control, for both studies, the displacement applied in 2D model was derived and measured from 3D images. The model labrum apex displacement was compared with the maximum labrum displacement in the tissue. The model total contact force was compared with the load cell reading in the experiment, as a measurement of the reaction force in both studies.

### 5.2.6 Sensitivity studies

The following sensitivity studies were all carried out on both models; PH10 and PH12.

#### 5.2.6.1 Experimental femoral alignment

The femur and acetabulum were experimentally aligned by hand, as mentioned in Chapter 3, in order to replicate cam-related impingement loading. The femoral head position was shifted -1 mm (Figure 5.14-A) and +1 mm (Figure 5.14-C) normal to the direction of load which is equivalent to the axial direction of the femur pot. The effect of femoral head position was investigated in order to assess the manual aspect in experimental alignment.

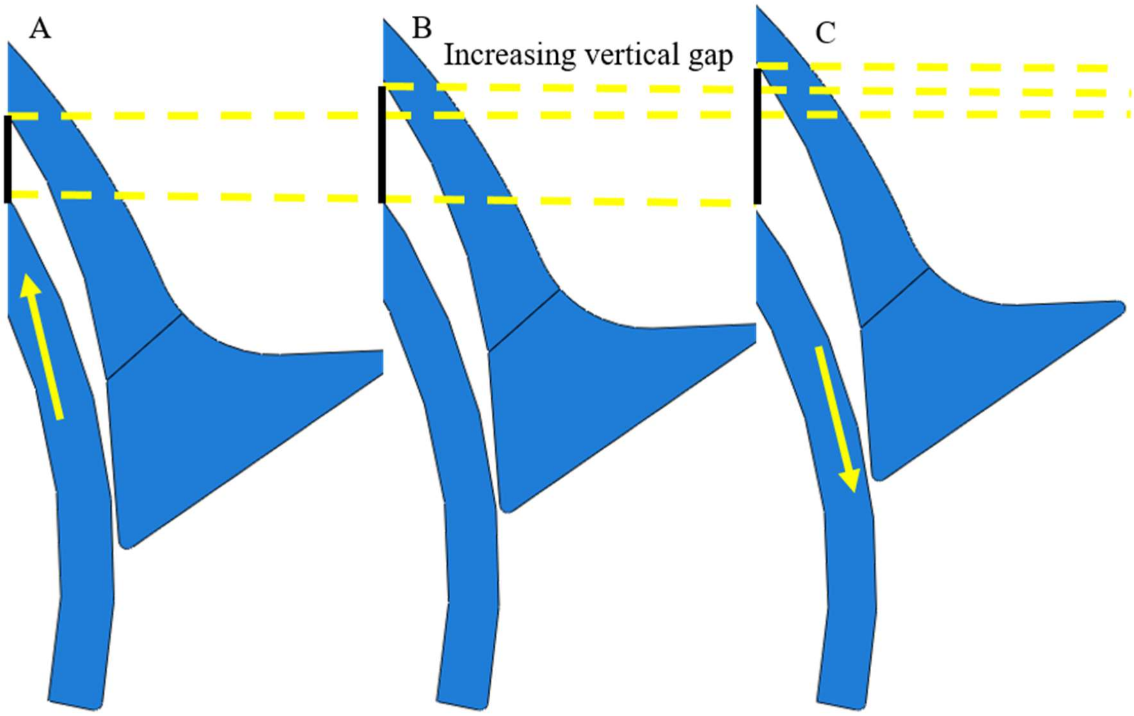

**Figure 5.14 Investigation of femoral head position. A, femoral head shifted by 1 mm towards the fossa; B, femoral head at neutral position; C, femoral head shifted by 1 mm towards the apex.**

#### 5.2.6.2 Parametric analysis

The Young's Modulus of labrum was varied from 12 MPa to 24MPa, resulting the ratio to cartilage property from 1:1 to 2:1 (Table 5.3). There are two reasons for investigating the effect of labrum material properties: 1) Lack of understanding of labrum property *in vitro*, sensitivity of labrum property adopted was worth investigating; and 2) variation of labrum condition in the hip, labrum property may differ depending on location (Ferguson et al., 2001), species (Ishiko et al.,. 2005), age (Horii et al., 2002), or health conditions (Greaves et al., 2010).

For similar reasons, the location of cartilage-labral junction was also modified in both models. The partitioning line was moved 1 mm and 2 mm towards the acetabulum edge, effectively reducing the labrum coverage and varying the location of junction (Figure 5.15). The range of labrum coverage in the three cases covers the variation from young porcine (junction closest to the fossa) to elderly human (junction closest to the cup edge).

**Table 5.3 Labrum material**

| Case | L12 | L16 | L20 (baseline) | L24 |
|---|---|---|---|---|
| Labrum Young's Modulus (MPa) | 12 | 16 | 20 | 24 |
| Ratio to cartilage (12MPa) | 1:1 | 1.3:1 | 1.7:1 | 2:1 |

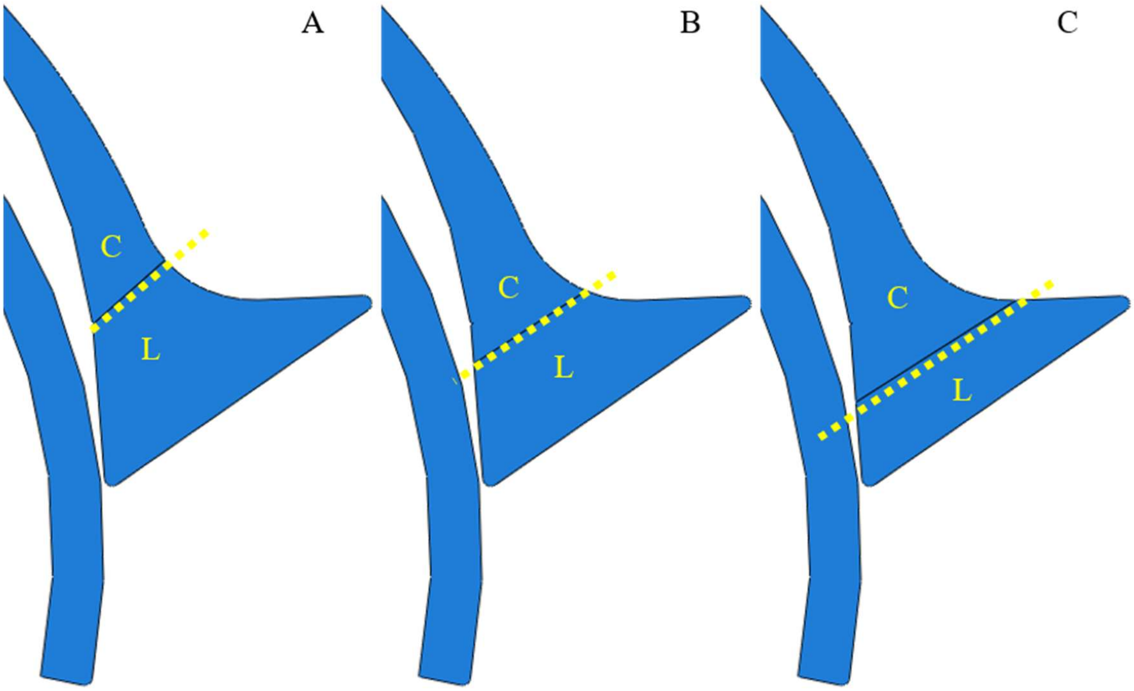

**Figure 5.15 Investigation of cartilage-labral junction location. C, cartilage material assigned; L, labrum material assigned.**

Summary of all the cases involved the sensitivity studies was listed in Table 5.4. The following outputs of interest were measured : 1) overall acetabular cartilage strain; 2) labrum apex displacement; 3)acetabulum contact force; and 4) cartilage tensile strain.

**Table 5.4 List of modelling cases in sensitivity studies**

| Parameter | Case code | Model | Description |
|---|---|---|---|
| Baseline | L20 | | Baseline model |
| Femoral head position | FHin | Both | Femoral head shifted -1 mm |
| | FHout | Both | Femoral head shifted +1 mm |
| Cartilage thickness | ThickR | PH10 | Repeated measurement for unloaded cartilage thickness |
| Bone boundaries | Rigid | PH12 | Rigid plate tied to acetabular subchondral bone surface |
| Labrum Young’s Modulus | L12 | Both | Labrum modulus 12 MPa |
| | L16 | Both | Labrum modulus 16 MPa |
| | L24 | Both | Labrum modulus 24 MPa |
| Cartilage-labral junction location | JKmid | Both | Location of cartilage-labral junction move 1 mm outwards |
| | JKout | Both | Location of cartilage-labral junction move 2 mm outwards |

## 5.3 Results

### 5.3.1 Introduction

This section presents the output measures of the FE models developed in section 5.2. The section covers results of the verification processes, a direct comparison with the experimental results, and the results from sensitivity studies. Overall cartilage strain was measured on a set of points across the socket noted as “distance from cartilage-labral junction” (Chapter 4). The distance measure starts just above the subchondral bone support. Larger the distance is recorded, closer the point is to the fossa.

For most of the cases for PH10, the models run to 100% of the applied displacement of 1.8 mm. Models PH10_L12 (labrum modulus at 12 MPa, proceeded to 98%) and PH10_FHin (femoral head shifted inwards, proceeded to 83%) aborted early due to high tensile strain at the cartilage-labral junction on the subchondral bone. The model PH12 did not proceed well due to: 1) better conformity which results in higher elastic strain; and 2) larger head displacement measured in scan. However, comparison between models was performed at the same level of completion of interest (e.g. PH10_FHin at 83%, therefore PH10_FHout being drawn back to 83% as well). A full list of model progress for each case can be found in Table 5.5. The average run time of one case is 30-35 minutes running on four parallel cores.

Measurement of overall cartilage strain and labrum apex displacement were compared between experimental and computational studies.

Measurement of overall cartilage strain, acetabulum contact force, and cartilage tensile strain were compared between FE models. The labrum displacement was neglected in the parametric study because the differences (0.02 mm) were smaller than image resolution (0.1 mm).

**Table 5.5 Model progress for each case each sample**

| Parameter | Case | Progress (%) | Case | Progress (%) |
|---|---|---|---|---|
| Baseline | PH10_L20 | 100 | PH12_L20 | 62 |
| Femoral head | PH10_FHin | 83 | PH12_FHin | 14 |
| | PH10_FHout | 100 | PH12_FHout | 84 |
| Labrum modulus | PH10_L12 | 98 | PH12_L12 | 61 |
| | PH10_L16 | 100 | PH12_L16 | 62 |
| | PH10_L24 | 100 | PH12_L24 | 62 |
| Cartilage-labral junction | PH10_JKin | 100 | PH12_JKin | 61 |
| | PH10_JKout | 100 | PH12_JKout | 61 |

### 5.3.2 Mesh convergence verification

The labrum apex displacement (Figure 5.16) varied from 2.08 mm to 2.10 mm with different mesh size. The range of the data set was 0.02 mm which accounts 0.96% of the smallest value. The displacement increased quickly, by 0.7%, from seed size of 0.14 mm (2.08 mm) to seed size of 0.07 mm (2.10 mm). Then the results increased slightly, by 0.16%, from seed size of 0.07 mm (2.098 mm) to seed size of 0.035 mm (2.102 mm). The decrease in rate of change showed the evidence of convergence.

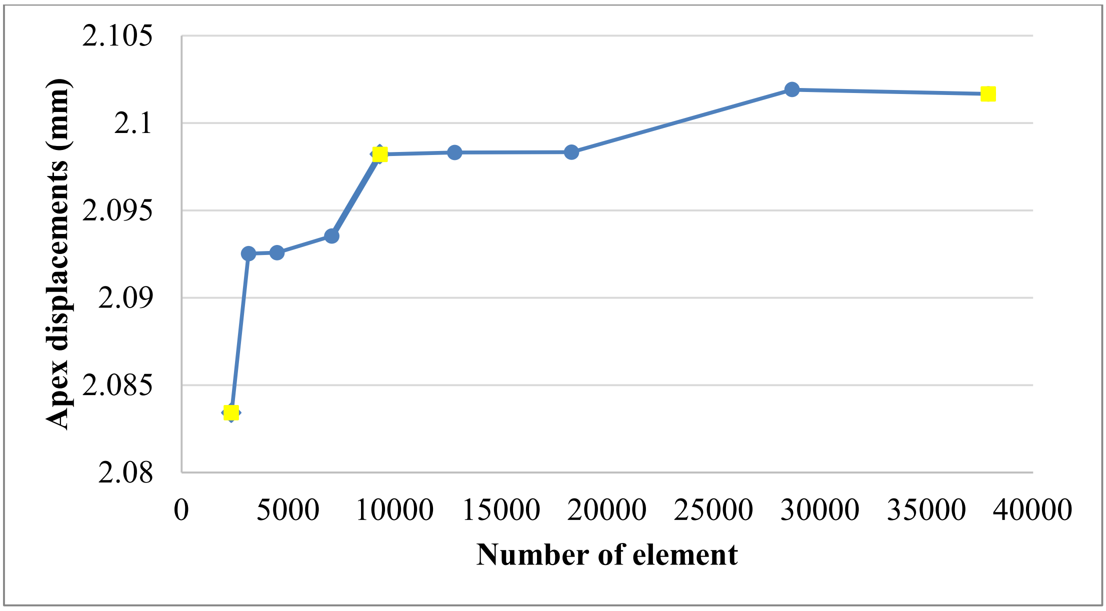

**Figure 5.16 Mesh sensitivity study on PH10 labrum apex displacement.**

The cartilage tensile strain (Figure 5.17) varied from 28.62% to 29.25%. The range of the data set was 0.63% which accounts for 2.2% of the smallest value. The strain increased quickly, by 2.2%, from seed size of 0.14 mm (28.62%) to seed size of 0.07 mm (29.25%). Then the results increased slightly, by 0.01%, from seed size of 0.07 mm( 29.2485%) to seed size of 0.035 mm (29.2509%). The decrease in rate of change showed the evidence of converge.

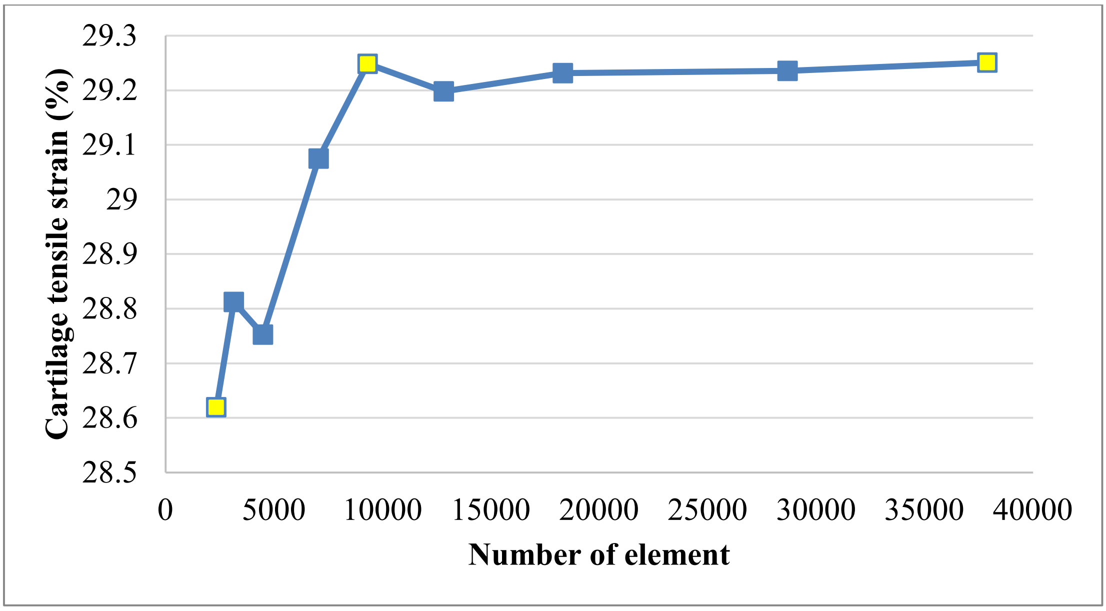

**Figure 5.17 Mesh sensitivity study on PH10 cartilage tensile strain.**

The acetabulum contact force (Figure 5.18) varied from 51.11 N to 51.21 N. The range of the data set was 0.1 N which accounts for 1.96% of the smallest value. The strain decreased quickly, by -0.1%, from seed size of 0.14 mm (51.21 N) to seed size of 0.07 mm (51.13 N). Then the results decreased slightly, by -0.04%, from seed size of 0.07 mm (51.13 N) to seed size of 0.035 mm (51.11 N). The decrease in rate of change showed the evidence of converge.

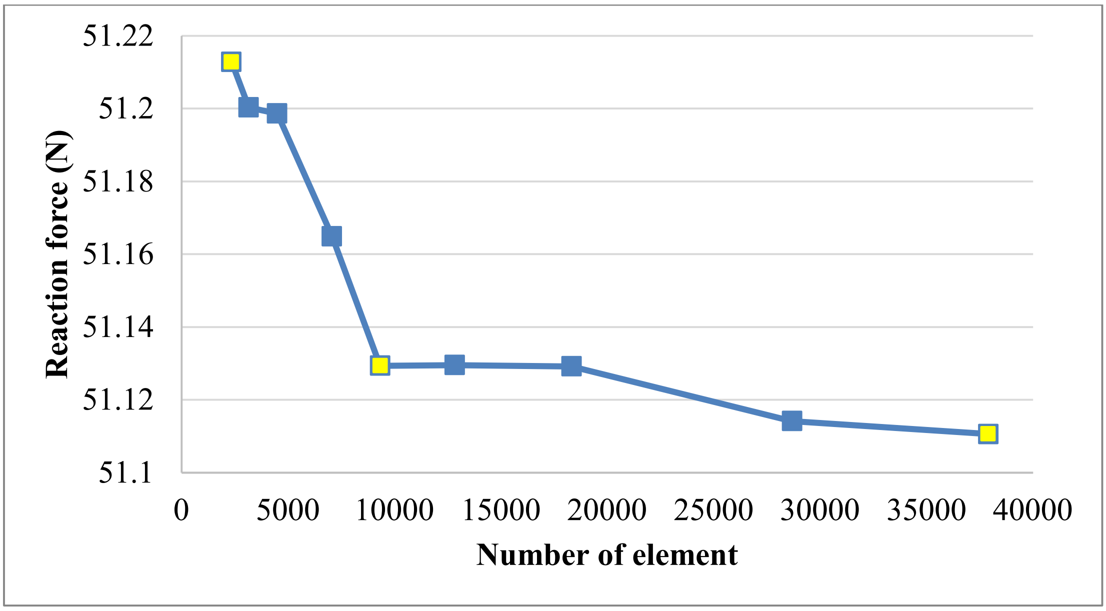

**Figure 5.18 Mesh sensitivity study on PH10 acetabulum contact force.**

In order to achieve appropriate level of model reliability, element size of 0.035 mm was adopted for the FE models in this study. The total number and type of elements can be found in Table 5.6.

**Table 5.6 Element number and element type for baseline models**

| Baseline model | Number of quadrilateral elements | Number of triangular elements |
|---|---|---|
| PH10 | 36443 | 1051 |
| PH12 | 43007 | 1331 |

### 5.3.3 Verification of geometry capture for the unloaded acetabular cartilage thickness

Unloaded cartilage thickness of model PH10 was measured repetitively for three times (Figure 5.19) as the assessment of intra-observer repeatability. The upper layer of the acetabular cartilage was well captured in the plot with small differences up to 0.7%. The variation on the horizontal direction reflects the inconsistency in selecting the end point for cartilage measurement. The averaged deviation for thickness measured from 0 – 6.4 mm to the bone support is 0.075 mm which is acceptable since the image resolution was set to 0.1 mm. The manual error increased as the measurement was taken closer to the fossa, from about 0.03 mm to up to about 0.1 mm.

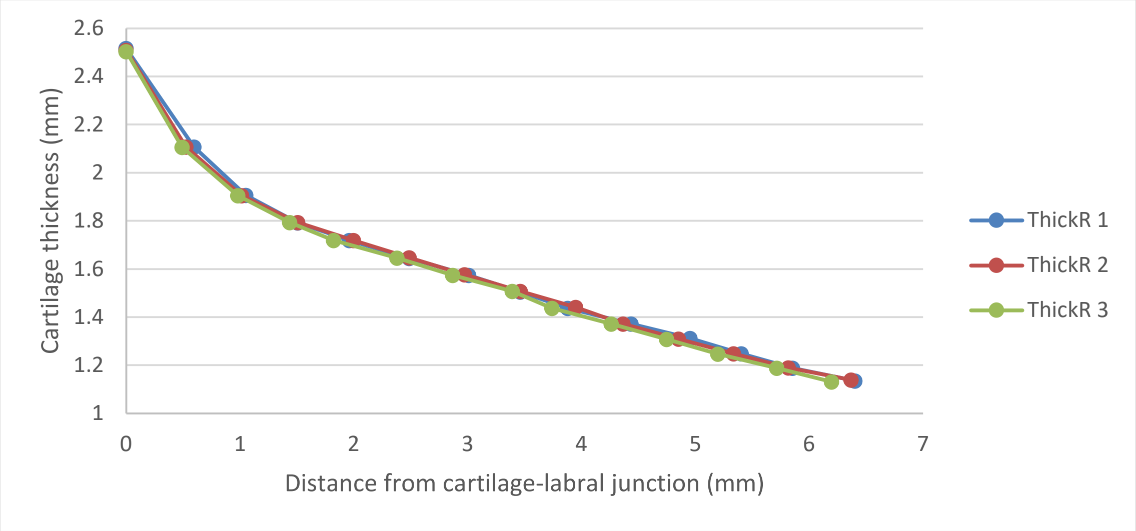

**Figure 5.19 Verification of thickness measurement for PH10**

The cartilage in model PH10 was up to 25% thicker than that in sample PH10 at 0 – 3 mm to bone support (Figure 5.20). However the middle portion of the cartilage in sample PH10 deviated from an arc and was up to 25% thicker than that in model PH10. The coordinates of the points used for measurement all share the same error of ± 0.05 mm. For a cartilage with thickness of 1 mm, the error could add up to 10% of the total thickness. The deviation between experimental and computational thickness (25%) was still close to the error

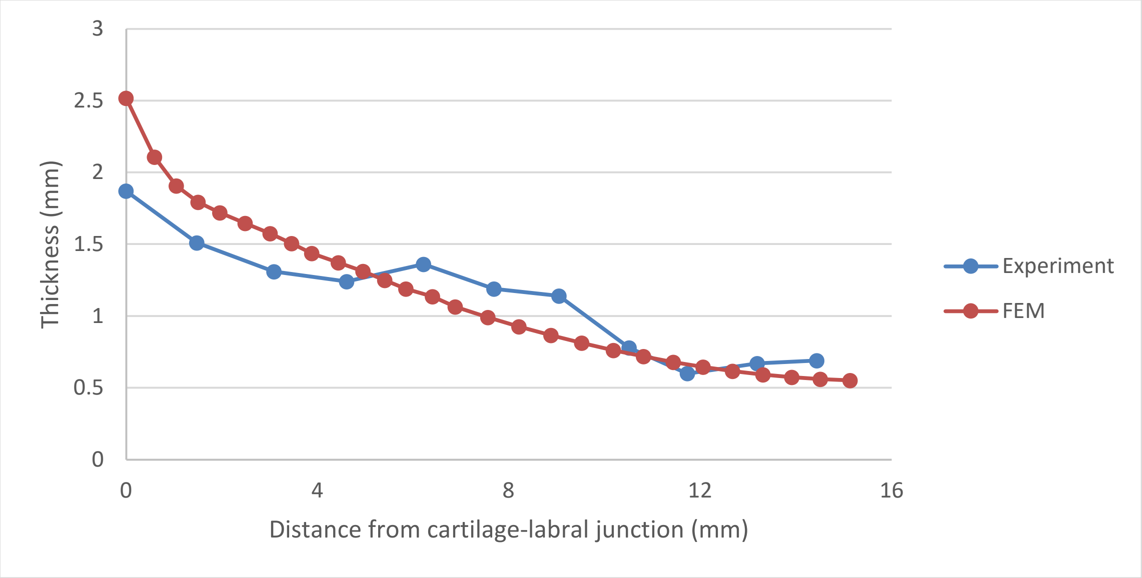

**Figure 5.20 Verification of cartilage modelling for PH10**

The cartilage in model PH12 was up to 40% thicker than that in sample PH12 for the first 0.5 mm to the bone support (Figure 5.21). The two cartilages fitted well in the plot from 1 – 8 mm to the bone support with percentage error up to 0.24%. The geometry of the acetabular cartilage away from the labral junction was very well captured in sample PH12. The image resolution was 0.1 mm which means there could be an error of 5 – 10% of the total thickness.

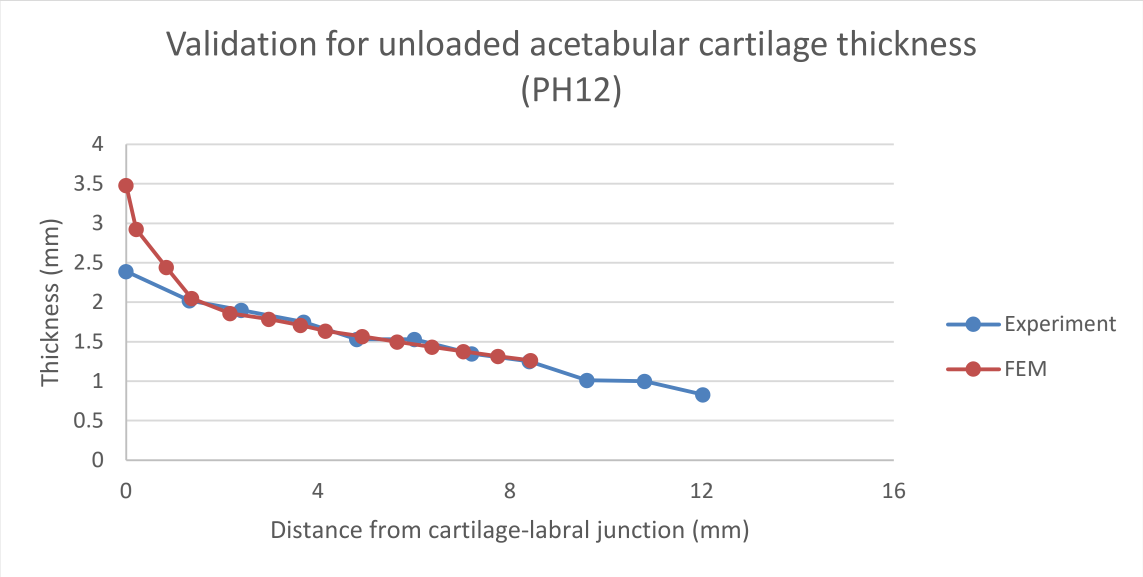

**Figure 5.21 Verification of cartilage modelling for PH12**

### 5.3.4 Verification of simplifications in the subchondral surface boundary conditions

Visual differences between different simplifications of the acetabular subchondral bone surface are illustrated in Figure 5.22 and Figure 5.23. The soft tissues effectively deformed over the bone in the baseline model for PH12. The rigid bone plate in Figure 5.23 stopped the soft tissue from deforming over the bone surface.

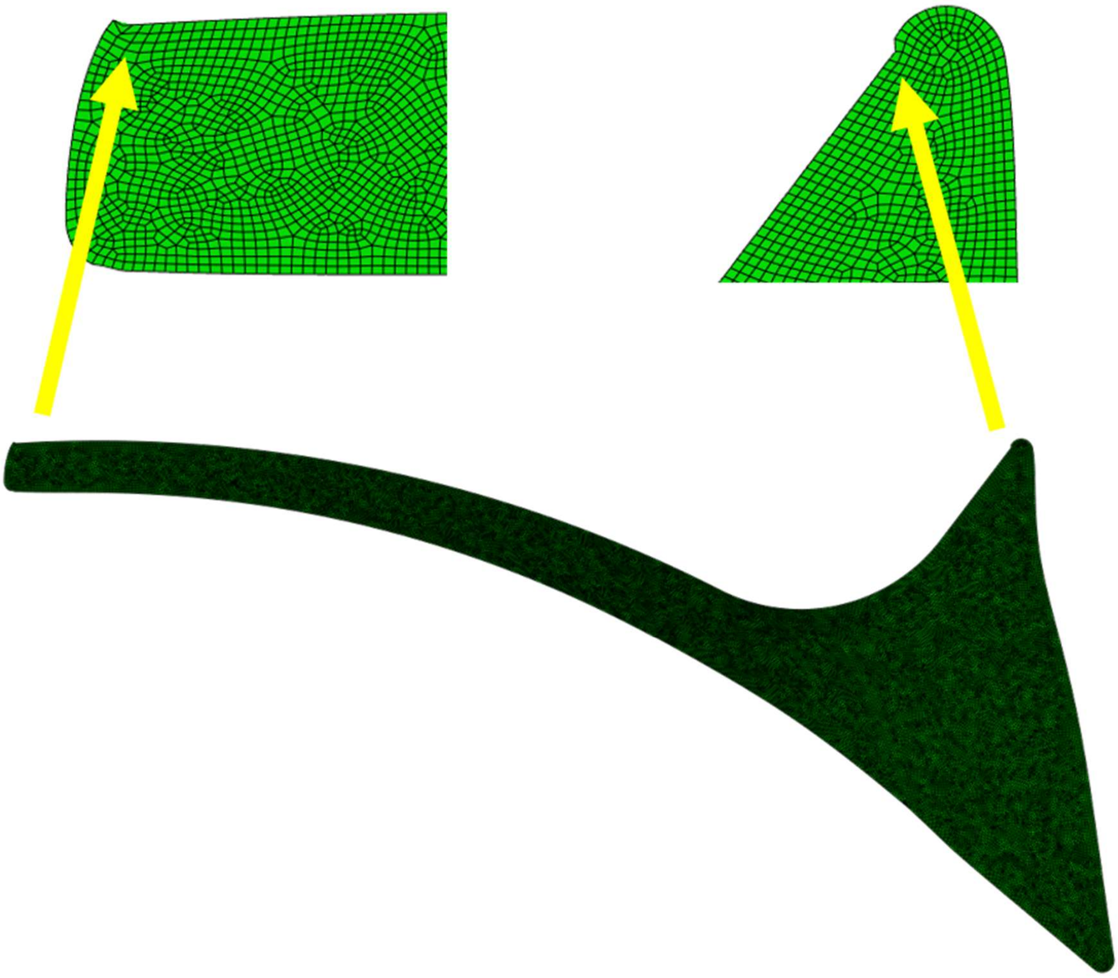

**Figure 5.22 Soft tissue behaviour around subchondral bone edges in baseline model**

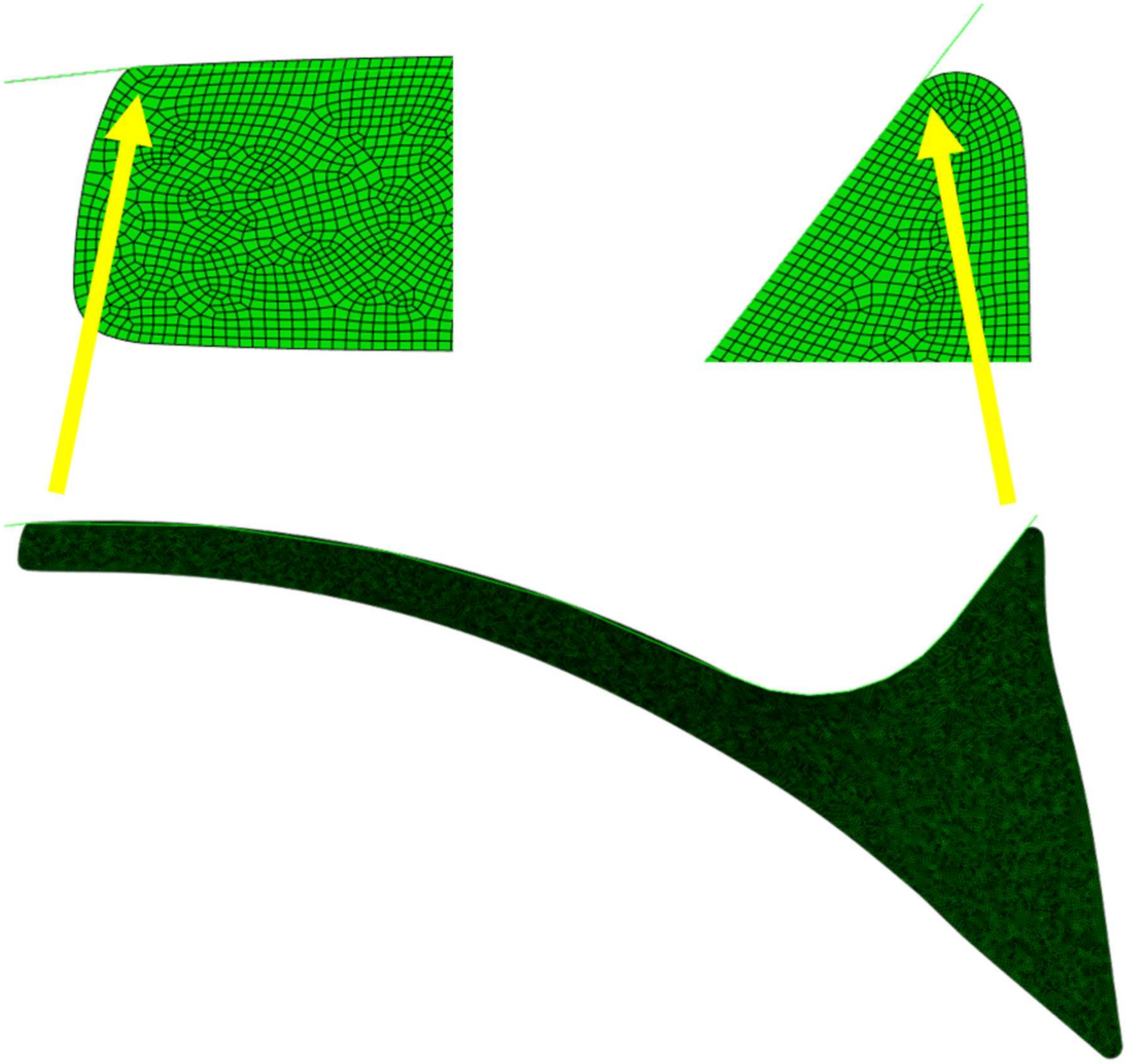

**Figure 5.23 Soft tissue behaviour around subchondral bone edges with rigid supporting plate.**

While there were differences in the tissue behaviour where boundary conditions are applied, the overall cartilage strain was almost identical for baseline model and model with rigid bone plate, with percentage error up to 1.3% (Figure 5.24).

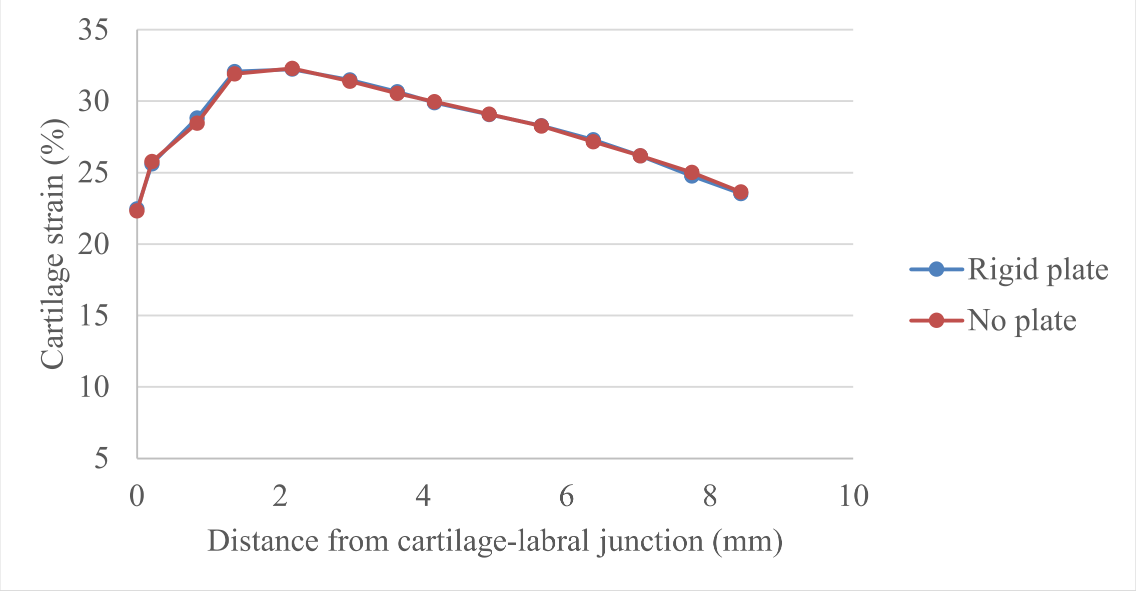

**Figure 5.24 Overall cartilage strain under change of subchondral bone boundaries for PH12.**

Similarly, the total acetabulum contact force was 95.1 N in “PH12_Rigid” case, compared to 94.8 N in the baseline model, with percentage difference of +0.23% (Figure 5.25). Both cartilage and labrum undertook more load (3.8% and 0.2% respectively) than in the baseline model.

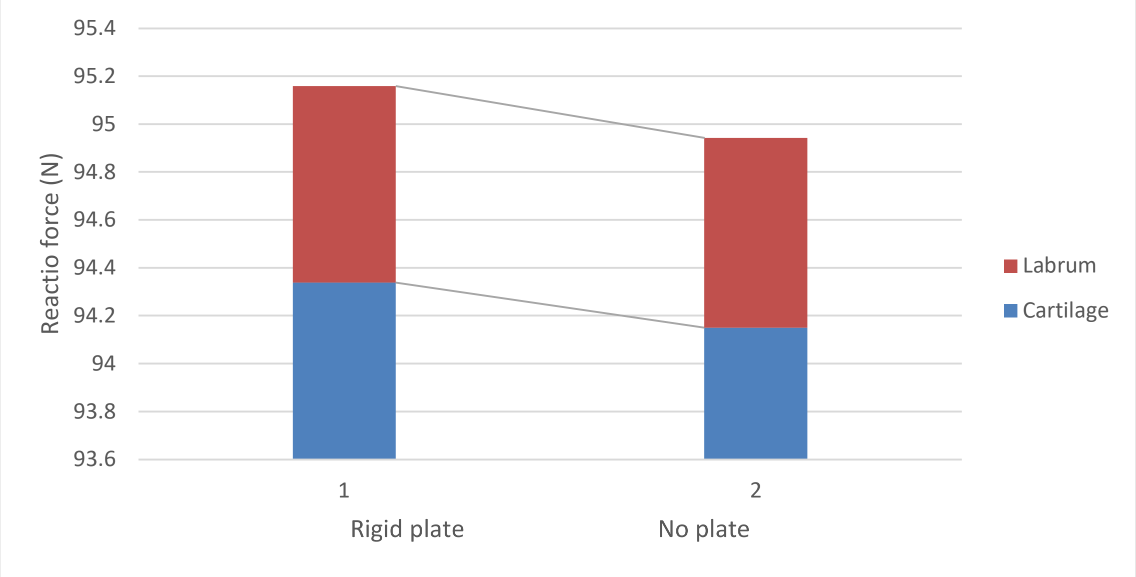

**Figure 5.25 Acetabulum contact force under change of subchondral bone boundaries for PH12.**

Finally, the model with rigid bone plate shows a small increase of 1.34% in the cartilage tensile strain (7.68%) than that in the baseline model (7.79%).

### 5.3.5 Comparison with experimental results

The overall cartilage strain in model PH10 was up to 33% smaller than that in sample PH10 from 0 – 3 mm to the bone support (Figure 5.26 - Figure 5.27). However the experimental strain increased as moving towards the fossa while the strain in model PH10 was gradually decreasing. The mechanism of these trends is explained in section 5.4.

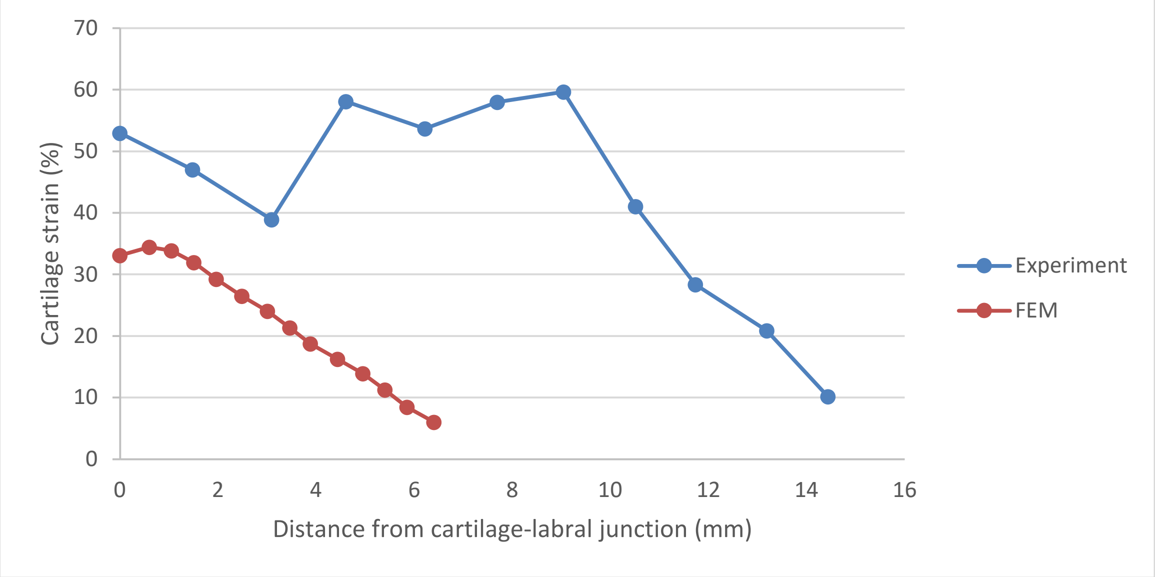

**Figure 5.26 Comparison on overall cartilage strain for PH10**

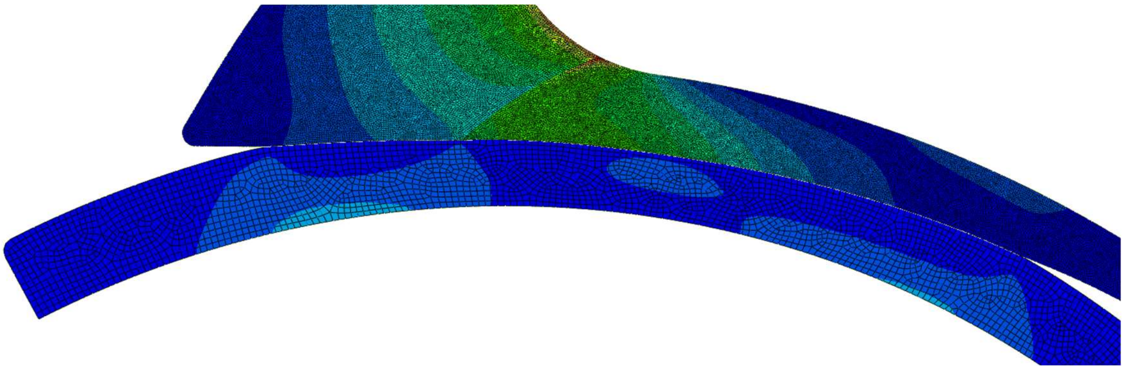

**Figure 5.27 Strain contour plot for PH10.**

The curve in dark red (Figure 5.28 - Figure 5.29) was plotted from the computed result of model PH12. As mentioned in section 5.3.1, the model PH12 only proceeded to about 61% of the total displacement step. Even though, the computed overall cartilage strain was larger than that in experiment from 4 – 8 mm to the bone support.

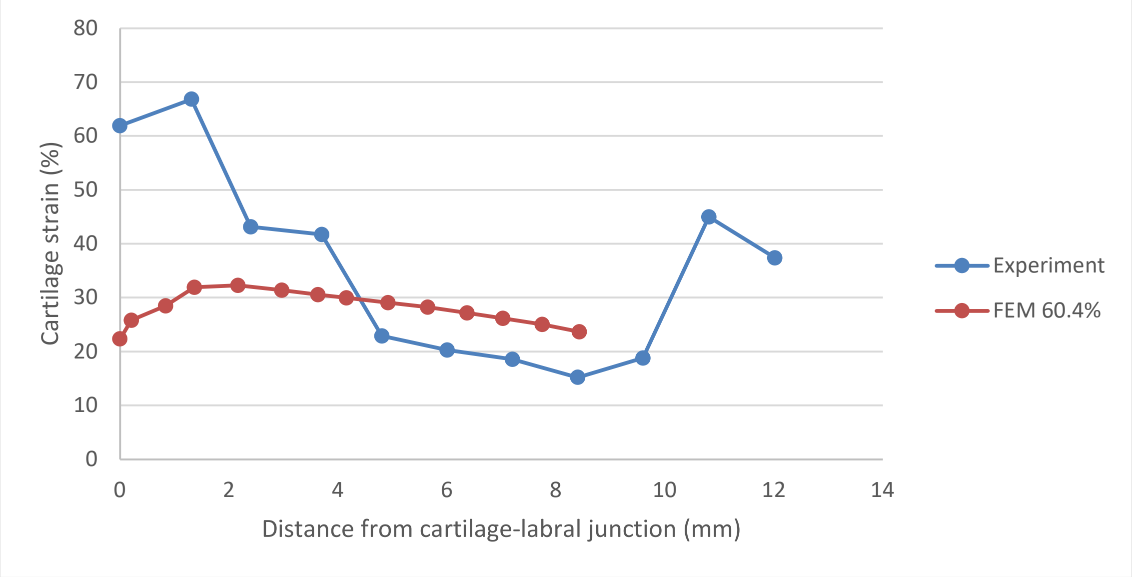

**Figure 5.28 Comparison on overall cartilage strain for PH12**

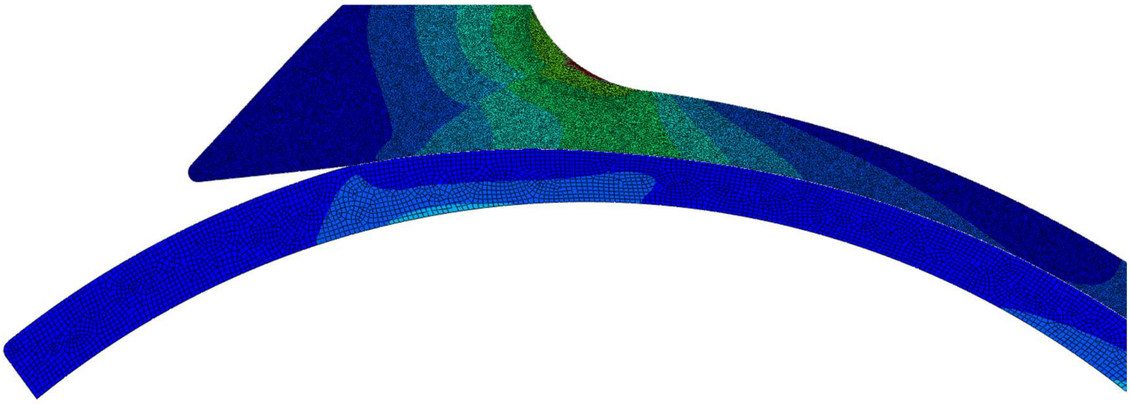

**Figure 5.29 Strain contour plot for PH12.**

The apex displacement in model (Figure 5.30) PH10 was 8.7% smaller than that in sample PH10 (2.3 mm). For a total displacement of 2.3 mm, the image resolution of 0.1 mm could cause error of up to 8.7%.

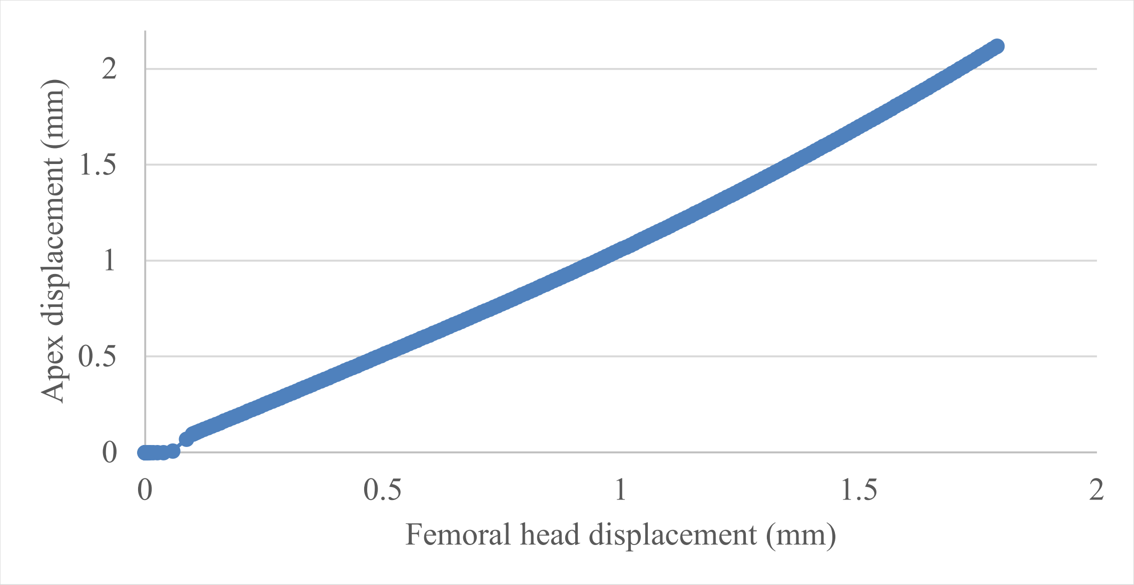

**Figure 5.30 Labrum apex displacement against applied displacement on femoral head for PH10**

The apex displacement in model PH12 (Figure 5.31) was 47.4% smaller than that in sample PH12 (3.8 mm), while the model was 40% of the total step away from full completion.

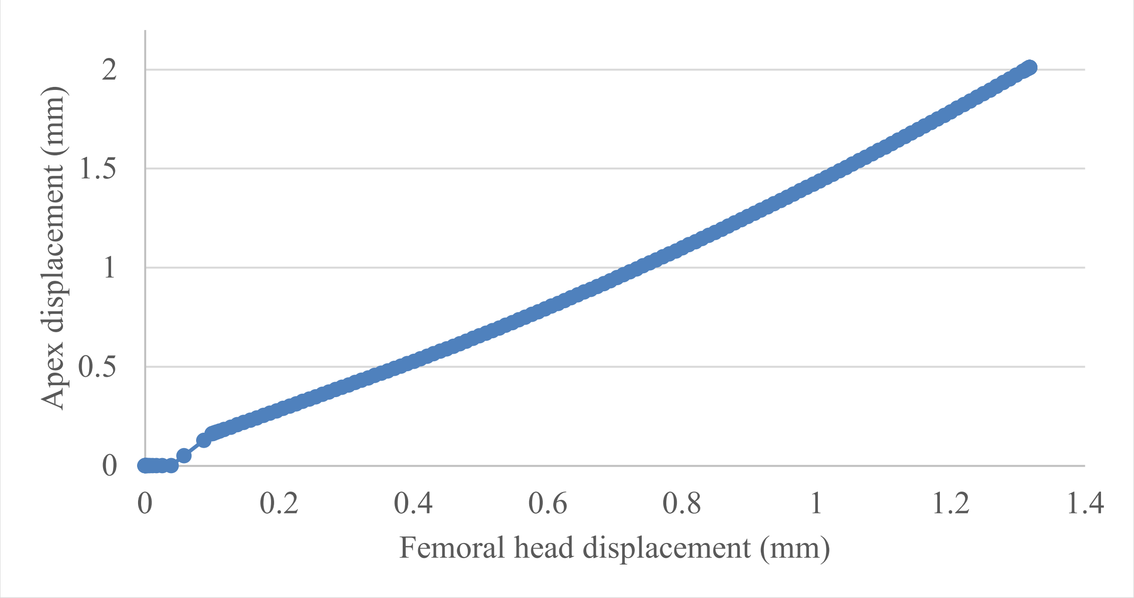

**Figure 5.31 Labrum apex displacement against applied displacement on femoral head for PH12**

The computational total contact force, adding up the acetabular cartilage and acetabular labrum contact forces, were recorded in Table 5.7. However, the computational contact forces were not comparable with the experimental load cell reading (discussed in section 5.4). The load share was investigated by reading the contact forces on the cartilage and the labrum separately, which is discussed in later sections.

**Table 5.7 Comparison between model total contact force and experimental load cell reading**

| Sample | Model progress (%) | Total contact force (N) | Experimental reaction force (N) | Model displacement (mm, 2D) | Experimental displacement (mm, in slice) |
|---|---|---|---|---|---|
| PH10 | 100 | 47 | 183 | 1.8 | 2.3 |
| PH12 | 60.4 | 95 | 230 | 2.1 | 3.8 |

### 5.3.6 Effect of femoral head position

For PH10, the overall cartilage strain (Figure 5.32) increased when femoral head is shifted inwards the socket. The cartilage strain varied from 34.3% to 20.1% with a smaller rate of decrease than that in the baseline model. Cartilage strain of 20.1% was observed at 6.4 mm from the bone support in the PH10_FHin case. However the contact region ended at 5.4 mm from the bone support in the baseline model. The peak strain was also shifted to the fossa at 1 mm from the bone support.

The overall cartilage strain (Figure 5.32) decreased when femoral head is shifted closer to the rim. The cartilage strain varied from 18.6% to 1.5% across the distance 0 – 3 mm from cartilage-labral junction, with a higher rate of decrease. The edge of the contact region was shifted outwards at about 4 mm from the bone support.

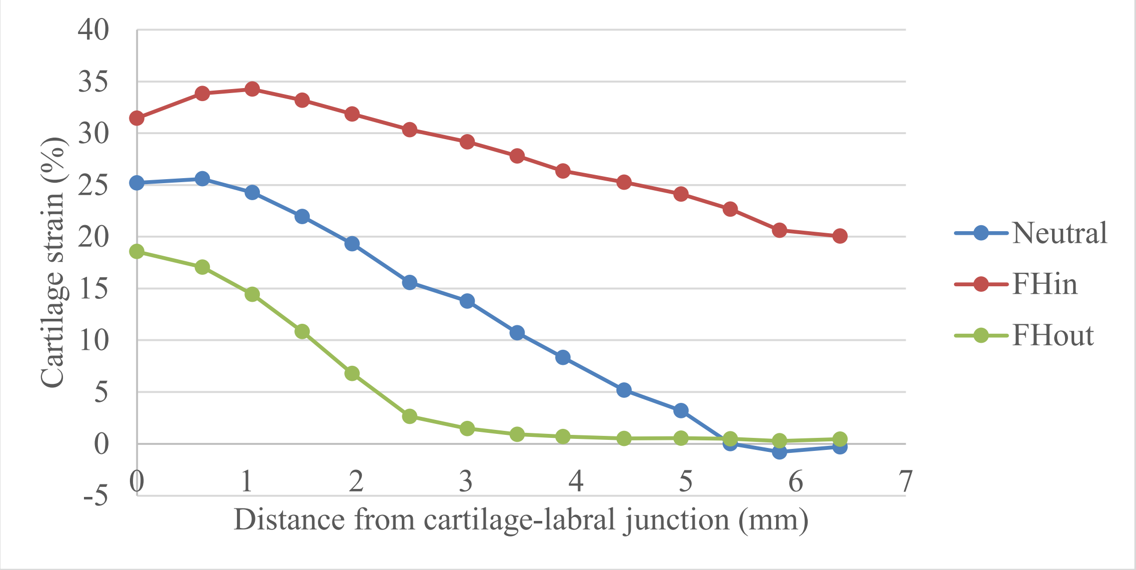

**Figure 5.32 Overall cartilage strain under change of femoral head position for PH10**

For PH12, the overall cartilage strain (Figure 5.33) increased to 6.9% - 15.0% and was increasing along the bone support. Due to the low completion of model PH12 (14%), both baseline model and PH12_FHout experienced low cartilage strain (<5%) at 0 – 3 mm from the bone support. The cartilage strain was even lower when femoral head is shifted outwards from the socket up to 0.9%.

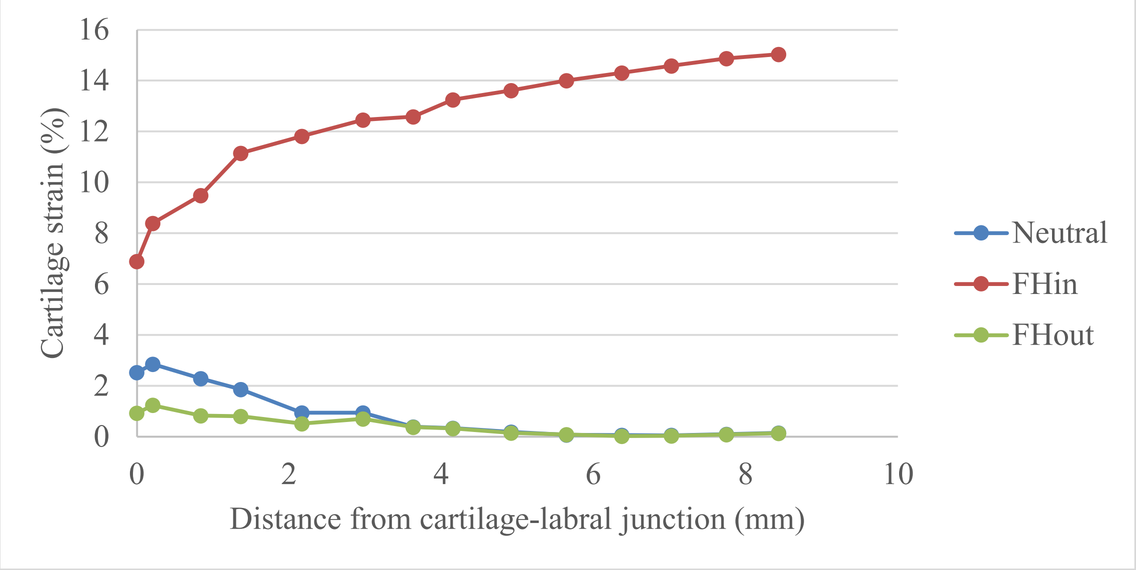

**Figure 5.33 Overall cartilage strain under change of femoral head position for PH12**

The acetabulum total contact force was 29.1 N in the baseline model. The contact force increased by 163% in the PH10_FHin case, with labrum contact force decreased by 11.8% and cartilage contact force increased by 237.4%. The contact force decreased by 46.4% in the PH10_FHout case, with labrum contact increased by 4.7% and cartilage contact force decreased by 67.5%. As the femoral head shifted outwards from the socket, the cartilage contact force decreased and the labrum contact force increased. The percentage of force undertaken by cartilage was 90.0%, 70.7% , and 42.7% for the FHin, baseline, and FHout case respectively.

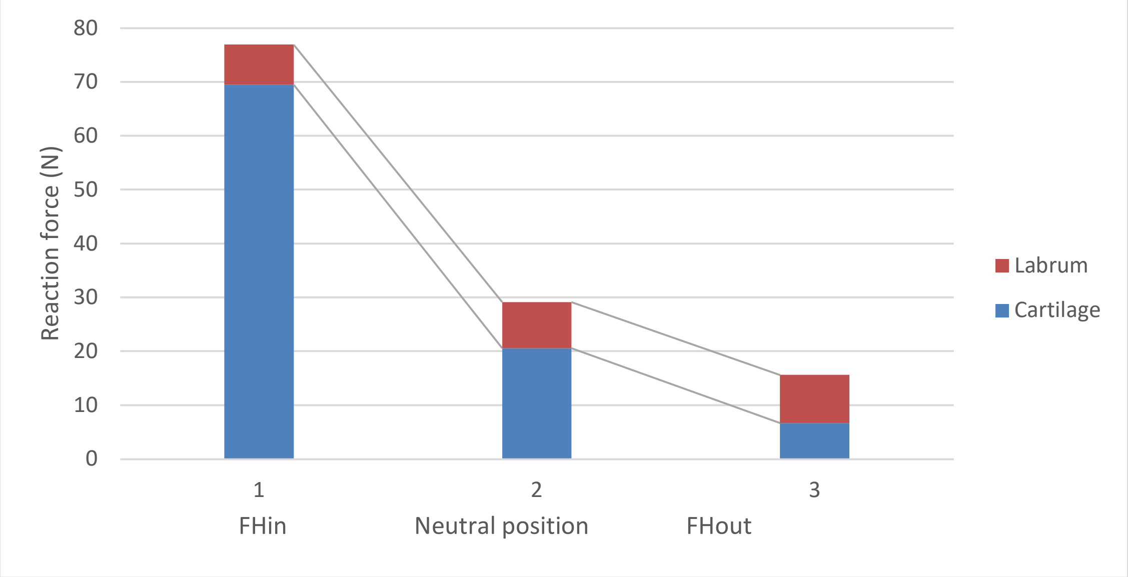

**Figure 5.34 Acetabulum contact force under change of femoral head position for PH10**

Similarly, for PH12 the total contact force in FHin and FHout cases were 2912% and 33% of that in the baseline model. The percentage of force undertaken by cartilage was 99%, 40%, and 0% for the FHin, baseline, and FHout case respectively.

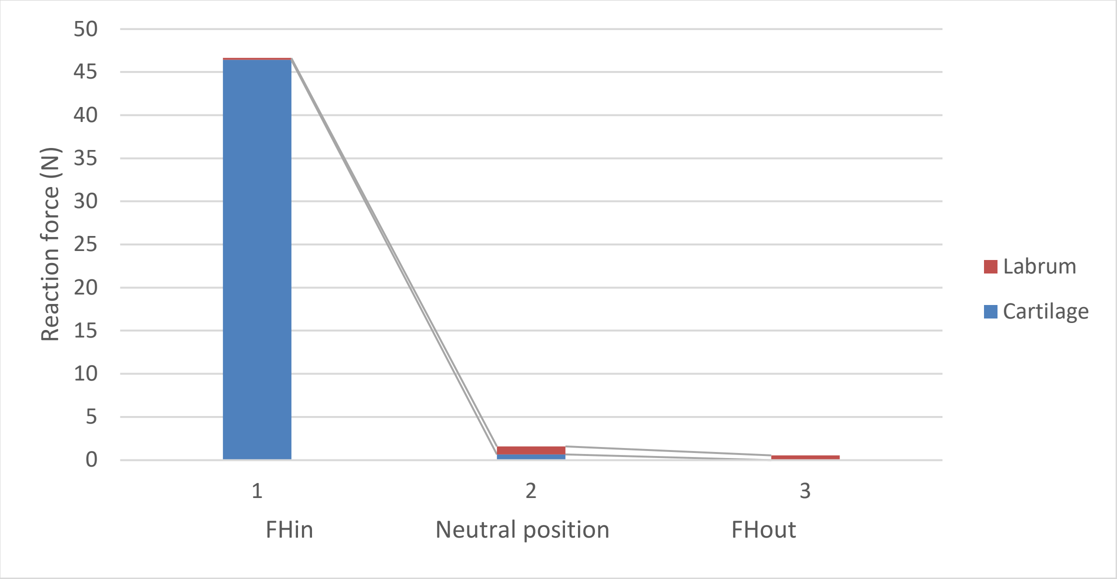

**Figure 5.35 Acetabulum contact force under change of femoral head position for PH12**

The cartilage tensile strain decreased when femoral head was shifted inwards or outwards from the socket for PH10, but increased for PH12. In both FHin cases, the tensile strain had a higher reduction compared to FHout cases.

**Table 5.8 Cartilage tensile strain under change of femoral head position**

| Model PH10 | | | Model PH12 | | |
|---|---|---|---|---|---|
| Case | Strain (%) | Percentage change (%) | Case | Strain (%) | Percentage change (%) |
| FHin | 21.72 | -10.38 | FHin | 2.56 | -40.14 |
| Baseline | 24.23 | 0 | Baseline | 2.27 | 0 |
| FHout | 24.00 | -0.95 | FHout | 3.35 | -21.53 |

### 5.3.7 Effect of labrum Young’s Modulus

For PH10, the overall cartilage strain (Figure 5.36) increased with the decrease of labrum Young’s Modulus from 0 – 1 mm to the bone support. The variation of overall cartilage strain was up to 1.4% across the four cases.

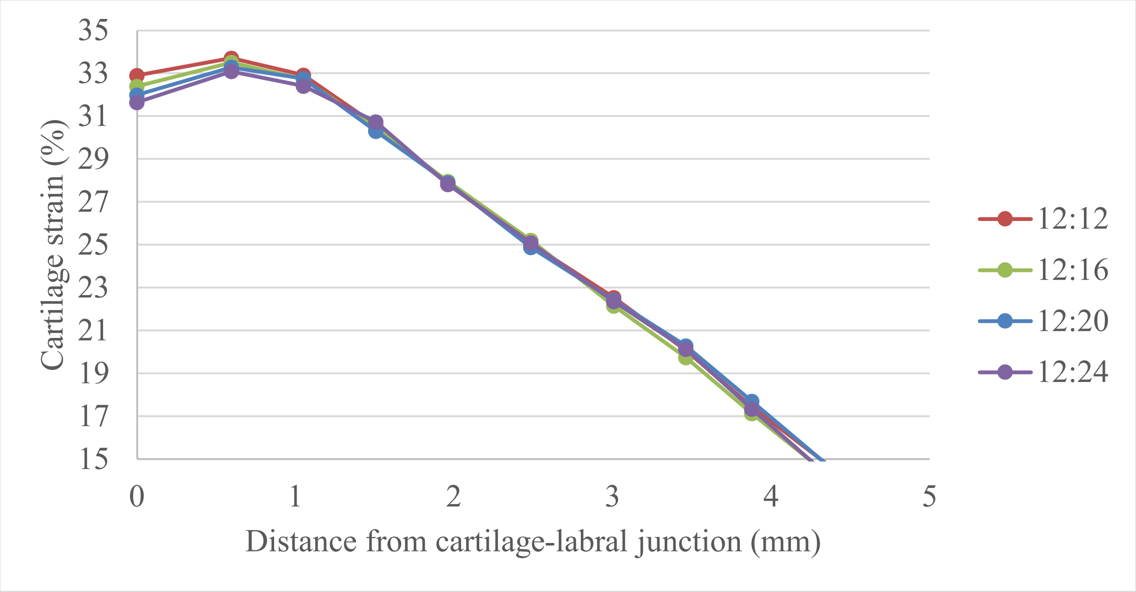

**Figure 5.36 Overall cartilage strain under change of labrum Young's Modulus for PH10. The ratio of Young's Modulus of cartilage with labrum was presented in the legend where 12:20 is the baseline model.**

Similarly, for PH12 the overall cartilage strain (Figure 5.37) increased with the decrease of labrum Young's Modulus from 0 – 1.4 mm to the bone support. The variation of overall cartilage strain was up to 1.0% across the four cases.

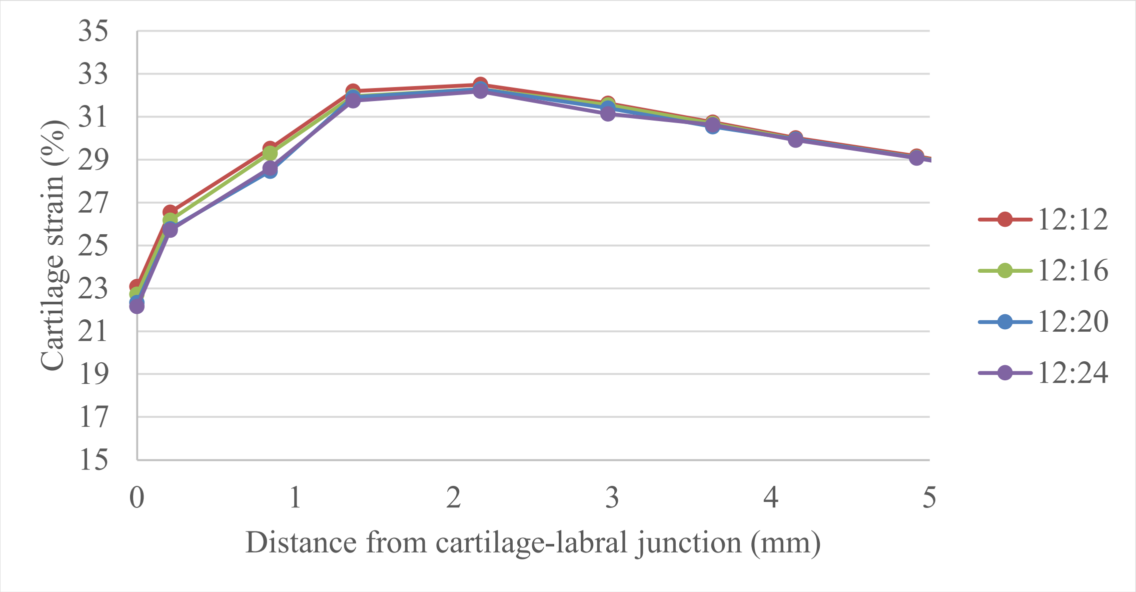

**Figure 5.37 Overall cartilage strain under change of labrum Young's Modulus for PH12.**

For PH10, the acetabulum total contact force (Figure 5.38) increased with the increase of labrum Young’s Modulus. The cartilage undertook 85.8% - 78.3% of the total contact force of 41.8 – 49.8 N. Increase in the force distribution was observed in labrum from 14.2% - 21.7% with the increase in labrum Young’s Modulus.

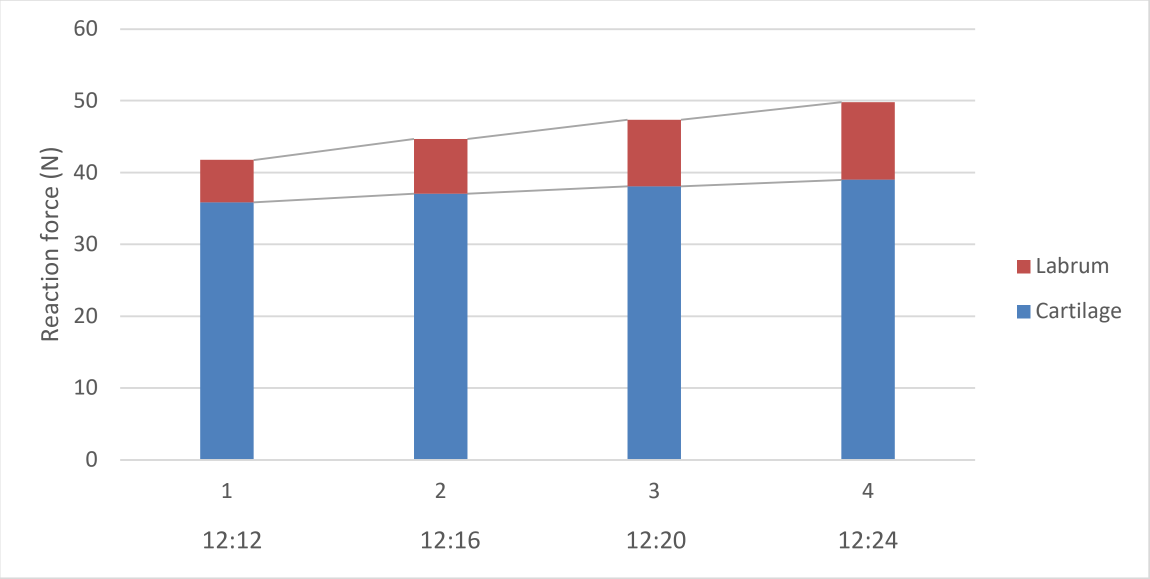

**Figure 5.38 Acetabulum contact force under change of labrum Young’s Modulus for PH10.**

Similarly, for PH12 the acetabulum total contact force (Figure 5.39) increased with the increase of labrum Young’s Modulus. The cartilage undertook 99.6% - 103.2% of the total contact force of 92.1 – 96.2 N. Labrum contact force increased by 68.2% - 231.0% with increase in Labrum Young’s Modulus.

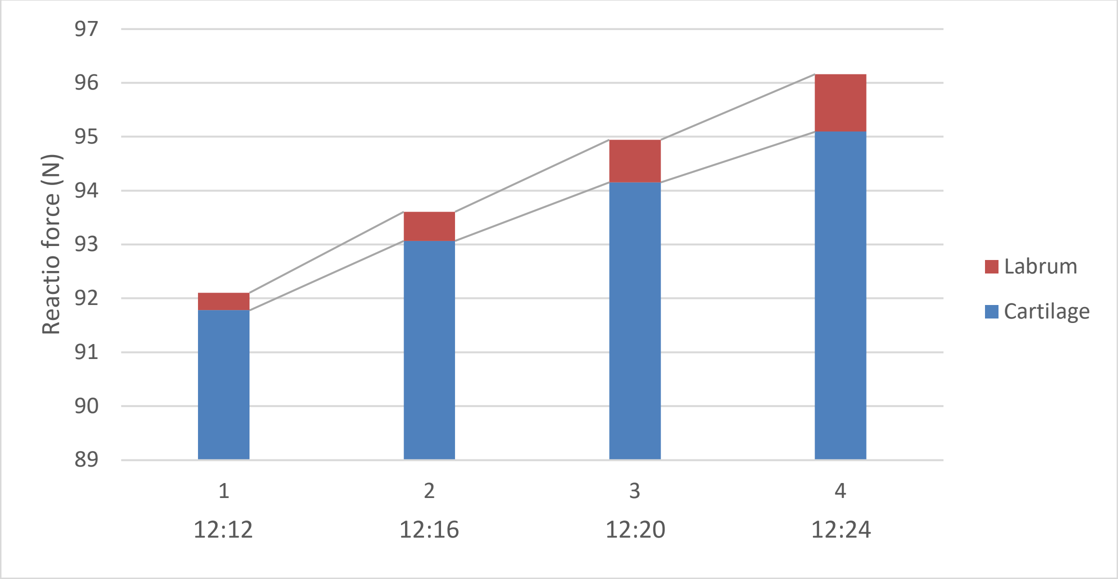

**Figure 5.39 Acetabulum contact force under change of labrum Young's Modulus for PH12.**

In both models, the cartilage tensile strain increased with the increase of labrum Young's Modulus. The cartilage tensile strain changed by about -25%, 11.6%, and +10.3% when labrum Young's Modulus varied by -40%, -20%, and +20%.

**Table 5.9 Cartilage tensile strain under change of labrum Young's Modulus.**

| Model PH10 | | | Model PH12 | | |
|---|---|---|---|---|---|
| Case | Strain (%) | Percentage change (%) | Case | Strain (%) | Percentage change (%) |
| L12 | 19.74 | -25.97 | L12 | 5.82 | -24.21 |
| L16 | 23.49 | -11.91 | L16 | 6.81 | -11.28 |
| L20 (baseline) | 26.67 | 0 | L20 (baseline) | 7.68 | 0 |
| L24 | 29.20 | 10.48 | L24 | 8.46 | 10.17 |

### 5.3.8 Effect of cartilage-labral junction location

The overall cartilage strain for PH10 (Figure 5.40) increased by about 1% at 0 – 1 mm to the bone support, with the cartilage-labral junction shifting away from the fossa. Subtle change (<0.3%) was found when the junction shifted further.

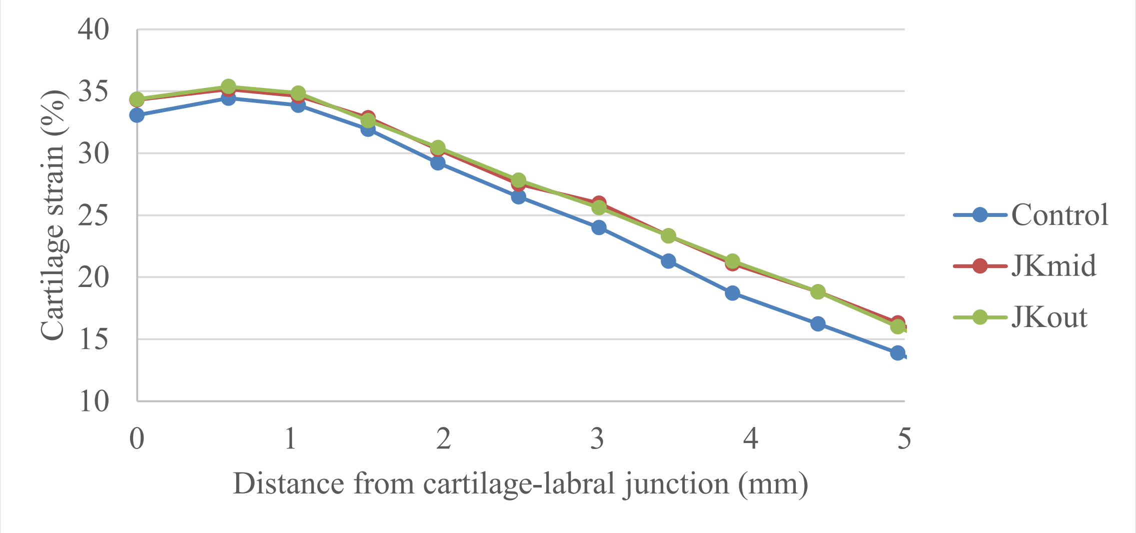

**Figure 5.40 Overall cartilage strain under change of cartilage-labral junction location for PH10.**

The overall cartilage strain for PH12 (Figure 5.41) increased by about 1% at 0.2 – 1.4 mm to the bone support, with the cartilage-labral junction shifting away from the fossa.

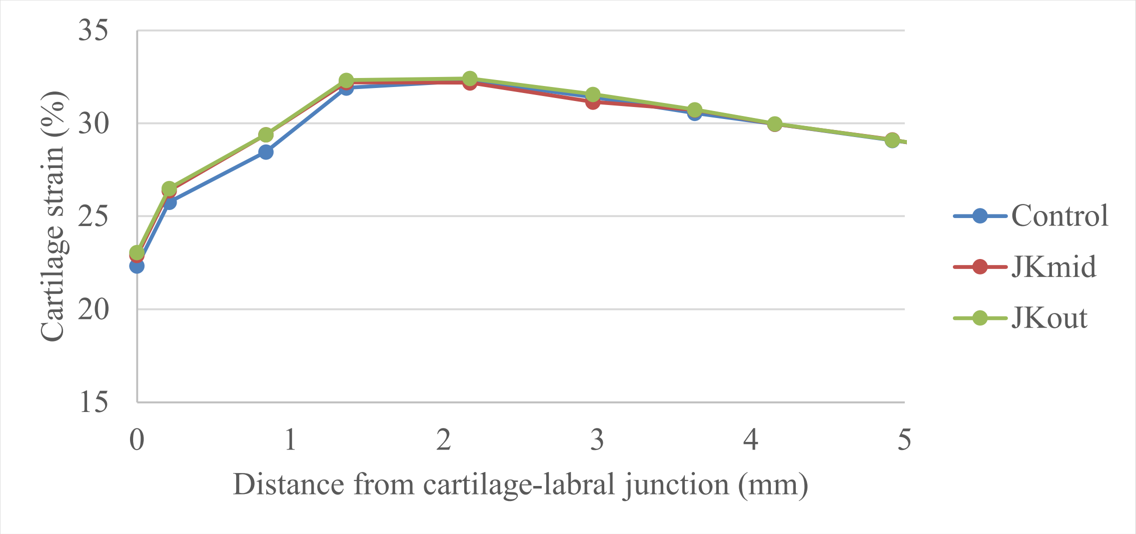

**Figure 5.41 Overall cartilage strain under change of cartilage-labral junction location for PH12**

For PH10, the acetabulum total contact force decreased by 11.2% and 14.4% with the cartilage-labral junction shifting 1 mm and 2 mm away from the fossa (Figure 5.42). Small change (<3%) was found in the contact force in cartilage tissue. The contact force applied to the labrum decreased by 49.3% and 85.7% with the cartilage-labral junction shifting 1 mm and 2 mm away from the fossa.

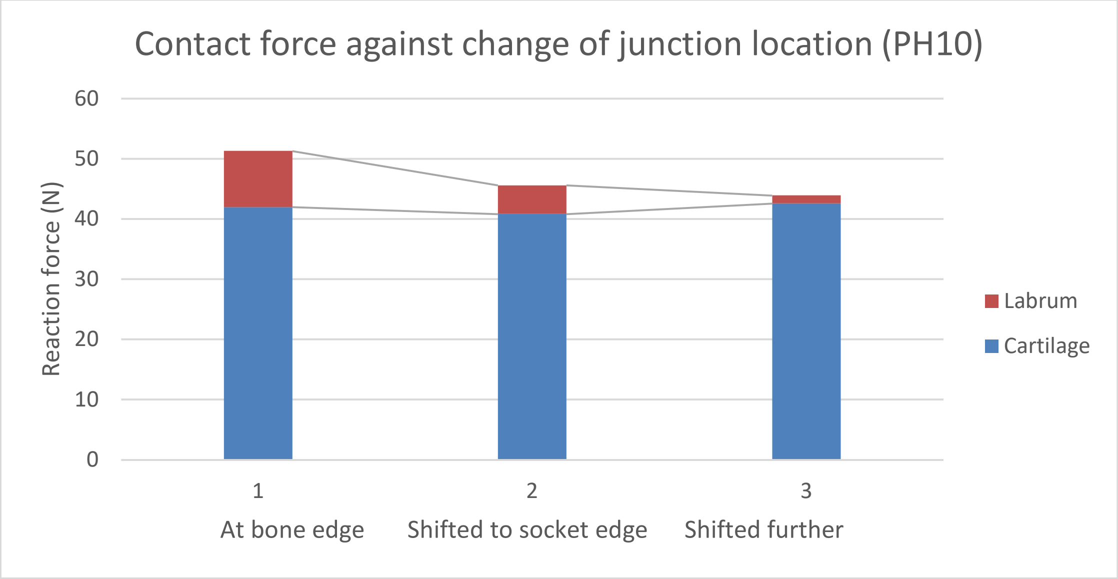

**Figure 5.42 Acetabulum contact force under change of cartilage-labral junction location for PH10. Note that the y-axis does not start at 0 for clarity of the difference.**

For PH12, the acetabulum contact force and cartilage contact force all decreased by a small amount (<0.2%) with the cartilage-labral junction shifting away from the fossa (Figure 5.43). The labrum contact force decreased by 10.7% and 11.7% with the cartilage-labral junction shifting 1 mm and 2 mm away from the fossa.

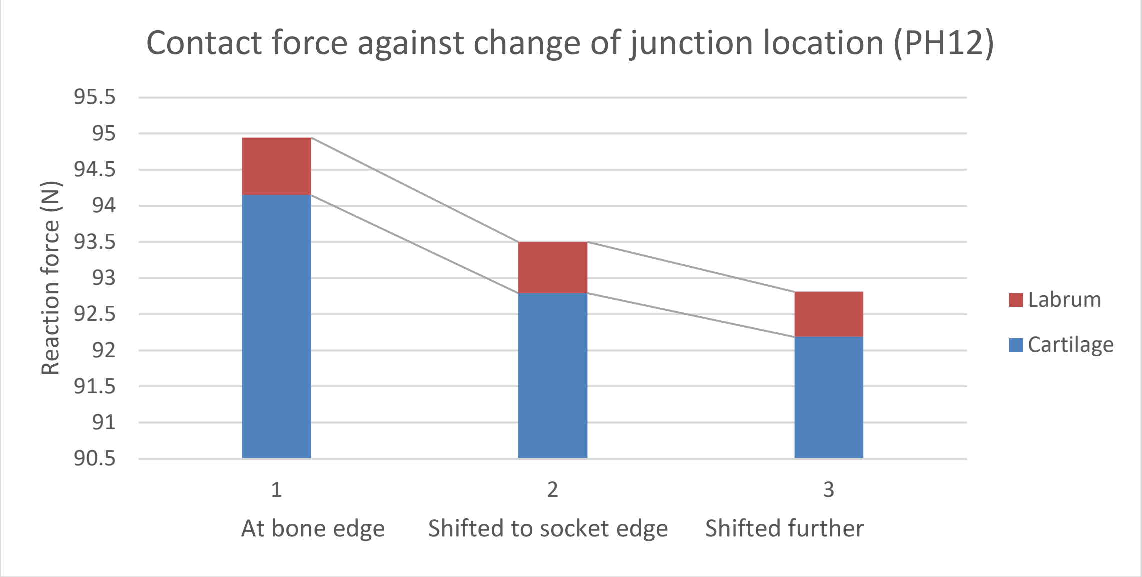

**Figure 5.43 Acetabulum contact force under change of cartilage-labral junction location for PH12. Note that the y-axis does not start at 0 for clarity of the difference.**

In model PH10, both JKmid and JKout cases showed decrease in cartilage tensile strain of 10.1% and 15.6%. However, in model PH12, the peak tensile strain was obtained in PH12_JKmid case, being increased by 19.3% compared to baseline model. Subtle decrease (-0.9%) was found in JKout case.

**Table 5.10 Cartilage tensile strain under change of cartilage-labral junction location.**

| Model PH10 | | | Model PH12 | | |
|---|---|---|---|---|---|
| Case | Strain (%) | Percentage change (%) | Case | Strain (%) | Percentage change (%) |
| Baseline | 26.59 | 0 | Baseline | 7.68 | 0 |
| JKmid | 23.44 | -10.07 | JKmid | 9.16 | 19.34 |
| JKout | 22.19 | -15.69 | JKout | 7.60 | -0.93 |

## 5.4 Discussion

The preceding chapter developed FE models based on two of the six samples, PH10 and PH12, for comparison with the experimental results and for investigation of the model parameters regarding soft tissue displacement. The achievements and findings were:

Model development and verification

- Generated semi-subject-specific FE models of PH10 and PH12, capturing the characteristic geometry features on the acetabulum.
- Replicated the constraints and displacements which were applied in the experimental study.
- Conducted mesh sensitivity testing, resulting in an element size choice of 0.035 mm, where the percentage difference was less than 3% and had a trend of decrease.
- Conducted verification on representation of the acetabular cartilage geometry. The percentage differences were between 8% and 25% for PH10, and between 5% and 10% for PH12, with image resolution at 0.1 mm.

Validation against experimental results

- The cartilage strain in model PH10 was up to 33% lower than that in sample PH10 from 0 - 3 mm to the bone support. The cartilage strain in model PH12 was also lower than the experimental results from 0-3 mm to the bone support, but higher from 4 - 8 mm to the bone support.
- The apex displacement in model PH10 was 2.1 mm, 8.7% smaller than that measured in the experiment (2.3 mm). The apex displacement in model PH12 was 2.0 mm, 47.4% smaller than that measured in the experiment (3.8 mm). It is worth mentioning that the model PH12 was 40% of the total displacement step away from full completion.
- The computational total contact forces for model PH10 and PH12 were 47N and 95N, referring to the experimental reaction forces of 183N and 230N, respectively. One fact that the applied displacement in the model was derived from the CT image as a component of the experimental

displacement, 1.8 out of 3.8 mm and 2.1 out of 4.3 mm for PH10 and PH12 respectively.

Parametric, sensitivity testing

- Investigated the effect of femoral head position by shifting the femoral head by 1 mm inwards or outwards from the acetabular socket. The further the femoral head was from the acetabulum, the higher strain the acetabular cartilage was experiencing. The variation of cartilage strain was up to 15% in both models.
- Investigated the effect of labrum Young's Modulus by assigning 60%, 80%, 100% and 120% of the original value to the model. The overall acetabular cartilage strain decreased as the labrum Young's Modulus increased, however only at the 0 – 1 mm from the bone support. The variation in cartilage strain was up to 1.4%.
- Investigated the effect of cartilage-labral junction location by shifting the transition line outwards from the acetabular socket by 1 or 2 mm. The overall acetabular cartilage strain increased by 1.4% when the junction was been moved further from the acetabulum. Only small differences up to 0.4% was observed between 1 mm and 2 mm case.

Finite element methods were previously used for investigation of the mechanics in femoroacetabular impingement. The FE models were typically developed in 3D space with the femoral abnormality obtained either from patient CT data (Jorge et al., 2014), or from geometry modification (Hellwig et al., 2016). Models were validated with the experimental results (Anderson et al., 2008 and Li et al., 2014) in terms of the contact pressure. Parametric study was carried out to investigate the effect of hip size, hip clearance, cartilage properties, and cartilage thickness on the hip joint contact mechanics (Li et al., 2013). Ultimately, the tissue material properties can be calibrated by altering the model parameters regarding the experimental results (Li et al., 2013; Hua et al., 2015). Ferguson et al. (2000) considered the hip joint being axisymmetric, with uniform cartilage layers and labrum with constant cross-sectional view.

In this work, the FE model captured subject-specific features from images, the acetabulum geometry in particular, which allowed analysis of the differences between individual samples. The variation in acetabular cartilage thickness along the radial direction was captured, rather than having a constant thickness. The model was capable of generating the cartilage-labral junction reasonably quickly via the parameterised approach. This enabled tests across a population of “virtual specimens”, alternatively the parametric study, which would help build understanding in the joint contact mechanism while avoid the use of so many experimental samples.

The superficial layer of the acetabular cartilage was been separated due to the focused load at the cartilage-labral junction (Figure 5.44 - Figure 5.45). The elements near the junction were deforming in opposite direction along the near-radial (U2) direction. This result provided evidence that labrum tear is likely to happen when the labrum tissue and the attached cartilage are deforming in the opposite directions. The acetabular cartilage overall strain was sensitive to the femoral head position. This offset femoral head position in geometry may be reflected by the femur abnormality in clinic. The result provided evidence that good conformity of the hip joint would help reduce concentrated strain on the cartilage at the deformity. The acetabular cartilage was undertaking higher load when labrum modulus increased, reflecting the calcification of labrum in clinic. This result provided the evidence that cartilage degeneration is likely to be associated with labrum degeneration (Hawellek et al., 2018).

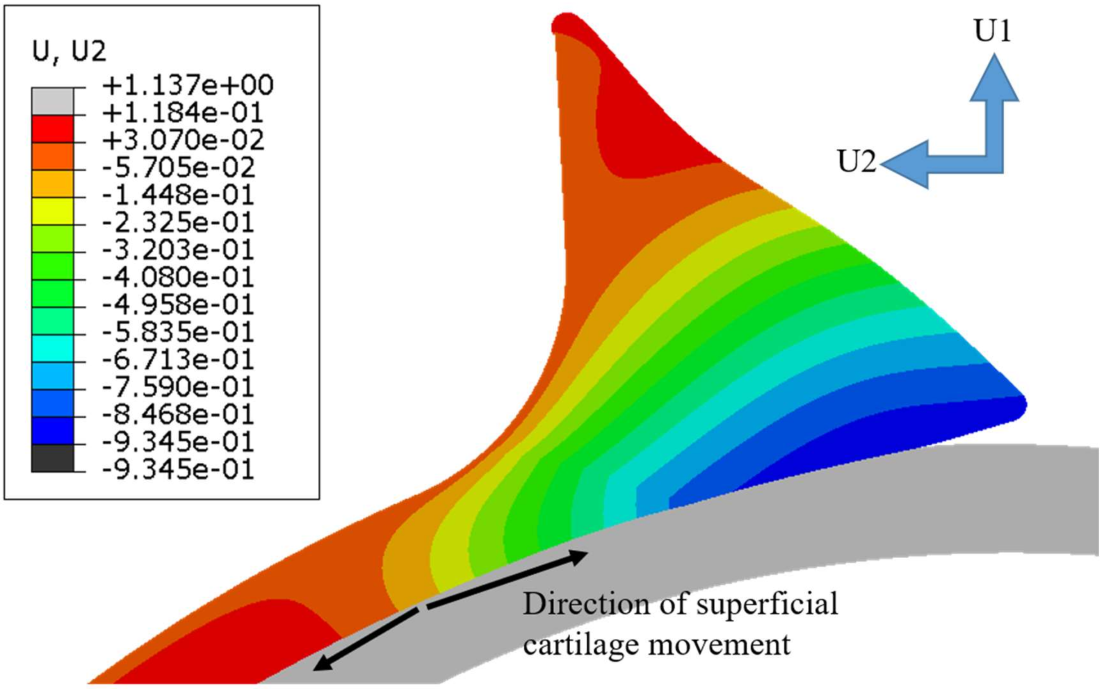

**Figure 5.44 Acetabular cartilage displacement in radial direction in PH10.**

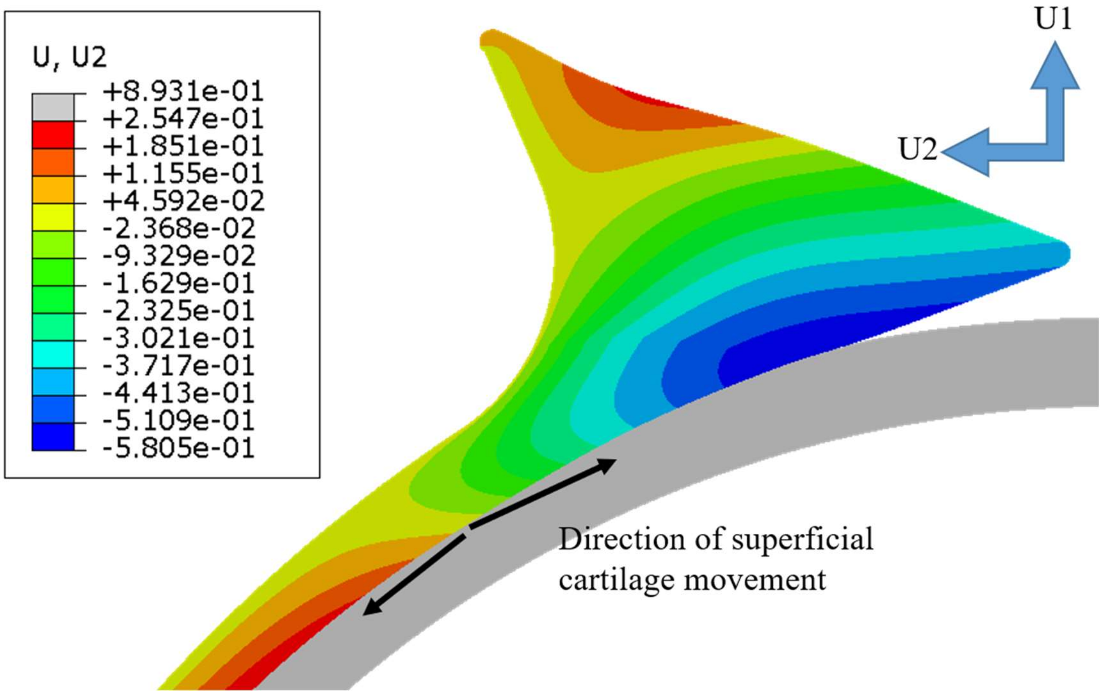

**Figure 5.45 Acetabular cartilage displacement in radial direction in PH12.**

Only two out of six experiment samples, PH10 and PH12, were involved in the FE study. The tissue samples were chosen for the smooth contact surface particularly at the cartilage-labral junction. Sharp angles due to the labrum overhang were observed in other four samples, which led to concentrated contact pressure and fail in model contact problem. The FE models in this study were developed in 2D plane, based on CT slices with image resolution of 0.1 mm. The modelled acetabular cartilage thickness varied from 0.6 mm – 2.5 mm, where the error from image resolution accounted for 4.0% - 16.7% of the total thickness. Therefore, it was crucial to model the cartilage in the way that the deformation on the cartilage can be monitored and measured. The 2D models allowed 15 – 50 elements to be assigned across the acetabular cartilage thickness, which provides decent resolution for cartilage modelling. In this study, element size of 0.035 mm allowed adequate details across the acetabular cartilage which had thickness around 1 – 2 mm. It is impractical to achieve element size at this level in 3D models without smart localised meshing. However, the accuracy used in the mesh sensitivity analysis appeared to be much higher than actually needed. Based on the image resolution of 0.1 mm and the cartilage thickest portion of 2.5

mm, the accuracy for labrum displacement and cartilage strain would only be no smaller than 0.01 mm and 0.4%. Therefore, the suggested element size could just be 0.05 mm for this particular study, which is half of the image resolution.

The z-axis (out of plane) was neglected and the models were restricted to three degrees of freedom. Plane strain element was assigned in this case. Hence the entire acetabulum and femur were treated as long beams with constant cross-section as sketched in the model geometry. The effect of the circumferential resistance in the labrum was therefore ignored, which would cause higher apex deformation in soft tissues. The variation in the cross-section geometry along the out-of-plane direction was also missing in the model. The cartilage layer was compressed and expanded within the socket during experimental loading. The acetabular expansion may explain the higher cartilage strain in the experiment than in the 2D model. However, the use of 2D models help improve the model stability when solving complex problems with linear elastic material experiencing large strains and rapid changes in geometrical features. Even though, the model for sample PH12 failed to complete under the experimental loading scenario applied. In addition, 2D models substantially reduces the computational cost, and makes large parametric studies viable. It is suggested that for FE study of the whole hip joint *in situ*, a 3D model is necessary for representation of the full geometry and for investigation of the tissue behaviour in all degrees of freedom.

Both baseline models had a thicker acetabular cartilage than the real specimens in the 2 mm closest to the acetabular rim. This was due to the 3-mm fillet added to the bone edge, and caused the model to underestimate overall cartilage strain in that region. The rest of the modelled acetabular cartilage fitted well compared to the tissue scan for PH12. Variation was observed on the outer cartilage surface (Figure 5.46) in PH10 which makes it difficult to fit onto one single arc. The excessive cartilage outside the arc would cause a low assumption of the overall acetabular cartilage strain in the model. The gap between the fitting curve and the actual cartilage surface would cause an overestimated cartilage thickness in the model. It is clear that the capture of the original cartilage thickness is key to the investigation of cartilage deformation. Spline, with more reference point than a three-point arc, may be fitted to the original acetabular cartilage, particularly when the tissue sample has a rough cartilage surface.

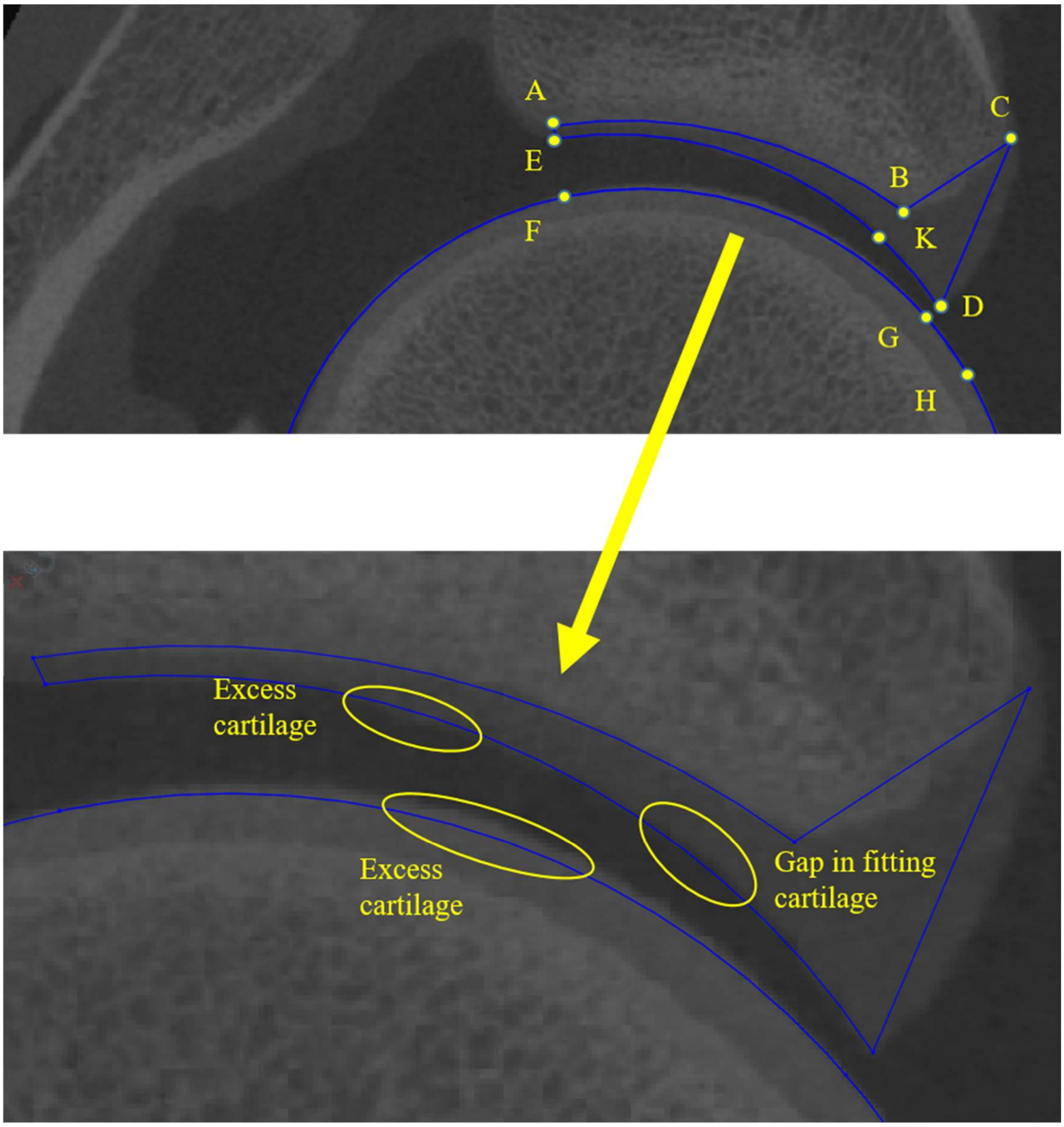

**Figure 5.46 Error in arc-fitting on outer cartilage surface in PH10**

Concave cartilage surface, as the natural feature of the tissue, was found on the femoral articular cartilage in PH12 (Figure 5.47). The end of the ligament of the head of femur was involved in the experimental loading, for PH12 (Figure 5.47). The ligament tissue was treated as cartilage in the FE models and would cause high assumption in the overall acetabular cartilage strain. Besides, the radius of the femoral cartilage was defined by the femur outline at the contact region. The femoral cartilage was treated as a sector of a perfect circle. However, neither porcine or human femur has a spherical shape. Cooper et al. (2017) fitted ellipses at the head-neck junction and fitted circles at the head cap, to represent and parameterise the human femoral head. The poor fit in the femoral head shape and femoral cartilage would lead to low strain assumption and bad conformity in the hip joint. The current FE model provides simple geometry and can be used for mechanical characterisation under various cartilage-labral junction conditions. Spline, with more reference points than a three-point arc, may be fitted to the original femoral cartilage, for better representation of the femoral cartilage surface.

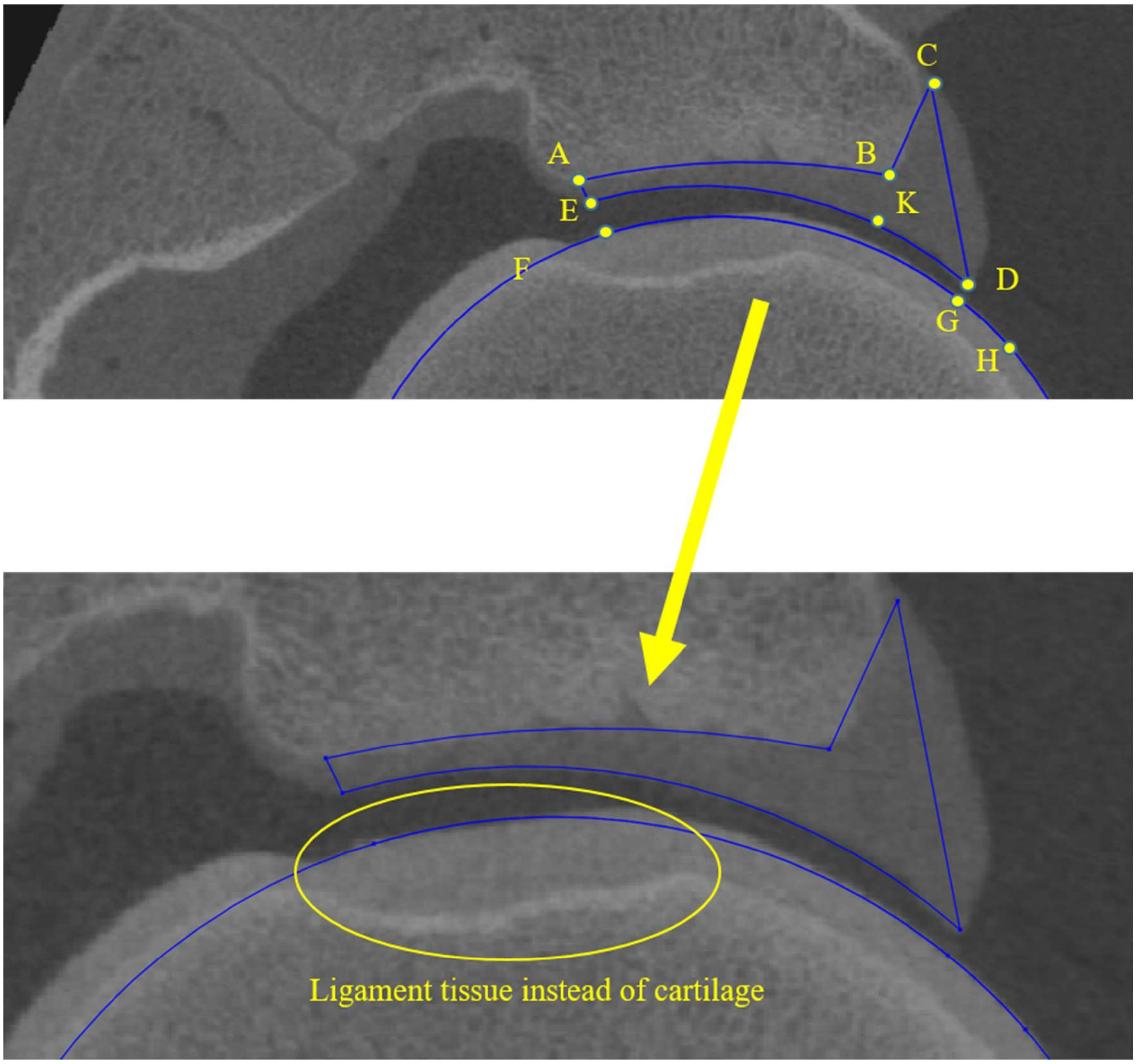

**Figure 5.47 Error in arc-fitting on outer femoral cartilage in PH12**

Bone tissue was considered rigid in previous finite element studies (Ferguson et al., 2001 and Hellwig et al., 2016). Li et al. (2013) reported that the difference in contact stress was within 5% between representing all cortical bone and representing all trabecular bone. It is convincing that the modulus of either bone type is much higher than that of the soft tissues. The subchondral bone in this study was not modelled and represented by the constraints on the subchondral cartilage surfaces. Soft tissue then deformed to wrap around the bone edge due to shortage of bone support. An extended rigid bone plate was tied to the subchondral cartilage surface to model the complete bone tissue. It is suggested to define surface contact between the bone plate and outer soft tissue surface in order to prevent soft tissue from “penetrating” the subchondral bone surface. In addition, the subchondral bone surface at the rim could be playing a role in the impingement loading since the cartilage-labral junction was targeted. It is worth investigating the effect of bone deformation when edge loading is involved.

The labrum was fitted in a triangular shape, losing part of the external tissues. The labrum was simplified and modelled as isotropic linear elastic material, hence stiffer and less conforming with the femoral head. The local deformation may be even overestimated due to the absence of circumferential stress since the model was generated from a 2D image slice. However, the computational apex displacement were about 8.7% smaller than that in the experimental study for PH10, and 47.4% smaller when the model was 40% away from completion. This suggests that the location of maximum labrum apex displacement was not coincident with the selected 2D image slice at the focused contact region.

The computational total contact force was much lower than the experimental reaction force for both samples. The main reason is that the total contact force was actually a component force of the total reaction force, since the two-dimensional displacement was derived and measured from 3D image. Remaining differences in the reaction force would be related to other components undertaking the force in the system, such as growth plates, bones, or tissue pots.

When the labrum Young’s modulus was increased, the cartilage-labral junction became stiffer, therefore the cartilage was constrained by the labrum from expanding laterally. Consequently, the labrum carried a higher percentage of the contact force in the acetabulum total contact force. It is clear that the ratio between the cartilage and labrum material properties plays a role in the tissue behaviour near the cartilage-labral junction. However the cartilage inside the socket was not affected too much, beyond 3.5 mm to the rim in particular.

The cartilage-labral junction was simplified and treated as a straight line across the cartilage. The biological structure of the transition zone is discussed in Chapter 6. From modelling perspective, the abrupt change of material properties would lead to spurious strain concentration at the transition line. The overall cartilage strain increased as the junction shifted outwards from the socket, effectively increasing the amount of cartilage tissue being involved at the contact site. Since the cartilage had a lower Young's Modulus, the soft tissues in contact was easier to deform. Similarly, the cartilage undertook more percentage of the contact force as the junction location being shifted outwards from the socket. The cartilage tensile strain decreased in model PH10 since the junction was shifting away from the contact site. Peak cartilage tensile strain was observed when junction location was shifted 1 mm outwards from the socket in PH12. The direction of femur movement was coincident with the transition line after shifting therefore the increase in tensile strain was observed. Depending on the conformity of the hip joint and the direction of femoral head movement, the location of cartilage-labral junction can affect the soft tissue behaviour across the acetabular radius. It is important to correctly model the junction in order to investigate the load condition targeted at the acetabular edge.

The femora head position, alternatively the conformity of the hip joint, plays a key role regarding the cartilage behaviour due to load. The overall cartilage strain was most sensitive to the femoral head position. The cartilage strain in PH10 increased along with smaller slope of decrease across the bone support when femoral head was offset by 1 mm inwards the socket. The conformity in the hip was improved hence the contact initiated in the soft tissues at an earlier stage of the load step. The cartilage strain in PH12 also increased but along with a positive rate of increase across the bone support. Good conformity was established and the femoral head was pushed inwards due to the resistance from the arc-shaped labrum outline. Contact force in cartilage decreased quickly when femoral head was shifted outwards from the socket because less cartilage tissue was involved in the contact site. Consequently, the labrum undertook higher percentage of the acetabulum total contact force. Cartilage tensile strain decreased both ways due to the offset of femoral head, effectively changing the location of the contact site. The experimental loading scenario aimed at applying axial load onto the cartilage-labral junction. However, by offsetting the femoral head, the contact site did not focus on the junction any more. This finding demonstrated that the load distribution in the soft tissue is closely related to the head position and head shape. From the anatomy perspective, the abnormality in head shape (cam), or inversely in acetabulum (pincer), does lead to extreme mechanical environment in the hip joint. From the research perspective, the alignment of joint position, or representation of femoral head, is crucial to the study of soft tissue behaviour.

The FE models managed to represent the variation in acetabular cartilage by two arcs. However there was local features in the natural tissue that made the full geometry difficult to capture. The overall cartilage strain was sensitive to femoral head position, effectively the conformity of the hip joint. High cartilage tensile strain was observed when the femoral head aimed at applying concentrated force onto the cartilage-labral junction. Labrum, as a stiffer material to the cartilage, played a key role in protecting the cartilage circumferentially, but also undertook increasing contact force when labrum properties was strengthened.

The current FE model uses a highly refined mesh for smooth strain field across the cartilage and labrum. Bone could be modelled as deformable under this 2D model that allow wider view of load response in the joint. The model also included fine details of the cartilage-labral junction while allowing large parametric studies within reasonable runtime. It is possible to build understanding on the effect of acetabular parameters regarding the soft tissue behaviour under load.

The established computational methodology can be used for further investigation of soft tissue behaviour at specific region on the acetabulum. By varying the geometry and loading conditions, various pathology loading may be investigated, such as pincer-type FAI and dysplasia, in terms of the soft tissue behaviour and sensitivity studies. The model can also be used for investigating the role of labrum, or even the labrectomy case (Kim et al., 2018) by comparing the contact metrics between the two types of tissue.

The local soft tissue behaviour can be investigated in a more realistic way if the FE models is developed in 3D space. The conformity was crucial in the load response of soft tissues. Therefore, both acetabular and femoral cartilage surface require accurate capture of geometry. More comments on resolution and improvement of loading scenario is discussed in Chapter 6.

# Chapter 6

# Overall discussion and conclusions

## 6.1 Summary of achievements

The experimental methodology was successful in creating contact patch at the superior-anterior portion of the acetabulum across all porcine hip samples. The contact patch on the femoral head was not consistent with the ligament of the head of femur joining the contact region. Focused compressive loading was applied axially, reflecting part of the impingement situation in cam-type FAI, onto the cartilage-labral junction across all porcine hip samples. The effect of labrum circumferential tension, reflecting soft tissue lesions such as labrum tear in clinic, was also investigated. The followed image processing was successful in registering the bone tissue before and during load where the error in thickness was roughly within the image resolution. The *in situ* acetabular cartilage strain and labrum apex displacement was measured after loading, implying the possible damage mechanism for cartilage defibrillation and labrum tear.

Overall cartilage strain was measured on a selected 2D image plane near the centre of the contact region. Labrum apex displacement was measured in 3D on the reconstructed labrum apex point cloud. The cartilage strain was up to 67% and the labrum maximum displacement was up to 5.0 mm, subject to individual loading scenario. A generalised labrum cut coefficient (lcc) was found at 1.4, meaning the labrum maximum displacement was increased, in the cut cases, to 1.4 times of that in the load cases.

Finite element (FE) models were developed for comparison with the experiment and for parametric studies. FE models were generated based on two out of six tissue samples. The remaining samples were neglected due to inappropriate labrum surface or unexpected direction of femoral head movement. The modelled acetabular cartilage had an error within 0.25 mm in thickness compared to the tissue sample. The overall cartilage strain ranged from 19% to 34% and the labrum apex displacement ranged from 2.0 to 2.2 mm at the selected cross-section view on which the models were based. The FE study showed lower acetabular cartilage strain than the experimental study did.

Sensitivity studies were conducted on the two FE models on: 1) the femoral head location, evaluating the experiment alignment setup and the conformity of hip joint when there is bone deformity in clinic; 2) the ratio of labrum-to cartilage Young's Modulus, evaluating the degeneration of labrum; and 3) cartilage-labral junction location, evaluating the representation of acetabulum anatomy. The output of interest for each case are: 1) overall acetabular cartilage strain; 2) cartilage tensile strain near the junction; and 3) contact force distribution between the cartilage and the labrum. The cartilage strain and load distribution in soft tissues were found to be sensitive to the femoral head position, with strain differences up to 41% and cartilage contact force differences up to 237% when the head position was adjusted by 1 mm. Labrum Young's modulus affected the tensile strain at the cartilage-labral junction by up to 14% when labrum properties were adjusted by 25% of the original value. The position of cartilage-labral junction shown effect on the total contact force on the soft tissue by up to 49% when the junction was adjusted outwards from the acetabular socket by 1 mm.

## 6.2 Experimental investigation of soft tissue behaviour

The experimental methodologies developed in this study enabled measurement of local acetabular cartilage strain and radial labrum apex displacement under load. The alignment tools allowed replication of loading scenario related to cam-type FAI. The methods can be applied to future investigation of *in situ* soft tissue behaviour under various loading conditions such as dysplasia, impingement, or specified load cycles.

Overall cartilage strain between 10% and 67% was observed under displacement-controlled loading up to 4.6 mm. Maximum labrum apex displacement was measured at between 1.5 mm and 5.0 mm, following an applied load of 230N for one hour. A generalised displacement-force relationship, the labrum cut coefficient (lcc), was calculated to assess the extent of labrum maximum displacement before and after labrum cut. The labrum cut was proved to have an impact on the labrum that makes the labrum apex easier to deform under load when the value of lcc is greater than one. The lcc was found at 1.4±0.3 for all six samples, meaning the labrum cut contributed to the increase of maximum labrum displacement by 1.4 times of that in the hip with intact labrum. The contact patch was visually consistent for the intact and cut cases for each sample, however the effect of tissue re-loading is worth investigating in the future.

The labrum cut cases demonstrated the circumferential constraint in the labrum since increase in apex displacement was found after the labrum cut. The cut site was offset from the focused contact region at the posterior region, but still close to the edge of the contact patch. The location of peak apex displacement shifted towards the centre of the contact region in five out of six samples. The circumferential tension in the labrum may be more important when the cut site is on top of the cam entry. From the modelling perspective, 3D models would be required for investigation of labrum cut, as the pattern of labrum movement shifted in the circumferential direction. From the clinical perspective, labrum tear in the cam-type FAI would lead to excessive deformation of the labrum and accelerate the damage progression.

In this thesis, there was no clear increase in overall cartilage strain due to the labrum cut. However, Ito et al. (2017) reported a reduction in acetabular cartilage thickness of 20.4% due to the labral excision. Canine hip joints were loaded at 80kg for 2.5 hours before and after labral excision. The overall cartilage strain was reported at 35.3±17.4% with intact labrum and at 55.7±7.5% with labral excision. The work demonstrated the load bearing role of the labrum. It is reasonable that a full excision of the labrum would leave the cartilage edge exposed so that the fluid could flow out more easily, compared to the labrum cut in this thesis.

In this thesis, cam FAI was replicated by offsetting and loading the femoral head towards the cartilage-labral junction. Siebenrock et al. (2012) induced the loading scenario in ovine hip joint. Although ovine hip is considered to have a shallower socket, the femoral shape is considered to be similar to a flattened human femur with a cam abnormality. Labrum detachment from the adjacent cartilage, cartilage erosion and cartilage flap were reported after simulation of the ovine hip joint. The damage patterns agreed well with patients with cam FAI. It can be learned that the cam portion, in the cam FAI, is shearing at the cartilage-labral junction that pushes the labrum away from the junction while shearing the cartilage inwards from the acetabular socket. In this thesis, the shearing effect was not assessed since the rotation of femoral head was not included. It remains challenging to include four degrees of freedom in limited space for the microCT machine.

Greaves et al. (2010) studied the effect of labrum at four stages: 1) intact labrum; 2) torn labrum; 3) repaired labrum; and 4) resected labrum. The mean maximum femoral cartilage strain was reported at 45.2±9.0% and 46.2±7.4% for intact and torn labrum, respectively. No clear effect of the labrum cut was found in the torn labrum case. The mean maximum strain increased to 50.0±6.0% in the resected labrum case, which demonstrated the load bearing role of the labrum.

Static tests were performed throughout this thesis in order to obtain scanned images of the hip joint. The FAI-related load was applied up to two times to the soft tissues, whereby soft tissue damage was believed to be associated with repetitive movement (Leunig et al., 2009; (Agricola and Weinans, 2016). The time-dependent properties of soft tissues were also ignored in a static test. Rudert et al., (2014) inserted hip contact stress sensors between the femoral head and the acetabulum during hip movement. Dynamic hip contact stress may be recorded for investigation of the damage progression in cam-type FAI.

## 6.3 Computational analysis of cam-type FAI

Sensitivity tests on the labral material properties and cartilage-labral junction location helped illustrate the role of the labrum in the cam-type FAI. Increase in the labral Young's Modulus reduced the cartilage tensile strain near the cartilage-labral junction. The increase in labrum contact force at the same time demonstrated the protective function of the labrum. Since the FE models were generated in 2D, the circumferential effect of the labrum was ignored. This simplification may result in increased labral displacement, increased cartilage strain and decreased labrum contact stress, since the circumferential "sealing" effect is absent.

The location of cartilage-labral junction may affect the cartilage strain across the acetabulum radius, depending on the conformity of the hip joint. The cartilage may experience higher strain if there is less coverage of labrum. For the same loading scenario that aimed at the cartilage-labral junction, the cartilage content became more dominant at the contact region if the location of junction was shifted towards the acetabular rim. Since the labrum has a higher modulus than the cartilage, the cartilage was expected to undertake more load when there is less labrum protecting the cartilage. The total contact force decreased with less labral coverage of labrum. It is worth investigating the junction structure and correctly representing the junction in the model. From species perspective, it is clear that the human hip has richer content of labrum on the acetabular rim than porcine hip does. Therefore, the labrum may play a more important role in load distribution in human hip. From impingement perspective, the cartilage-labral junction may experience lower load than that in porcine hips.

The parametric study concluded that the femoral head position played a key role in the hip contact in terms of the acetabular cartilage strain and load distribution in soft tissues. From the experimental perspective, the femoral head position, relative to the cartilage-labral junction, can be affected by tissue alignment and femoral head shape. The methods of alignment should be carefully established in order to create the proposed loading scenario. For this work the mounting equipment is required to provide rigid and precise fixation of tissue samples before cementing and that fixation needs to be maintained for repeated loading scenarios. The tissue fixation may be improved by covering more cement to support the tissue in the tissue pot. The accuracy of alignment may be improved by adapting advanced mechanism that reduces error in manual operation.

The abnormality in femoral head shape could lead to concentrated hip contact. From the computational perspective, since the shape of the femoral head is important to the load distribution in the acetabulum, the representation of head shape needs to be carefully verified and validated. The shape of the femoral head made it less easy to control the exact position of the contact patch observed in the images. Wesseling et al. (2019) and Anderson et al. (2010) demonstrated the effect of geometry representation when investigating the hip contact. Cooper et al. (2017) established a parameterised methodology for femoral head representation. The femoral neck was fitted with ellipses and the femoral cap was considered spherical. However, the femoral head component could not be fitted with ellipses in this work, since only portion of the femoral head was included.

It is encouraged to apply hip activities to the samples in order to verify the replication of the cam-type FAI loading scenario. Chegini et al. (2009) and Hellwig et al. (2015) both adopted load patterns of normal walking and sitting down in the FE models, with cam on the femoral neck. The gait cycles are available from the work by Bergmann et al. (2003) and could bring variety of hip motions, such as flexion and internal rotation, into the hip contact. This would help build wider understanding on the effects of hip parameters regarding soft tissue behaviour under FAI.

It is suggested that using linear elastic soft tissue properties may overestimate the stress undertaken by the tissues. Hellwig et al. (2015) assigned biphasic properties to the cartilage, resulting in lower contact pressure compared to Chegini et al. (2009) and Jorge et al. (2014). However, from the experimental perspective, the assessment of biphasic material properties of *in vitro* soft tissue remains a challenge.

## 6.4 Comparison with clinical evidence and clinical significance

The applied loading conditions were not complete replication of cam-type FAI, either from anatomical perspective (Tannast et al., 2007), or referring to hip motions (Streit et al., 2012 and Martin et al., 2010). However, the contact region at anterior-superior acetabulum matched with the region of soft tissue damage commonly observed in cam-type FAI (Clohisy et al., 2013). The axial loading at the cartilage-labral junction implied part of the impingement conditions under cam-type FAI.

The labrum apex was found to experience larger displacement when labrum cut was made next to the contact region. This finding demonstrated the labrum circumferential tension and provided evidence of the load sharing role of the labrum. It is suggested that the labrum tear would progress rapidly under impingement-related loading with the existence of labrum lesion.

Higher acetabular cartilage strain was measured when the femoral head was offset further towards the acetabular rim. This type of bad conformity in hip joint could be reflected with impingement conditions caused by femur abnormality. The concentrated strain in cartilage implied the potential damage mechanism for cartilage defibrillation, which is one of the soft tissue lesions associated with cam-type FAI (Kuhns et al., 2015).

The acetabular cartilage at the superficial layer tended to be separated due to focused loading at the cartilage-labral junction. This pattern of soft tissue displacement provided evidence in the separation of cartilage and labrum under cam-type FAI (Banerjee et al., 2011).

The investigation of *in situ* soft tissue behaviour can help better understand the contact mechanism in the hip joint under pathologic loading conditions. In this thesis, the computational results were not well comparable to experimental measurement due to uncalibrated material properties and simplification made in the model development. More realistic tissue behaviour may be predicted and the initiation of damage may be understood if the models were well validated. Various pathologic loading conditions may also be investigated, in short term, regarding the *in situ* tissue behaviour. Conservative activities may be suggested in clinic at early stage of FAI using reverse-engineering.

## 6.5 Key limitations

### 6.5.1 Tissue preparation

The cam-type FAI-related load was applied to the same tissue sample on two occasions in this study, aiming at the superior-anterior portion of the cartilage-labral junction. The effect of the first loading cycle and the extent of recovery were not studied. A control study is necessary that applies the same load case to the tissue sample twice in order to investigate any difference in the second loading. The effect of the first load may contribute to any change in soft tissue displacement throughout the labrum cut cases in this study. Ito et al. (2017) applied static load of 80kg for 2.5 hours on canine hip joints before and after labral excision. Notably, the recovery rate was studied after keeping the tissue in saline solution for 14 hours after the first load. The articular cartilage thickness in the weight-bearing region recovered to 99.7±3.9% of the original thickness. Greaves et al. (2010) allowed 16.5 hours of recovery with PBS solution for human hips for a total of four loading scenarios. It is reported that the cartilage thickness tended to increase every time, with the coefficient of variation between each two consecutive procedures were within 3.5%. In this thesis, tissues were stored in a fridge and covered with PBS overnight for at least 16 hours between each test. Reasonable recovery time was allowed, based on the literature, and the effect of re-loading was expected to have an percentage error up to 7.6% in the strain.

The existence of the growth plate allowed the superior portion of the acetabulum to deform more easily. The deformation in bone would cause error during registration where the bone was considered rigid, and result in overestimated strain in the acetabular cartilage. From experiment perspective, it is suggested to use mature tissue samples to eliminate the influence of growth plates. Roels et al. (2014) reported the effect of growth plate that under hip external rotation, the growth plate is most likely to stimulate the development of cam FAI in the long term. It is clear that an open growth plate has effect on the contact mechanism in the hip joint.

To allow the use of cling film, the capsule had to be removed throughout the experiment. The stability and constraint provided by the capsule (Stewart et al., 2004; Elkins et al., 2011) were therefore neglected during loading. The capsule seals the hip joint and maintains synovial fluid in the contact. Previous studies reported that the capsule contributes to rotational constraints and construct stability (Arkel et al., 2015; Elkins et al., 2011). The soft tissue displacement at acetabular rim could be overestimated since the sealing effect from capsule was ignored. Studying the complete hip joint with intact capsule would be preferable in order to investigate the mechanical environment of the full hip in contact.

A cam-type FAI-related loading scenario was created that targeted the cartilage-labral junction. The alignment was challenging and the space for holding the tissue was also limited. The contact patch, effectively the actual contact region, appeared at the superior region in all tissue samples. However, the sample PH14 was loaded at the cartilage-labral junction through compressing into the labral rim. The femoral head should avoid moving straight into the labral rim (i.e. from labrum apex towards the subchondral bone). The femoral head ought to displace normal to the labrum surface, starting from the cartilage-labral junction. This concentrated loading at the junction replicated the excessive loading in the real FAI scenario when the cam is already in contact with the cartilage-labral junction. The rotation of the cam moving into the acetabulum socket was not included, restricted by the axial loading rig. Hence the shear force in the contact surfaces was not assessed, as the shear effect would be very small compared to the real FAI scenario. In addition to the load conditions, the labrum overhang was involved in the contact in three out of six samples, and the ligament of the femoral head was involved in the contact in two out of six samples. The labrum overhang added difficulties in the FE modelling. The ligament of the femoral head led to an overestimation of the acetabular cartilage strain. It is clearly suggested that larger tissue pots are preferred to allow more space for creating appropriate loading scenario relevant to cam-type FAI. Larger angle would then be allowed between the femur and the acetabulum, creating space for alignment and avoiding contact with the overhang.

As an alternative to offsetting the porcine femoral head towards the cartilage-labral junction at the acetabular rim, the ovine hip joint may be used. Siebenrock et al. (2012) induced cam impingement in ovine hip by performing a 15° intertrochanteric varus osteotomy on the ovine femur. The natural ovine femur has a flattened head-neck junction which is similar to a human femur with cam-type abnormality. The sheep were allowed to roam free after the operation. The study was able to assess the damage to soft tissues due to FAI under *in vivo* environment in sheep.

### 6.5.2 Tissue imaging

Soft tissue behaviour under load was investigated and quantified *in vitro* for six porcine hip joints. The precision of the measurement of soft tissue displacement was limited by image resolution. The image resolution was 82 μm in the CT scanner and increased to 0.1 mm in the image processing, constrained by the computer processing time. The acetabular cartilage thickness, as measured from CT images, varied between 0.5 mm to 2.5 mm, meaning the image resolution can account for up to 20% of the thickness. In addition, the cartilage experienced strain between 10% and 67%, as measured from CT images. The image resolution can be responsible for a strain measure of ±10%, regarding a cartilage thickness of 1.0 mm. Therefore, images with higher resolution, around 50 μm, are preferred to capture and investigate the cartilage deformation due to load.

CT imaging reflects the bone in detail, while MR imaging could provide additional information on soft tissues such as the labrum and cartilage. However, the MR scans, for assessment of people with FAI, usually allow an image resolution between 0.3-0.5 mm (Samaan et al., 2017; Ito et al., 2017) and slice thickness between 3-4 mm (Samaan et al., 2017; Kaddah et al., 2017). The clinical MR equipment allows reasonable field of view of up to 20cm and is used for static diagnosis in clinical studies. But the clinical MR is not suitable for measuring soft tissue displacement where the resolution accounts for more than a third of the cartilage thickness. Even though it is possible to generate isotropic high resolution images using MR equipment for research purpose, the limitation is that any metal components is not allowed in the loading rig. In this work, for ease of access and precision of deformation measurement, the CT machine with image resolution of 82 μm nominal isotropic was used. On the other hand, any increase in the resolution of the images translates into an increase in the computational resource needed for the image processing and tissue deformation calculations. Balancing between the measurement accuracy and computational cost, the resolution was further increased to 0.1 mm. For an averaged cartilage thickness of 1 mm, the error from images is already responsible for ±10% in the cartilage strain. It is still a challenge of hardware for monitoring soft tissue deformation at an adequate resolution.

Separation of the acetabular soft tissue surface, from the femoral surface, was successful in the CT image with the aid of NaI solution. However, the soft tissue visualisation was only possible on one side of the hip joint, either the femur or the acetabulum. The NaI can be absorbed across the cartilage thickness and mixed up with subchondral bone in the images. In the experimental study of this work, the femoral head was applied with the contrast agent and wrapped with cling film to prevent the solution being transferred onto the acetabulum side.

The soft tissues from both sides, acetabulum and femur, were successfully separated in the image segmentation at the contact patch. The acetabular soft tissues at the region of interest were clearly isolated for measurement before and during load. Only the posterior portion of the acetabular rim was not clearly separated after automated segmentation. Manual operation was required to separate the posterior acetabulum from the femoral neck. During preparation the tissue samples, only femoral head was soaked into the contrast agent. Therefore, any contact between acetabular rim with femoral neck would still be a “soft on soft” contact without the aid of radiopaque solution, which leads to similar greyscale in the CT images. The hip joint should either avoid contact at the posterior region, or to be applied with contrast agent at the femoral neck, in order to separate the soft tissue surfaces on each side at posterior region.

The CT images were segmented and compared before and during tissue loading, in order to obtain a cross-sectional image slice at the centre of the contact patch. The acetabular cartilage strain was calculated on the selected image slice as the change in total cartilage thickness. The strain measurement not only monitored the cartilage movement *in vitro* under FAI-related loading, but also provided quantified output for comparison with FE models. Labrum apex displacement was investigated in 3D space and measured almost in radial direction. Since rotation of the femoral head was not considered in the loading scenario, the circumferential movement of labrum may be neglected. The measurement of labrum apex displacement not only helped determine the location of maximum labrum movement under FAI-related loading, but also assessed the effect of labrum cut on the labrum movement. Due to the ellipsoidal shape of the porcine femoral head, the peak cartilage strain and peak labrum displacement did not necessarily occur at the same position on the acetabulum. Therefore, the labrum movement was also obtained at the centre of contact patch for comparison with FE models.

### 6.5.3 Computational modelling

Four out of six samples were eliminated for the computational studies due to labrum folding at the focused contact region. From the modelling perspective, the folded tissue created sharp angle on the contact surface and was also subject to self-contact when the cartilage-labral junction is being loaded. This brings difficulties into the stress analysis and was avoided in this study. From the mechanical perspective, the labral rim was not only be pushed but also squeezed by the femoral head. This is not realistic since the natural labral apex conforms with and seals the femoral cartilage. Loading on such folded tissue may underestimate the labral apex displacement. The labrum fold occurred after disarticulation and before the FAI-related load can be applied. It is important to recover the labrum conformity with the femoral head during alignment and make sure the two components stay reasonably close to each other in the loading rig.

The FE modelling of the porcine hip aimed to capture the individual shape of the acetabulum and to simplify the femoral head with a constant radius. Anderson et al. (2010) analysed the effects of representation of hip joint articular cartilage. The differences in mean pressure was up to 50% of that in the subject-specific cartilage when the cartilage was fitted with sphere or conchoid. In this thesis, acetabular cartilage thickness was measured in both PH10 and PH12 models and compared with the related tissue samples. The cartilage thickness in the FE models demonstrated an error between 5% and 25% of the thickness measured in CT scans. These errors can be caused by the image resolution error. For cartilage with a thickness of 1 mm, the image resolution (0.1 mm) is responsible for 10% of the original thickness. The femoral head was fitted by another arc at the contact region. Although the overall shape of femoral head was not well represented, the femoral cartilage region that in contact with the acetabulum was well captured. With the error in total thickness capture, the cartilage strain could be influenced by the same percentage, as long as the deformation was kept the same in experimental and computational studies. Further error can be caused by the assumption of fitting one arc to the cartilage surface which is not always as smooth as a perfect arc. Success was demonstrated in PH12 by fitting the smooth acetabular cartilage surface with two three-point-arc. The percentage difference was smaller than that caused by image resolution. The variation in cartilage thickness was also captured across the acetabulum radius. However, for rough cartilage surface in PH10, a spline with more reference points may be suggested as a better representation of the variable thickness.

Two isolated arcs were used to capture the variation in the acetabular cartilage thickness. The geometry capture worked well in sample PH10, with a percentage error within 0.24% in the thickness. The percentage error was up to 25% (0.25 mm) for sample PH12 due to the roughness on the articular cartilage surface. The computational cartilage strain was lower and showed a smoother trend, compared to the experimental results. This finding agreed with Anderson et al. (2010) who investigated the effect of simplified joint geometry on the cartilage contact stress. It is reported that smoothed articular cartilage underestimated the pressures and provided evenly distributed patterns of contact.

The representation of the sub-chondral bone provided challenges for both model stability and cartilage thickness representation. The subchondral bone formed beneath the acetabular cartilage and stopped around the cartilage-labral junction. Hence the subchondral bone formed a sharp angle in the geometry and made the model difficult to solve. A fillet was added to the bone edge in order to help the model solution to progress, while overestimating the cartilage thickness at the corner. This assumption could lead to low overall cartilage strain at the rim, since the total thickness has been increased while creating the fillet. Alternatively, a thin layer of deformable bone may be suggested to spread the stress between soft tissue and rigid bones.

In addition, Anderson et al. (2010) showed that models with rigid bones resulted in higher pressure than model with deformable bones. This makes it challenging to find a balance between geometry representation and computational cost. The contact stress may be overestimated in an impingement model.

The cartilage-labrum junction was represented by a straight line across the cartilage thickness. The abrupt change of tissue structure is not true in natural tissues and would result in concentrated stress at the junction. The load distribution between cartilage and labrum was also dependent on the location of such transition line of tissue types. A transition zone was reported in both porcine and human acetabular rim (Pallan, 2016). Further investigation on the cartilage-labral junction location has demonstrated that the load distribution in cartilage and labrum was dependent on the location of such “transition zone”. Gradual change in material properties is necessary for realistic load distribution in the acetabular soft tissues, as well as to avoid concentrated pressure from modelling perspective.

The capsule was not included in the FE models, keeping consistent from the experimental studies. However, Elkins et al. (2011) and Stewart et al. (2004) both highlighted the importance of capsule in dislocation resistance. From the morphological perspective, the cam abnormality is defined where the femoral head stops being spherical or ellipsoidal. During cam-type FAI, the acetabular rim does not conform with the cam shape and deforms outwards from the socket due to femur rotation. By ignoring the stability provided by the capsule, the contact force may be overestimated in the cartilage and labrum if the capsule was neglected.

## 6.6 Future work

From the experimental perspective, the loading conditions may be expanded to include hip rotation and to replicate specific hip motions that tend to cause cam-type FAI. The methodology may be applied to human tissues to obtain more realistic geometry when investigating the tissue behaviour.

From the modelling perspective, the model may be developed in 3D to better represent the geometry of specimens. The material properties may be calibrated in terms of the tissue behaviour measured *in situ*.

From the clinical perspective, the sample may be aligned in the position that is more relevant to cam-type FAI. The parameters such as alpha angle may be represented to allow comparison with clinical situation. The methodology may be further applied to wider range of pathologic loadings, such as pincer-type FAI and dysplasia, to better understand the damage mechanism. By applying reverse engineering, conservative hip activities may be concluded as early-stage treatment for hip abnormality to slow down the damage progression.

## 6.7 Conclusion

In this thesis, acetabular soft tissues were separated in CT scan, for the investigation of 2D overall cartilage strain and 3D labrum apex displacement. Semi-subject-specific finite element models were developed, for comparison with the experimental results and for parametric study on the acetabular soft tissue behaviour. The circumferential effect of acetabular labrum was reported. The soft tissue behaviour was sensitive to the femoral head shape and position. It is highlighted that accurate sample alignment and 3D modelling are preferred. By investigating the *in situ* tissue behaviour, damage mechanism under pathologic loadings can be better understood if the models were well calibrated.

# Bibliography

Agricola, R., & Weinans, H. (2015). What causes cam deformity and femoroaccetabular impingement: still too many questions to provide clear answers. *British Journal of Sports Medicine, 50*, pp.263-264.

Agricola, R., Heijboer, M. P., Bierma-Zeinstra, S. M., Verhaar, J. A., Weinans, H., & Waarsing, J. H. (2013). Cam impingement causes osteoarthritis of the hip: a nationwide prospective cohort study (CHECK). *Clinical and epidemiological research, 72*, pp.918-923.

*Anatomical Planes*. (2014). Retrieved from Wikimedia commons: https://upload.wikimedia.org/wikipedia/commons/thumb/3/31/Anatomical_Planes.svg/650px-Anatomical_Planes.svg.png

Anderson, A. E., Ellis, B. J., & Maas, S. A. (2008). Validation of Finite Element Predictions of Cartilage Contact Pressure in the Human Hip Joint. *Journal of Biomechanical Engineering, 130*, pp.1-10.

Anderson, A. E., Ellis, B. J., Maas, S. A., & Weiss, J. A. (2010). Effects of idealized joint geometry on finite element predictions of cartilage contact stresses in the hip. *Journal of Biomechanics, 43*, pp.1351-1357.

Arkel, R. J., Amis, A. A., Cobb, J. P., & Jeffers, J. R. (2015). The capsular ligaments provide more hip rotational restraint than the acetabular labrum and the ligamentum teres. *The Bone and Joint Journal, 97-B*, pp.484-491.

Ateshian, G. A., Ellis, B. J., & Weiss, J. A. (2007). Equivalence between short-time biphasic and incompressible elastic material responses. *Jouranl of Biomechanical Engineering, 129*(3), pp.405-412.

Banerjee, P., & Melean, C. R. (2011). Femoroacetabular impingement: a review of diagnosis and management. *Current Reviews in Musculoskeletal Medicine, 4*, pp.23-32.

*Basic anatomy of the hip joint*. (2011). Retrieved from Wikimedia commons: https://upload.wikimedia.org/wikipedia/commons/5/5f/Figure_1._Basic_anatomy_of_the_hip_joint.png

Beck, M., Kalhor, M., Leunig, M., & Ganz, R. (2004). Hip morphology influences the pattern of damage to the acetabular cartilage. *The Journal of Bone and Joint Surgery, 87-B*(7), pp.1012-1018.

Bergmann, G., Deuretzbacher, G., Heller, M., Graichen, F., Rohlmann, A., Strauss, J., & Duda, G. N. (2001). Hip contact forces and gait patterns from routine activities. *Journal of Biomechanics, 34*, pp.859-871.

Bieri, M., Beck, M., Limacher, A., Wyatt, M. C., Leunig, M., Jüni, P., & Reichenbach, S. (2018). Increased subchondral bone thickness in hips with cam-tyupe femoroacetabular impingement. *HIP International, 29*(4), pp.430-437.

Bint-E-Siddiq, A. (2019). *Mechanical Characterisation and Computational Modelling of Spinal Ligaments.* Leeds: University of Leeds.

Brandt, K. D., Radin, E. L., Dieppe, P. A., & Putte, L. v. (2006). Yet more evidence that osteoarthritis is not a cartilage disease. *Annals of the rheumatic Diseases, 65*, pp.1261-1264.

Bsat, S., Frei, H., & Beaulé, P. E. (2016). The acetabuluar labrum: A review of its function. *The Bone and Joint Journal, 98-B*, pp.730-735.

Byrd, J. T. (2013). Femoroacetabular Impingement in Athletes: Current Concepts. *Clinical Sports Medicine Update, 42*(3), pp.737-751.

Chegini, S., Beck, M., & Ferguson, S. J. (2009). The Effects of Impingement and Dysplasia on Stress Distributions in the Hip Joint during Sitting and Walking: A Finite Element Analysis. *Journal of Orthopaedic Research*, pp.195-201.

Clohisy, J. C., Baca, G., Beaulé, P. E., Kim, Y.-J., Larson, C. M., Millis, M. B., . . . Zaltz, I. (2013). Descriptive Epidemiology of Femoroacetabular Impingement. *The American Journal of Sports Medicine, 41*(6), pp.1348-1356.

Cobb, J., Logishetty, K., Davda, K., & Iranpour, F. (2010). Cams and Pincer Impingement Are Dinstinct, Not Mixed. *Clinical Orthopaedics and Related Research, 468*, pp.2143-2151.

Cooper, R. J., Mengoni, M., Groves, D., Williams, S., Bankes, M. J., Robinson, P., & Jones, A. C. (2017). Three-dimensional assessment of impingement risk in geometrically parameterised hips compared with clinical measures. *International Journal for Numerical Methods in Biomedical Engineering*, pp.1-10.

Crawford, M. J., Dy, C. J., Alexander, J. W., Thompson, M., Schroder, S. J., Vega, C. E., . . . Noble, P. C. (2007). The Biomechanics of the Hip Labrum and the Stability of the Hip. *Clinical Orthopaedics and Related Research, 465*, pp.16-22.

Czuppon, S., Prather, H., Hunt, D. M., Steger-May, K., Bloom, N. J., Clohisy, J. C., . . . Harris-Hayes, M. (2016). Gender-Dependent Differences in Hip Range of Motion and Impingement Testing in Asymptomatic College Freshman Athletes. *Journal of Physical Medicine and Rehabilitation*, pp.1-8.

Dalstra, M., Huiskes, R., & Erning, L. v. (1995). Development and Validation of a Three-Dimensional Finite Element Model of the Pelvic Bone. *Journal of Biomechanical Engineering, 117*, pp.272-278.

Dalstra, M., Huiskes, R., Odgaard, A., & Erning, L. v. (1993). Mechanical and Textural Properties of Pelvic Trabecular Bone. *Journal of Biomechanics, 26*(4/5), pp.523-535.

*Diagram of the bony pathology of both cam and pincer impingement*. (2011). Retrieved from Wikimedia commons: https://upload.wikimedia.org/wikipedia/commons/thumb/0/07/Figure_6._Diagram_of_the_bony_pathology_of_both_cam_and_pincer_impingement..png/710px-Figure_6._Diagram_of_the_bony_pathology_of_both_cam_and_pincer_impingement..png

Dy, C. J., Thompson, M. T., Crawford, M. J., Alexander, J. W., McCarthy, J. C., & Noble, P. C. (2008). Tensile Strain in the Anterior Part of the Acetabular Labrum During Provocative Maneuvering of the Normal Hip. *The Journal of Bone and Joitn Surgery, 90*, pp.1464-1472.

Elkins, J. M., Stroud, N. J., Rudert, M. J., Tochigi, Y., Pedersen, D. R., Ellis, B. J., . . . Brown, T. D. (2011). The Capsule's Contribution to Total Hip Construct Stability - A Finite Element Analysis. *Journal of Orthopaedic Research, 29*, pp.1642-1648.

El-Liethy, N. E., Zeitoun, R., Kamal, H. A., & El-Azzeem, A. H. (2019). Magnetic Resonance Arthrography, a valuable pre-operative imaging modality in femoroacetabular impingement. *Egyptian Journal of Radiology and Nuclear Medicine, 50*(79), pp.1-9.

Erasmus, L. J., Hurter, D., Naudé, M., Kritzinger, H. G., & Acho, S. (2004). A short overview of MRI artefacts. *South Africa Journal of Radiology, 8*(2), pp.13-17.

Fagan, M. J. (1992). *Finite element analysis: theory and practice.* Harlow: Longman Scientific & Technical.

Ferguson, S. J., Bryant, J. T., & Ito, K. (2001). The material properties of the bovine acetabular labrum. *Journal of Orthopaedic Research, 19*, pp.887-896.

Ferguson, S. J., Bryant, J. T., Ganz, R., & Ito, K. (2000). The acetabular labrum seal: a poroelastic finite element model. *Clinical Biomechanics, 15*, pp.463-468.

Ferguson, S. J., Bryant, J. T., Ganz, R., & Ito, K. (2000). The influence of the acetabular labrum on hip joit cartilage consolidation : a poroelastic finite element model. *Journal of Biomechanics, 33*, pp.953-960.

Fermor, H. L., Mclure, S., Taylor, S. D., Russel, S. L., Williams, S., Fisher, J., & Ingham, E. (2015). Biological, biochemical and biomechanical characterisation of articular cartilage from the porcine, bovine and ovine hip and knee. *Bio-Medical Materials and Engineering, 25*, pp.381-395.

Ferro, F. P., Philippon, M. J., Rasmussen, M. T., Smith, S. D., LaPrade, R. F., & Wijdicks, C. A. (2015). Tensile Properties of the Human Acetabular Labrum and Hip Labral Reconstruction Grafts. *The American Journal of Sports Medicine, 23*, pp.1222-1227.

Freutel, M., Schmidt, H., Dürselen, L., Ignatius, A., & Galbusera, F. (2014). Finite element modeling of soft tissues: Material models, tissue interaction and challenges. *Clinical Biomechancis, 29*, pp.363-372.

Ganz, R., Parvizi, J., Beck, M., Leunig, M., & Notzli, H. (2003). Femoroacetabular Impingement: A Cause of Osteoarthritis of the Hip. *Clinical Orthopaedics and Related Research, 417*, pp.112-120.

Ganz, R., Parvizi, J., Beck, M., Leunig, M., Nötzli, H., & Siebenrock, K. A. (2003). Femoroacetabular Impingement. *Clinical Orthopaedics and Related Research, 417*, pp.112-120.

Geiger, M., Forasiep, A. M., Koyabu, D., & Sánchez-Villagra, M. R. (2014). Heterochrony and post-natal in mammals - an examination of growth plates in limbs. *Journal of Evolutionary Biology, 27*, pp.98-115.

Gignac, P. M., & Kley, N. J. (2018). The Utility of DiceCT Imaging for High-Throughput Comparative Neuroanatomical Studies. *Brain, Behaviour and Evolution, 91*, pp.180-190.

Goldring, M. B., & Goldring, S. R. (2007). Osteoarthritis. *Journal of Cellular Physiology, 213*, pp.626-634.

Grant, A. D., Sala, D. A., & Davidovitch, R. I. (2012). The labrum: structure, function, and injury with femoro-acetabular impingement. *Journal of Children's Orthopaedics, 6*, pp.357-372.

Greaves, L. L., Gilbart, M. K., Yung, A. C., Kozlowski, P., & Wilson, D. R. (2010). Effect of acetabular larbarl tears, repair and resection on hip cartialgte strain: A 7 T MR study. *Journal of Boimechanics, 43*, pp.858-863.

Groves, D., Fisher, J., & Williams, S. (2017). An in vitro simulation method for the tribological assessment of complete natural hip joints. *PLOS ONE, 12*(9), pp.1-15.

Haider, I., Speirs, A., Alnabelseya, A., Beaulé, P., & Frei, H. (2016). Femoral subchondral bone properties of patients with cam-type femoroacetabular impingement. *Osteoarthritis and Cartilage, 24*, pp.1000-1006.

Hannah, G., Siegmund, G., & Cripton, P. (2016). Comparison os Strain Rosettes and Digital image Correlation for Measuring Vertebral Body Strain. *Journal of Biomechanical Engineering, 138*, pp.1-6.

Hawellek, T., Hubert, J., Hischke, S., Krause, M., Bertrand, J., Schmidt, B. C., . . . Niemeier, A. (2018). Calcification of the acetabular labrum of the hip: prevalence in the general population and relation to hip articular cartilage and fibrocartilage defeneration. *Arthritis Research and Therapy, 20*(104), pp.1-10.

Hellwig, F. L., Tong, J., & Hussell, J. G. (2016). Hip joint degeneration due to cam impingement: a finite element analysis. *Computer Methods in Biomechanics and Biomedical Engineering, 19*(1), pp.41-48.

Hemmerich, A., Brown, H., Smith, S., Marthandam, S., & Wyss, U. (2006). Hip, Knee, and Ankle Kinematics of High Range of Motion Activities of Daily Living. *Journal of Orthopaedic Research*, pp.770-781.

Henak, C. R., Ellis, B. J., Harris, M. D., & Anderson, A. E. (2011). Role of the acetabular labrum in load support across the hip joint. *Journal of Biomechanics, 44*, pp.2201-2206.

Hingsammer, A. M., Miller, P. E., Millis, M. B., & Kim, Y.-J. (2015). Does Periacetabular Osteoytomy Have Depth-related Effects on the Articular Cartilage of the Hip? *Clinical Orthopaedics and Related Research, 473*, pp.3735-3743.

Hogervorst, T., Bouma, H. W., & Vos, J. d. (2009). Evolution of the hip and pelvis. *Acta Orthopaedica, 80*, pp.1-39.

Hua, X., Junyan Li, R. K., Fisher, J., & Jones, A. C. (2015). Geometric parameterisation of pelvic bone and cartilage in contact analysis of the natural hip: An initial study. *Journal of Eningeering in Medicine, 229*(8), pp.570-580.

Ishiko, T., Naito, M., & Moriyama, S. (2005). Tensile properties of the human acetabular labrum: the first report. *Journal of Orthopaedic Research, 23*, pp.1448-1453.

Ito, H., Nakamura, T., Sato, T., Nishida, Y., Tanino, H., & Higa, M. (2017). Early Deformation of Hip Articular Cartilage Under A High Load Before and After Labral Excision. *Journal of Arthritis, 6*(2), pp.1-5.

Jorge, J. P., Simões, F., Pires, E. B., Rego, P. A., Tavares, D. G., Lopes, D. S., & Gasper, A. (2014). Finite element simulations of a hip joint with femoroacetabular impingement. *Computer Methods in Biomechanics and Biomedical Engineering, 17*(11), pp.1275-1284.

Kaddah, R. O., & Khalil, M. E. (2017). MR Arthrography versus conventional MRI in evaluation of labral and chondral lesions in different types of femoroacetabular impingement. *The Egyptian Journal of Radiology and Nuclear Medicine, 48*, pp.169-178.

Kakar, S., Breighner, R. E., Leng, S., McCollough, C. H., Moran, S. L., Berger, R. A., & Zhao, K. D. (2016). The Role of Dynamic (4D) CT in the Detection of Scapholunate Ligament Injury. *Journal of Wrist Surgery, 5*, pp.306-310.

Kapron, A. L., Aoki, S. K., Peters, C. L., & Anderson, A. E. (2014). Subject-specific Patterns of Femur-labrum Contact are Complex and Vary in Asymptomatic Hips and Hips with Femoroacetabular Impingement. *Clinical Orthopaedics and Related Research, 472*, pp.3912-3922.

Kim, Y., Giori, N. J., Lee, D., Ahn, K. S., Kang, C. H., Shin, C. S., & Song, Y. (2019). Role of the acetabular labrum on articular cartilage consolidation patterns. *Biomechanics and Modeling in Mechanobiology, 18*, pp.479-489.

Konrath, G. A., Hamel, A. J., Olson, S. A., Bay, B., & Sharkey, N. A. (1998). The Role of the Acetabular Labrum and the Transverse Acetabular Ligament in Load Transmission in the Hip. *The Journal of Bone and Joint Surgery, 80A*(12), pp.1781-1788.

Kuhns, B. D., Weber, A. E., Levy, D. M., & Wuerz, T. H. (2015). The Natural History of Femoroacetabular Impingement. *Frontiers in Surgery, 2*(58), pp.1-7.

Leunig, M., Beaulé, P. E., & Ganz, R. (2009). The Concept of Femoroacetabular Impingement. *Clinical Orthopaedics and Related Research, 467*, pp.616-622.

Li, J., Hua, X., Jin, Z., Fisher, J., & Wilcox, R. K. (2014). Biphasic investigation of contact mechanics in natural human hips during activities. *Journal of Engineering in Medicine, 228*(6), pp.556-563.

Li, J., Stewart, T. D., Jin, Z., Wilcox, R. K., & Fisher, J. (2013). The influence of size, clearance, cartilage properties, thickness and hemiarthroplasty on the contact mechanics of the hip joint with biphasic layers. *Journal of Biomechanics, 46*, pp.1641-1647.

Li, J., Wang, Q., Jin, Z., Williams, S., Fisher, J., & Wilcox, R. K. (2014). Experimental validation of a new biphasic model of the contact mechanics of the porcine hip. *Journal of Engineering in Medicine, 228*(6), pp.547-555.

Mäkelä, J., Huttu, M., & Korhonen, R. (2012). Structure-function relationships in osteoarthritic human hip joint articular cartilage. *Osteoarthritis and Cartilage, 20*, pp.1268-1277.

Malviya, A. (2016). Pathophysiology of FAI. *Early Intervention in Hip Surgery.* London.

Martin, H. D., Kelly, B. T., Leunig, M., Philippon, M. J., Clohisy, J. C., Martin, R. L., . . . Safran, M. R. (2010). The pattern and Technique in the Clinical Evaluation of the Adult Hip: The Common Physical Examination Tests of Hip Specialists. *The Journal of Arthroscopic and Related Surgery, 26*(2), pp.161-172.

Masjedi, M., Marquardt, C. S., Drummond, I. M., Harris, S. J., & Cobb, J. P. (2013). Cam type femoro-acetabular impingement: quantifying the diagnosis using three dimensional head-neck ratios. *Skeletal Radiol, 42*, pp.329-333.

Meng, Q., Jin, Z., Fisher, J., & Wilcox, R. (2013). Comparison between FEBio and Abaqus for biphasic contact problems. *Journal of Engineering in Medicine, 227*(9), pp.1009-1019.

Miki, H., Yamanashi, W., Nishii, T., Sato, Y., Yoshikawa, H., & Sugano, N. (2007). Anatomic Hip Range of Motion After Implantation During Total Hip Arthroplasty as Measured by a Navigation System. *The Journal of Arthroplasty, 22*(7), pp.946-952.

Moglo, K. E., & Shirazi-Adl, A. (2003). On the coupling between anterior and posterior cruciate ligaments, and knee joiint response under anterior femoral drawer in flexion: a ginite element study. *Clinical Boimechanics, 18*, pp.751-759.

Ng, K. C., Rouhi, G., Lamontagne, M., & Beaulé, P. E. (2012). Finite Element Analysis Examining the Effects of Cam FAI on Hip Joint Mechanical Loading Using Subject-Specific Geometries During Standing and Maximum Squat. *Hospital for Special Surgery, 8*, pp.206-212.

Ng, V. Y., & Ellis, T. J. (2012). Cam Morphology in the Human Hip. *Orthopedics, 35*(4), pp.320-327.

NHS. (2019). *Musculoskeletal*. Retrieved February 26, 2020, from https://www.england.nhs.uk/elective-care-transformation/best-practice-solutions/musculoskeletal/

Nishimura, T., & Hirasawa, Y. (2002). Development of the Acetabulum and the Acetabular Labrum in the Normal Child: Analysis with Radial-Sequence Magnetic Resonance Imaging. *Journal of Pediatric Orhopaedics, 22*, pp.222-227.

Palastanga, N., & Soames, R. (2011). *Anatomy and human movement: structure and function.* Edinburgh: Churchill Livingstone.

Pallan, R. L. (2016). *characterisation and in vitro simulation of the natural hip.* Leeds: The University of Leeds.

Pawaskar, S. S., Grosland, N. M., Ingham, E., Fisher, J., & Jin, Z. (2011). Hemiarthroplasty of hip joint: An experimental validation using porcine acetabulum. *Journal of Boimehanics*, pp.1536-1542.

Pua, Y.-H., Wrigley, T. W., Cowan, S. M., & Bennell, K. L. (2008). Intrarater Test-Retest Reliability of Hip Range of Motion and Hip Muscle Strength Measurements in Persons With Hip Osteoarthritis. *Archives of Physical Medicine and Rehabilitation, 89*, pp.1146-1154.

Ridzwan, M. I., Sukjamsri, C., Pal, B., Arkel, R. J., Bell, A., Khana, M., . . . Hansen, U. N. (2016). Femoral Fracture Type Can Be Predicted From Femoral Structure: A Finite Element Study Validated by Digital Volume Correlation Experiments. *Journal of Orthopaedic Research, 36*, pp.993-1001.

Roels, P., Agricola, R., Oei, E., Weinans, H., Campoli, G., & Zadpoor, A. (2014). Mechanical factors explain development of cam-type deformity. *Osteoarthritis and Cartilage, 22*, pp.2074-2082.

Röling, M. A., Mathijssen, N. M., & Bloem, R. M. (2020). Diagnostic sensitivity and specificity of dynamic three-dimensional CT analysis in detection of cam and pincer type femoroacetabular impingement. *BMC Musculoskeletal Disorders, 21*(37), pp.1-8.

Safran, M. R., Giordano, G., Lindsey, D. P., Gold, G. E., Rosenberg, J., Zaffagnini, S., & Giori, N. J. (2011). Strains Across the Acetabular Labrum

During Hip Motion: A Cadaveric Model. *The American Journal of Sports Medicine, 39*, pp.92-102.

Samaan, M. A., Pedoia, V., Zhang, A. L., Gallo, M. C., Link, T. M., Souzza, R. B., & Majumdar, S. (2018). A Novel MR-Based Method for Detection of Cartilage Delamination in Femoroacetabular Impingement Patients. *Journal of Orthopaedic Research, 36*, pp.971-978.

Seldes, R. M., Tan, V., Hunt, J., Katz, M., Winiarsky, R., & Fitzgerald, R. H. (2001). Anatomy, Histologic Features, and Vascularity of the Adult Acetabular Labrum. *Clinical Orthopaedics and Related Research, 382*, pp.232-240.

Siebenrock, K. A., Fiechter, R., Tannast, M., Mamisch, T. C., & Rechenberg, B. v. (2013). Experimmentally Induced Cam Impingement in the Sheep Hip. *Journal of Orthopaedic Research, 31*, pp.580-587.

Smith, C. D., Masouros, S., Hill, A. M., Amis, A. A., & Bull, A. M. (2009). A biomechanical basis for tears of the human acetabular labrum. *British Journal of Sports Medicine, 43*, pp.574-578.

*Sobo 1909 214*. (2013). Retrieved from Wikimedia commons: https://commons.wikimedia.org/wiki/File:Sobo_1909_214.png

Stewart, K. J., Pedersen, D. R., Callaghan, J. J., & Brown, T. D. (2004). Implementing capsule representation in a total hip dislocation finite element model. *The Iowa Orthopaedic Journal, 24*, pp.1-8.

Streit, J. J., Fortun, C. M., & Salata, M. J. (2012). Cam-Type Femoroacetabular Impingement. *Operative Techniques in Sports Medicine, 20*, pp.295-300.

Tannast, M., Siebenrock, K. A., & Anderson, S. E. (2007). Femoroacetabular Impingement: Radiographic Diagnosis-What the Radiologist Should Know. *The American Journal of Roentgenology, 188*, pp.1540-1552.

Taylor, S. D., Tsiridis, E., Ingham, E., Jin, Z., Fisher, J., & Williams, S. (2011). Comparison of human and animal femoral head chondral properties and geometries. *Journal of Engineering in Medicine, 226*(1), pp.55-62.

Tibor, L. M., & Leunig, M. (2012). The pathoanatomy and arthroscopic management of femoroacetabular impingement. *Bone and Joint Research, 1*, pp.245-257.

Versus Arthritis. (2018). *Osteoarthritis*. Retrieved February 26, 2020, from https://www.versusarthritis.org/about-arthritis/conditions/osteoarthritis/

Walters, B. L., Cooper, J. H., & Rodriguez, J. A. (2014). New Findings in Hip Capsular Anatomy: Dimensions of Capsular Thickness and Pericapsular Contributions. *The Journal of Arthroscopic and Related Surgery, 30*(10), pp.1235-1245.

Wesseling, M., Rossom, S. V., Jonkers, I., & Henak, C. R. (2019). Subject-specific geometry affects acetabular contact pressure during gait more than subject-specific loading patterns. *Computer Methods in Biomechanics and Biomedical Engineering, 22*(16), pp.1323-1333.

Won, Y.-Y., Chung, I.-H., Chung, N.-S., & Song, K.-H. (2003). Morphological Study on the Acetabular Labrum. *Yonsei Medical Journal, 44*(5), pp.855-862.

Zadpoor, A. A. (2015). Etiology of femoroacetabular Impingement in Athletes: A Review of Recent Findings. *Sports Medicine, 45*, pp.1097-1106.

Zapata-Cornelio, F. Y., Day, G. A., Coe, R. H., Sikora, S. N., Wijayathunga, V. N., Tarsuslugil, S. M., . . . Wilcox, R. K. (2017). Methodology to Produce Specimen-Specific Models of Vertebrae: Application to Different Species. *Annals of Biomedical Engineering, 45*(10), pp.2451-2460.

# Appendix A

## Engineering drawing of the acetabulum pot

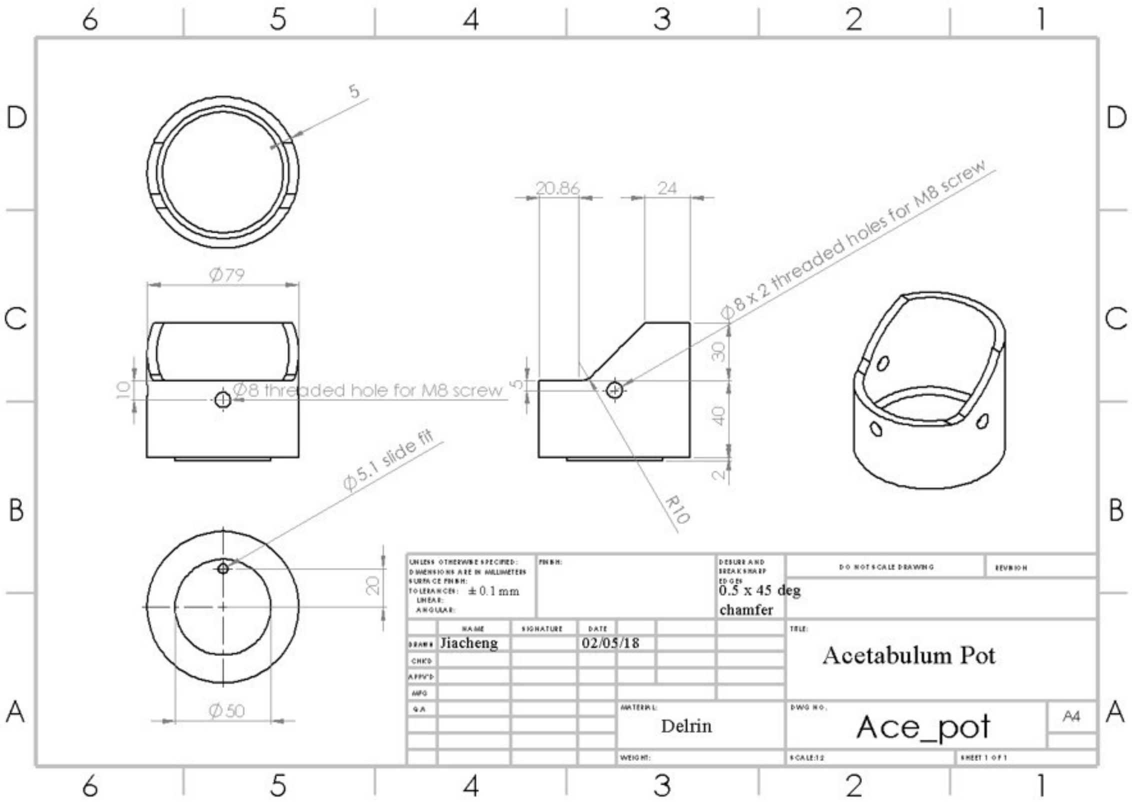

Engineering drawing of the acetabulum pot as described in section 3.4.3.

# Appendix B

## Engineering drawing of the femur pot

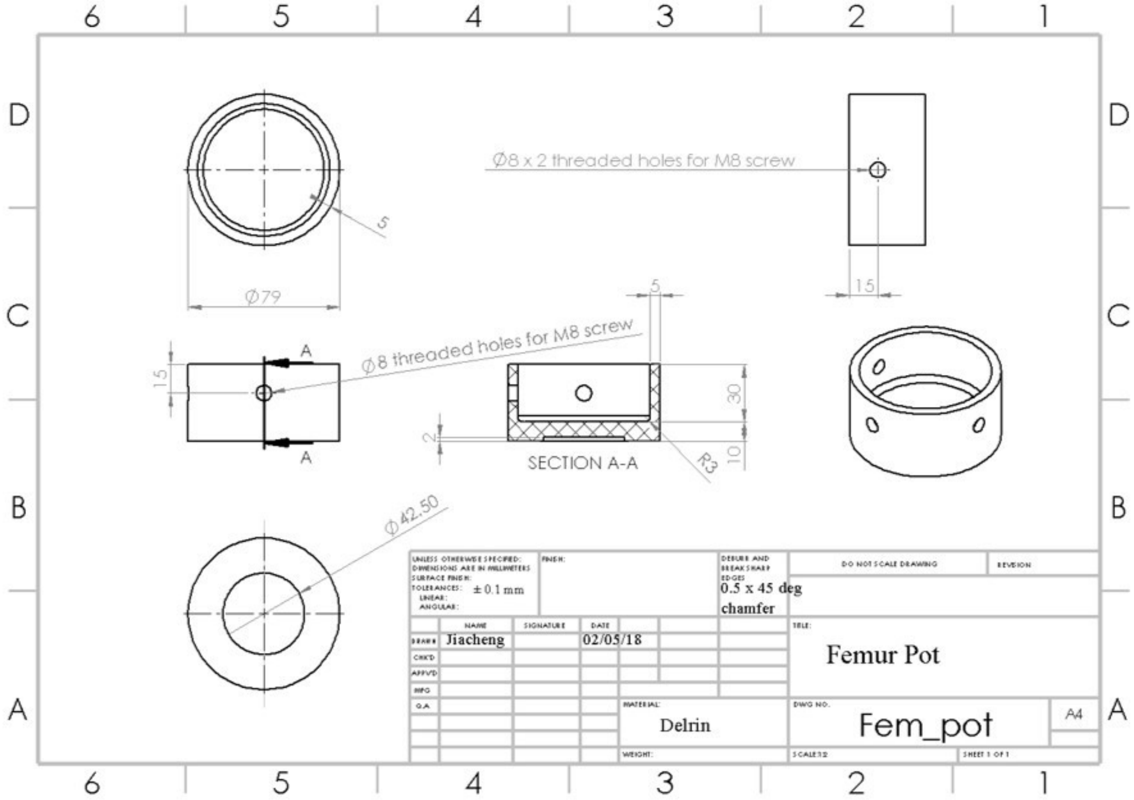

UNLESS OTHERWISE SPECIFIED:
DIMENSIONS ARE IN MILLIMETERS
SURFACE FINISH:
TOLERANCES: ± 0.1 mm
LINEAR:
ANGULAR:
FINISH:
DEBURR AND BREAK SHARP EDGES 0.5 x 45 deg chamfer
DO NOT SCALE DRAWING
REVISION

| | NAME | SIGNATURE | DATE |
|---|---|---|---|
| DRAWN | Jiacheng | | 02/05/18 |
| CHK'D | | | |
| APPV'D | | | |
| MFG | | | |
| Q.A | | | |

TITLE: Femur Pot
MATERIAL: Delrin
DWG NO. Fem_pot
A4
WEIGHT:
SCALE:1:2
SHEET 1 OF 1

Engineering drawing of the femur pot as described in section 3.4.3.

# Appendix C

## MATLAB code for creating acetabulum local coordinate system

```
%% Aim is to develop local coordinate system based on acetabular bone
% Pick three points A, B and C based on local bony features
% Find the projection of C on line AB, point P, so that CP is
perpendicualr
% to AB and intersects AB at P
clear
clc

%% Input coordinates of point A, B and C
title = 'Input coordinates';
prompt = {'Enter point A x:', 'Enter point A y:','Enter point A
z:',...
    'Enter point B x:', 'Enter point B y:', 'Enter point B z:',...
    'Enter point C x:','Enter point C x:', 'Enter point C x:'};
answer = inputdlg(prompt, title);

% Matrices for storing the coordinates of three points
xa = str2double(answer{1});
ya = str2double(answer{2});
za = str2double(answer{3});
xb = str2double(answer{4});
yb = str2double(answer{5});
zb = str2double(answer{6});
xc = str2double(answer{7});
yc = str2double(answer{8});
zc = str2double(answer{9});
CoA = [xa, ya, za];
CoB = [xb, yb, zb];
CoC = [xc, yc, zc];

%% Find equation for line AB
Vab = CoB - CoA; % vector AB, say (j, k, l)
% In this case all the points on line AB allow (x-xa)/j=(y-ya)/k=(z-
za)/l

if Vab(1)*Vab(2)*Vab(3) == 0; % check if AB is parallel to one of the
axis
    if Vab(1) == 0; % AB is in the plane parallel to plane yz
        syms x y z
        eqn1 = Vab(2)*(y-yc)+Vab(3)*(z-zc) == 0;
        eqn2 = (y-ya)*(Vab(3)) == (z-za)*(Vab(2));
        eqn3 = x == xa;
        sol = solve([eqn1, eqn2, eqn3]);
        xsol = double(sol.x);
        ysol = double(sol.y);
        zsol = double(sol.z);
    elseif Vab(2) == 0;
        syms x y z
        eqn1 = Vab(1)*(x-xc)+Vab(3)*(z-zc) == 0;
        eqn2 = (x-xa)*(Vab(3)) == (z-za)*(Vab(1));
        eqn3 = y == ya;
        sol = solve([eqn1, eqn2, eqn3]);
```

```
        xsol = double(sol.x);
        ysol = double(sol.y);
        zsol = double(sol.z);
    else
        syms x y z
        eqn1 = Vab(1)*(x-xc)+Vab(2)*(y-yc) == 0;
        eqn2 = (x-xa)*(Vab(2)) == (y-ya)*(Vab(1));
        eqn3 = z == za;
        sol = solve([eqn1, eqn2, eqn3]);
        xsol = double(sol.x);
        ysol = double(sol.y);
        zsol = double(sol.z);
    end
else
    % Let the dot product of AB and CP to be zero, which gives a whole
plane of
    % points that allow CP to be perpendicualr to AB
    % Find where line AB intersects the plane
    syms x y z
    eqn1 = Vab(1)*(x-xc)+Vab(2)*(y-yc)+Vab(3)*(z-zc) == 0;
    eqn2 = (x-xa)*(Vab(2)) == (y-ya)*(Vab(1));
    eqn3 = (x-xa)*(Vab(3)) == (z-za)*(Vab(1));
    sol = solve([eqn1, eqn2, eqn3]);
    xsol = double(sol.x);
    ysol = double(sol.y);
    zsol = double(sol.z);
end
CoP = [xsol, ysol, zsol];
disp(['The coordinates of point P, which let CP to be perpendicular to
AB, are (', num2str(CoP(1)), ', ', num2str(CoP(2)), ', ',
num2str(CoP(3)), ')']);
%%
figure
if xa == xb;
    ym = [ya, yb];
    yab = min(ym):1:max(ym);
    xab = yab*0+xa;
    zab = (yab-ya)*Vab(3)/Vab(2)+za;
else
    xm = [xa, xb];
    xab = min(xm):1:max(xm);
    yab = (xab-xa)*Vab(2)/Vab(1)+ya;
    zab = (xab-xa)*Vab(3)/Vab(1)+za;
end

plot3(xab, yab, zab) % plot line AB
hold on
grid on
plot3(xc, yc, zc, '*') % plot point C in blue star
plot3(xsol, ysol, zsol, 'r*') % plot point P in red star
```

MATLAB code for creating acetabulum local coordinate system as described in section 3.6.1.

# Appendix D

## MATLAB code for labrum apex reconstruction and measurement

```
%% Function that imports data from text file.
% Script for importing data from specified text file:
%% Initialize variables.
function Nodes = Labrumread(x)
filename = x;
delimiter = ',';


%% Format string for each line of text:
%   column2: double (%f)
%   column3: double (%f)
%   column4: double (%f)
% For more information, see the TEXTSCAN documentation.
formatSpec = '%*s%f%f%f%[^\n\r]';

%% Open the text file.
fileID = fopen(filename,'r');
startRow = 31;

c = 1;
line = fgetl(fileID);
while (strcmp(line, '**NODE DATA END')==0);
    line = fgetl(fileID);
    c = c+1;
end
endRow = c-2;
fclose('all');
fileID = fopen(filename, 'r');

%% Read columns of data according to format string.
% This call is based on the structure of the file used to generate
this
% code. If an error occurs for a different file, try regenerating the
code
% from the Import Tool.
dataArray = textscan(fileID, formatSpec, endRow-startRow+1,
'Delimiter', delimiter, 'EmptyValue' ,NaN,'HeaderLines', startRow-1,
'ReturnOnError', false);

%% Close the text file.
fclose(fileID);

%% Post processing for unimportable data.
% No unimportable data rules were applied during the import, so no
post
% processing code is included. To generate code which works for
% unimportable data, select unimportable cells in a file and
regenerate the
% script.

%% Create output variable
Nodes = [dataArray{1:end-1}];
%% Clear temporary variables
```

```
clearvars filename delimiter startRow endRow formatSpec fileID
dataArray ans;


% The aim is to capture point cloud of the labrum apex
% Divide the cylindrical space into pies by defining an increment
angle
% Import the coordinates of all nodes on the soft tissues surface
% Find the "highest" point in each pie

%% Initialise variables
prompt = {'Enter the increment angle in degree:','Enter the number of
large displacement looking for:',...
    'Enter the first .inp location:','Enter the second .inp
location:'};
title = 'Input';
answer = inputdlg(prompt,title);

% Set resolution for apex reconstruction
Increment = str2double(answer{1});
TotalPie = 360/Increment;
Apex = zeros(TotalPie, 3);
Apex = min(Apex, -15);
Apex2 = zeros(TotalPie, 3);
Apex2 = min(Apex2, -15);
TotalDisp = str2double(answer{2});

% Read coordinates at rest from .inp and translate centre to (0,0,0)
Nodes = Labrumread(answer{3});
sz = size(Nodes);
TotalNode = sz(1);
Mean = mean(Nodes);
MeaN = repmat(Mean,TotalNode,1);
Nodes = Nodes - MeaN;

% Read coordinates during load and translate using the previous vector
Nodes2 = Labrumread(answer{4});
sz2 = size(Nodes2);
TotalNode2 = sz2(1);
MeaN2 = repmat(Mean,TotalNode2,1);
Nodes2 = Nodes2 - MeaN2;

%% Find node angle and combine into node matrix
NodeAngle = zeros(TotalNode, 1);
NodeNo1 = 1;
while NodeNo1 <= TotalNode
    if Nodes(NodeNo1, 1) >= 0 && Nodes(NodeNo1, 2) >= 0
        NodeAngle(NodeNo1) = atand(Nodes(NodeNo1, 2)/Nodes(NodeNo1,
1));
    elseif Nodes(NodeNo1, 1) >= 0 && Nodes(NodeNo1, 2) < 0
        NodeAngle(NodeNo1) = atand(Nodes(NodeNo1, 2)/Nodes(NodeNo1,
1))+360;
    else
        NodeAngle(NodeNo1) = atand(Nodes(NodeNo1, 2)/Nodes(NodeNo1,
1))+180;
    end
    NodeNo1 = NodeNo1 + 1;
end
Nodes = [Nodes(:,1:3) NodeAngle];

% Find apex in [Node], acetabulum at rest
PieNo1 = 1;
```

```
while PieNo1 <=TotalPie
    Anglemin = Increment*(PieNo1 - 1);
    Anglemax = Increment*PieNo1;
    NodeNo2 = 1;
    while NodeNo2 <= TotalNode
        if Anglemin <= Nodes(NodeNo2, 4) && Anglemax > Nodes(NodeNo2,
4) && Nodes(NodeNo2, 3) >= Apex(PieNo1, 3)
            Apex(PieNo1, 3) = Nodes(NodeNo2, 3);
            Apex(PieNo1, 1) = Nodes(NodeNo2, 1);
            Apex(PieNo1, 2) = Nodes(NodeNo2, 2);
        end
        NodeNo2 = NodeNo2 + 1;
    end
    PieNo1 = PieNo1+1;
end

% Repeat the procedure for [Nodes2], acetabulum during load
NodeAngle2 = zeros(TotalNode2, 1);
NodeNo3 = 1;
while NodeNo3 <= TotalNode2
    if Nodes2(NodeNo3, 1) >= 0 && Nodes2(NodeNo3, 2) >= 0
        NodeAngle2(NodeNo3) = atand(Nodes2(NodeNo3, 2)/Nodes2(NodeNo3,
1));
    elseif Nodes2(NodeNo3, 1) >= 0 && Nodes2(NodeNo3, 2) < 0
        NodeAngle2(NodeNo3) = atand(Nodes2(NodeNo3, 2)/Nodes2(NodeNo3,
1))+360;
    else
        NodeAngle2(NodeNo3) = atand(Nodes2(NodeNo3, 2)/Nodes2(NodeNo3,
1))+180;
    end
    NodeNo3 = NodeNo3 + 1;
end
Nodes2 = [Nodes2(:,1:3) NodeAngle2];

PieNo2 = 1;
while PieNo2 <=TotalPie
    Anglemin = Increment*(PieNo2 - 1);
    Anglemax = Increment*PieNo2;
    NodeNo4 = 1;
    while NodeNo4 <= TotalNode2
        if Anglemin <= Nodes2(NodeNo4, 4) && Anglemax >
Nodes2(NodeNo4, 4) && Nodes2(NodeNo4, 3) >= Apex2(PieNo2, 3)
            Apex2(PieNo2, 3) = Nodes2(NodeNo4, 3);
            Apex2(PieNo2, 1) = Nodes2(NodeNo4, 1);
            Apex2(PieNo2, 2) = Nodes2(NodeNo4, 2);
        end
        NodeNo4 = NodeNo4 + 1;
    end
    PieNo2 = PieNo2+1;
end

%% Plot apex before and during load
figure
grid on
hold on
x = Apex(:,1);
y = Apex(:,2);
z = Apex(:,3);
plot3 (x,y,z, 'r*');
xlim([-20 40]);
ylim([-20 40]);
zlim([-20 40]);
x2 = Apex2(:,1);
```

```
y2 = Apex2(:,2);
z2 = Apex2(:,3);
plot3 (x2,y2,z2, 'bo');
view(3);

% Find n largest displacement
NodeNo5 = 1;
Disp = zeros(TotalPie,1);
while NodeNo5 <= TotalPie
    Disp(NodeNo5) = sqrt((Apex2(NodeNo5,1)-
Apex(NodeNo5,1))^2+(Apex2(NodeNo5,2)-
Apex(NodeNo5,2))^2+(Apex2(NodeNo5,3)-Apex(NodeNo5,3))^2);
    NodeNo5 = NodeNo5 + 1;
end
Order = (1:1:TotalPie);
Order = Order';
Disp = horzcat(Order, Disp);
Dispbk = Disp;

NodeNo6 = 1;
DispLarge = zeros(TotalDisp,2);
while NodeNo6 <= TotalDisp
    count = 1;
    while count <= TotalPie
        if Dispbk(count, 2) > DispLarge(NodeNo6, 2)
            DispLarge(NodeNo6, 2) = Dispbk(count, 2);
            DispLarge(NodeNo6, 1) = Dispbk(count, 1);
            Dispbk(count, 2) = 0;
        end
        count = count + 1;
    end
    NodeNo6 = NodeNo6 + 1;
end
```

MATLAB code for labrum apex reconstruction and measurement as described in section 0.

# Appendix E

# Experiment procedure

**1 Dissection** : To dissect the hip joint from the whole porcine leg

- Cut through and remove the skin
- Dissect the tissues around the femur
- Dissect the femur to leave the shaft at least 50 mm long
- Dissect the soft tissues around the hip joint but keep the capsule intact
- Spray the hip joint with PBS and cover with clean tissues
- Pack the hip joint in plastic bag and store in the fridge

**2 Cementing** : To disarticulate the joint and cement the femur and acetabulum in pots using PMMA

- Unpack the hip joint
- Carefully cut through the capsule and dissect the ligament of the head of femur
- Spray the femur with PBS and cover with clean tissues
- Remove the soft tissues around the acetabulum and labrum
- Try to fit the acetabulum into the pot
- Dissect the bone on the back of the acetabulum where necessary
- Align the superior-anterior portion of the cartilage-labral junction in the centre of the pot. Fix the acetabulum position using long supporting screws
- Cement the acetabulum component
- Remove the soft tissues around the femoral head and femoral neck
- Dissect the shaft where necessary
- Align the femoral head in the centre of the pot. Fix the femur position using long supporting screws
- Cement the femur component
- Unscrew the supporting screws

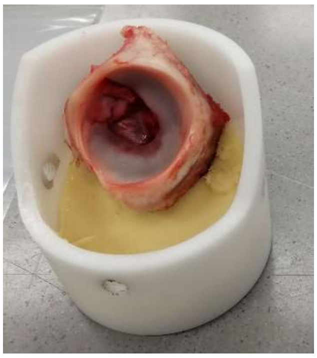

**3 Assembly** : To bring the femur and acetabulum together and assemble the hip loading rig

- Warm up X-ray
- Apply NaI solution by soaking the femoral head into the liquid for five minutes. Also cover the proximal end of the femoral neck in case the neck will have contact with acetabulum at inferior
- Disassemble the cap and base of the rig
- Attach the femur pot under the load cell
- Bring the acetabulum and femur together
- Attach the acetabulum pot to the base
- Screw and seal the cap of the rig
- Screw and seal the base of the rig
- Make a note of the relative position of the pots to the rig

**4 First scan** : To obtain CT images of the hip joint before load

- Connect the load cell reader
- Apply displacement through the cap until the femur and acetabulum are just in contact
- Scan the joint using XtremeCT

**5 Second scan** : To obtain CT images of the hip joint during load

- Connect the load cell reader
- Apply displacement through the cap with two full turns and record the load
- Wait for one hour and record the load
- Scan the joint using XtremeCT
- Record the load and disassemble the rig
- Store the two pots in the fridge with PBS

**6 Labrum cut** : To induce labrum damage

- Unpack the two pots
- Cut through the labrum where close to the edge of the contact region. Stop when the blade reaches the bone
- Repeat procedure 3

**7 Third scan** : To obtain CT images of the hip joint during load with labrum cut

- Repeat procedure 5 but skip the storage step
- Dispose cemented tissues
- Clean equipment

The experiment procedure as described in section 4.3.

# Appendix F

## Modelling of labrum overhang: model PH11

The selected image slice for model PH11 is shown in Figure G6.1-A. As mentioned in section 5.2.1, the labrum overhang was observed at the contact site. In Figure G6.2-B, for sample PH11 under load, the labrum was pushed and deformed to fit the femoral shape. Good conformity was established in PH11 under load. The geometry around the labrum apex looked similar to the initial condition (unloaded tissue) in PH10 and PH12.

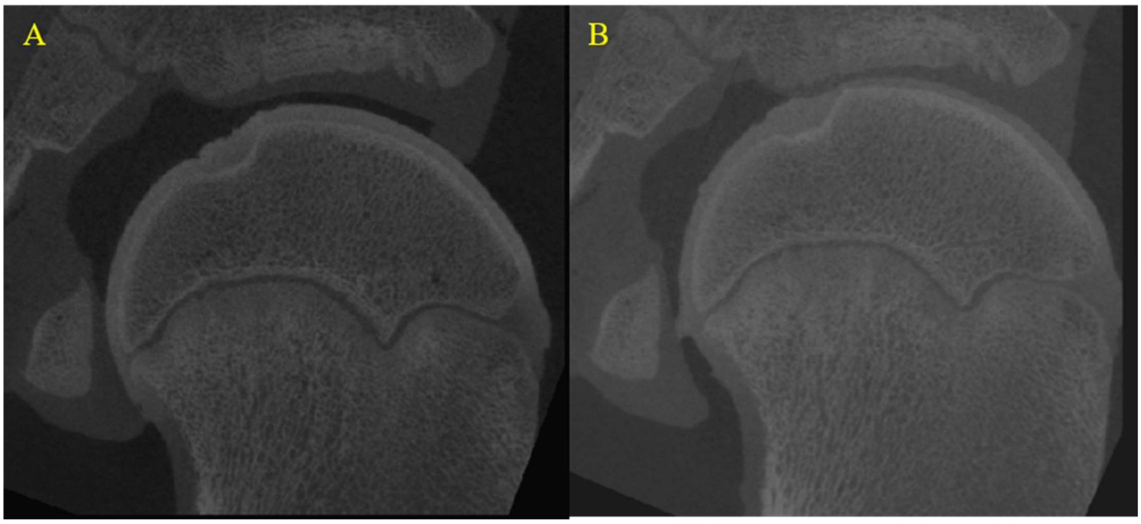

**Figure G6.1 Image slice at focused contact area for PH11. A, sample PH11 before load; B, sample PH11 under load.**

The contact pressure of PH11 was illustrated in Figure G6.2 at an early abortion at 31.36% of the total load step. Peak contact pressure of 9 MPa was measured at the corner of the labrum overhang. The sharp edge of the overhang was causing high pressure on the femoral cartilage and refused to deform to fit the femoral head shape.

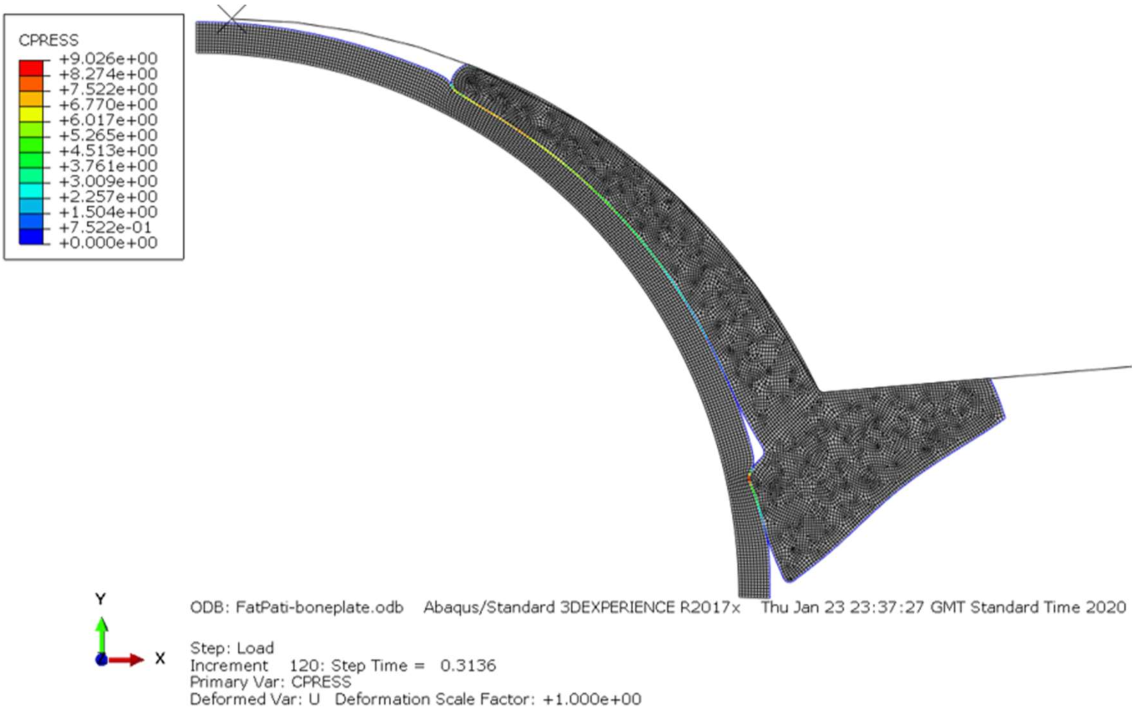

**Figure G6.2 Contact pressure in model PH11 at 31.36% of the load step.**

# Appendix G

## List of citation of figures

1. Figure 2.1 Structure and components of human hip joint (figure source: Gileshugo 2011, under CC0 license), free permission.
2. Figure 2.3 Cross section view of acetabular rim. Solid line indicates the boundary between labrum and cartilage at the coincidence of concave acetabulum and convex rim. Dotted line suggests an alternative boundary at medial where the labrum is relatively longer. (figure source: Henak et al., 2011, under CC-BY license), permission obtained.
3. Figure 2.4 Anatomical planes of human body and clinical directions (figure source: Carl Fredrik Sjöland 2014, under CC0 license), free permission.
4. Figure 2.5 Schematic of hip motions. (figure source: Gileshugo 2011, under CC0 license), free permission.
5. Figure 2.6 Hip angle of rotation during daily activities with wide ROM. Flex, flexion; Extn, extension; Abdt, abduction; Addt, adduction; ER, external rotation; IR, internal rotation., figure produced from published data.
6. Figure 2.7 Classification of femoroacetabular impingement (figure source: Smith & Nephew 2011, under CC0 license), free permission.
7. Figure 2.8 Radiographic measurements for femoral head shape abnormality. A, measurement of centrum collum disphyseal; B, measurement of alpha angle; C, measurement of centre edge angle., free permission.
8. Figure 2.9 A hip with cam-type FAI before and after rotation at the cross section view of the cam deformity. , free permission.